

N O T I C E

THIS DOCUMENT HAS BEEN REPRODUCED FROM
MICROFICHE. ALTHOUGH IT IS RECOGNIZED THAT
CERTAIN PORTIONS ARE ILLEGIBLE, IT IS BEING RELEASED
IN THE INTEREST OF MAKING AVAILABLE AS MUCH
INFORMATION AS POSSIBLE

NASA CR-165408

(NASA-CR-165408) COOLED VARIABLE-AREA
RADIAL TURBINE TECHNOLOGY PROGRAM Final
Report (Garrett Turbine Engine Co.) 303 p
HC A14/MF A01 CSCL 21E

N82-19221

Unclass
G3/07 09240

COOLED, VARIABLE-AREA RADIAL TURBINE PROGRAM

G.D. Large

L.J. Meyer

Garrett Turbine Engine Company
A Division of the Garrett Corporation

JANUARY 1982



Prepared for

NATIONAL AERONAUTICS AND
SPACE ADMINISTRATION

Lewis Research Center

Under Contract No. NAS3-22004

1. Report No. NASA CR-165408	2. Government Accession No.	3. Recipient's Catalog No.	
4. Title and Subtitle Final Report - Cooled Variable-Area Radial Turbine Technology Program		5. Report Date January 1982	
		6. Performing Organization Code	
7. Author(s) G. D. Large and L. J. Meyer		8. Performing Organization Report No. 21-3914	
		10. Work Unit No.	
9. Performing Organization Name and Address Garrett Turbine Engine Company 111 S. 34th Street, P.O. Box 5217 Phoenix, Arizona 85010		11. Contract or Grant No. NAS3-22004	
		13. Type of Report and Period Covered Contractor Report	
12. Sponsoring Agency Name and Address U.S. Army Research & Technology Laboratories (AVRADCOM) Propulsion Laboratory Lewis Research Center Cleveland, Ohio 44135		14. Sponsoring Agency Code 1L162209AH76	
		15. Supplementary Notes Project Manager, Peter L. Meitner, U.S. Army Research and Technology Laboratories (AVRADCOM), Propulsion Laboratory, Lewis Research Center, Cleveland, Ohio 44135.	
16. Abstract <p>The objective of this study was a conceptual evaluation and design analyses of a cooled variable-area radial turbine capable of maintaining nearly constant high-efficiency when operated at a constant speed and pressure ratio over a range of flows corresponding to 50- to 100-percent maximum engine power. The results showed that a 1589K (2400°F) turbine was feasible that would satisfy a 4000-hour duty cycle life goal. The final design feasibility is based on 1988 material technology goals. A peak aerodynamic stage total efficiency of 0.88 was predicted at 100 percent power. Two candidate stators were identified: an articulated trailing-edge and a locally movable sidewall. Both concepts must be experimentally evaluated to determine the optimum configuration. A follow-on test program is proposed for this evaluation.</p>			
17. Key Words (Suggested by Author(s)) Radial Turbine Variable Geometry Cooled Turbine Cooled Vane		18. Distribution Statement	
19. Security Classif. (of this report) UNCLASSIFIED	20. Security Classif. (of this page) UNCLASSIFIED	21. No. of Pages 285	22. Price*

* For sale by the National Technical Information Service, Springfield, Virginia 22161

TABLE OF CONTENTS

	<u>Page</u>
1.0 SUMMARY	1
2.0 INTRODUCTION	3
2.1 Background	3
2.2 Program Objective	3
2.3 Cooled Radial Rotor Technology	3
2.4 Major Program Considerations	4
3.0 AERODYNAMIC PERFORMANCE CORRELATIONS AND SYSTEM OPTIMIZATION TECHNIQUE	5
3.1 Design-Point Performance Evaluation	5
3.2 Off-Design Performance Evaluation	15
3.3 Effects of Cooling Flow and Nozzle Leakage	15
4.0 TASK I - STATOR AND ROTOR CONCEPTS EVALUATION	20
4.1 Variable-Area Radial Turbine Requirements	20
4.2 100-Percent Power Cycle Study	21
4.3 Preliminary Parametric Study (Stator/Rotor Concept Evaluation)	21
4.3.1 Design Point Study	21
4.3.2 Turbine Off-Design Performance Characteristics	37
4.4 Stator Concepts Aero/Mechanical Evaluation	43
4.4.1 Vane Profile Design for Stator Concepts	43
4.4.2 Full-Vane Rotation Concept	47
4.4.3 Articulated Trailing-Edge Concept	47
4.4.4 Insertable Minivane Concept	47
4.4.5 Locally Movable Sidewall Concept	50
4.5 Stator Material Evaluation	50
4.5.1 Airfoil	50
4.5.1.1 Stress Rupture	53
4.5.1.2 Coated Oxidation Resistance	53
4.5.1.3 Overtemperature Capability	56
4.5.1.4 Thermal Fatigue	56
4.5.2 Sidewall	57
4.6 Recommended Variable Stator Concepts	57
4.7 Turbine Rotor Materials Evaluation	58

TABLE OF CONTENTS (Contd)

	<u>Page</u>
4.8 Cooled Rotor Concept Aero/Mechanical Evaluation	59
4.9 Recommended Cooled Rotor Concept	65
5.0 TASK II - DETAILED PARAMETRIC STUDY	68
5.1 Selected Speed and Cycle Conditions	68
5.2 Effects of Stage Cooling Flows	71
5.3 Effects of Stator Leakage	75
5.4 Cooled Rotor Aerodynamic Analysis	77
5.5 Uncooled Rotor Aerodynamic Evaluation	89
5.6 Uncooled Rotor Mechanical Analysis	93
5.7 Cooled Rotor Mechanical Analysis	93
5.7.1 Influence of Radius Ratio on Rotor Stresses	93
5.7.2 Incorporation of Cooled, Dual-Alloy Configuration	98
5.7.3 Optimum Rotor Selection	109
5.8 Selected Stage Configuration	114
6.0 TASKS III AND IV - VARIABLE-AREA STATOR AERODYNAMIC AND MECHANICAL DESIGN	119
6.1 Detailed Aerodynamic Design Procedure	119
6.2 Articulated Trailing-Edge Stator - Detailed Aerodynamic Design	119
6.3 Detailed Aerodynamic Design of the Movable Sidewall Stator	122
6.4 Stator Flow Field - 3-Dimensional, Finite-Element Analysis	135
6.4.1 Background	135
6.4.2 Analysis and Program Description	137
6.4.3 Application of the Finite-Element Flow Analysis to the Variable Geometry Stator	138
6.5 Detailed Aerodynamic Design Conclusions	150
6.6 Articulated Trailing-Edge Stator - Mechanical Substantiation	159
6.6.1 Mechanical Description	159
6.6.2 Impact of Cycle Conditions on Stator Design	159
6.6.3 Stator Aerodynamic Boundary Conditions	160
6.6.4 Vane-Cooling Circuit Design	165
6.6.5 Sidewall Cooling Design	172

TABLE OF CONTENTS (Contd)

	<u>Page</u>
6.7 Movable Sidewall Stator - Mechanical Substantiation	177
6.7.1 Mechanical Description	177
7.0 TASKS III AND IV - COOLED ROTOR DETAILED AERODYNAMIC DESIGN AND MECHANICAL SUBSTANTIATION	196
7.1 Cooled Rotor Detailed Aerodynamic Design	196
7.1.1 Rotor-Blade Geometry Definition	196
7.1.2 Rotor Aerodynamic Flow Analysis	196
7.2 Detailed Substantiation of Cooled Rotor Design	201
7.2.1 Mechanical Configuration	201
7.2.2 Rotor Thermal Design Analysis	205
7.2.2.1 Rotor Blade Aerodynamic Boundary Conditions	205
7.2.2.2 Geometric Assumptions	206
7.2.2.3 Blade Cooling Configuration	206
7.2.2.4 Thermal Analysis Method	210
7.2.2.5 Blade Cooling Passage Design	210
7.2.2.5.1 Hub Supply Passage	210
7.2.2.5.2 Inducer Passages	211
7.2.2.5.3 Inducer Tip	211
7.2.2.5.4 Exducer Region	215
7.2.2.6 Thermal-Analysis Results	217
7.2.3 Rotor Mechanical Design Analysis	225
7.2.3.1 Blade Configuration	225
7.2.3.2 Disk Configuration	228
7.2.3.3 Stress Analysis	234
7.2.3.4 Vibration Analysis	254
7.2.3.5 Life Analysis	254
7.2.3.6 Rotor Design - Conclusions and Recommendations	263
8.0 FINAL PERFORMANCE EVALUATION - SELECTED COOLED, VARIABLE-AREA RADIAL TURBINE DESIGN	264
9.0 FOLLOW-ON TEST PROGRAM PLAN	270
9.1 Program Objective	270
9.2 Test Rig Description	270

TABLE OF CONTENTS (Contd)

	<u>Page</u>
9.3 Overall Turbine Performance Measurement Instrumentation	271
9.4 Program Plan	271
10.0 CONCLUSIONS AND RECOMMENDATIONS	275
11.0 REFERENCES	277

LIST OF ILLUSTRATIONS

<u>Figure</u>	<u>Title</u>	<u>Page</u>
1	NASA Specific Speed Correlation Corrected to Zero Clearance	6
2	Variation of Optimum Tip Speed with Turbine Stage Specific Work	7
3	Cooled, Variable-Area Radial Turbine, System Definition	8
4	Effects of Swirl on Interstage Duct Loss Coefficient	10
5	Results of System Optimization for TARADCOM Advanced Radial Turbine	12
6	Summary of Radial Turbine Rotor Clearance Effects	14
7	Predicted and Tested Off-Design Efficiency Characteristic Comparison	16
8	Predicted and Tested Off-Design Flow Characteristic Comparison	17
9	1-Dimensional Vector Diagram Comparison (100-Percent and 50-Percent Inlet Corrected Flows)	18
10	Cooled, Variable-Area Radial Turbine Study, $T_4 = 1533\text{K}$ (2300°F) at Maximum (100-Percent) Power	23
11	Cooled, Variable-Area Radial Turbine Study, $T_4 = 1589\text{K}$ (2400°F) at Maximum (100-Percent) Power	24
12	Cooled, Variable-Area Radial Turbine Study, $T_4 = 1644\text{K}$ (2500°F) at Maximum (100-Percent) Power	25
13	Uncooled, Variable-Area Radial Turbine Study, $T_4 = 1478\text{K}$ (2200°F) at Maximum (100-Percent) Power	26
14	Preliminary Parametric Study for Cooled Rotor Concepts, 12:1 Cycle Pressure Ratio, $T_4 = 1644\text{K}$ (2500°F), $N = 6178$ rad/s (59,000 RPM)	29

LIST OF ILLUSTRATIONS (Contd)

<u>Figure</u>	<u>Title</u>	<u>Page</u>
15	Preliminary Parametric Study for Cooled Rotor Concepts at 16:1 Cycle Pressure Ratio, $T_4 = 1644$ (2500°F) $N = 6807$ rad/s (65,000 RPM)	30
16	Preliminary Parametric Study for Cooled Rotor Concepts at 20:1 Cycle Pressure Ratio, $T_4 = 1644K$ (2500°F), $N = 7435$ rad/s (71,000 RPM)	31
17	Parametric Study for Cooled Rotor Concepts, 1644K (2500°F) Case	32
18	Effect of Cycle Pressure Ratio on Flow-Path Geometry	33
19	Characteristic Rotors for Evaluation of Concepts	34
20	Effect of Rotational Speed on Turbine Performance and Geometry at 1644K (2500°F)	35
21	Effects of Stator Exit Angle on Stage and Nozzle Design at 1644K (2500°F), 7435 rad/s (71,000 RPM) and at 671 m/s (2200 Ft/Sec)	36
22	Selected Maximum Power Design Points for Off-Design Analysis. 16:1 Cycle Pressure Ratio, $T_4 = 1645K$ (2500°F) and $N = 6807$ rad/sec (65,000 RPM)	38
23	Off-Design Turbine Characteristics for Case No. 1 at 1644K (2500°F), 6807 rad/s (65,000 RPM), and 640 m/s (2100 Ft/Sec)	39
24	Off-Design Turbine Characteristics for Case No. 2 at 1644K (2500°F), 6807 rad/s (65,000 RPM) and 671 m/s (2200 Ft/Sec)	40
25	Off-Design Turbine Characteristics for Case No. 3 at 1644K (2500°F) 6807 rad/s (65,000 RPM) and 671 m/s (2200 Ft/Sec)	41
26	Case No. 3 Turbine 1-Dimensional Vector Diagrams for 60- and 100-Percent Power at 1644K (2500°F), 6807 rad/s (65,000 RPM) and $R/R = 0.643$	42
27	Stator Profile Design for Variable Area Concepts Evaluation (19 Vanes)	45

LIST OF ILLUSTRATIONS (Contd)

<u>Figure</u>	<u>Title</u>	<u>Page</u>
28	Stator Ring at Maximum Power Setting	46
29	Full Vane Rotation, Nozzle Area Variation Concept	48
30	Articulated Trailing-Edge Nozzle Area Variation Concept	49
31	Insertable Minivane, Nozzle Area Variation Concept	51
32	Locally Movable Sidewall, Nozzle Area Variation Concept	52
33	Larson-Miller Parameter Showing Stress Life Capabilities of Candidate Superalloys	54
34	Stress-Rupture Capabilities of Candidate Turbine Superalloys	55
35	Tensile Properties of Hub Materials, Dual-Alloy Turbine Rotor	60
36	Comparison of 4000-Hour Mission Life and Density-Corrected Stresses at Inducer Tip at 640 m/s (2100 Ft/Sec)	62
37	USARTL Cooled, Laminated Rotor Design	63
38	Preliminary Cooled Radial Rotor Design	64
39	Recommended Cooled Rotor Concept	67
40	Cooled, Variable-Area Radial Turbine Compressor Speed Study	69
41	Compressor Turbine Efficiency Product Characteristics	70
42	Turbine Cooling Flow Model for the Detailed Parametric Study	72
43	Articulated Trailing-Edge Nozzle, Sidewall Clearance Loss Models	76
44	Effect of Stator Leakage on Off-Design Performance	78

LIST OF ILLUSTRATIONS (Contd)

<u>Figure</u>	<u>Title</u>	<u>Page</u>
45	Detailed Parametric Study, $\beta_B = 0$ radian (0°), Maximum Power Condition	79
46	Detailed Parametric Study, $\beta_B = 0.17$ radian (10°), Maximum Power Condition	80
47	Detailed Parametric Study, $\beta_B = 0.35$ radian (20°), Maximum Power Condition	81
48	Cooled Rotor Configurations from Detailed Parametric Study	83
49	Off-Design Turbine Characteristics With $\lambda_4 = 1.04$ 1589K (2400°F), 5969 rad/s (57,000 RPM), and 640 m/s (2100 Ft/Sec), R/R = 0.60, $\beta_B = 0$. rad (0°).	84
50	Off-Design Turbine Characteristics with $\lambda_4 = 1.0$, 1589K (2400°F), 5969 rad/s (57,000 RPM), and 640 m/s (2100 Ft/Sec), R/R = 0.65, $\beta_B = 0$ rad (0°)	85
51	Off-Design Turbine Characteristics with $\lambda_4 = 1.0$, 1589K (2400°F), 5969 rad/s (57,000 RPM) and 640 m/s (2100 Ft/Sec), R/R = 0.65, $\beta_B = 0.17$ rad (10°)	86
52	Off-Design Turbine Characteristics With $\lambda_4 = 1.0$, 1589 K (2400°F), 5969 rad/s (57,000 RPM) and 640 m/s (2100 Ft/Sec), R/R = 0.65, $\beta_B = 0.35$ Rad (20°)	87
53	Off-Design Turbine Characteristics with $\lambda_4 = 1.0$, 1589K (2400°F), 5969 rad/s (57,000 RPM), 640 m/s (2100 Ft/Sec), R/R = 0.70, $\beta_B = 0$ rad (0°)	88
54	Detailed Parametric Study for Uncooled rotor with 14 Blades at Maximum Power, 5969 rad/s (57,000 RPM), 1478K (2200°F), and 640 m/s (2100 Ft/Sec)	90
55	Off-Design Analysis for Uncooled Rotor at 1478K (2200°F), $\beta_B = 0.17$ rad (10°), $\lambda_4 = 0.975$, R/R = 0.65, 640 m/s (2100 Ft/Sec) and 5969 rad/s (57,000 RPM)	91
56	Uncooled Rotor Configuration	92
57	Mode Temperature Distribution, Uncooled Rotor	94

LIST OF ILLUSTRATIONS (Contd)

<u>Figure</u>	<u>Title</u>	<u>Page</u>
58	Normal Thickness Distribution, Uncooled Rotor	95
59	Uncooled 1478K (2200°F) Rotor, 2-Dimensional Finite-Element Model	96
60	Effect of Rotor Flow Path on Disk Stress	99
61	Thickness Distribution for 0.67-Radius-Ratio Configuration	100
62	Normal Blade Wall Thickness, Dual-Alloy Geometry Study	102
63	Single-Alloy Solid Rotor at Room Temperature	103
64	Dual-Alloy Rotor With and Without Full-Cooling Passage at Room Temperature	105
65	Dual-Alloy Solid Rotor with Full-Cooling Passage at Maximum Temperature	106
66	Dual-Alloy Solid Rotor with Bondline at Largest Practical Radius, Room Temperature	107
67	Dual-Alloy Solid Rotor with Bondline at Largest Radius and With Full-Cooling Passage, Room Temperature	108
68	Dual-Alloy Rotor, Highest Bondline Radius, Full-Cooling Passage, Maximum Power Temperature	110
69	Assumed Temperatures and Equivalent Stresses	112
70	Effects of Radius Ratio and Inlet Blade Angle on System Performance at 60-Percent Power	115
71	Selected Cooled Rotor, Meridional Flow Path at 1589K (2400°F), U_{T_4} of 640 m/s (2100 Ft/Sec) and 5969 rad/s (57,000 RPM)	116
72	1-Dimensional Vector Diagram for Selected Cooled-Stage Configuration, 100-Percent Power	117
73	Articulated Trailing-Edge Vane Concept	120
74	Articulated Trailing-Edge at 100-Percent Power Design Point (Rotated Closed at 60-Percent Flow)	121

LIST OF ILLUSTRATIONS (Contd)

<u>Figure</u>	<u>Title</u>	<u>Page</u>
75	Articulated Trailing-Edge Configuration, Vane Velocity Distributions for 100-Percent Power Design Point (Stream-Function Solutions)	122
76	Articulated Trailing-Edge, 60-Percent Power Design Point (Rotated Open at 100-Percent Flow)	124
77	Articulated Trailing-Edge Configuration, Vane Velocity Distribution for 60-Percent Power Design Point (Stream Function Solution)	125
78	Final Articulated Trailing-Edge 17 Vane Profile Design for 80-Percent Power Design Point	126
79	Articulated Trailing-Edge Concept, Final Stator, Inlet Meridional Geometry	127
80	Vane Velocity Distribution for Final Articulated Trailing-Edge Stator Design (17 Vanes)	128
81	Movable Sidewall Original Configuration	129
82	Movable Sidewall Configuration (Purely Rotating Insert), Schematic Diagram	131
83	Movable Sidewall Configuration (Rotating-Translating Insert), Schematic Diagram	132
84	Final Vane Profile, Movable Sidewall Concept	133
85	Movable Sidewall Stator Vane Velocities with 19 Vanes (Stream-Function Solution)	134
86	Stator Finite-Element Analysis Discretization Model	139
87	Articulated Trailing-Edge Configuration, 60-Percent Power Setting, 80-Percent Power Design Point	140
88	Articulated Trailing-Edge Configuration, 100-Percent Power Setting, at 80-Percent Power Design Point	141
89	Finite-Element Model for 100-Percent Flow Geometry	142

LIST OF ILLUSTRATIONS (Contd)

<u>Figure</u>	<u>Title</u>	<u>Page</u>
90	Finite-Element Model for Movable Sidewall Configuration, (Purely Rotating Insert) at 60-Percent Power Setting	143
91	Finite-Element Model for Movable Sidewall Configuration, (Rotating-Translating Insert) at 60-Percent Power Setting	144
92	Contours of the Flow Passage Axial Width Within the Purely Rotating Insert at 60-Percent Flow Setting	145
93	Contours of the Flow-Passage Axial Width within the Rotating-Translating Insert at 60-Percent Flow Setting	146
94	Stator Geometry and Station Designation	147
95	Articulated Trailing-Edge Configuration Vane Velocity Distribution for 100-Percent Power Setting (Design Point: 80-Percent Power)	148
96	Articulated Trailing-Edge Configuration Vane Velocity Distribution for 60-Percent Power Setting (Design Point at 80-Percent Power, 3-Dimensional Finite-Element Analysis)	149
97	Movable Sidewall Configuration Vane Velocity Distribution for 100-Percent Power	151
98	Purely Rotating Sidewall Configuration Vane Velocity Distribution for 60-Percent Power	152
99	Rotating-Translating Movable Sidewall Configuration, Vane Velocity Distribution for 60-Percent Power Setting	153
100	Movable Sidewall Configuration, Critical Mach No. Contours for 100-Percent Power Setting (3-Dimensional Finite-Element Analysis)	154
101	Purely Rotating Sidewall Configuration, Critical Mach No. Contours for 60-Percent Power Setting (3-Dimensional Finite-Element Analysis)	155
102	Rotating-Translating Sidewall Configuration, Critical Mach No. Contours for 60-Percent Power Setting (3-Dimensional Finite-Element Analysis)	156

LIST OF ILLUSTRATIONS (Contd)

<u>Figure</u>	<u>Title</u>	<u>Page</u>
103	Comparison of Flow Properties at Stator Exit Station (Three-Dimensional Finite Element Analysis	157
104	Inlet Gas Temperature Versus Coolant-Added Variable-Area Stator	161
105	Articulated Trailing-Edge Stator Vane Velocities at 100-Percent Power, Katsanis Solution	162
106	Articulated Trailing-Edge Stator Vane Velocities at 60-Percent Power	163
107	Articulated Trailing-Edge Stator Vane Static Pressure Distribution	164
108	Articulated Trailing-Edge Stator Vane, Suction-Side Surface Heat-Transfer Coefficients	166
109	Articulated Trailing-Edge Stator Vane, Pressure-Side Surface Heat-Transfer Coefficients	167
110	Thermal Loading on Articulated Trailing-Edge (No Film Cooling)	168
111	Articulated Trailing-Edge Stator Vane Forward Section, Cooling Configuration	170
112	Articulated Trailing-Edge Stator Vane Cooling Configuration	171
113	Articulated Trailing-Edge Stator Vane	173
114	Articulated Trailing-Edge Stator Vane Cooling Flow Summary	174
115	Articulated Trailing-Edge Stator Sidewall Viewed from Flow-Path Side	176
116	Movable Sidewall - Baseline Configuration	178
117	Variable Sidewall Concept with Purely Rotating Insert	179
118	Variable Sidewall Concept with Rotating-Translating Insert	183

LIST OF ILLUSTRATIONS (Contd)

<u>Figure</u>	<u>Title</u>	<u>Page</u>
119	Rotating-Translating Sidewall Concept, Surface Static Pressure Distribution	185
120	Rotating-Translating Sidewall Concept Heat Transfer Coefficients	187
121	A Preliminary Concept for the Movable Sidewall Vane	188
122	Movable Sidewall Configuration Showing Vane Cooling	189
123	Movable Sidewall Configuration Vane, Flow Distribution	191
124	Static Pressure Distribution Along the Midchannel Streamline of the Rotating-Translating Sidewall Stator	192
125	Rotating-Translating Sidewall Configuration Cooling, Forward Sidewall at 60-Percent Power	194
126	Rotating-Translating Movable Sidewall Stator, Heat Transfer Coefficients, Midchannel Streamlines	195
127	Radial Rotor Geometry Program Capabilities	197
128	Final Variable-Area Radial Turbine Meridional Flow Path with Articulated Trailing Edge Stator Shown at 100-Percent Power	199
129	Final Rotor Blade Angle Distribution	200
130	Rotor Blade Velocity Distribution at 60- and 100-Percent Power Condition (14 Blades)	202
131	Variable-Area Radial Turbine Vector Diagram, 60-Percent Power Condition	203
132	Variable-Area Radial Turbine Vector Diagram, 100-Percent Power Condition	204
133	Airfoil Cooling, Final Configuration	208
134	Cooling Passage Internal Pressure at Blade Periphery (Choke Discharge Orifice Requirement)	209
135	Hub Supply Passage for Blade Cooling Configuration	212

LIST OF ILLUSTRATIONS (Contd)

<u>Figure</u>	<u>Title</u>	<u>Page</u>
136	Final Inducer Cooling Configuration Showing Cooling Flow Passages	213
137	Inducer Wall Target Temperatures Versus Achieved Temperatures	214
138	Inducer Tip Cooling Configuration with Impingement Cooling Techniques	216
139	Exducer Cooling Passage Configuration	218
140	Final Rotor Cooling Flow Design (Percent of Core Flow at 60- and 100-Percent Power)	219
141	Pressure-Side External Surface Temperature Distribution at 100-Percent Power	220
142	Pressure-Side Internal Surface, Temperature Distribution at 100-Percent Power	221
143	Suction-Side Internal Surface Temperature Distribution at 100-Percent Power	222
144	Suction-Side External Surface Temperature Distribution at 100-Percent Power	223
145	Disk Axisymmetric Temperature Distribution at 100-Percent Power	224
146	Blade Temperature Distribution for Cooled Rotor Configuration at 100-Percent Power	226
147	Blade Thickness Distribution for Cooled Rotor Configuration	227
148	Rake Angle and Polar Angle Relationships	229
149	Suction-Side Surface Wall Thickness Distribution, Final Configuration	230
150	Pressure-Side Surface Wall Thickness Distribution, Final Configuration	231
151	Total Wall Thickness Distribution (Pressure Plus Suction Side Thickness)	232
152	Blade Total Surface-to-Surface Distance Distribution	233

LIST OF ILLUSTRATIONS (Contd)

<u>Figure</u>	<u>Title</u>	<u>Page</u>
153	2-Dimensional Finite-Element Stress Model	235
154	3-Dimensional Finite-Element Stress Model, Axiometric View	236
155	3-Dimensional Finite-Element Stress Model, End View	237
156	Initial Turbine Design Equivalent Elastic Blade Stress, Pressure-Side External Surface (Fore-shortened View). Uniform Temp - 294K (70°F)	238
157	Initial Turbine Design Blade Pressure-Side Internal Surface Equivalent Stress at 5969 rad/s (57,000 RPM) Uniform Temp - 294K (70°F)	239
158	Initial Turbine Design Blade Suction-Side Internal Surface Equivalent Stress at 5969 rad/s (57,000 RPM). Uniform Temp - 294K (70°F).	240
159	Initial Turbine Design Blade Suction-Side External Surface Equivalent Stress, 100-Percent Power at 5969 rad/s (57,000 RPM). Uniform Temp - 294K (70°F)	241
160	Blade Pressure-Side External Surface Equivalent Stress, Optimized Design at 5969 rad/s (57,000 RPM). Uniform Temp - 294K (70°F)	242
161	Blade Pressure-Side Internal Surface Equivalent Stress, Optimized Design at 5969 rad/s (57,000 RPM). Uniform Temp - 294K (70°F)	243
162	Blade Suction-Side Internal Surface Equivalent Stress, Optimized Design at 5969 rad/s (57,000 RPM). Uniform Temp - 294K (70°F)	244
163	Blade Suction-Side External Surface Equivalent Stress, Optimized Design at 5969 rad/s (57,000 RPM). Uniform Temp - 294K (70°F)	245
164	Initial Design Disk Radial Stress at 5969 rad/s (57,000 RPM). Uniform Temp - 294K (70°F)	246
165	Initial Design Disk Tangential Stress at 5969 rad/s (57,000 RPM). Uniform Temp - 294K (70°F)	247
166	Initial Design Disk Equivalent Stress at 5969 rad/s (57,000 RPM). Uniform Temp - 294K (70°F)	248
167	Final Design Blade Pressure-Side External Surface Equivalent Stress at 100-Percent Power	249

LIST OF ILLUSTRATIONS (Contd)

<u>Figure</u>	<u>Title</u>	<u>Page</u>
168	Final Design Blade Suction-Side External Surface Equivalent Stress, Optimized Design at Maximum Power	250
169	Final Design Disk Radial Stress at Maximum Power	251
170	Final Design Disk Tangential Stress at Maximum Power	252
171	Final Design Disk Equivalent Stress, 100-Percent Power Condition	253
172	Campbell Diagram Showing Interference Between Natural Blade Frequencies and Engine Excitation Orders at Room Temperature	255
173	Campbell Diagram Showing Interference Between Natural Blade Frequencies and Engine Excitation Orders at Maximum Power	256
174	Mode Shape No. 1 with Normalized Displacements at 5969 rad/s (57,000 RPM)	257
175	Mode Shape No. 2 with Normalized Displacements at 5969 rad/s (57,000 RPM)	258
176	Mode Shape No. 3 with Normalized Displacements at 5969 rad/s (57,000 RPM)	259
177	Mode Shape No. 4 with Normalized Displacements at 5969 rad/s (57,000 RPM)	260
178	Mode Shape No. 5 with Normalized Displacements at 5969 rad/s (57,000 RPM)	261
179	Part-Power Efficiency Characteristics for the Selected Cooled, Variable-Area Radial Turbine With the Articulated Trailing-Edge Stator Concept	266
180	Cooled, Variable-Area Radial Turbine Component Cold-Air Test Rig	272
181	Cooled, Variable-Area Radial Turbine, Program Schedule	274

LIST OF TABLES

<u>Table</u>	<u>Title</u>	<u>Page</u>
I	100-Percent Power Parameters Used for Cycle Analysis	22
II	Stress-Rupture Capabilities of Candidate Turbine Superalloys	53
III	Overtemperature Capabilities of Candidate Stator Materials	56
IV	Elastic Moduli (Room Temperature) of Candidate Superalloys	57
V	Evaluation of Cooled rotor Life As a Function of Rotor-Inlet Temperature, Duty Cycle, and Tip Speed	66
VI	Mechanical Analyses of Uncooled Rotor Disk	97
VII	Comparison of Mechanical Properties for Cooled Rotor Models	111
VIII	Selected Cooled, Variable-Area Radial Turbine Stage Characteristics	118
IX	Final Vane Design Parameters for Selected Variable-Area Stator Concepts	136
X	Estimated cooled, Variable-Area Radial Turbine Efficiency for Selected Stage Configuration (100-Percent Power)	265
XI	Instrumentation for Overall Turbine Performance	273

ABBREVIATIONS AND SYMBOLS

b	Stator and rotor passage width, cm (in.)
g	Force-mass conversion factor $32.174 \text{ lb}_m\text{-ft}/\text{lb}_f\text{-sec}^2$
W	Mass flow, kg/s (lb/sec)
$W\sqrt{\theta}/s$	Stage inlet corrected flow, kg/s (lb/sec)
A_{CR}	Critical velocity, m/s (ft/sec)
A_N/A_{ND}	Variable geometry stator throat area ratio
A_t	Stator throat area, cm^2 (in. ²)
A_5	Rotor exit annular area, cm^2 (in. ²)
B	Trailing edge blockage, $\frac{t_t}{S_p}$
C	Stator sidewall clearance, mm (in.)
C_A	Inducer - shroud axial clearance, mm (in.)
C_B	Backface axial clearance, mm (in.)
C_R	Exducer - shroud radial clearance, mm (in.)
HPC	High pressure compressor
HPT	High pressure turbine
j	Mechanical equivalence of heat, $778.0 \text{ ft-lb}_f/\text{Btu}$
L	Rotor axial length, cm (in.)
M	Meridional distance, cm (in.)
M_{NR}	Relative mach number
N	Rotational speed, rpm
N_B	Number of rotor blades
N_V	Number of stator vanes
$N/\sqrt{\theta}$	Corrected speed, rpm
O	Throat dimension, mm (in.)
P_C	Compressor discharge pressure, N/m^2 (psia)

ABBREVIATIONS AND SYMBOLS (Contd)

P_{RC}	Compressor pressure ratio
PR	Pressure ratio
P_T	Total pressure, N/m^2 (psia)
$P/P)_{T-T}$	Total-to-total STAGE pressure ratio
q	Dynamic pressure $\frac{\rho_s V^2}{2}$ N/m^2 (psia)
R	Radial coordinate, cm (in.)
R_E	Reynold's number
R_{H5}	Exducer hub radius, cm (in.)
R_{STG}	Stage reaction
R_{T4}	Rotor tip radius, cm (in.)
R_{T5}	Exducer tip radius, cm (in.)
R/R	Rotor Exducer tip-to-inducer tip radius ratio
S_P	Spacing, cm (in.)
t_t	Tangential Thickness, cm (in)
T	Temperature, °K (°R)
T_{N2}	Stator vane leading edge normal thickness, mm (in.)
T_{N3}	Stator vane trailing edge normal thickness, mm (in.)
T_{REL}	Total temperature based on the relative velocity, °K (°R)
U_T	Rotor tip speed, m/s (ft/sec)
V	Absolute velocity, m/s (ft/sec)
V_R	Radial velocity component, m/s (ft/sec)
V_U	Tangential velocity component, m/s (ft/sec)
V_X	Axial velocity component, m/s (ft/sec)
W	Relative velocity, m/s (ft/sec)
W_C	Cooling flow rate, kg/s (lb/sec)

ABBREVIATIONS AND SYMBOLS (Contd)

X, Y, Z	Cartesian coordinates cm (in.)
α	Angle of absolute velocity vector with reference to radial direction, degrees
α_{EXIT}	Rotor exit absolute angle at mean radius rad. (degrees)
α_{2V}	Stator vane inlet angle, degrees
α_{pivot}	Flow angle at the pivot axis, degrees
β	Angle of relative velocity vector, degrees
β_B	Rotor blade inlet angle, degrees
ΔH	Stage specific work (total-to-total) kJ/kg (Btu/lb)
η_{ave}	Average cooling effectiveness
η_C	Total-to-total compressor efficiency
$\eta_{critical}$	Cooling effectiveness at life critical section
η_L	Total-to-total stage efficiency with the stator sidewall leakage included
η_{T-T}	Total-to-total efficiency
λ	Work Coefficient
λ_2	Rotor inlet work coefficient
λ_{5M}	Mean work coefficient based on the mean wheel speed at the rotor exit
ρ_s	Static density kg/m ^e (slug/ft ³)
$\bar{\omega}$	Pressure loss coefficient

Subscripts:

BASE	Refers to base total stage efficiency from specific speed curve
BFS	Refers to the rotor backface seal
BORE	Refers to the rotor bore

ABBREVIATIONS AND SYMBOLS (Contd)

Subscripts (Contd)

C	Refers to compressor
EW	Refers to endwall
EXT	Refers to rotor exducer tip cooling flow discharge
IND	Refers to rotor inducer cooling flow
H	Refers to the rotor hub
I	Refers to individual cooling flow components
M	Refers to properties at the mean rotor exit radius
MIX	Refers to mixed flow properties
P	Refers to primary turbine mass flow
PS	Refers to the pressure surface
RBF	Refers to the rotor backface
RI	Refers to rotor internal cooling
RS	Refers to the rotor shroud
S	Refers to the shroud
SCALLOP	Refers to rotor backface scallop
STG	Refers to parameters concerning the turbine stage
SYS	Refers to parameters concerning the entire system with the interturbine duct included
SS	Refers to the suction surface
T-T	Refers to total-to-total conditions
TE	Refers to the trailing edge
V	Refers to the stator vane
VI	Refers to vane internal cooling

ABBREVIATIONS AND SYMBOLS (Contd)

Turbine System Station Nomenclature:

- 1 Combustor discharge
- 2 Stator inlet
- 3 Stator exit
- 4 Rotor inlet
- 5 Rotor exit
- 6 Interturbine duct exit

**FINAL REPORT
COOLED, VARIABLE-AREA RADIAL TURBINE PROGRAM**

1.0 SUMMARY

This is the final report for the conceptual evaluation and design analysis for the Cooled, Variable-Area Radial Turbine Technology Program. This program was conducted by the Garrett Turbine Engine Company and was funded by the U.S. Army Research and Technology Laboratory. The program was jointly monitored by the U.S. Army Research and Technology Laboratory and the NASA-Lewis Research Center under NASA Contract No. NAS3-22004.

The objective of the program was to evaluate the aerodynamic and mechanical potential of a variable-area radial turbine capable of maintaining a nearly constant high efficiency when operated at a constant speed and pressure ratio over a range of flows corresponding to 50- to 100-percent maximum engine power.

The program consisted of four major tasks:

- o Task I - Nozzle-area variation and rotor-cooling concepts evaluation.
- o Task II - Detailed aero/mechanical parametric studies based on the concepts selected in Task I to determine the optimum turbine geometry. Heat-transfer and stress analyses were conducted in sufficient depth to ensure meeting the 4000-hour turbine-life requirement.
- o Task III - Detailed aerodynamic designs of the variable-area stator and the selected rotor.
- o Task IV - Heat-transfer and mechanical-design analyses to substantiate the design.

After completion of Task IV, a follow-on test program was defined which consisted of completion of the detailed design, preparation of fabrication drawings, actual rotor fabrication, and aerodynamic testing of the selected radial turbine rotor.

In general, the results of the program showed that a 1589K (2400°F) cooled, variable-area radial turbine was feasible that would satisfy the 4000-hour duty cycle life goal. The parametric-study showed that although a relatively constant aerodynamic efficiency could be achieved at from 60- to 95-percent power, the predicted penalties for interturbine duct loss, cooling flows, stage reaction, and stator leakage resulted in severe part-power

performance degradation. These calculated penalties, however, were based on limited data, and in some instances extrapolations from axial turbine data. Therefore, actual part-power performance must be established experimentally. The final cooled rotor selection was based on 1988 materials technology, and features directionally solidified (DS) Mar-M 247 cooled laminated blades with 0.17-radian (10-degree) rotor inlet angle, a 0.26 radian (15 degrees) inlet rake angle and a powder-metal disk that allowed a rotor tip speed 640 m/s (2100 ft/sec). A peak aerodynamic stage uncooled total efficiency of 0.88 was predicted at 100 percent power.

The program identified two candidate variable-area stators. These were designated the articulated trailing-edge and rotating-translating movable sidewall concepts. However, detailed aerodynamic and mechanical analysis comparisons failed to identify an optimum configuration. To determine an optimum configuration, both concepts must be experimentally evaluated in the follow-on test program outlined in Section 9.0.

2.0 INTRODUCTION

2.1 Background

The current world-wide fuel shortage has placed increased emphasis on minimizing future engine fuel consumption. Even with the development of synthetic fuels, costs are still expected to be relatively high when compared to pre-crisis oil costs. Under these conditions, complex, higher-cost engine concepts become more attractive if significant reductions in fuel usage can be achieved. Two such engine concepts are the variable-flow capacity engine and the recuperated-regenerated engine.

2.2 Program Objective

The objective of this program was to evaluate the aerodynamic and mechanical potential of a high-temperature, variable-area radial turbine for use in a variable-flow capacity engine for rotorcraft application. For such applications, the gas-turbine engine is required to operate over a wide range of power settings. With conventional fixed-geometry engines, part-power operation is achieved by reducing engine speed (pressure ratio) and temperature, thus reducing cycle efficiency.

However, a variable-flow capacity turboshaft engine has the potential to significantly reduce specific fuel consumption (SFC) at cruise conditions. A combination of a variable-diffuser centrifugal compressor and a variable-stator radial turbine would allow reduced engine power, while maintaining nearly constant compressor pressure ratio and turbine inlet temperature. The power range over which this operating mode could be maintained is a function of both the variable-geometry components and the effect of variable-geometry operation on engine match and component efficiencies.

2.3 Cooled Radial Rotor Technology

Recently, the radial turbine has received considerable attention for both automotive and small turboshaft and turboprop applications. It is recognized that in smaller-flow class engines, the radial turbine has the ability to achieve higher efficiencies at higher stage work levels than its low-aspect-ratio axial turbine counterpart. Unfortunately, the inability to internally cool the radial turbine rotor has restricted its use to primarily lower temperature auxiliary power unit (APU) and turbocharger applications. However, recent advances in lamination techniques⁽¹⁾ have shown that a mechanically viable, high-temperature cooled rotor is now feasible. A small, high-temperature, cooled radial turbine rotor was designed and manufactured utilizing the Garrett laminate process developed under Army Contract No. DAAJ02-77-C-0032.

2.4 Major Program Considerations

To realize the benefits associated with the variable-flow capacity engine, the variable-area radial turbine must provide a nearly constant efficiency from cruise through maximum power settings. For a given turbine efficiency, minimum SFC will occur at relatively high turbine inlet temperatures and cycle pressure ratios. Thus, high stage-work levels will be required. Given these considerations, the following issues were addressed in the program:

- o The aerodynamic performance potential of a radial turbine as a function of cycle pressure ratio and inlet temperature using projected 1988 material properties;
- o The design procedures necessary to optimize radial turbine performance over the entire duty cycle from 50- to 100-percent power;
- o The effects of turbine cooling flows, and the maximum allowable inlet temperature for a cooled or uncooled rotor configuration with a duty-cycle-life of 4000 hours;
- o Definition of variable-geometry techniques that could minimize performance decrements from both a leakage and vane loading standpoint.

3.0 AERODYNAMIC PERFORMANCE CORRELATIONS AND SYSTEM OPTIMIZATION TECHNIQUE

3.1 Design-Point Performance Evaluation

The maximum attainable (base) efficiency for radial turbines is currently correlated from either a specific speed relationship, or from stator and rotor loss coefficients derived from experimental data. The goals of each method are to evaluate the basic profile and secondary flow losses occurring in the radial turbine for a required combination of rotational speed, flow rate, and work levels. Although the evaluation of individual stator and rotor loss levels on a more fundamental stator and rotor loss coefficient basis was desirable, the actual benefits associated with this approach have not been achieved for arbitrary designs due to the complex 3-dimensional flows that exist in the radial turbine.

For this program, the maximum attainable efficiency of the radial turbine was based on the specific speed correlation established by NASA in TND-6605(2) and on recent Garrett turbine designs. The NASA correlation corrected to zero clearance is presented in Figure 1. The reduction in peak efficiency at low specific speed is associated with low-aspect ratio blading, while the reduction in performance at high specific speed is associated with high Mach number. It should be emphasized that the NASA data was established for relatively low pressure-ratio stages, and that achievement of these performance levels at higher pressure ratios is based on the assumption of equivalent loss coefficients. However, correlation with recent Garrett radial turbine designs has indicated that this is a good assumption, as long as stator and rotor exit shock losses are not present.

Regardless of how a base efficiency is established, previous in-house studies have shown that the primary deterrent to achieving peak performance is the inability to achieve optimum tip speed. The speed required for peak radial turbine efficiency can be established from the centrifugal compressor slip factor derived by Stanitz(3) and is a function of the overall work level, as shown in Figure 2. It was concluded that high-work radial turbines are generally tip-speed-limited, and peak efficiency would not be achieved. However, studies have shown(4,5) that, under these conditions, an optimization procedure based on a system analysis approach could be utilized to arrive at maximum system performance. The system for this program was defined as a variable-area stator, a radial turbine stage, and included the downstream interturbine duct, as shown in Figure 3. The objective of the system analysis was to minimize the combined losses associated with nonoptimum tip speed (incidence) and interturbine duct loss. For an overall imposed stage work coefficient (λ_{STAGE}), the

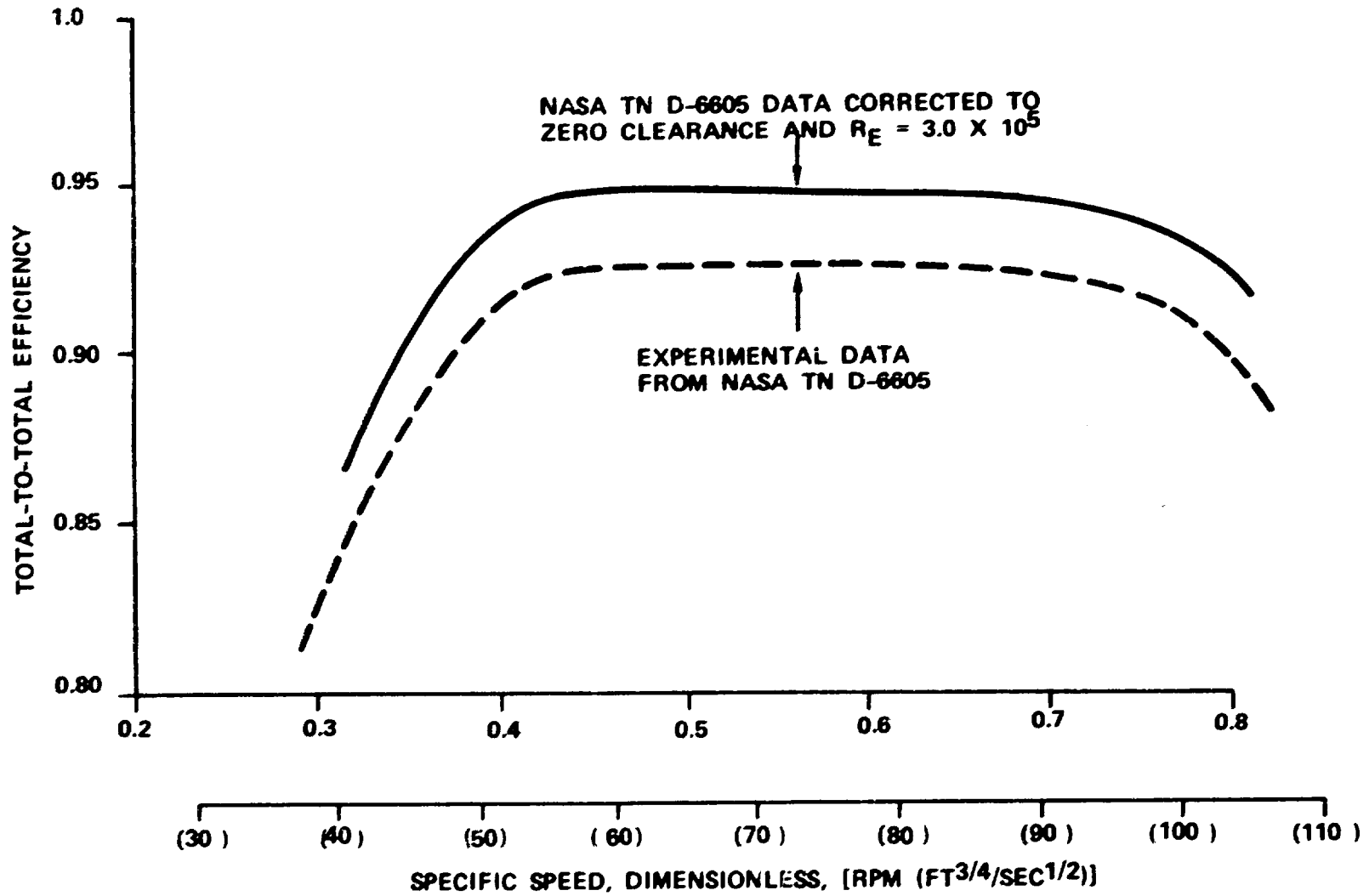


Figure 1. NASA Specific Speed Correlation Corrected to Zero Clearance.

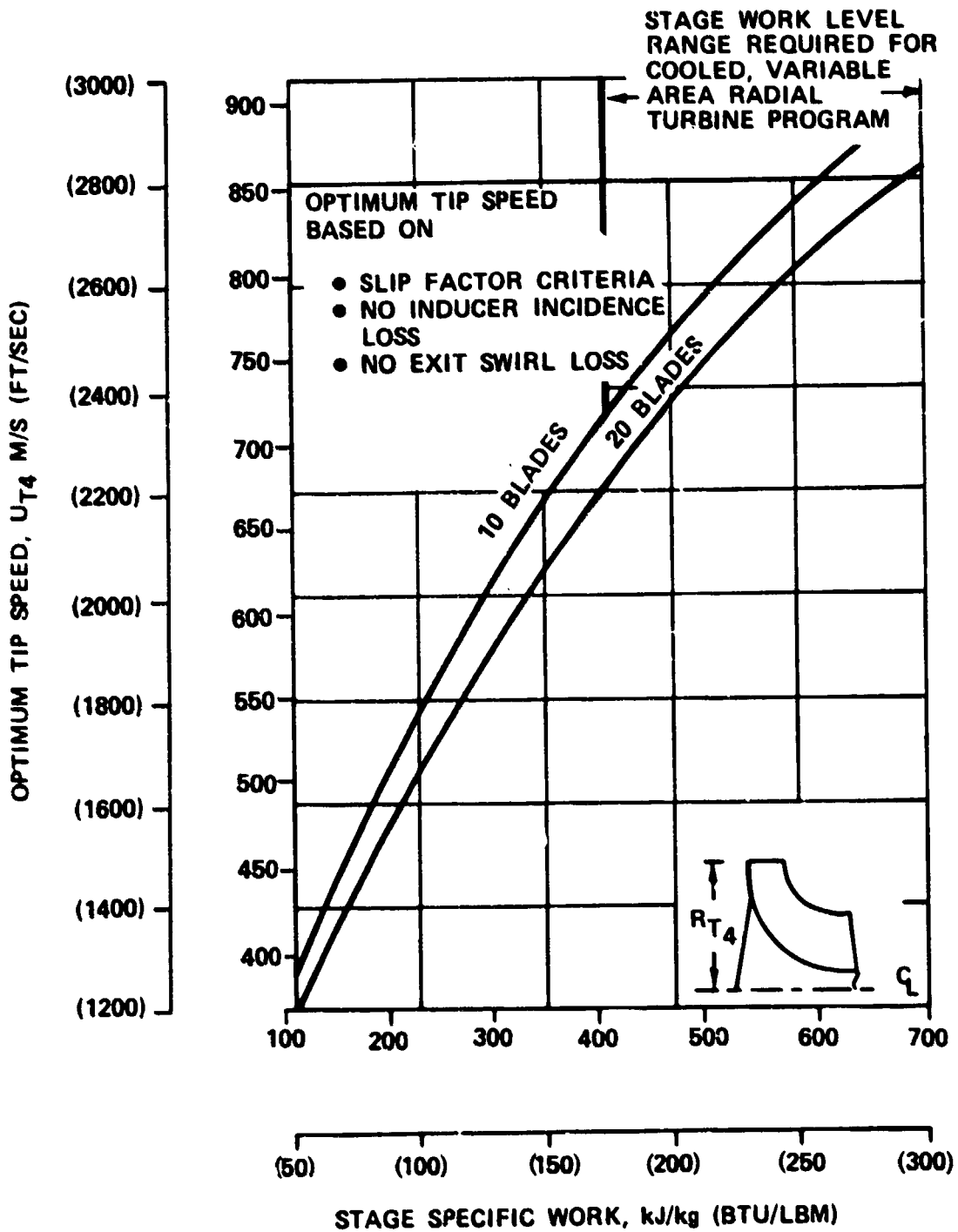


Figure 2. Variation of Optimum Tip Speed with Turbine Stage Specific Work.

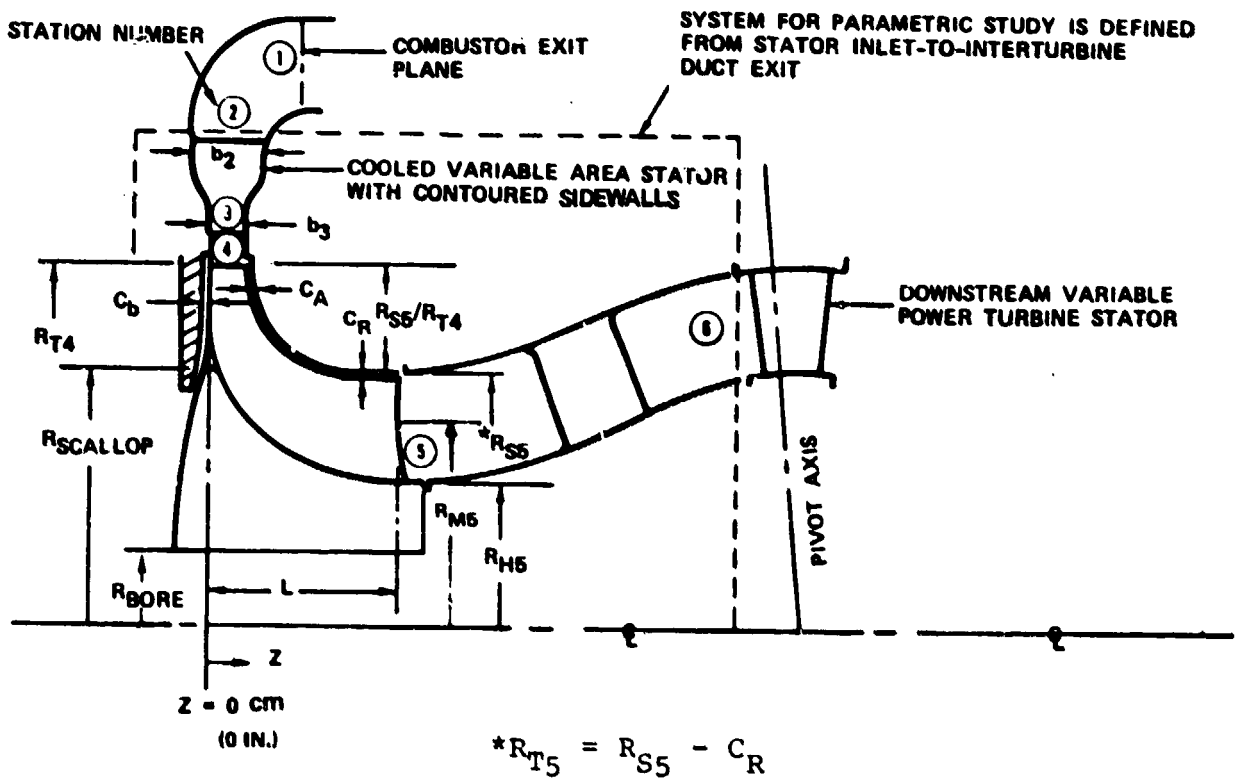


Figure 3. Cooled, Variable-Area Radial Turbine, System Definition.

magnitude of the incidence loss is a direct function of the inducer-to-exducer work split selected. This relationship is expressed in the following manner:

$$\frac{gJ\Delta H_{T-T}}{U_{T_4}^2} = \lambda_4 - \left(\frac{R_{M5}}{R_{T_4}} \right)^2 \lambda_{M5} = \lambda_{STAGE} \quad (1)$$

Therefore, the imposed rotor inlet work coefficient (λ_4) depends on the selected rotor exit work coefficient λ_{M5} as well as the exducer-to-inducer radius ratio R_{M5}/R_{T_4} . This, combined with the continuity equation, established the rotor-exit swirl and Mach number level.

When the incidence loss is calculated from the kinetic-energy difference between nonoptimum stage rotor-inlet work coefficient ($\lambda_{4,ACT}$) and an ideal work coefficient ($\lambda_{4,IDEAL}$) based on the Stanitz slip factor, the following relationship was derived for the ratio of efficiency with incidence to the efficiency using optimum rotor-inlet conditions:

$$\eta'/\eta'_{BASE} = \frac{1}{1 + \frac{\eta'_{BASE}}{2\lambda_{STAGE}} (\lambda_{4,ACT} - \lambda_{4,IDEAL})^2} \quad (2)$$

where: λ_{STAGE} = Imposed stage work coefficient due to a specified work and allowable tip speed

$\lambda_{4,ACT}$ = Imposed rotor-inlet work coefficient

$\lambda_{4,IDEAL} = 1 - \frac{2}{N_E}$ (slip factor with radial blades).

This relationship shows that there is a strong incentive to reduce the rotor-inlet work coefficient ($\lambda_{4,ACT}$). However, reducing $\lambda_{4,ACT}$ by increasing λ_{5M} increases the losses of the downstream interstage duct. This is due to increases in rotor-exit kinetic energy and swirl. The variation of interstage duct loss (as a function of average rotor-exit swirl) is presented in Figure 4. The data was normalized by the minimum loss coefficient measured for two separate tests and shows good agreement for the range of exit swirl angles investigated. However, the minimum loss coefficient varied significantly for each duct configuration. This indicates that, in addition to the level of swirl, the duct configuration also influenced the magnitude of the duct loss. Inlet duct experiments made by Dovzhik et al. (6) were based on uniform temperature and pressure, with straight duct sidewalls. The Garrett Model GTP305-2 (7) duct data shown in Figure 4 was based on actual rotor-exit conditions (inlet-duct conditions), using moderately curved sidewalls and radius ratios between turbines. The minimum duct-loss coefficient of 0.148 was derived

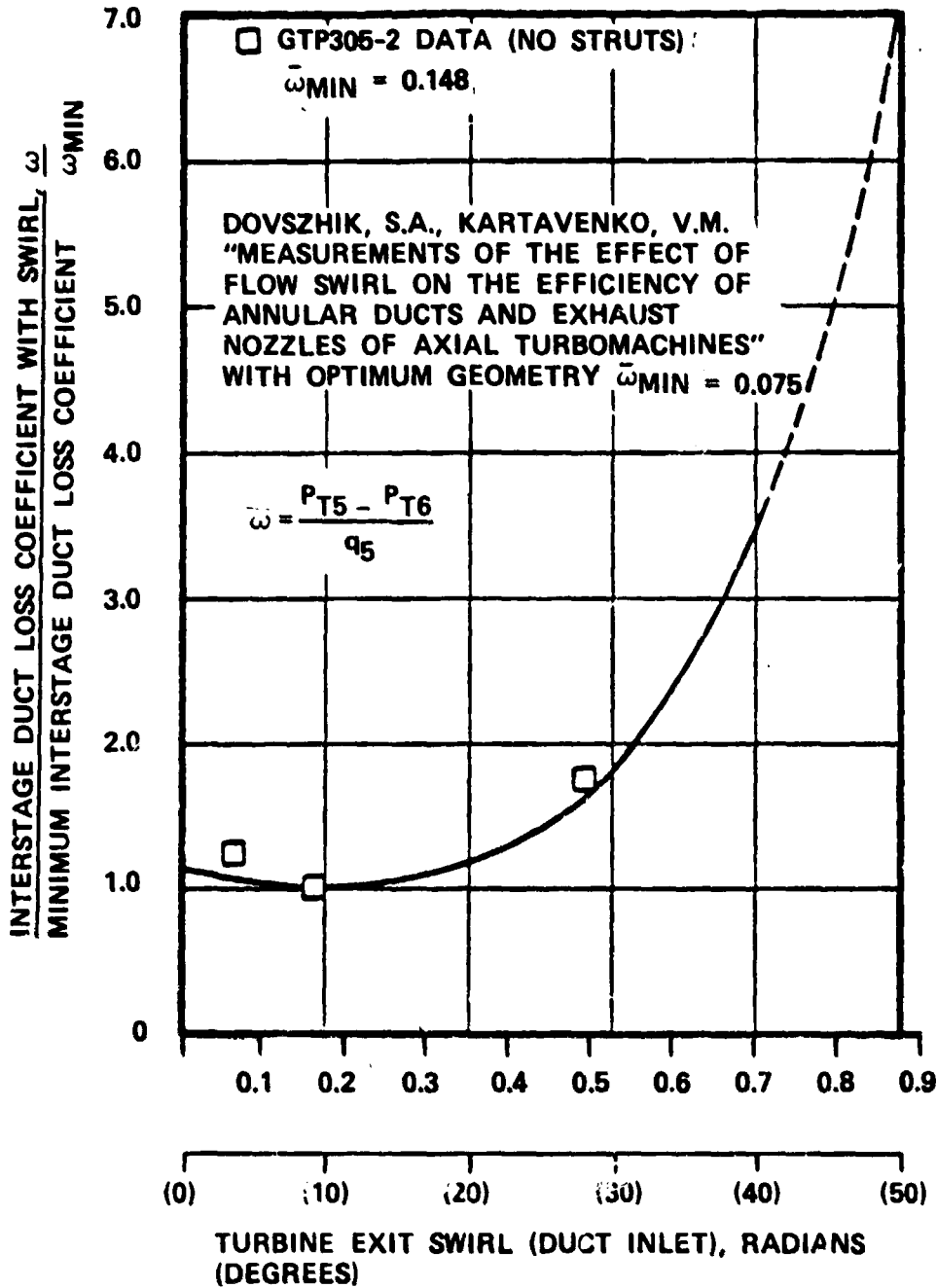


Figure 4. Effects of Swirl on Interstage Duct Loss Coefficient.

from the GTP305-2. However, the variable flow-capacity engine concept will require a variable geometry power turbine with conventional axial rotating vanes. Interturbine duct struts will be needed to support the duct hub contour. Under these conditions, the duct minimum loss coefficient will increase. Previous in-house experimental programs have shown that, when struts are required, a minimum loss coefficient of 0.200 is representative.

When the effects of rotor-inlet incidence and interturbine duct loss are combined and examined over a range of rotor-inlet work coefficients, peak system performance is achieved for a range of rotor tip speeds (Figure 5). This determination was based on a study conducted by Garrett for TARADCOM for an Advanced Armored Vehicle Gas Turbine Engine (under Army Contract No. DAAK30-C-0093). Two turbine rotor blade configurations were studied; a conventional radial blade [$\beta_B = 0$ radian (0 degrees)], and a 3-dimensional, nonradial rotor blade [$\beta_B = 0.35$ radian (20 degrees)] at the rotor inlet. The potential benefits of both are shown in Figure 5.

Another recent study⁽⁵⁾ using 3-dimensional rotor blades was conducted by Garrett for 1644K (2500°F) automotive radial turbine. This study was based on projected ceramic material technology ceramic stress capability of 621 MPa (90 ksi) and a Weibull modulus of 15.

It was concluded from this study that:

- o Exceptionally high rotor-tip speeds 701 m/s (2300 ft/sec) were feasible for radial-bladed rotors.
- o Nonradial rotors could achieve equivalent performance at lower tip speeds. However, the increased mechanical design complexity did not justify nonradial blades for this application.

In 1978, a Garrett company-sponsored research program was conducted to investigate the aerodynamic and mechanical feasibility of metallic, nonradial-bladed rotors. An existing radial rotor was modified to a 3-dimensional design for application in an APU with a 1311K (1900°F) turbine-inlet temperature, a tip speed of 549 m/s (1800 ft/sec), and a 0.35-radian (20-degree) blade angle. Rig test results showed that the increased performance achieved was in good agreement with that predicted from a decrease in inducer incidence loss. However, it must be determined whether the favorable aerodynamic characteristics offset the mechanical-design complexity involved. This would depend on material development and application. If dual-alloy rotors with DS blades allowed optimum tip speed to be approached, then the increased

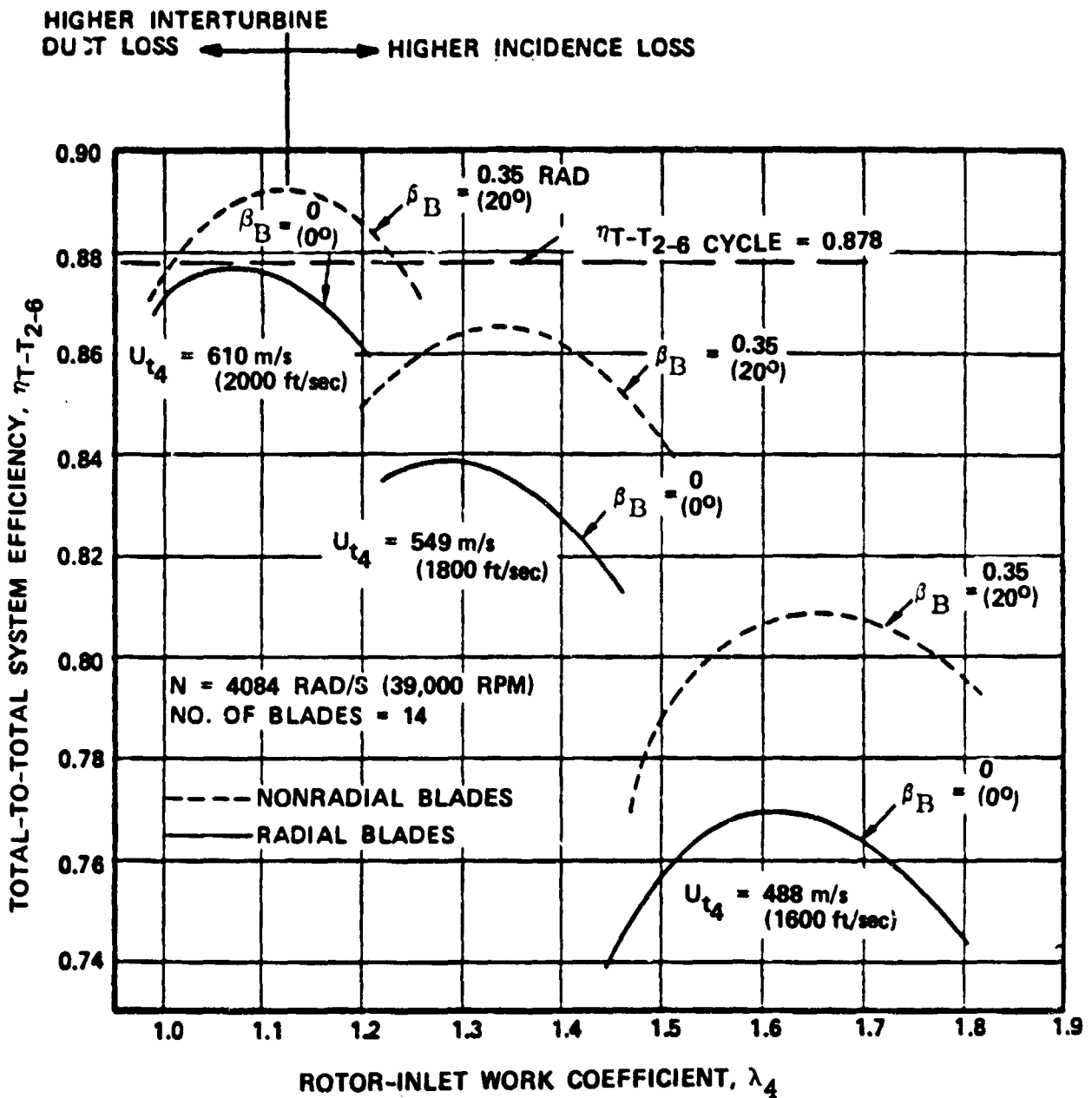


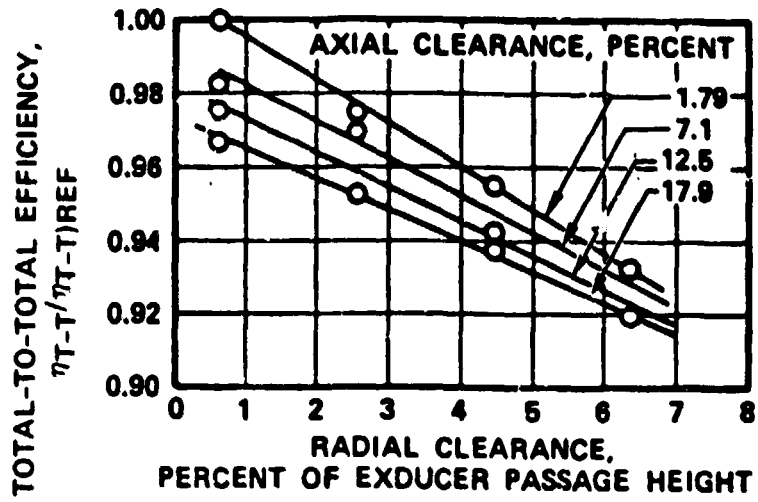
Figure 5. Results of System Optimization for TARADCOM Advanced Radial Turbine.

benefits and mechanical complexity of nonradial blades would not be warranted. However, in variable-flow capacity engine application, rotor-inducer loading increases with reduced power. Under these conditions, the added complexity of nonradial blading may be justified. Therefore, the effects of rotor inlet-blade angles of from 0 to 0.35 radian (0 to 20 degrees) were evaluated for this program.

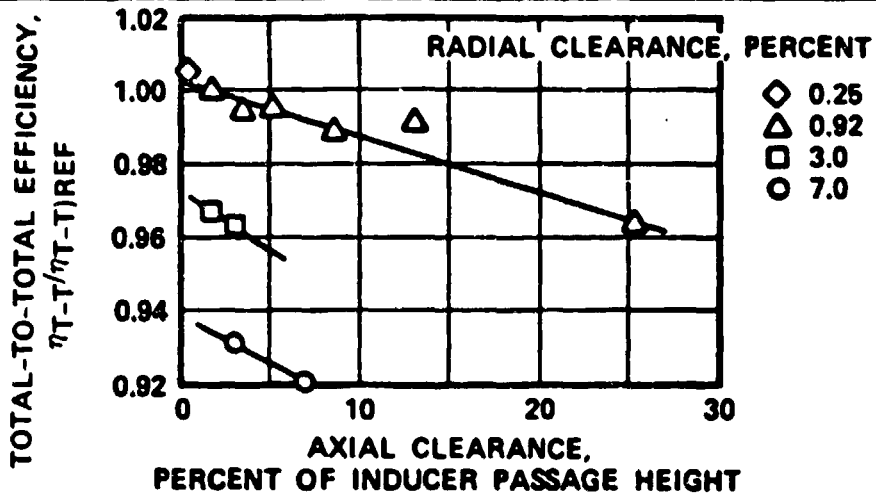
In addition to rotor incidence and duct loss, additional losses are incurred that must be accounted for in the parametric study. The correlations are described in the following paragraphs:

- o Reynolds Number Effect: Based on results from NASA(8) data.
- o Rotor Clearance Effects: Based on correlations derived from several sources(9,10) and on Garrett test results. The performance penalties are a function of both axial (Ca) and radial (Cr) clearance. The experimental data from these sources is presented in Figures 6A and 6B. Additional rotor clearance effects are present with rotor scallops. The performance effects as a function of backface clearance recently have been evaluated for the Model GTP305-2 turbine(7) and are presented in Figure 6C. In addition, the results of a 1978 Garrett-sponsored radial turbine research program showed the effects of scallop depth on radial turbine performance. These data will be used to supplement the correlation derived from the Model GTP305-2 turbine.
- o Rotor Blade Number Effects: Based on the Models GTP305-1, GTP306-4, and published Pratt and Whitney data(11). The resultant change in turbine efficiency represents the effect of increased blade loading as blade number is reduced for a given work requirement.
- o Rotor Backface Disk Friction Effects: Estimated based on the results of References(12, 13). It should be noted that tab loss is based on a full rotor backface disk. The rotor scallop effect on rotor disk friction is currently not available.

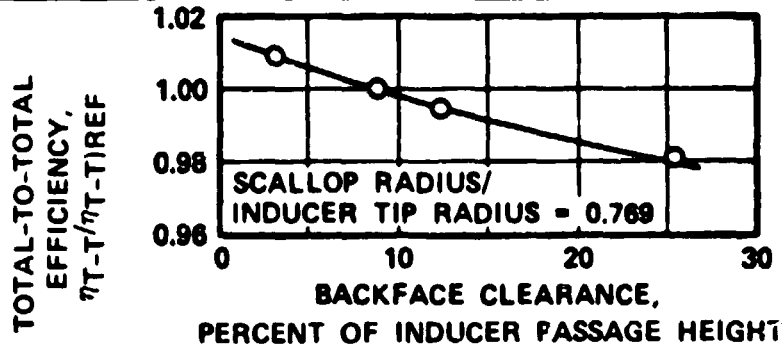
Experience gained from axial turbine designs has shown that the effects of rotor-exit hub blockage and stage reaction should not be ignored during the program turbine design process. At present, only preliminary correlations are available for these two effects(5). However, recent investigations conducted by Meitner(14) and McLallin(15) will allow further refinement for the effects of reaction and blockage.



(A) Summary of Radial and Axial Clearance Effects on Total Stage Efficiency (9).



(B) Summary of Radial and Axial Clearance Effects on Total Stage Efficiency at Design Equivalent Values of Speed and Pressure Ratio (10).



(C) Effect of Rotor Backface Clearance on Stage Total Efficiency at Design Conditions (7).

Figure 6. Summary of Radial Turbine Rotor Clearance Effects.

3.2 Off-Design Performance Evaluation

The accurate prediction of off-design performance characteristics of the cooled, variable-area radial turbine was a major aspect of this program. A design point, as such, is not meaningful from an aerodynamic standpoint, since the normal mode of operation was between 50- and 100-percent maximum flow. The radial turbine off-design performance prediction technique used for the program was similar to that used by NASA(16), except that the incidence model was based on a slip factor. An intermediate loss coefficient was included between the stator and rotor to account for stator trailing-edge mixing and secondary-flow loss, in addition to the vaneless-space loss. Radial stator flow calibrations indicated that the flow coefficient up to the stator throat was between 0.985 and 0.995. If losses higher than this are assigned, then the predicted flow characteristics (as a function of speed and pressure ratio) would be in error. Input to the program consists of the optimized vector-diagram quantities. Based on previous test results, an initial loss split between stator and rotor was specified. Loss coefficients used in the off-design mode were then calculated. The computer program ability to accurately predict the off-design radial-turbine efficiency and flow characteristics is illustrated in Figures 7 and 8. The comparisons shown are relative to the tested performance of the advanced Model GTP305-2 radial turbine(7). For the cooled, variable-area radial turbine, the objective is to establish a design point between 50- and 100-percent flow that would result in maximum efficiency. The off-design computer model was modified to account for both 3-dimensional rotor blading and downstream interturbine duct loss. The duct-loss correlation used in the off-design calculation was identical to the design-point system-optimization correlation. This allowed the off-design system performance to be evaluated in a consistent manner. The selection of several design points allowed optimization of system performance over the entire 50- to 100-percent flow range. Figure 9 illustrates the extremes in turbine operating conditions that will exist with the variable-area radial turbine.

3.3 Effects of Cooling Flow and Nozzle Leakage

The inability to internally cool radial turbine rotors has been a significant deterrent to their use and to the amount of research devoted to this component. The advent of laminated construction, however, not only eliminated this constraint, but also increased radial turbine applications. Unfortunately, little data on the effects of rotor internal-cooling flow on the performance of radial turbines is available. Three cooling approaches appeared feasible:

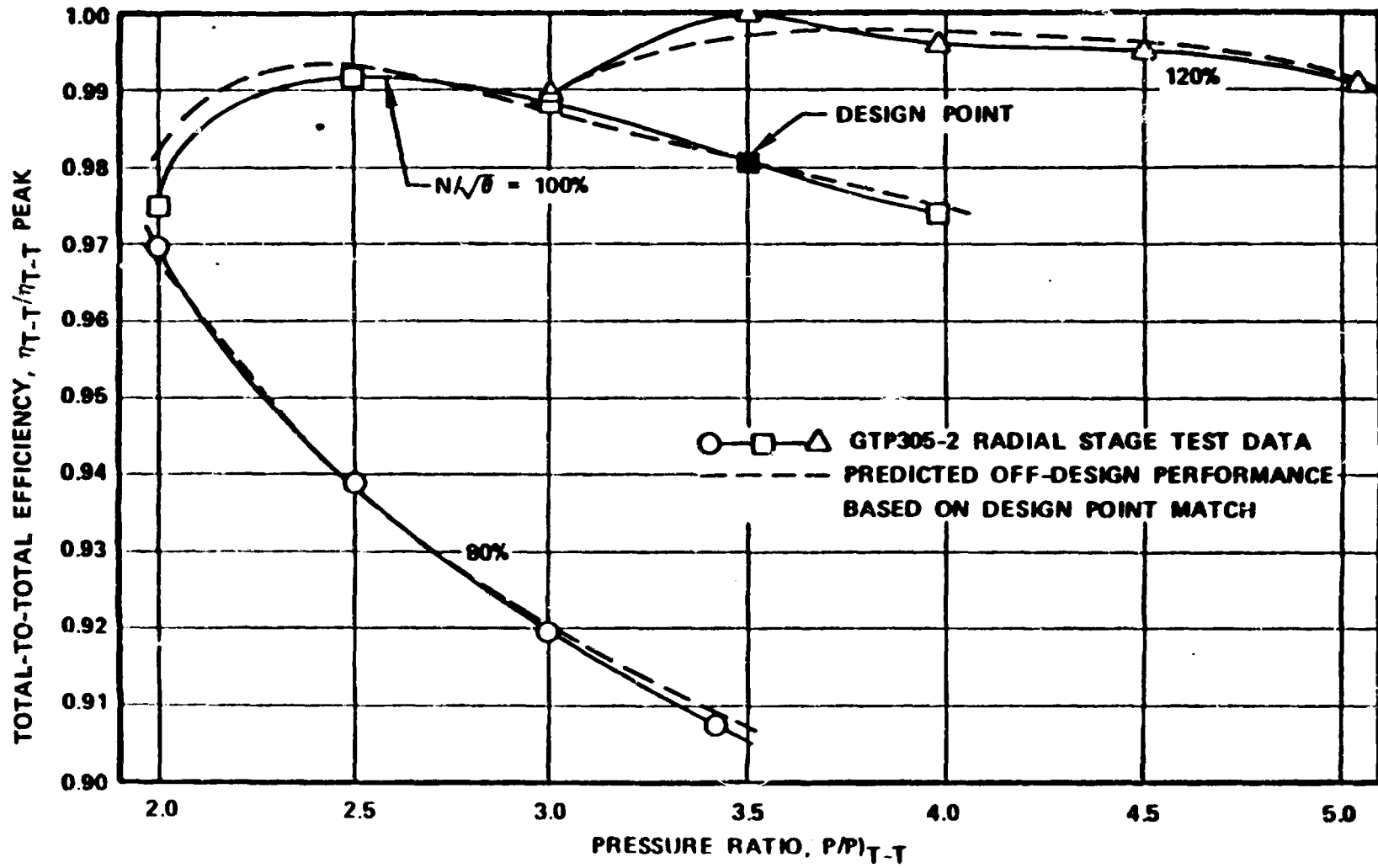


Figure 7. Predicted and Tested Off-Design Efficiency Characteristic Comparison.

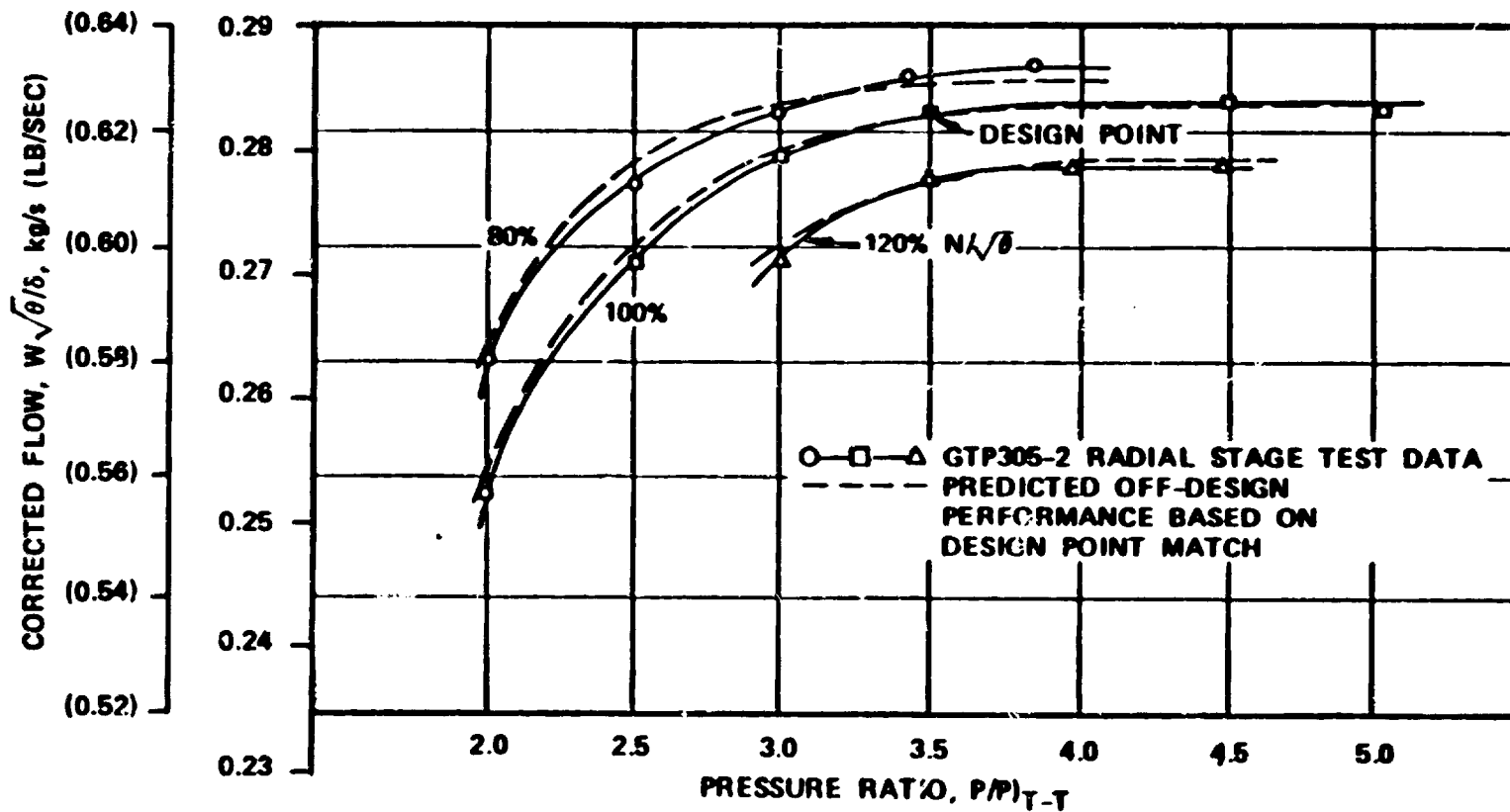
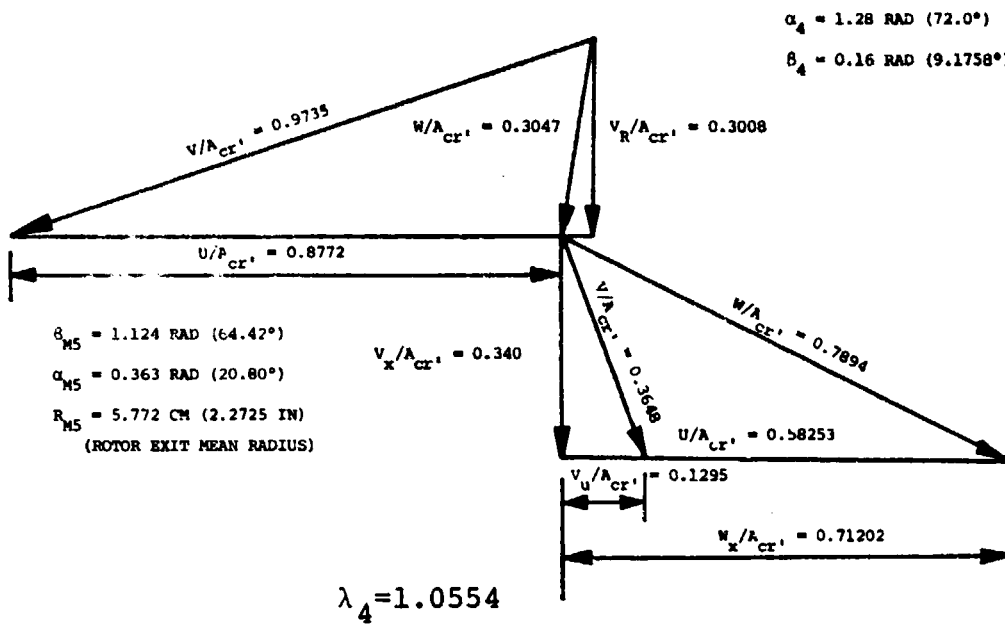


Figure 8. Predicted and Tested Off-Design Flow Characteristic Comparison.

100% CORR. FLOW ($W\sqrt{\theta}/\delta$)



50% CORR. FLOW ($W\sqrt{\theta}/\delta$)

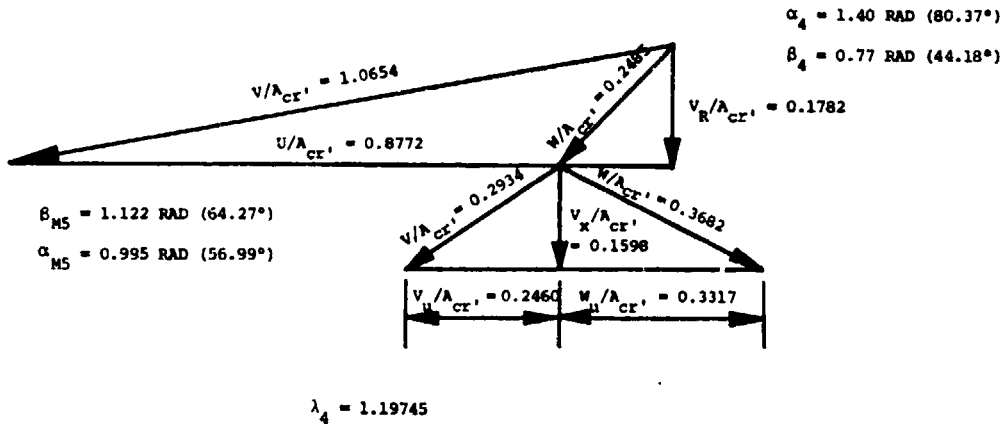


FIGURE 9. 1-Dimensional Vector Diagram Comparison (100-Percent and 50-Percent Inlet Corrected Flows).

- o The first assumes that the majority of the cooling flow is discharged in the rotor-shroud region. This would require pumping into these regions. Depending on the magnitude of cooling flow required, this would result in a performance decrement of 2 to 3 efficiency points.
- o The second approach assumes that the cooling flow is discharged at the same location. However, the pumping penalty is offset by a corresponding reduction in tip-clearance leakage effects. The feasibility of this approach was demonstrated using axial-turbine test data with tip-discharge cooling.
- o The third possibility assumes that the majority of the cooling flow could be discharged at the rotor trailing-edge. Under these conditions, the cooling-flow penalty would be in between the previous two effects due to replacing the lower-momentum, trailing-edge wake region with the higher-momentum cooling flow.

These assumptions not only result in predicted performance uncertainty, but also indicate the importance of a comprehensive test program.

Even for uncooled rotors, a certain amount of cooling along the rotor backface (approximately 1.0 percent) is required to prevent hot gas from recirculating in this region. This effect was evaluated during the GTP305-2 test program.(7) The test results showed that the required pumping work (to the scallop rotor speed) was offset by expansion of the cooling flow through the rotor.

The utilization of variable-area stators will also result in a certain amount of endwall leakage flow. At high-temperature levels, the minimum feasible clearance will require careful mechanical analysis. Previous Garrett variable-area stator radial turbine designs have used full-vane rotation similar to conventional axial stator designs. Test results conducted on these designs have shown similar leakage effects. This implies that sidewall clearances of from 0.0051 to 0.0127-cm (0.002- to 0.005-in.) are required to achieve equivalent axial stator performance with 0.0127-cm (0.005-in.) clearance. On this basis, alternate variable-area concepts must be carefully evaluated during Task I.

4.0 TASK I - STATOR AND ROTOR CONCEPTS EVALUATION

4.1 Variable-Area Radial Turbine Requirements

The basic requirements and goals established for the Cooled, Variable-Area Radial Turbine Program were:

- o Single-stage radial turbine defined as the gas-generator (high-pressure) turbine in the variable-flow-capacity engine;
- o Turbine specific work is between 407 and 698 kJ/kg (175 and 300 Btu/lbm);
- o Turbine-inlet temperature goal:
Cooled configuration = 1644K (2500°F)
Uncooled configuration = 1478K (2200°F)
- o Turbine mass flow is nominally 2.27 kg/s (5.0 lb/sec);
- o Turbine material properties: Based on 1988 metal technology;
- o Turbine mission-cycle life goal: 4000 hours.
- o The turbine will operate at constant speed and pressure ratio over a range of flows from 50- to 100-percent maximum engine power.

The objective of Task I was to define and evaluate potential variable-area stator and internal rotor cooling concepts. An engine configuration was defined, and cycle performance was evaluated over a range of radial turbine inlet temperatures and cycle pressure ratios at 100-percent power. A preliminary parametric study was then performed over a range of power settings from 50-to 100-percent power. The preliminary study allowed early evaluation of the variable-area radial turbine and indicated trends that were used as guidelines for selecting a representative stage configuration for the aerodynamic and mechanical concept evaluation.

The variable-flow-capacity turboshaft engine configuration selected consisted of a 2-stage, variable-diffuser centrifugal compressor, a reverse-flow annular combustor, a single-stage variable geometry radial turbine, and a 2-stage, variable-geometry free-power turbine. With this configuration, the variable-geometry radial turbine specific work would fall between 419 and 512 kJ/kg (180 and 220 Btu/lbm) and compressor pressure ratio would be between 14:1 and 20:1.

4.2 100-Percent Power Cycle Study

A cycle analysis with estimates of engine/component performance was conducted at 100-percent power for cooled rotor configurations at 1533K (2300°F), 1589K (2400°F), and 1644K (2500°F) rotor inlet temperatures. In addition, an uncooled configuration at 1478K (2200°F) was also evaluated. The following basic assumptions were used for these analyses:

- o Engine mass flow = 2.27 kg/s (5.0 lbm/sec)
- o Burner efficiency = 0.995
- o Burner total pressure loss (including a 1.57-radian (90-degree) bend upstream of the turbine stator) = 0.04;
- o Interturbine duct total pressure loss = 0.015;
- o Two-stage, variable-geometry power-turbine total-to-diffuser-exit static efficiency = 0.875;
- o Gearbox efficiency = 0.98;
- o Gas-generator spool mechanical efficiency = 0.995;
- o Two-stage, variable-geometry, centrifugal compressor efficiency levels based on compressor design study projections (Table I), and
- o A range of variable-geometry radial turbine stage total-to-total efficiencies from 0.84 to 0.90.

The 100-percent power parameters used for the cycle analysis are also listed in Table I. This table includes the two-stage compressor efficiency, leakage flow, and turbine cooling flows used to define cycle performance as a function of compressor pressure ratio. The results of the cycle analysis are presented in Figures 10 through 12 for the cooled rotors, while Figure 13 shows the results for the uncooled configuration.

4.3 Preliminary Parametric Study (Stator/Rotor Concept Evaluation)

4.3.1 Design Point Study

Using the design conditions established in the cycle analysis, a preliminary parametric study was performed over a wide range of cycle pressure ratios. The objective of this study was to examine the relationship between turbine performance, geometry, duct loss, and rotor relative temperature over a range of

TABLE I. 100-PERCENT POWER PARAMETERS
USED FOR CYCLE ANALYSIS

$\frac{P}{K}$	η_c^*	$\frac{W_{Leakage}}{W_A}$	$W_{Cooling}/W_A$			
			T4 = 1644K (2500°F)	T4 = 1589K (2400°F)	T4 = 1533K (2300°F)	T4 = 1478K (2200°F)**
10	0.829	0.0064	0.062	0.052	0.042	0.010
12	0.823	0.0075	0.069	0.058	0.045	0.010
14	0.817	0.0088	0.074	0.063	0.049	0.010
16	0.812	0.010	0.079	0.068	0.052	0.010
18	0.806	0.0112	0.084	0.072	0.054	0.010
20	0.800	0.0125	0.087	0.075	0.056	0.010
22	0.795	0.0138	0.090	0.0775	0.057	0.010
24	0.790	0.0150	0.091	0.078	0.057	0.010

*Total-to-total efficiency levels based on compressor design study projections minus 1.0-point for variable geometry.

**Uncooled rotor: 1.0-percent cooling flow for rotor backface

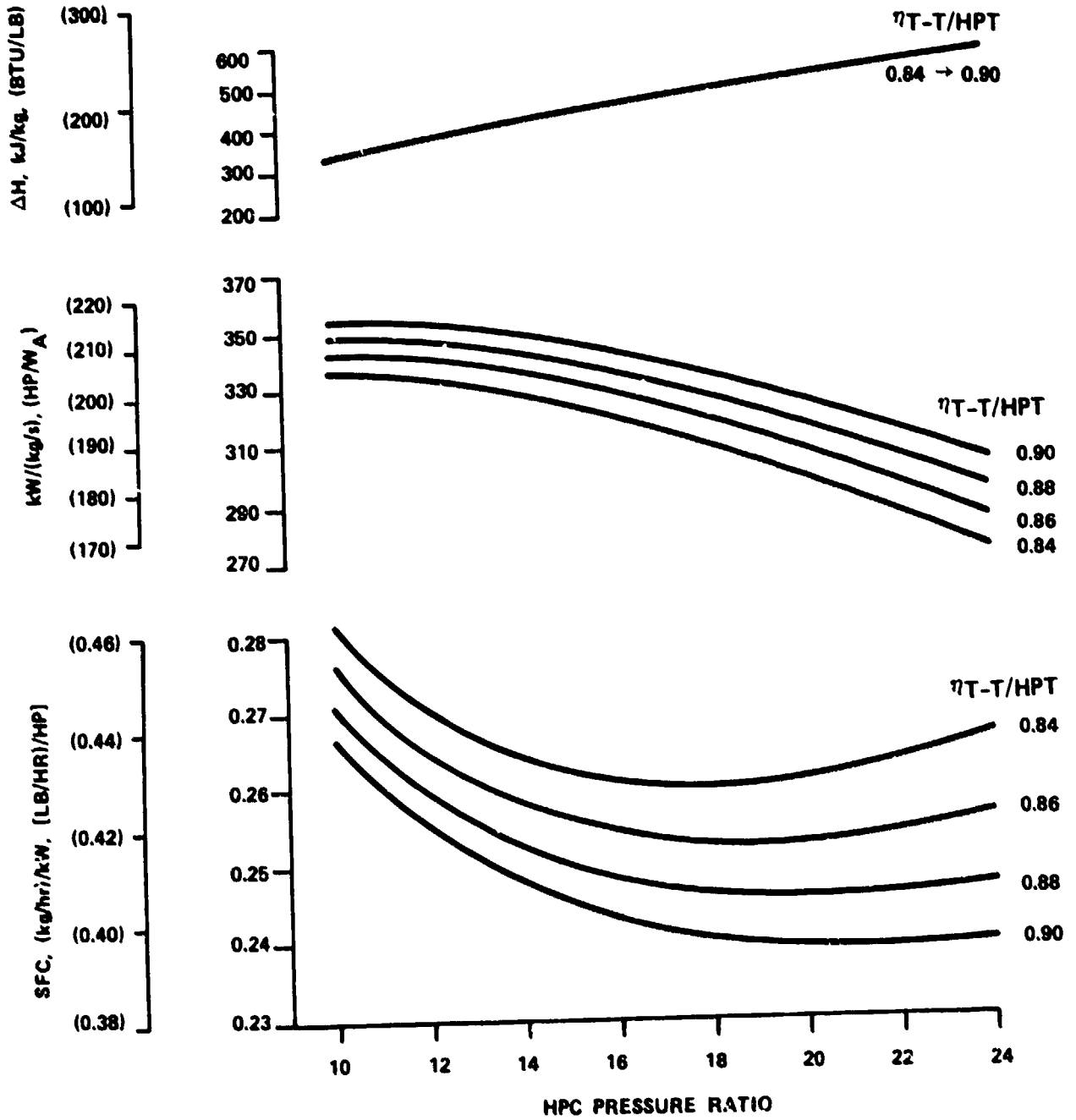


Figure 10. Cooled, Variable-Area Radial Turbine Study, $T_4 = 1533\text{K}$ (2300°F) at Maximum (100-Percent) Power.

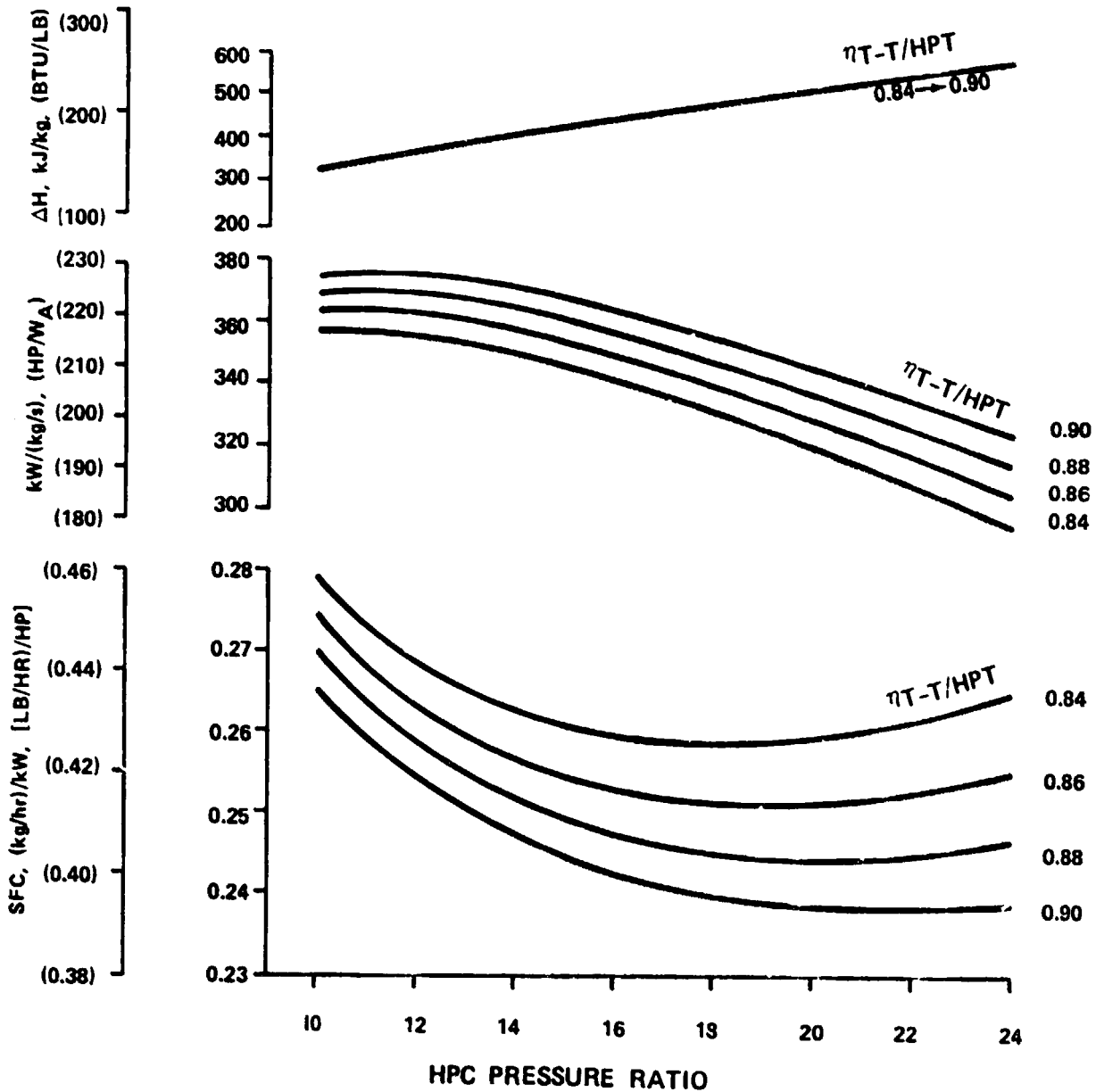


Figure 11. Cooled, Variable-Area Radial Turbine Study, $T_4 = 1589K$ (2400°F) At Maximum (100-Percent) Power.

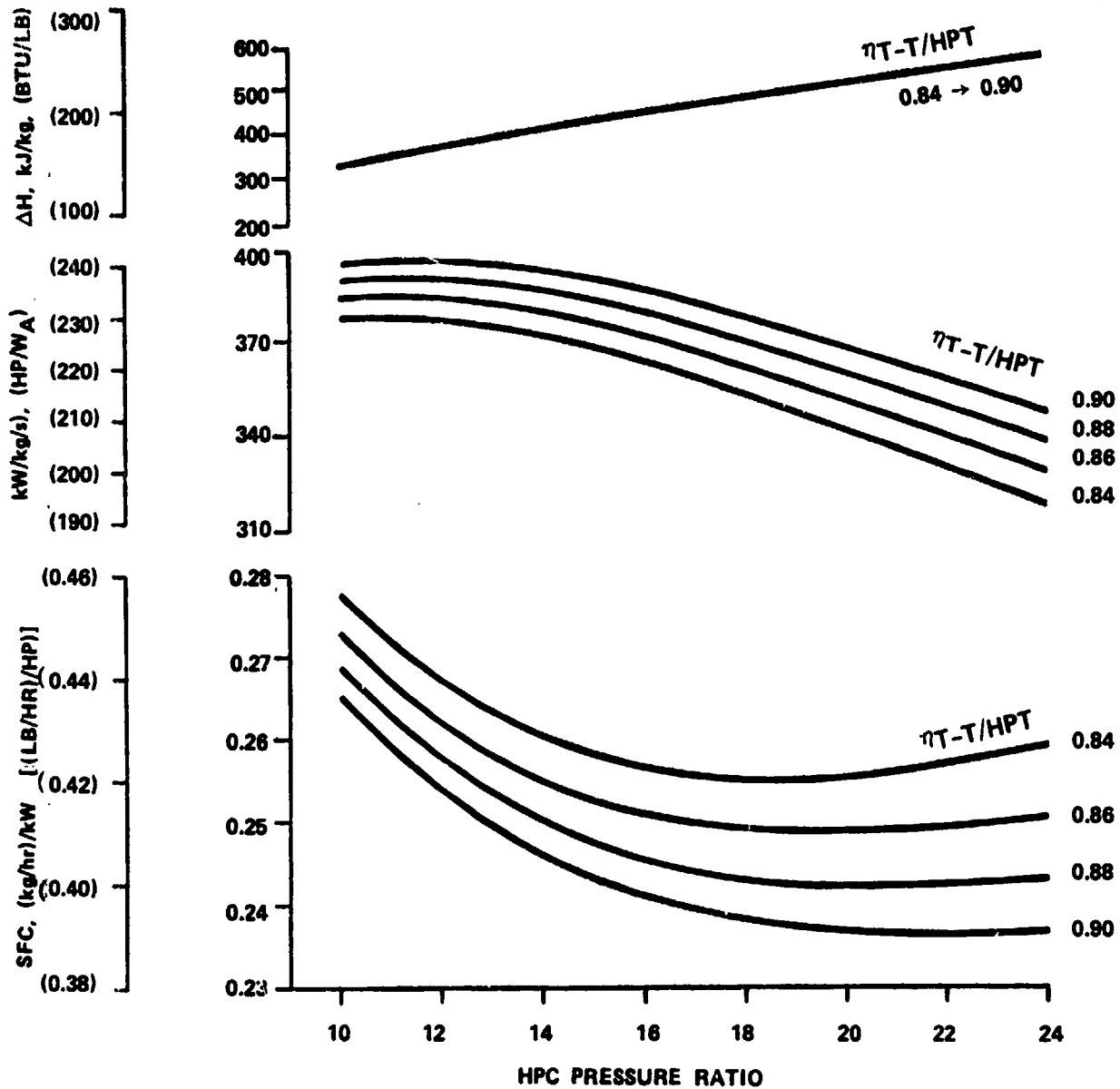


Figure 12. Cooled, Variable-Area Radial Turbine Study, $T_4 = 1644\text{K}$ (2500°F) At Maximum (100-Percent) Power.

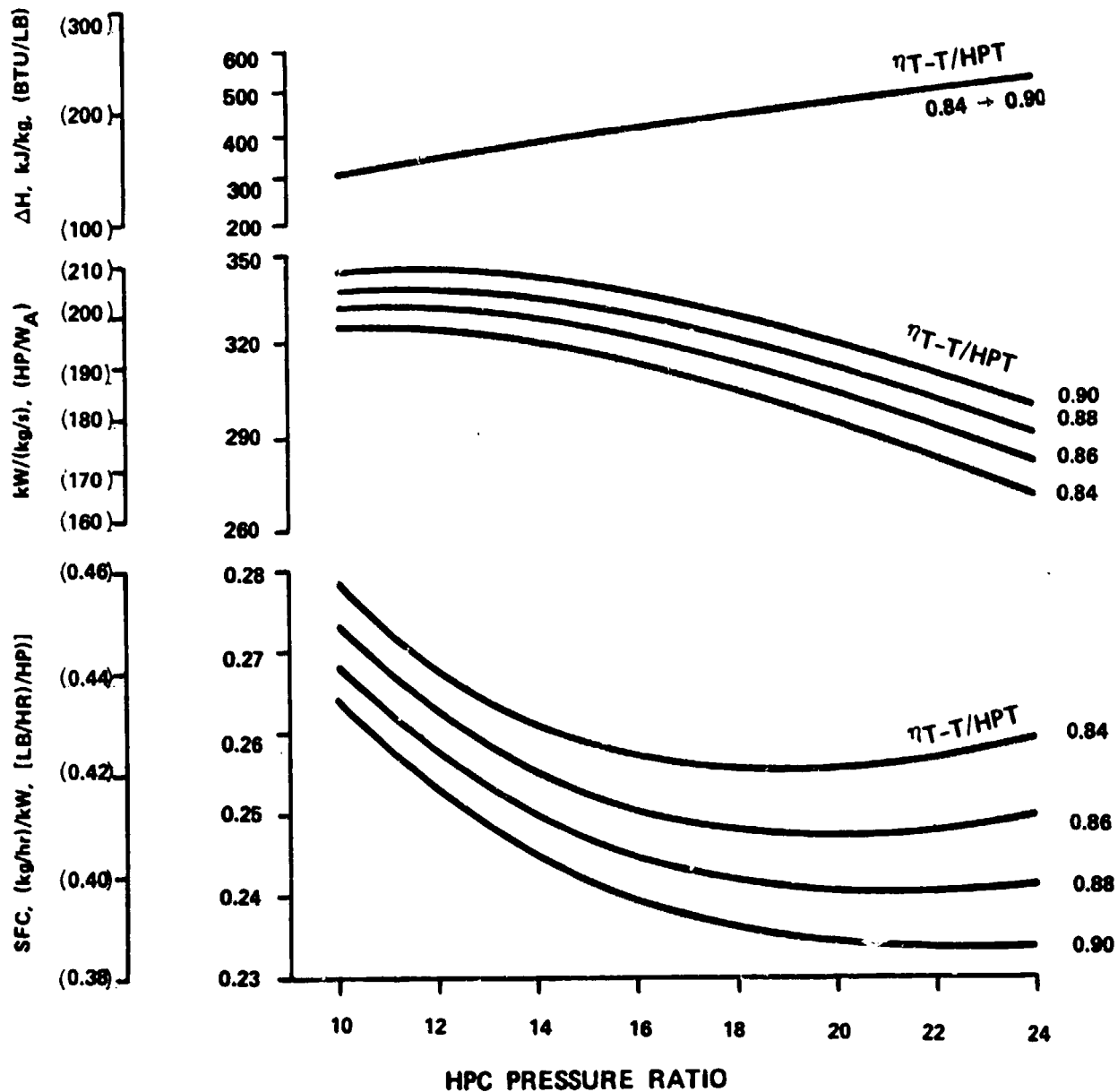


Figure 13. Uncooled, Variable-Area Radial Turbine Study, $T_4 = 1478\text{K}$ (2200°F) At Maximum (100-Percent) Power.

cycle pressure ratios and rotor-inducer tip speeds. This study also provided the characteristic turbine stator and rotor geometry used in the detailed concepts evaluation.

The 1644K (2500°F) cooled configuration was based on a 1-dimensional aerodynamic analysis and accounted for the following effects:

- o Required turbine operating conditions for each selected cycle pressure ratio;
- o A rotational speed for each cycle pressure ratio resulting in a specific speed to maintain peak attainable efficiency.
- o Effects of rotor inlet incidence for a range of rotor-inducer tip speeds.
- o Reynolds number effects.
- o Rotor-clearance effects based on a shroud clearance of 0.038 cm (0.015 in.) and a rotor backface clearance of 0.078 cm (0.030 in.). The backface-clearance effects were updated in the model to account for backface scallop saddle-to-inducer tip radius ratio. This radius ratio was set equal to the specified exducer tip-to-inducer tip radius ratio.
- o Blade number effects = 14 full blades.
- o Rotor exit-hub radius = 3.9 cm (1.55 in.). This radius was representative of previous designs and accounted for a bore radius of 2.2 cm (0.85 in.) plus a 1.8-cm (0.7-in.) disk between the bore and rotor exit hub contour.
- o Rotor backface disk friction effects.
- o Rotor reaction effects.
- o System performance (stage plus interturbine duct) was evaluated as a function of rotor exit swirl with a minimum loss coefficient ($\bar{\omega}$) of 0.200;
- o Effects of rotor exit blockage will be accounted for in the detailed parametric study (Section 7). (However, with the large rotor exit-hub radii required with the bore, rotor-exit blockage was not a significant factor);

- o Current state-of-the-art performance levels;
- o Radial rotor blades.

Cycle pressure ratios of 12:1, 16:1, and 20:1 were selected for the preliminary parametric analysis. This pressure-ratio range covered the minimum turbine stage work level of 407 kJ/kg (175 Btu/lb) and the minimum SFC. The results of this parametric study are presented in terms of both system and stage results. System results were taken from stations 2.0 to 6.0, while the stage results were taken from stations 2.0 to 5.0. (Total conditions in both cases.)

Detailed results of the parametric study are presented in Figures 14 through 16 for a range of specified rotor inlet work coefficients ($\lambda_4 = V_{u4}/U_{t4}$)*. As expected, peak performance was achieved for a given cycle pressure ratio and specified tip speed. Figure 17 shows the results obtained when the loci of peak system efficiencies were plotted as a function of cycle pressure ratio. Although the results shown are for a turbine inlet temperature of 1644K (2500°F), lower temperatures results would be similar. Also, all results are for maximum power. Therefore, the characteristics over the duty cycle have yet to be determined.

Rotor geometries for each cycle pressure ratio are presented in Figure 18 and show the effects of increased cycle pressure ratio on reduced rotor inlet corrected flow. The rotor flow paths shown are for relatively low exducer tip-to-inducer tip radius ratios (minimum disk designs). Changes in rotor geometries as a function of radius ratio for a cycle pressure ratio of 16:1 are presented in Figure 19. These geometries were defined as characteristic flow paths for the cooled rotor concept evaluation.

Figure 20 shows the effects of rotational speed on turbine stage efficiency, specific speed, and geometry for cycle pressure ratios of 16:1 and 20:1.

The basic parametric study was performed with a specified stator exit angle of 1.26 radians (72.0 degrees). Rotor clearance, reaction, and stator-geometry effects (as a function of stator exit flow angle) are presented in Figure 21. The representative rotor geometry shown in Figure 19 was used to evaluate the stator variable-geometry concepts.

*Dashed lines in the figures refer to parameters on the right side of the plots.

NOTES:

- DASHED LINES REFER TO RIGHT SIDE VARIABLES
- SOLID LINES REFER TO LEFT SIDE VARIABLES
- NOTATION ON CURVES REFERS TO INDUCER TIP SPEED (FT/SEC)

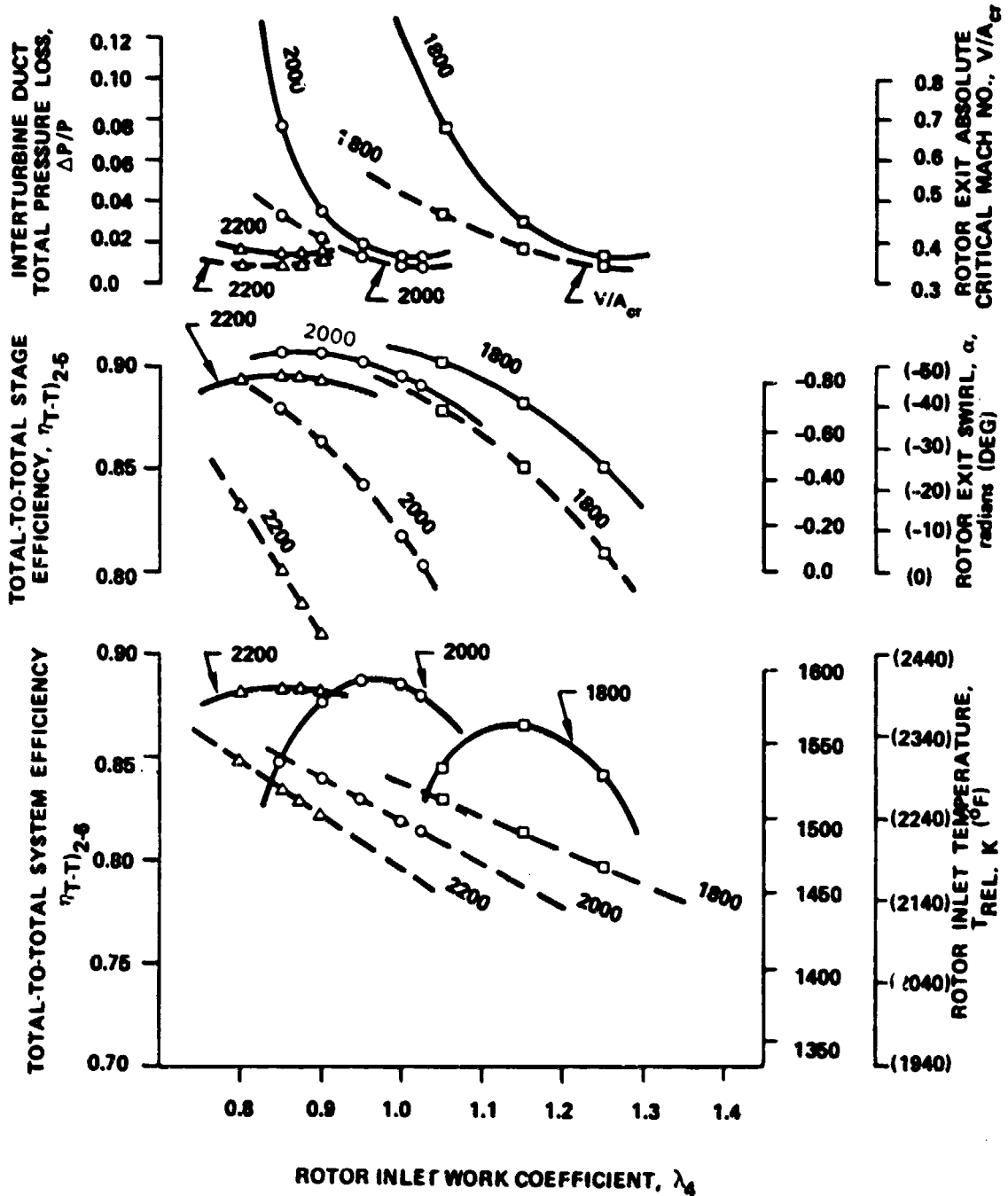


Figure 14. Preliminary Parametric Study for Cooled Rotor Concepts, 12:1 Cycle Pressure Ratio, $T_4 = 1644K$ (2500°F), $N = 6178$ rad/s (59,000 RPM)

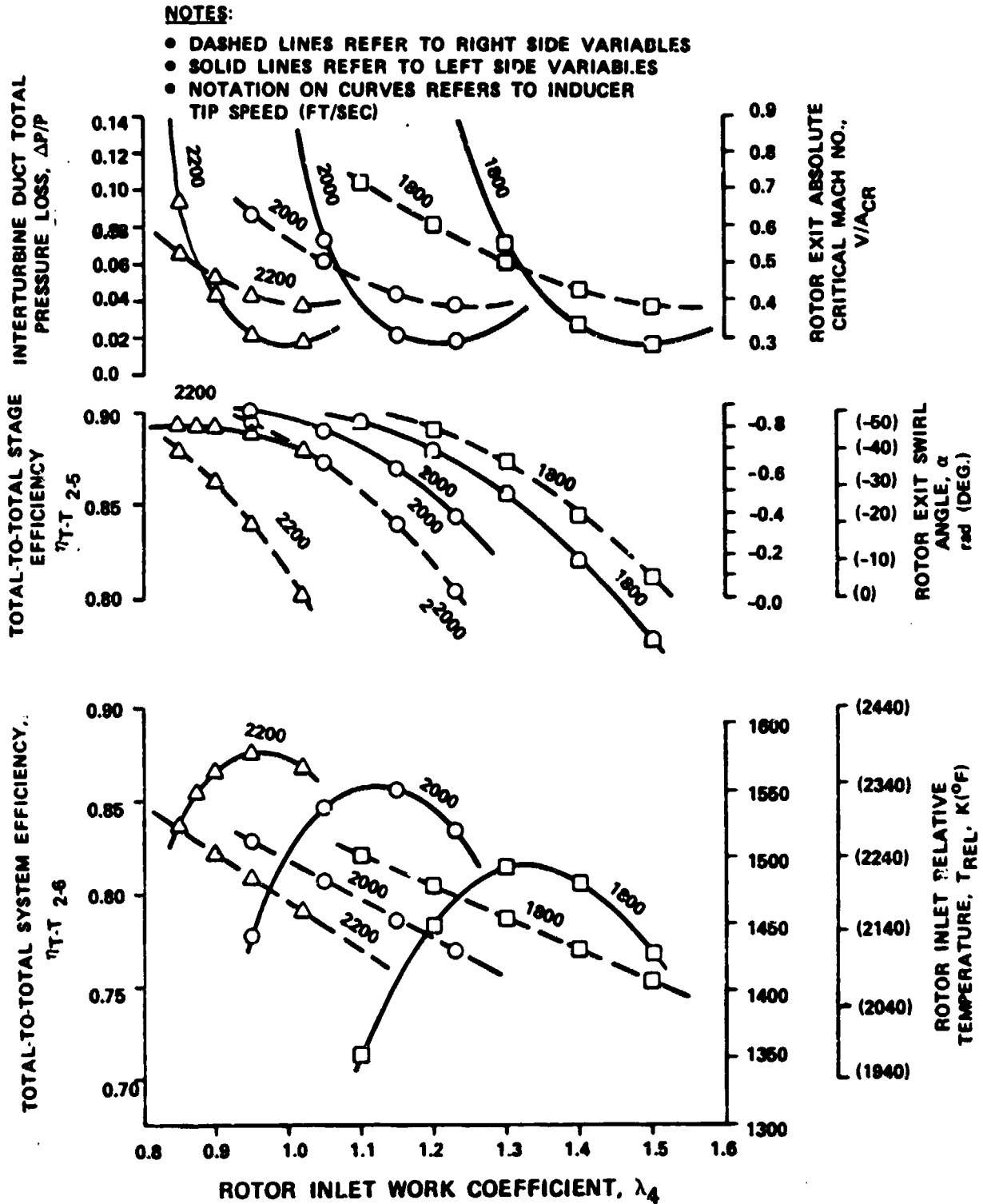


Figure 15. Preliminary Parametric Study for Cooled Rotor Concepts at 16:1 Cycle Pressure Ratio, $T_4 = 1644$ (2500 $^{\circ}$ F) $N = 6807$ rad/s (65,000 RPM).

- NOTES:
- DASHED LINES REFER TO RIGHT SIDE VARIABLES
 - SOLID LINES REFER TO LEFT SIDE VARIABLES
 - NOTATION ON CURVES REFERS TO INDUCER TIP SPEED (FT/SEC)

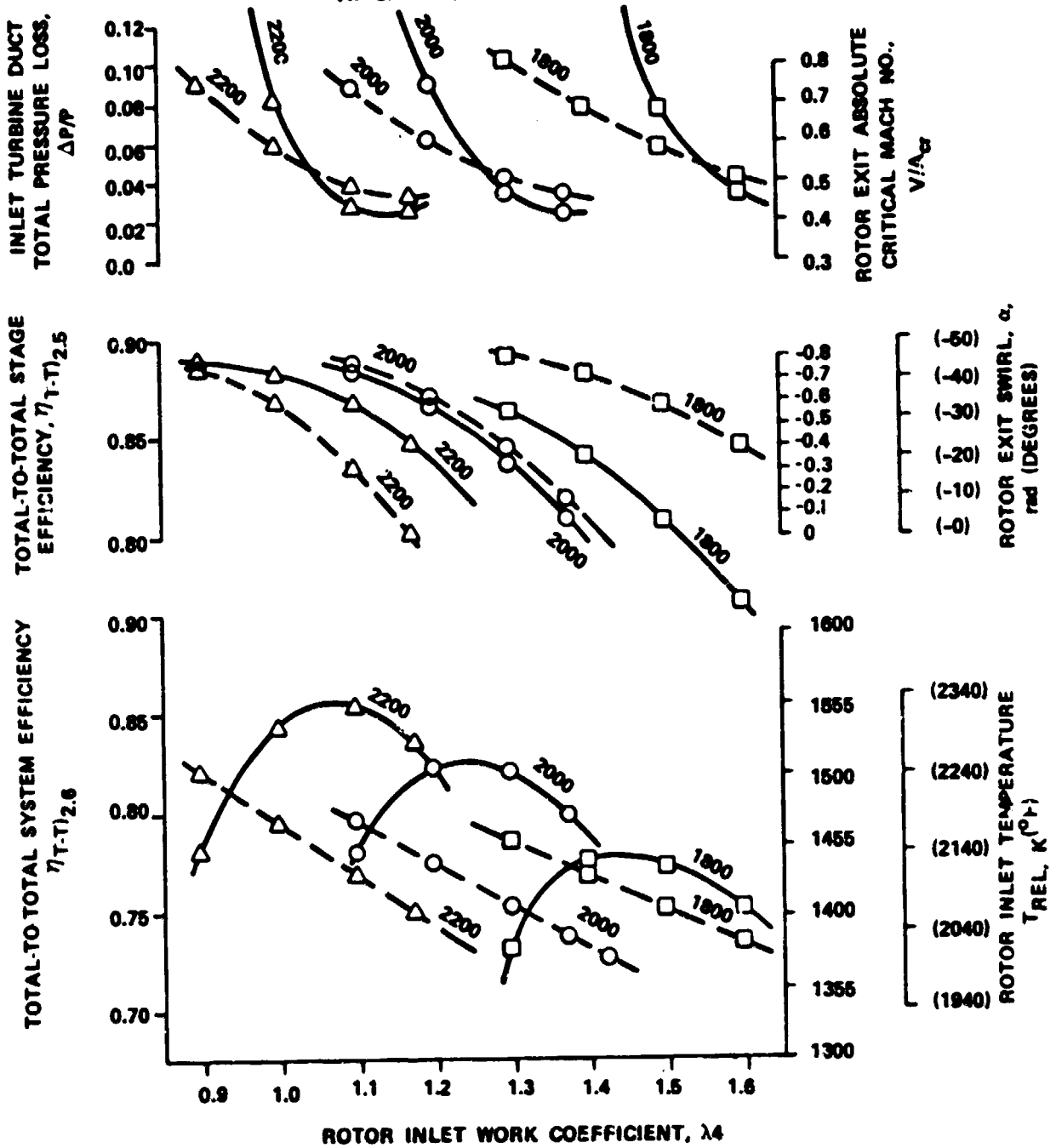


Figure 16. Preliminary Parametric Study for Cooled Rotor Concepts at 20:1 Cycle Pressure Ratio, $T_4 = 1644K$ (2500°F), $N = 7435$ rad/s (71,000 RPM).

NOTES:

- DASHED LINES REFER TO RIGHT SIDE VARIABLES
- SOLID LINES REFER TO LEFT SIDE VARIABLES
- NOTATION ON CURVES REFERS TO INDUCER TIP SPEED (FT/SEC)

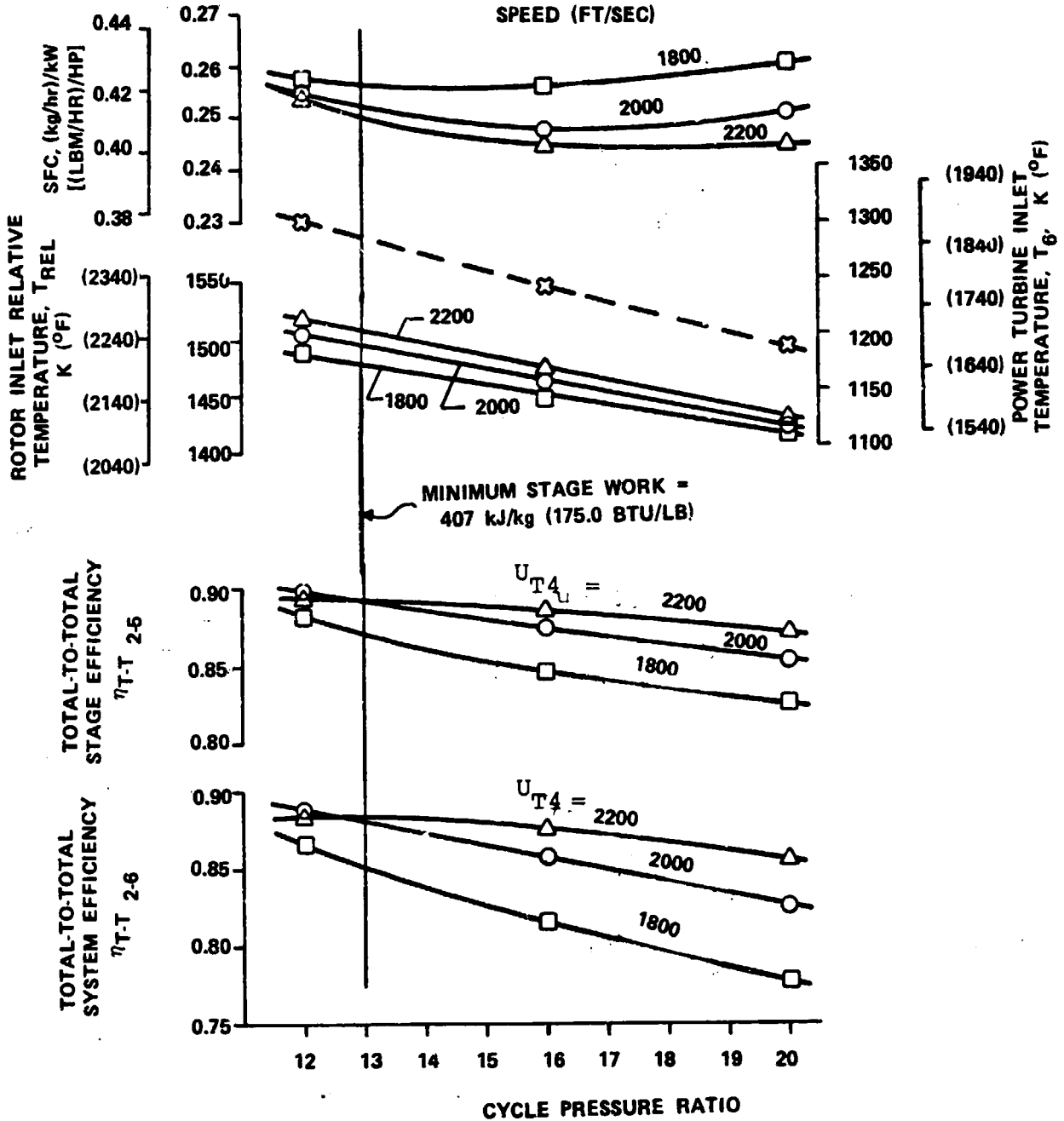


Figure 17. Parametric Study for Cooled Rotor Concepts, 1644K (2500°F) Case.

PR = 12:1

N = 6178 rad/s (59,000 RPM)

$(P/P)_{T-T_{2-5}} = 2.807$

$W\sqrt{\theta/\delta} = 0.4472 \text{ kg/s (0.986 LB/SEC)}$

$\Delta H = 384 \text{ kJ/kg (165 BTU/LB)}$

$\lambda_4 = 0.950$

$\eta_{T-T_{2-5}} = 0.901$

$T_{REL} = 1513\text{K (2264}^\circ\text{F)}$

PR = 16:1

N = 6807 rad/s (65,000 RPM)

$(P/P)_{T-T_{2-5}} = 3.57$

$W\sqrt{\theta/\delta} = 0.331 \text{ kg/s (0.729 LBS/SEC)}$

$\Delta H = 460 \text{ kJ/kg (198.0 BTU/LB)}$

$\lambda_4 = 1.040$

$\eta_{T-T_{2-5}} = 0.884$

$T_{REL} = 1469\text{K (2185}^\circ\text{F)}$

PR = 20:1

N = 7435 rad/s (71,000 RPM)

$(P/P)_{T-T_{2-5}} = 4.49$

$W\sqrt{\theta/\delta} = 0.26 \text{ kg/s (0.575 LB/SEC)}$

$\Delta H = 528 \text{ kJ/kg (227 BTU/LB)}$

$\lambda_4 = 1.075$

$\eta_{T-T_{2-5}} = 0.873$

$T_{REL} = 1437\text{K (2127}^\circ\text{F)}$

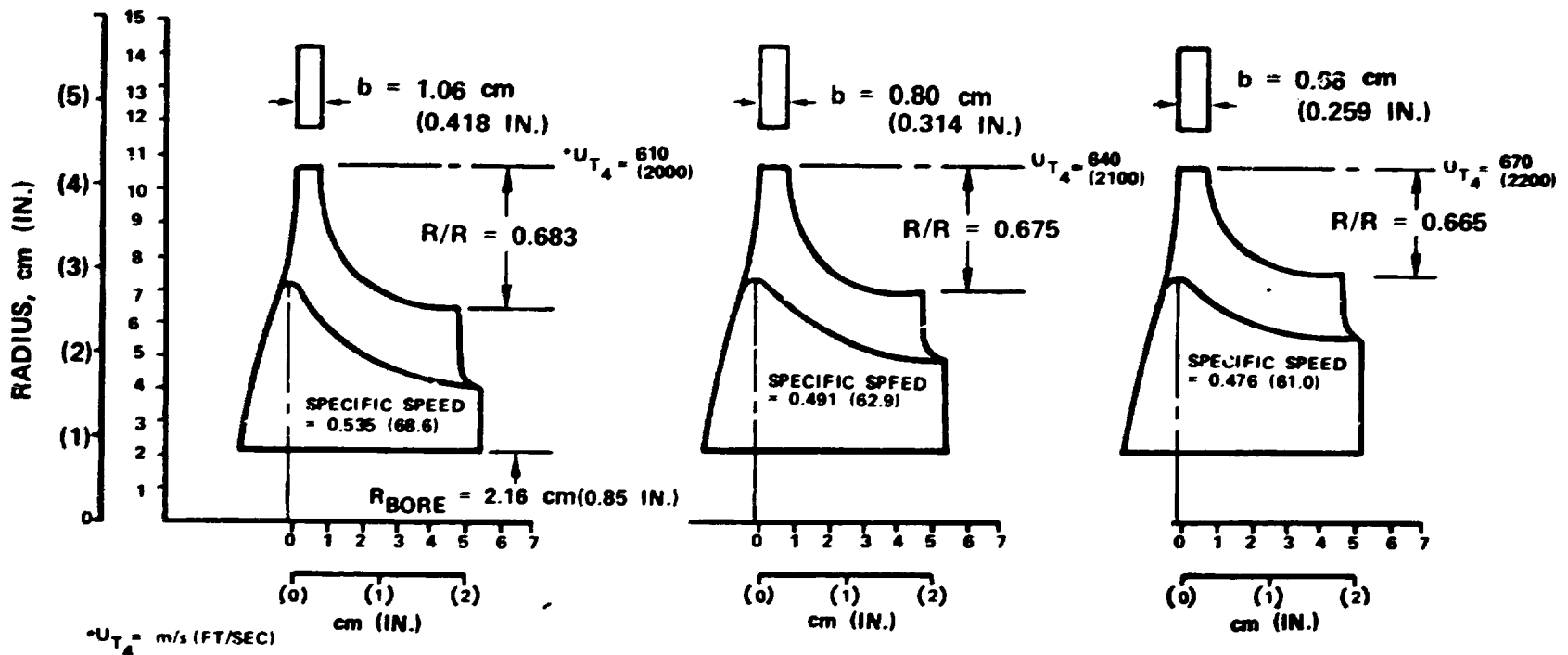


Figure 18. Effect of Cycle Pressure Ratio on Flow-Path Geometry.

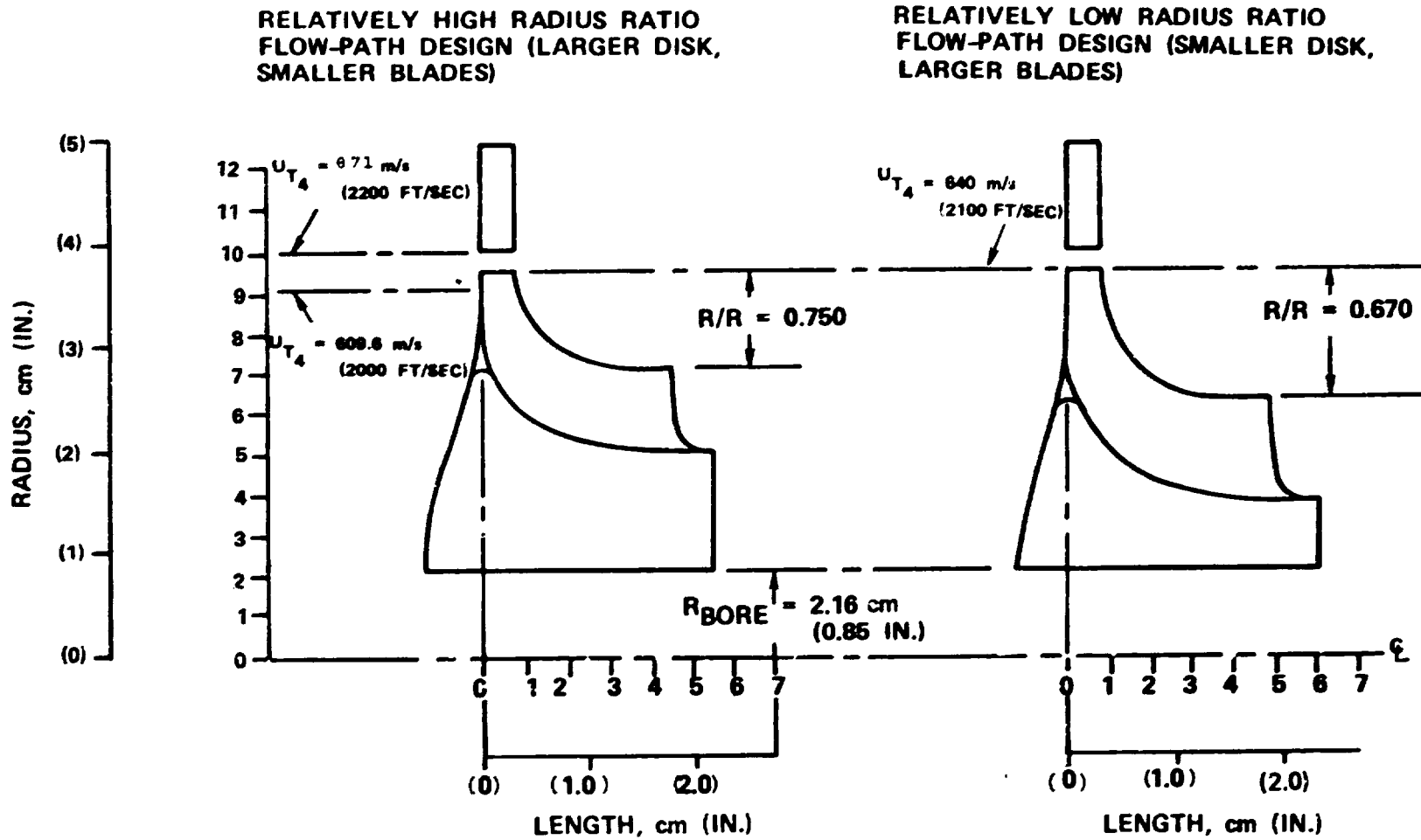


Figure 19. Characteristic Rotors for Evaluation of Concepts.

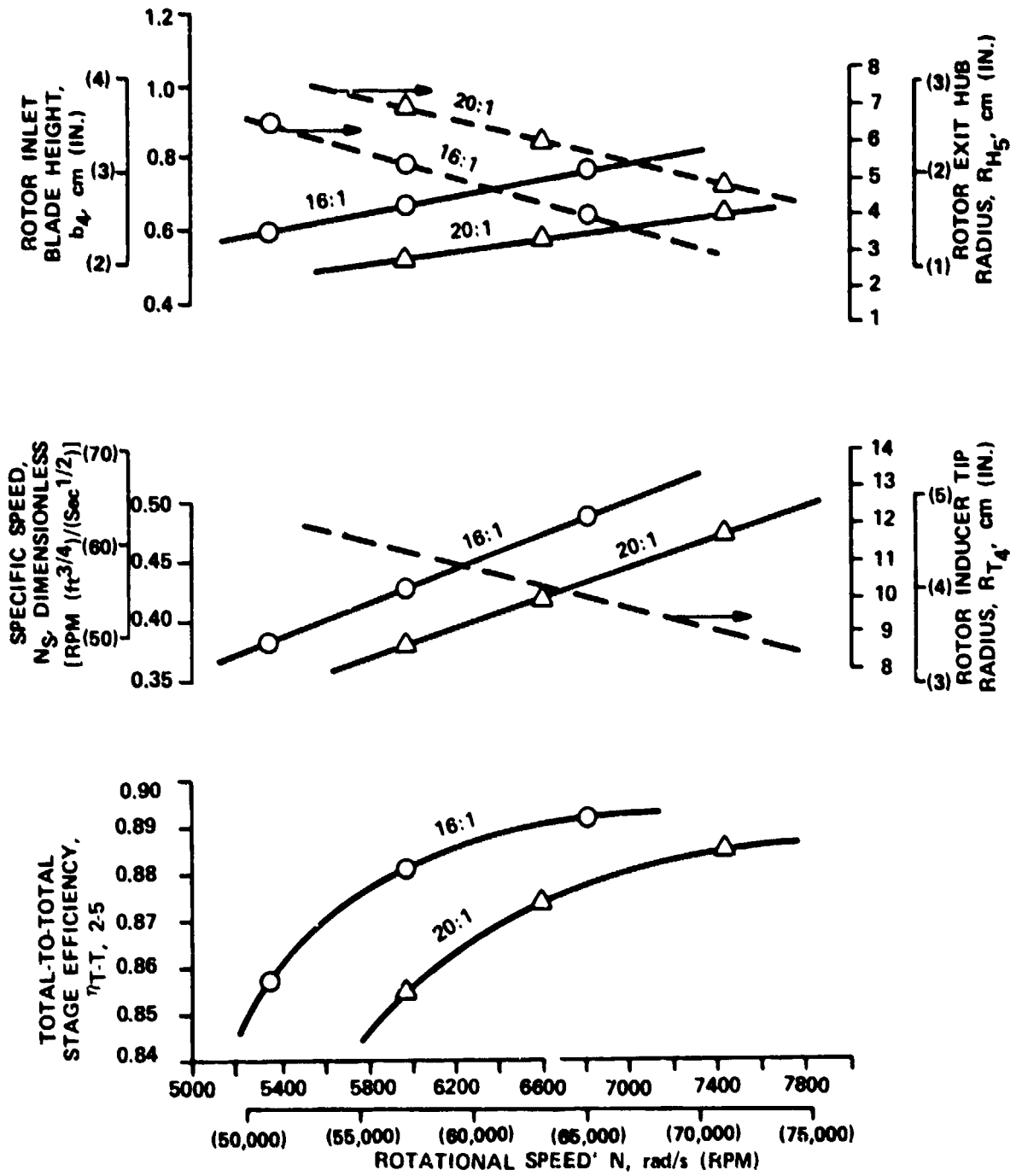


Figure 20. Effect of Rotational Speed on Turbine Performance and Geometry at 1644K (2500°F).

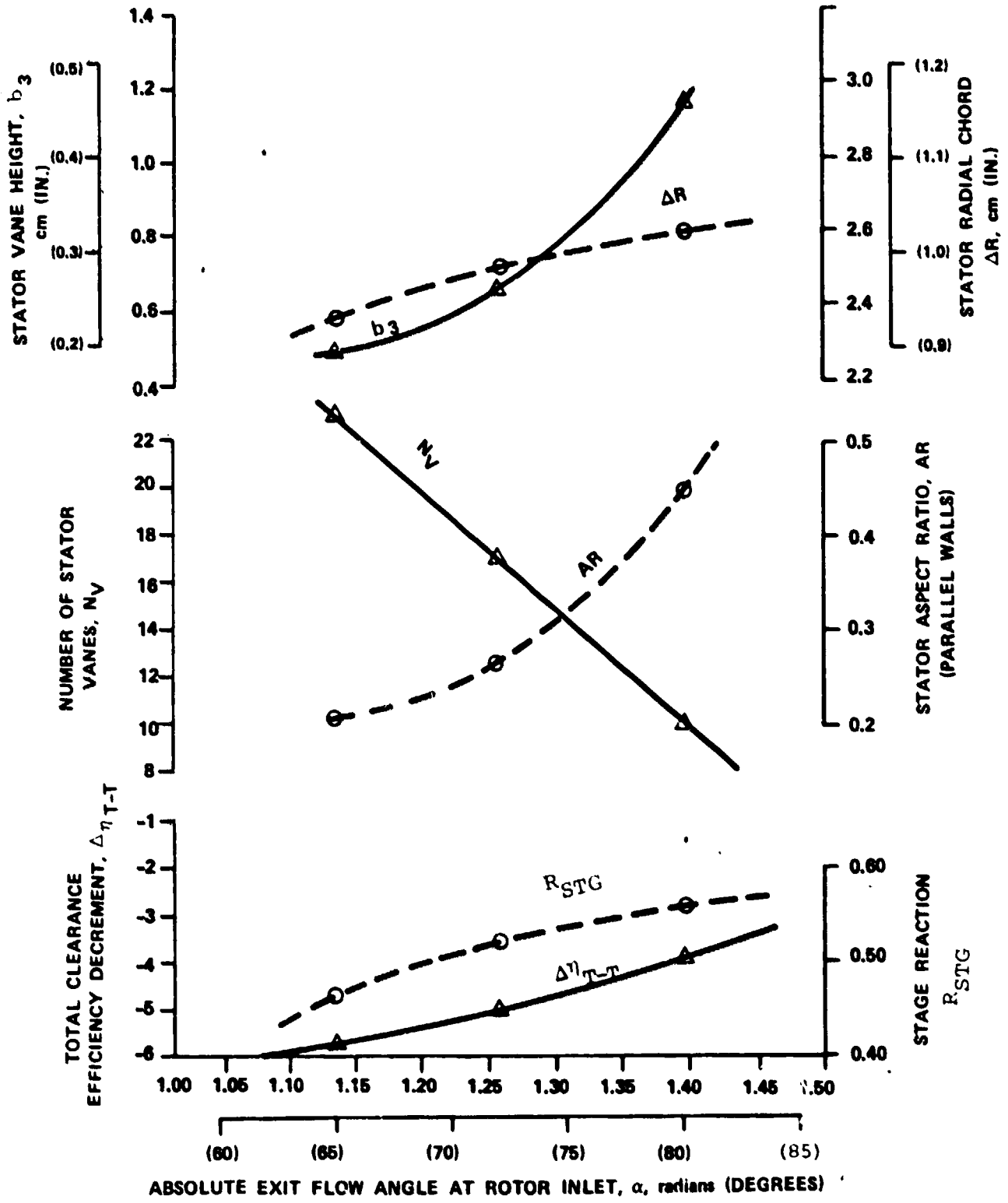


Figure 21. Effects of Stator Exit Angle on Stage and Nozzle Design at 1644K (2500°F), 7435 rad/s (71,000 RPM) and at 671 m/s (2200 Ft/Sec).

4.3.2 Turbine Off-Design Performance Characteristics

The preliminary parametric study established the turbine performance, geometry, duct loss, and rotor-inlet relative-temperature characteristics for a range of cycle pressure ratios and rotor-inducer tip speeds. Since these results were for the maximum power point, the objective of the off-design analysis was to evaluate the feasibility of maintaining constant performance over a range of engine powers using constant speed and pressure ratio. In addition, the effects of tip speed and rotor exducer tip-to-inducer tip radius ratio were also evaluated. Figure 22 shows the three cases selected for evaluation. The first case was based on the characteristic flow path with an inducer tip speed of 640 m/s (2100 ft/sec), a radius ratio of 0.75, and peak system efficiency. This condition was equivalent to an optimized design point at maximum power.

The off-design study was based on aerodynamic effects alone; the effects of stator and rotor cooling and leakage were not included. However, these effects were taken into consideration in the detailed parametric analysis. Figure 23 presents the predicted off-design characteristics for Case No. 1 from 50- to 100-percent engine power. The stage efficiency and rotor inlet relative temperature decreased uniformly from 100- to 50-percent power. However, when the effects of the interturbine duct loss were included in the stage efficiency, the system efficiency was fairly uniform down to 80-percent power. Below 60-percent power, however, duct loss significantly reduced system efficiency.

For the Case No. 2, the rotor radius ratio was maintained at 0.75, but inducer-tip speed was increased to 67 m/sec (2200 ft/sec), and rotor-exit swirl was increased from -0.31 to -0.53 radian (-17.8 to -30.4 degrees). Therefore, this configuration was equivalent to optimizing the design point at a lower engine power point. The off-design characteristics for this case are presented in Figure 24. Although the turbine stage efficiency decreased uniformly from 100- to 60-percent power, system efficiency was fairly flat from 100- to 70-percent power (± 1.0 point).

For Case No. 3, the effect of rotor inducer-to-exducer tip radius ratio was examined in relationship to Case No. 2. Decreasing the radius ratio from 0.75 to 0.6431 produced the results shown in in Figure 25. For this case, a fairly uniform system efficiency was achieved (± 1.2 points) between 60- and 90-percent power. A comparison of the 1-dimensional vector diagrams at 60- and 100-percent power is presented in Figure 26 for Case No. 3.

The general trends resulting from the off-design analysis are:

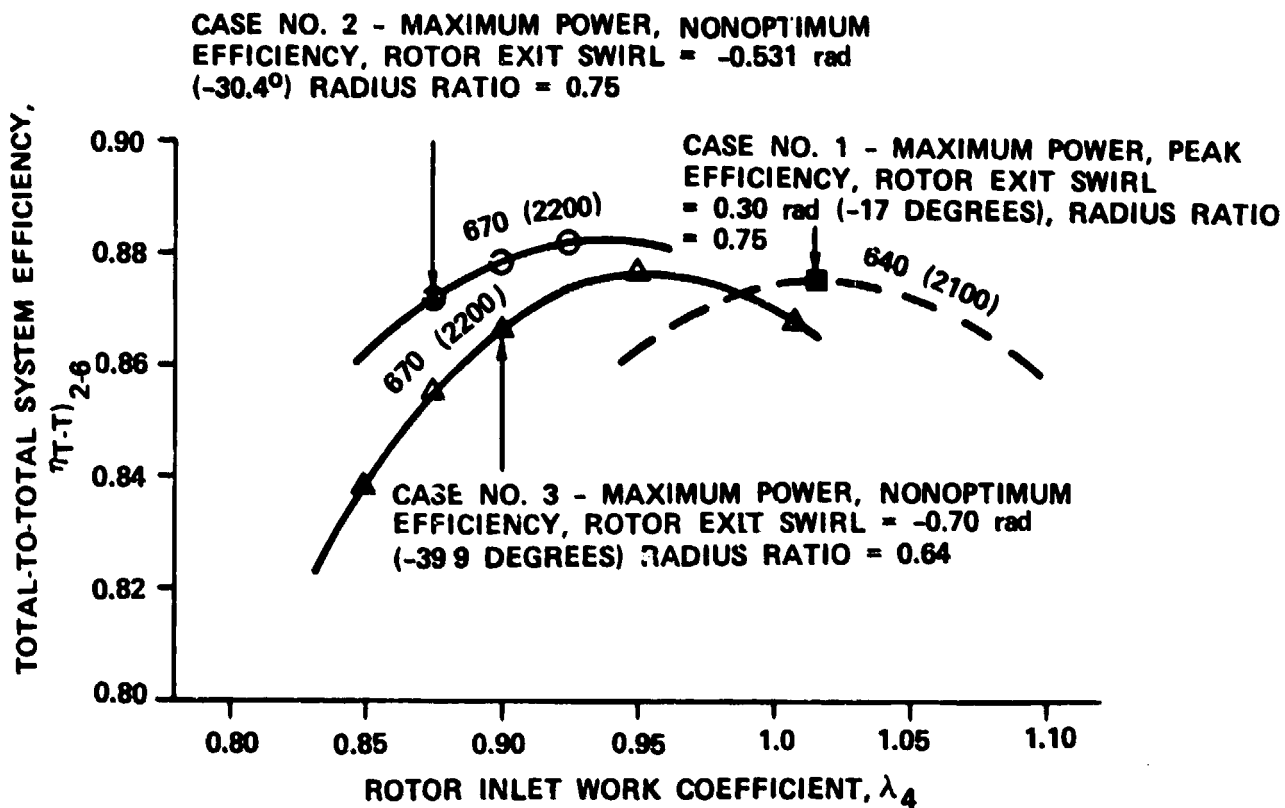


Figure 22. Selected Maximum Power Design Points for Off-Design Analysis. 16:1 Cycle Pressure Ratio, $T_4 = 1644K$ (2500°F) and $N = 6807 \text{ rad/s}$ (65,000 RPM)..

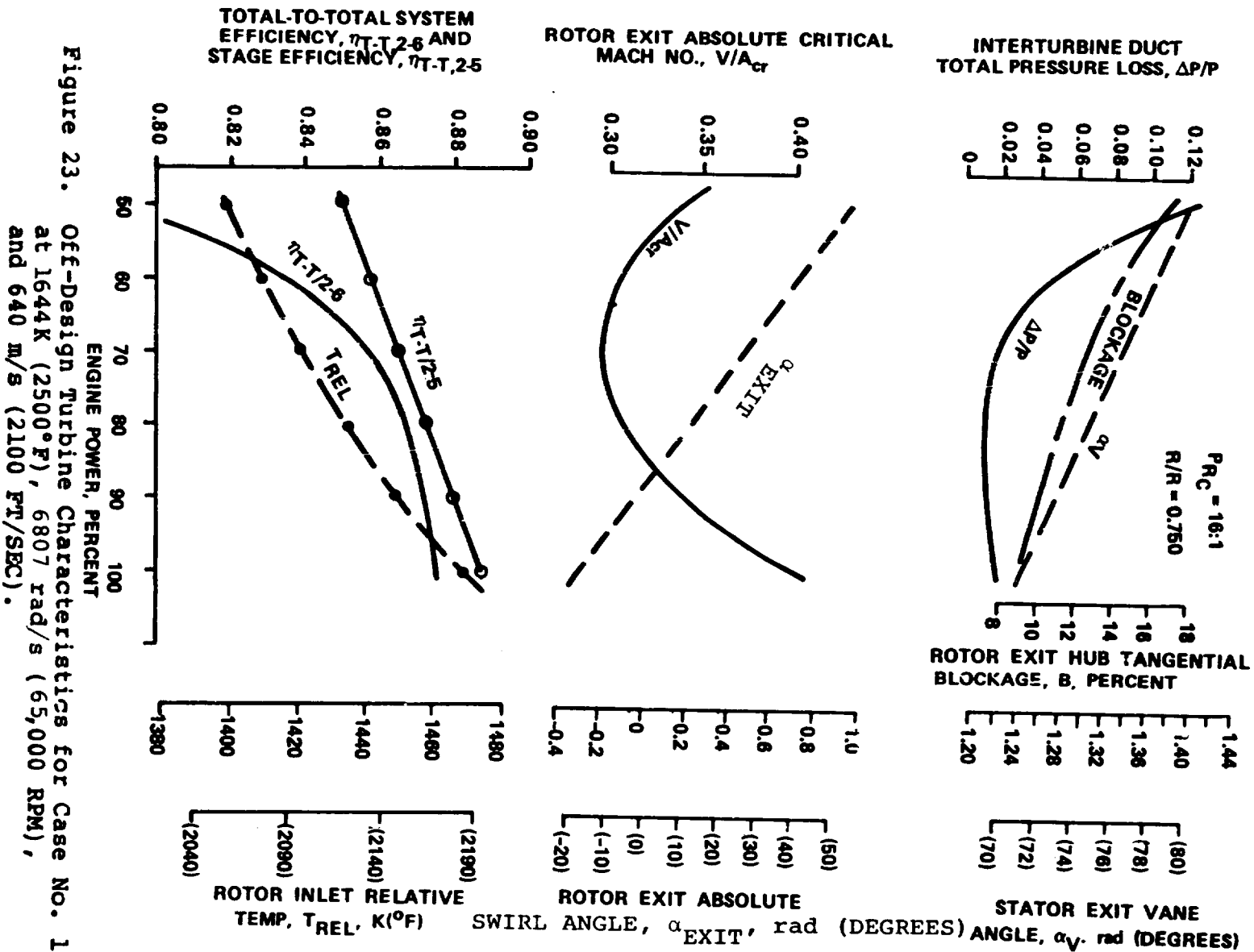


Figure 23. Off-Design Turbine Characteristics for Case No. 1 at 1644 K (2500°F), 6807 rad/s (65,000 RPM), and 640 m/s (2100 FT/SEC).

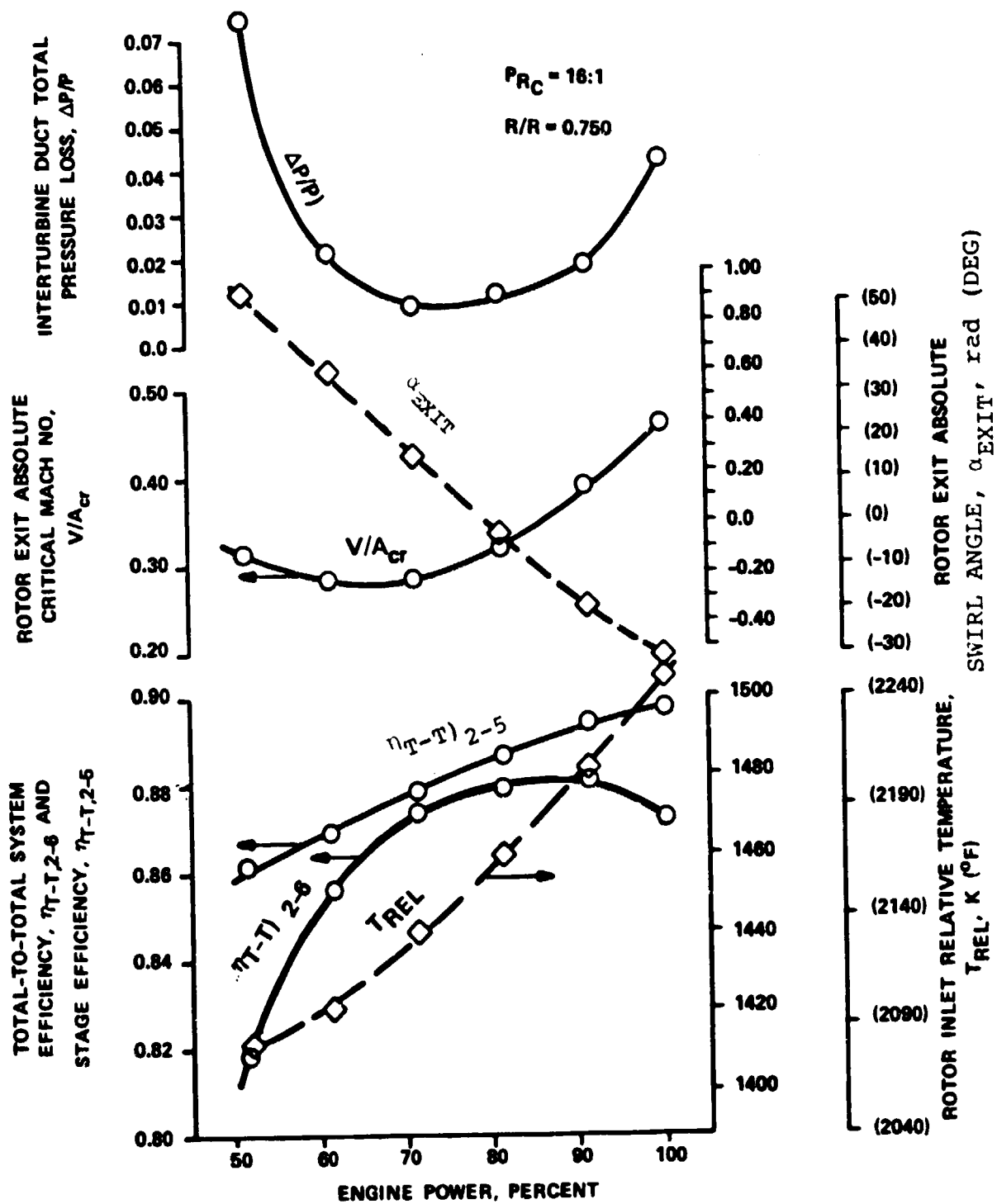


Figure 24. Off-Design Turbine Characteristics for Case No. 2 at 1644K (2500°F), 6807 rad/s (65,000 RPM) and 671 m/s (2200 Ft/Sec).

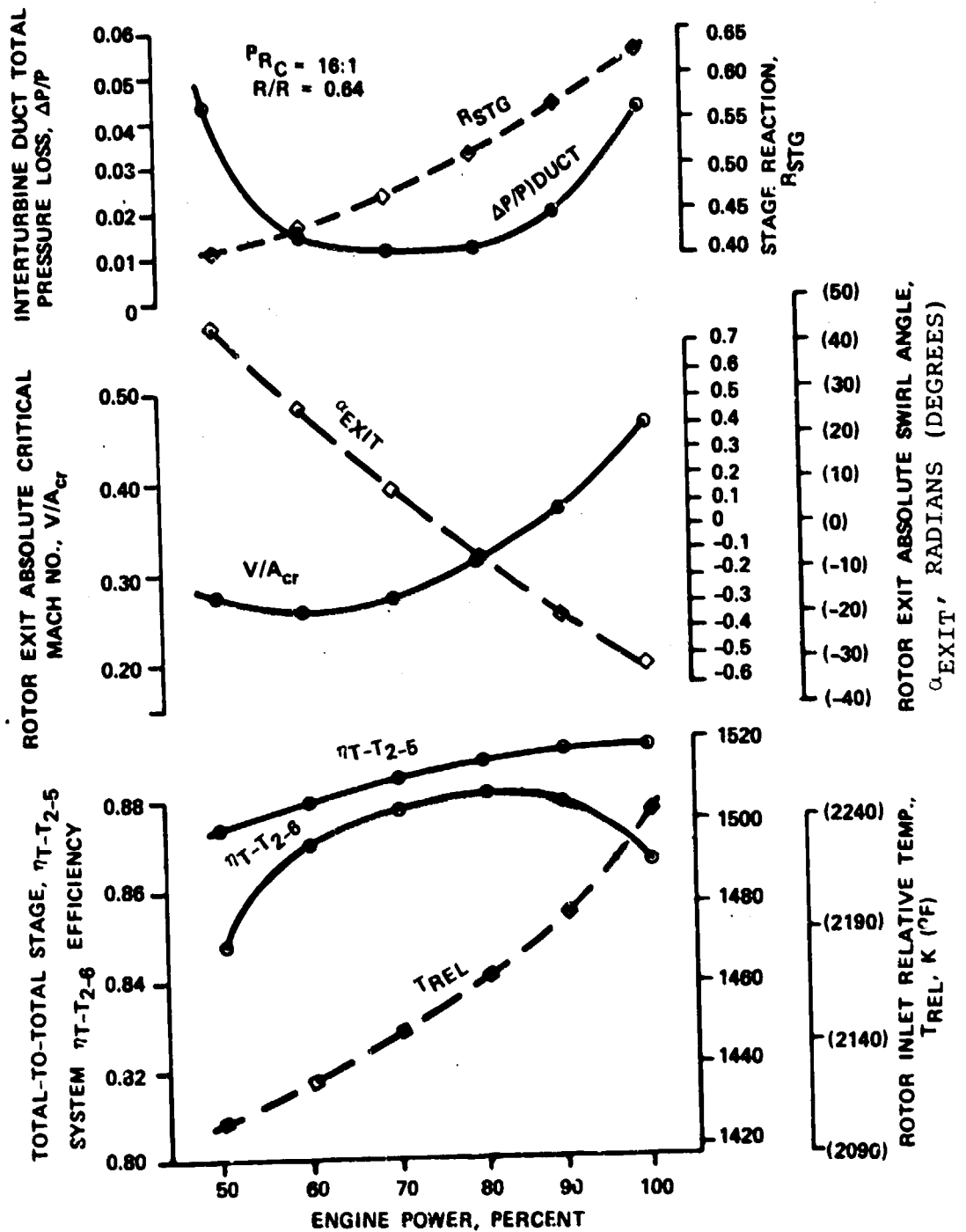


Figure 25. Off-Design Turbine Characteristics for Case No. 3 at 1644K (2500°F) 6807 rad/s (65,000 RPM) and 671 m/s (2200 Ft/Sec).

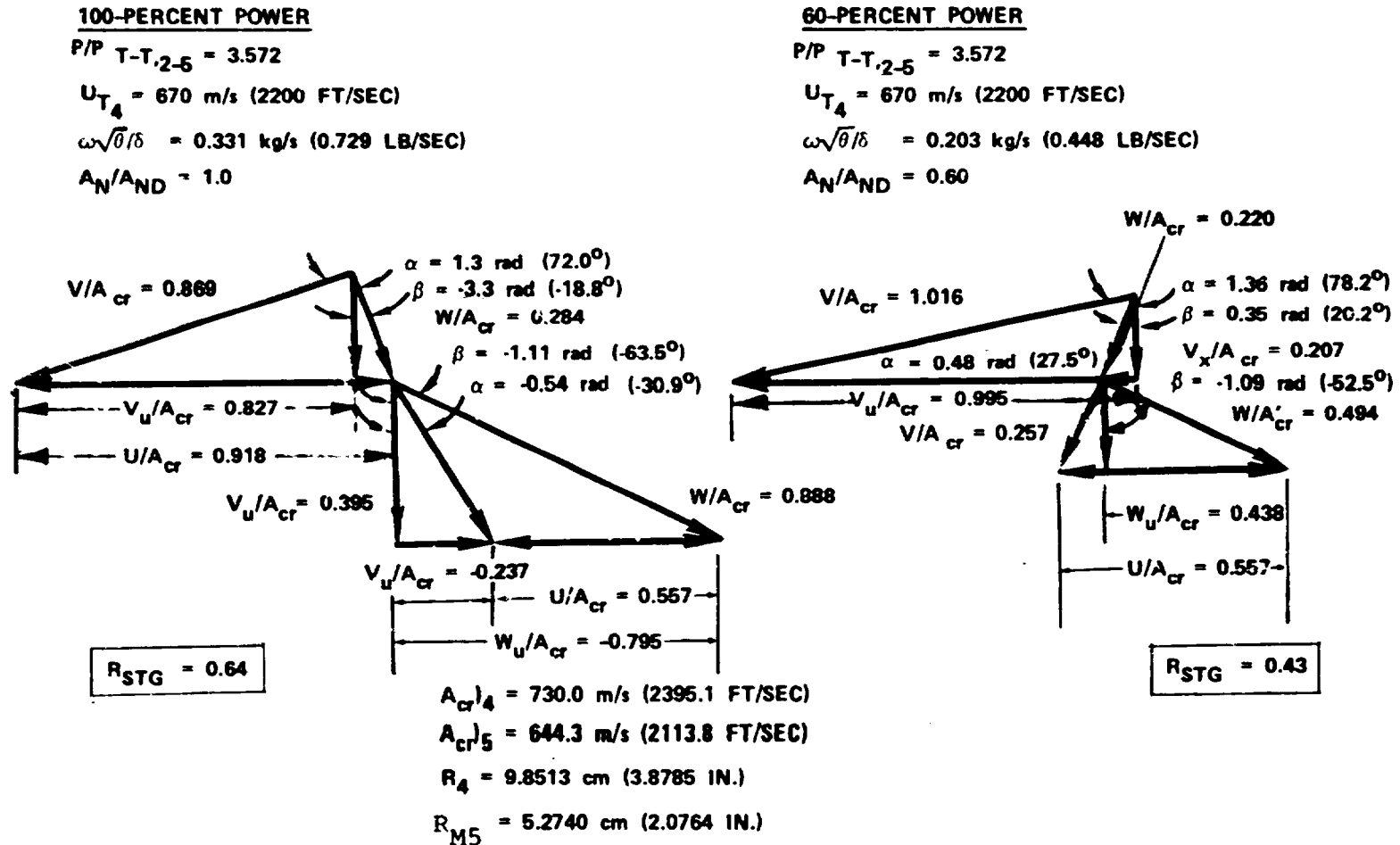


Figure 26. Case No. 3 Turbine 1-Dimensional Vector Diagrams for 60- and 100-Percent Power at 1644K (2500°F), 6807 rad/s (65,000 RPM) and $R/R = 0.643$.

- o Optimizing the turbine design point at maximum power resulted in significant performance penalties at lower power levels for Case No. 1.
- o All cases showed that limiting the flow reduction to 60 percent with a constant speed, pressure ratio, and temperature concept is desirable.
- o All cases showed a reduction in rotor inlet relative temperature (higher inducer loading) in excess of 311K (100°F) occurred from 100- to 60-percent power at a constant turbine-inlet temperature.
- o The change in rotor exit swirl is on the order of 1.05 radians (60 degrees) between maximum power and 60-percent power. [For example; Case No. 3 was -0.54 to 0.51 radian (-31.0 to +29.0 degrees)].
- o The change in rotor exit swirl and rotor inlet work coefficient is minimized between 100- and 60-percent power with lower radius ratio designs.
- o Rotor reaction decreases as engine power decreases (see Figure 25).
- o A relatively constant system efficiency (± 1.1 points) was maintained between 60- and 97.5-percent power for Case No. 3.

4.4 Stator Concepts Aero/Mechanical Evaluation

4.4.1 Vane Profile Design for Stator Concepts

A vane profile design for the stator concepts analysis was derived from the maximum-power 1-dimensional vector diagram shown in Figure 26 and the vane meridional flow path shown in Figure 19. The key stator design parameters used to optimize the vane loading were:

- o $R_{2INLET} = 12.50$ cm (4.92 in.);
- o $R_{3EXIT} = 9.896$ cm (3.896 in.);
- o $b = 0.798$ cm (0.314 in.);
- o $N_V = 18$ vanes
- o Stator inlet flow angle = 0.0 radian (0.0 deg.);
- o Stator exit flow angle = 1.23 radians (70.4 deg.);

- o Stator inlet critical velocity ratio = 0.1424 (with parallel endwalls);
- o Stator exit critical velocity ratio = 0.907.

The basic design procedure used for a radial stator is to define the profile in the axial plane (at a section corresponding to the nozzle trailing-edge radius) and then to transform this section to the radial plane. This conformal transformation increased the geometric throat dimension so that the radial-profile section surface had to be modified to reestablish the original throat dimension. The final airfoil shape was then established by successive iterations using the transformed vane shape and blade-to-blade velocity distributions. The stator vane profile design derived for the aerodynamic and mechanical stator concepts is shown in Figures 27 and 28. The design objective in both cases was to load the stator leading-edge. This minimized the blade-to-blade pressure gradient in the trailing-edge region, since loading increases at reduced nozzle-area settings in this region. The resultant high loading at the stator leading-edge can then be reduced by endwall contouring.

A screening study was then conducted to review the variable-area stator designs. The objectives of this study were:

- o To define variable-area nozzle methods that would allow arbitrary stator endwalls;
- o To eliminate the need for upstream struts for structural support;
- o To minimize stator leakage; and
- o To allow realistic mechanical actuation.

For a constant section vane profile with parallel endwalls, the stator throat area is:

$$A_t = N_v \cdot O \cdot b$$

where:

- N_v = Number of vanes;
- O = Throat dimension;
- b = Vane height.

Twelve possible stator concepts were defined using the three variables that affected the total throat area. An aerodynamic and mechanical screening process then reduced this number to four.

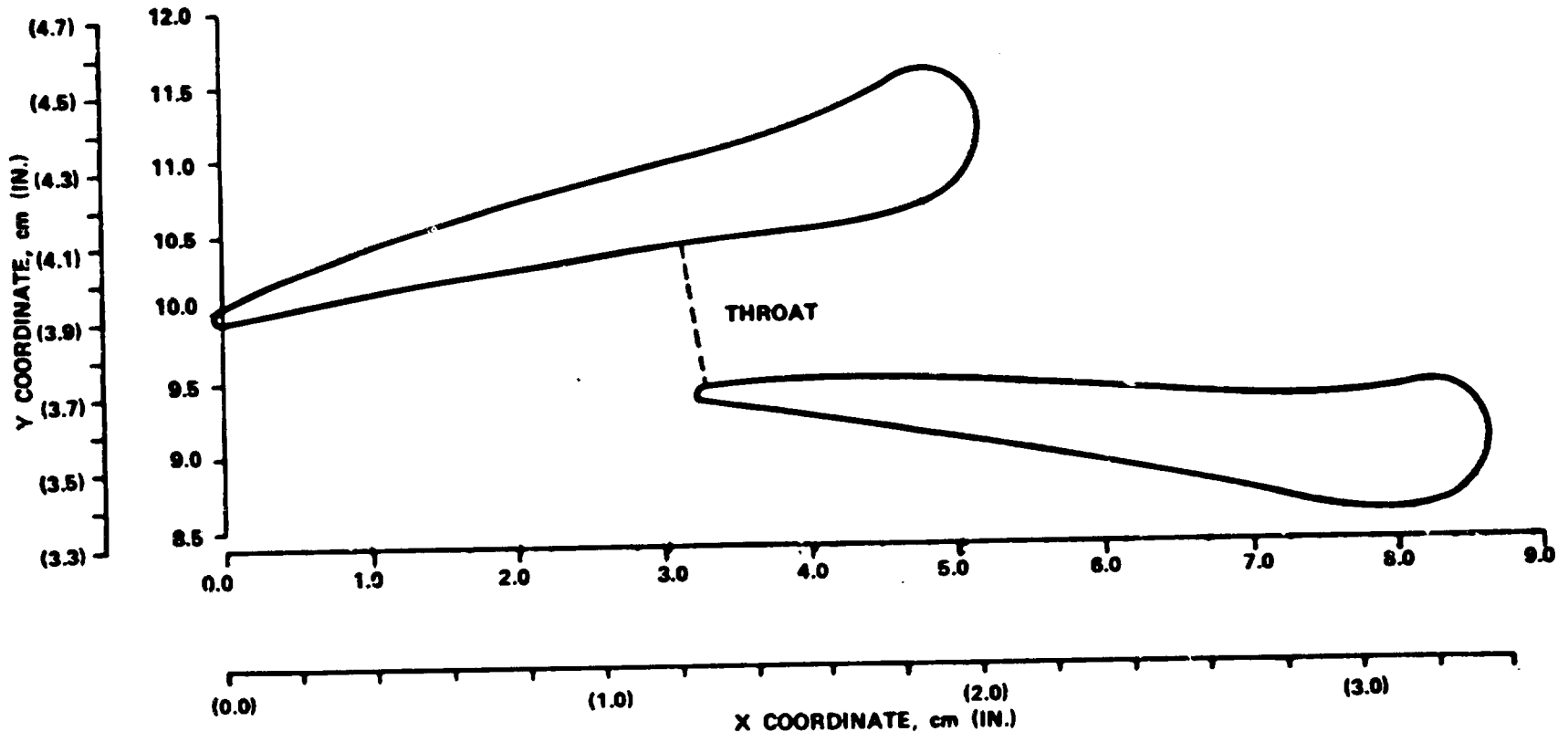


Figure 27. Stator Profile Design for Variable Area Concepts Evaluation (19 Vanes).

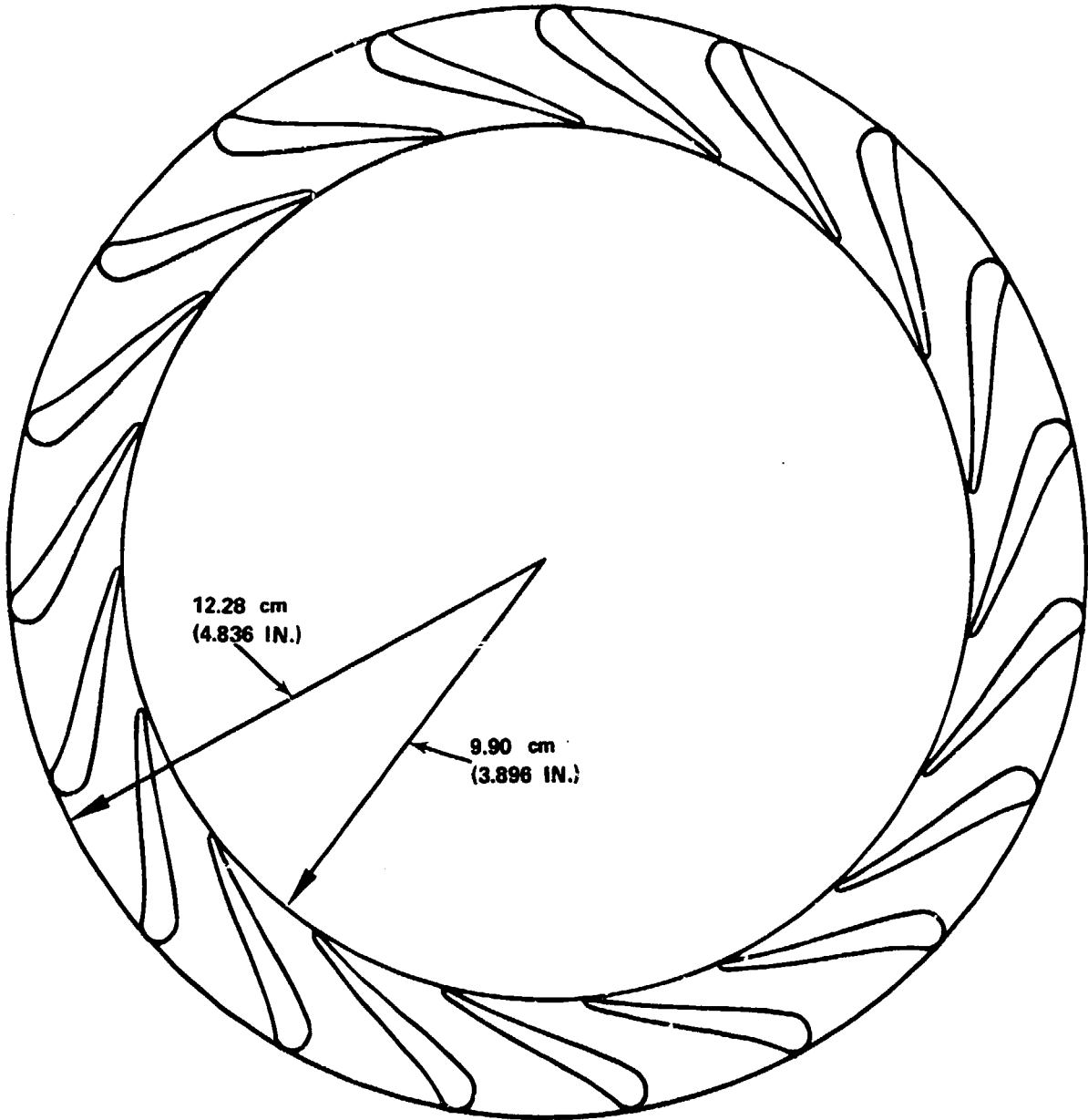


Figure 28. Stator Ring at Maximum Power Setting.

4.4.2 Full-Vane Rotation Concept

The full-vane rotation concept is considered the conventional approach, and has been successfully used in both axial turbines and compressors. For this particular application, a selected number of vanes would remain fixed for structural support of the vane sidewalls as shown in Figure 29. The major advantage of this approach is that it provides a single-piece, easily cooled vane with solid, stationary sidewalls.

The vane suction- and pressure-side surface velocity distributions for 60- and 100-percent power are also shown in Figure 29. While these velocity distributions do not take into account the effect of maintaining a portion of the vanes fixed, the extremes in vane-to-vane velocity variation would be expected to occur between 60- and 100-percent power. The aerodynamic and mechanical effects associated with the higher circumferential velocity gradients were difficult to assess. Previous experience with inlet scrolls has indicated that if significant turbine circumferential maldistribution is generated by the scrolls, overall stage performance would be decreased more than would be expected from scroll pressure loss alone. Mechanically, circumferential maldistribution could result in inducer blade vibration.

4.4.3 Articulated Trailing-Edge Concept

This concept was based on rotating the vane trailing-edge only. This allowed the vane leading-edge section to remain fixed for structural support as shown in Figure 30. The vane inlet sidewall could then be contoured to minimize vane loading. The sidewall leakage should be significantly less than that of the full-vane rotation concept.

Velocity distributions at 60- and 100-percent power indicate that the major drawback to this configuration is the high trailing-edge loading that results from rotating the vane to 60-percent power. The high static-pressure gradient in this region increases vane leakage unless an effective sidewall seal is provided. Mechanically, the smaller size of the articulated trailing-edge could complicate routing of internal cooling airflow to this region.

4.4.4 Insertable Minivane Concept

In the insertable minivane concept stator flow area is reduced by inserting minivanes between fixed primary vanes. This results in stationary sidewalls and single-piece vanes that can be readily cooled. The insertable minivane concept is compatible with contoured sidewalls, and provides support for the sidewalls, and should minimize leakage flows. Two methods of insertion were

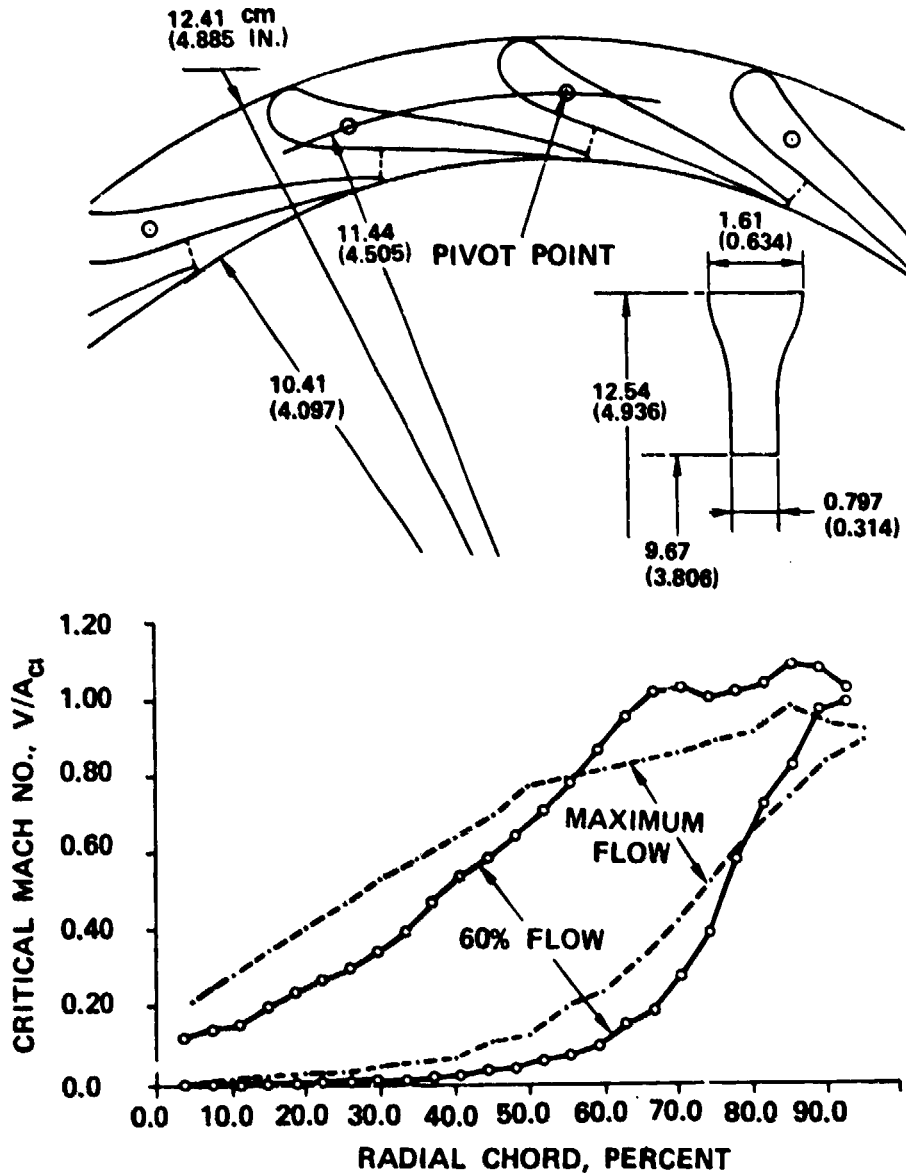


Figure 29. Full Vane Rotation, Nozzle Area Variation Concept.

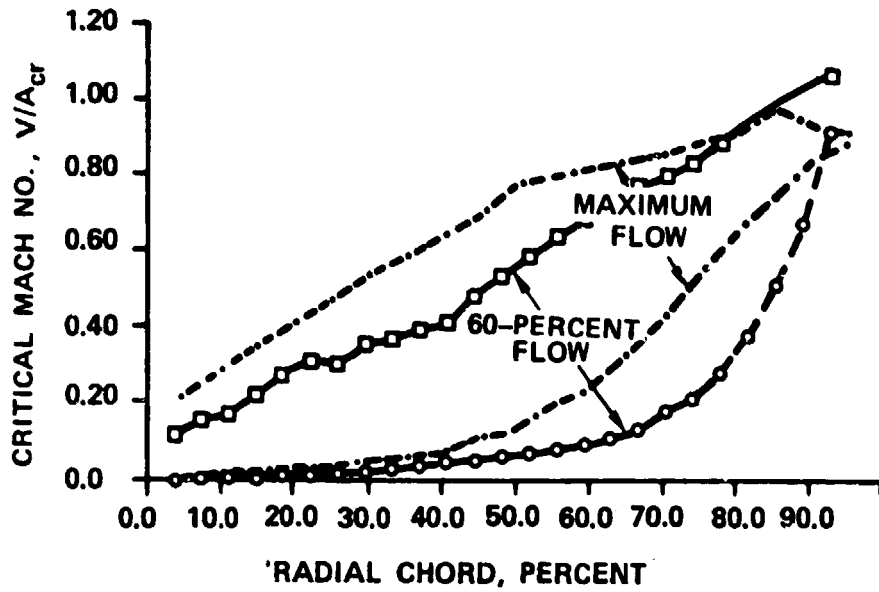
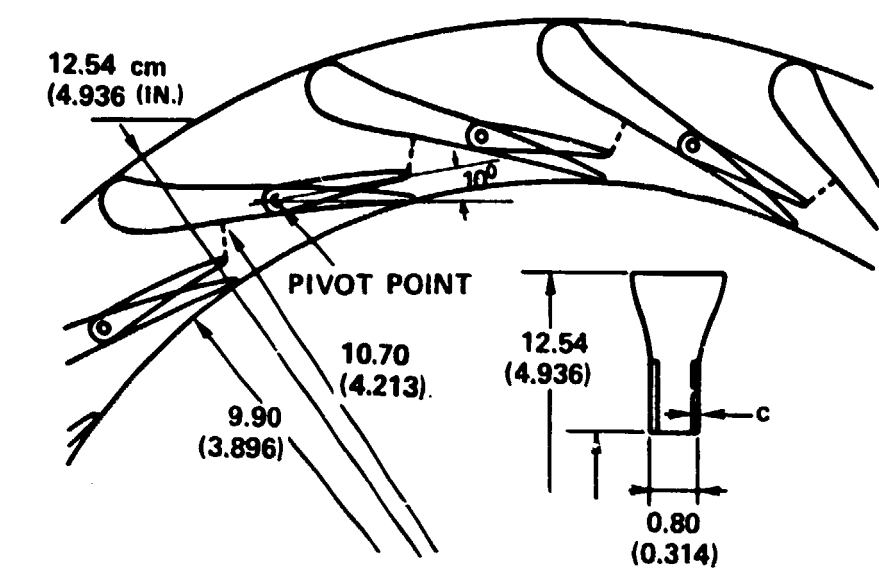


Figure 30. Articulated Trailing-Edge Nozzle Area Variation Concept.

considered feasible. In the first method, the immersion depth of all minivanes would be varied in unison. In the second method, a selected number of minivanes would be inserted along the full vane width. Sequencing the number of fully immersed minivanes results in a step change in turbine flow. This concept is presented in Figure 31.

The minivane design depends on maintaining a convergent passage on either side of the minivane. This results in a rather large trailing-edge thickness that significantly increases vane-exit blockage. Mechanically, the periodic vane trailing-edge wakes would vary from 0.31 to 0.63 radian (18 to 36 degrees), which could create serious rotor blade vibration problems. In addition, mechanical linkage would be complicated if an incremental insertion were used.

4.4.5 Locally Movable Sidewall Concept

This concept reduces the stator throat area via a local change in stator passage width as shown in Figure 32. A passage constriction is readily achieved by axial translation of a portion of the sidewall. The most favorable vane loading -- from 60- to 100-percent power -- results with this method. This design is compatible with contoured sidewalls and has many of the advantages of the inserted-minivanes concept--without the disadvantage of forced periodicity at the stator-exit flow. However, previous cold-air test data show that stator-passage width reduction results in relatively high dump losses due to the sudden expansion in passage width at the rotor inlet.

Subsequent evaluation of this concept showed that alternate methods could be used to restrict the passage width and thus eliminate the high dump losses. Two alternate methods were defined: a purely rotating sidewall segment and a rotating-translating sidewall segment. In each method, the sudden expansion at the stator exit was replaced with a smooth ramp. However, both methods would require more complex actuation mechanisms.

4.5 Stator Material Evaluation

4.5.1 Airfoil

The material selection for the cooled stator airfoil for the engine was based on the following parameters:

- o Stress-rupture capability;
- o Coated-oxidation resistance;
- o Overtemperature capability; and
- o Thermal-fatigue resistance.

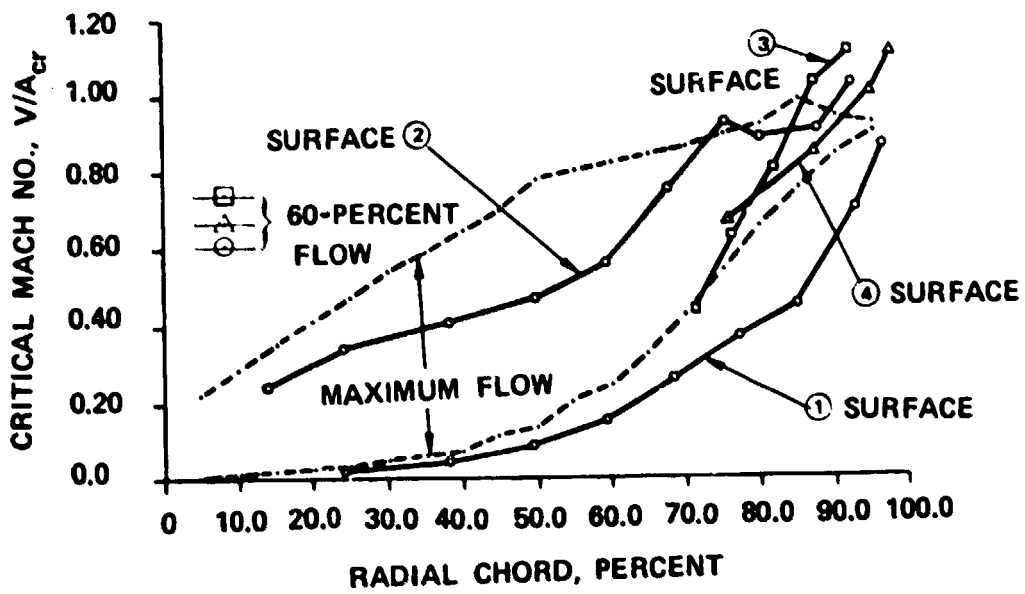
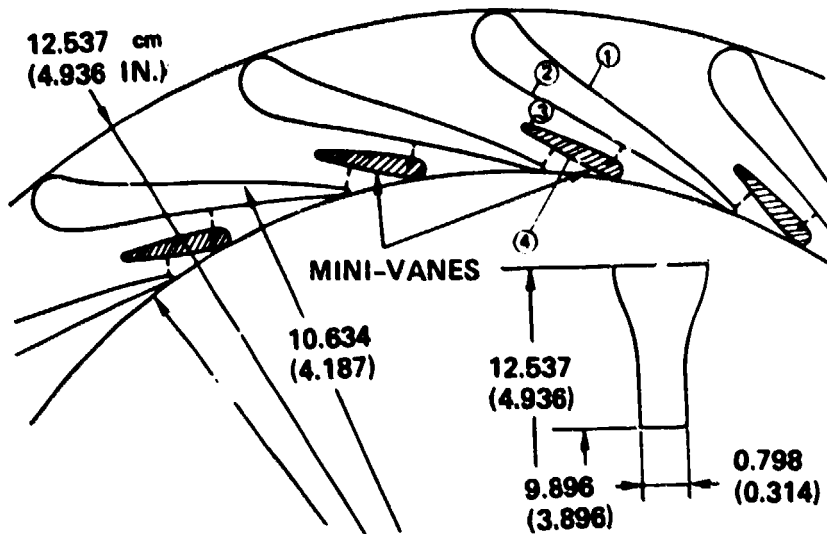


Figure 31. Insertable Minivane, Nozzle Area Variation Concept.

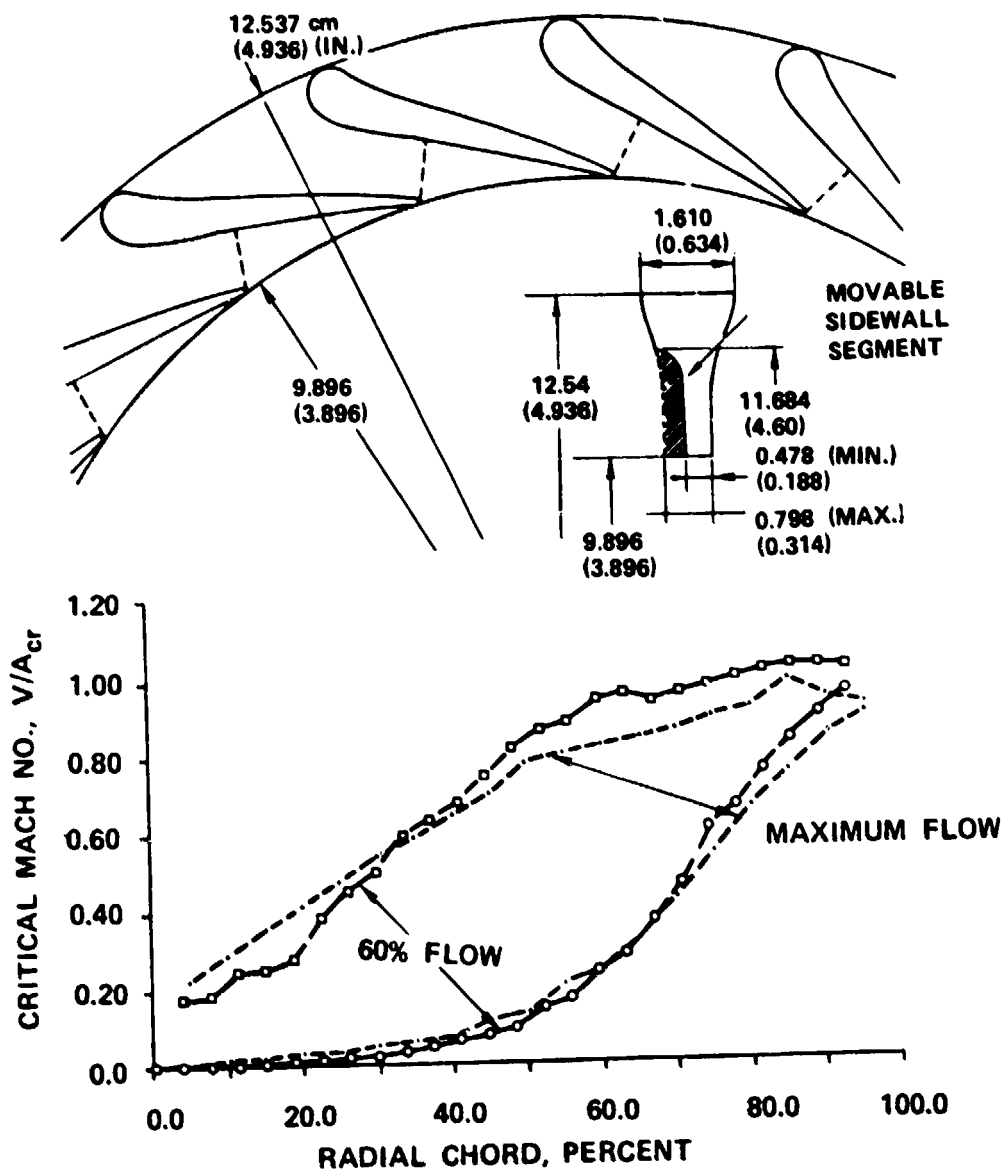


Figure 32. Locally Movable Sidewall, Nozzle Area Variation Concept.

The following material candidates were considered for the stator airfoils:

- o Equiaxed Mar-M 247
- o DS Mar-M 247
- o MA6000E
- o SC NASAIR 100

4.5.1.1 Stress Rupture

Stress-rupture capabilities of the candidate alloys (17,18) are shown in Figures 33 and 34. The temperatures for 1000- and 4000-hour rupture lives at 68.948-MPa (10-ksi) stress levels are shown in Table II. Table II also indicates that, with the possible exception of equiaxed Mar-M 247, all materials considered were viable candidates for the proposed vane application. It should also be noted that use of a thermal-barrier coating on the stationary airfoil either would result in improved durability, or would allow for higher gas temperatures.

TABLE II. STRESS-RUPTURE CAPABILITIES OF CANDIDATE TURBINE SUPERALLOYS

<u>69.948 MPa (10 ksi)</u>	<u>RUPTURE LIFE</u>	
	<u>1000-Hr</u>	<u>4000-Hr</u>
	<u>TEMPERATURE K (°F)</u>	
SC NASAIR 100	1394 (2049)	1358 (1985)
DS Mar-M 247	1324 (1923)	1290 (1862)
Equiaxed Mar-M 247	1290 (1862)	1257 (1803)
MA6000E	1478 (2200)	1478 (2200)

4.5.1.2 Coated Oxidation Resistance

The potential of oxidation resistance is a critical aspect for this application. Current coating systems have coating lives on the order of about 250 hours per 0.0254 mm (0.001 inch) of coating

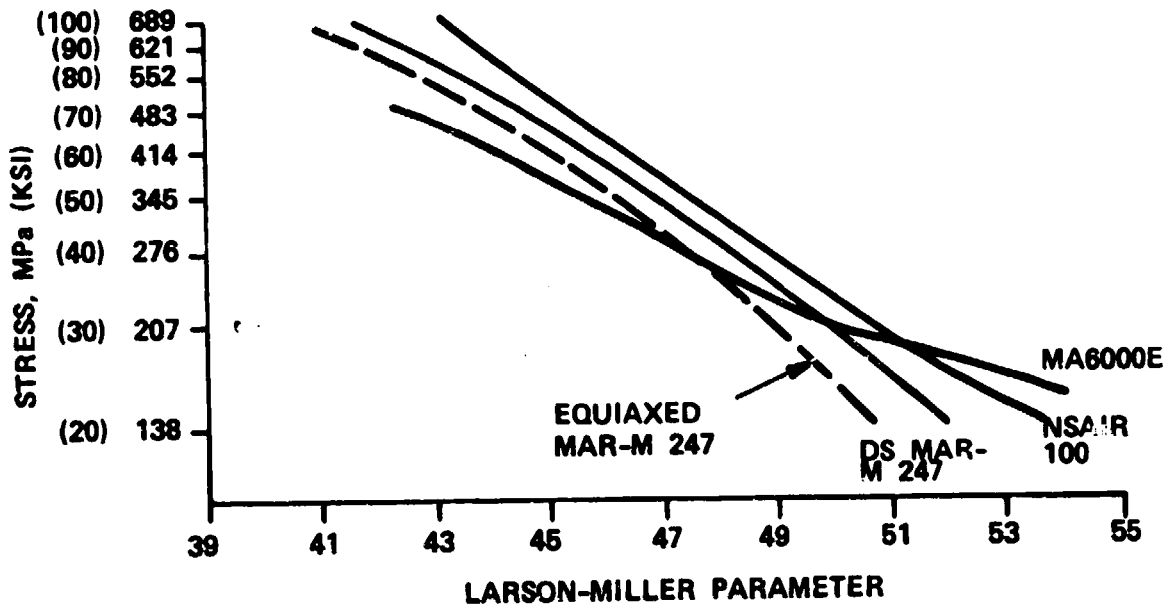


Figure 33. Larson-Miller Parameter Showing Stress Life Capabilities of Candidate Superalloys.

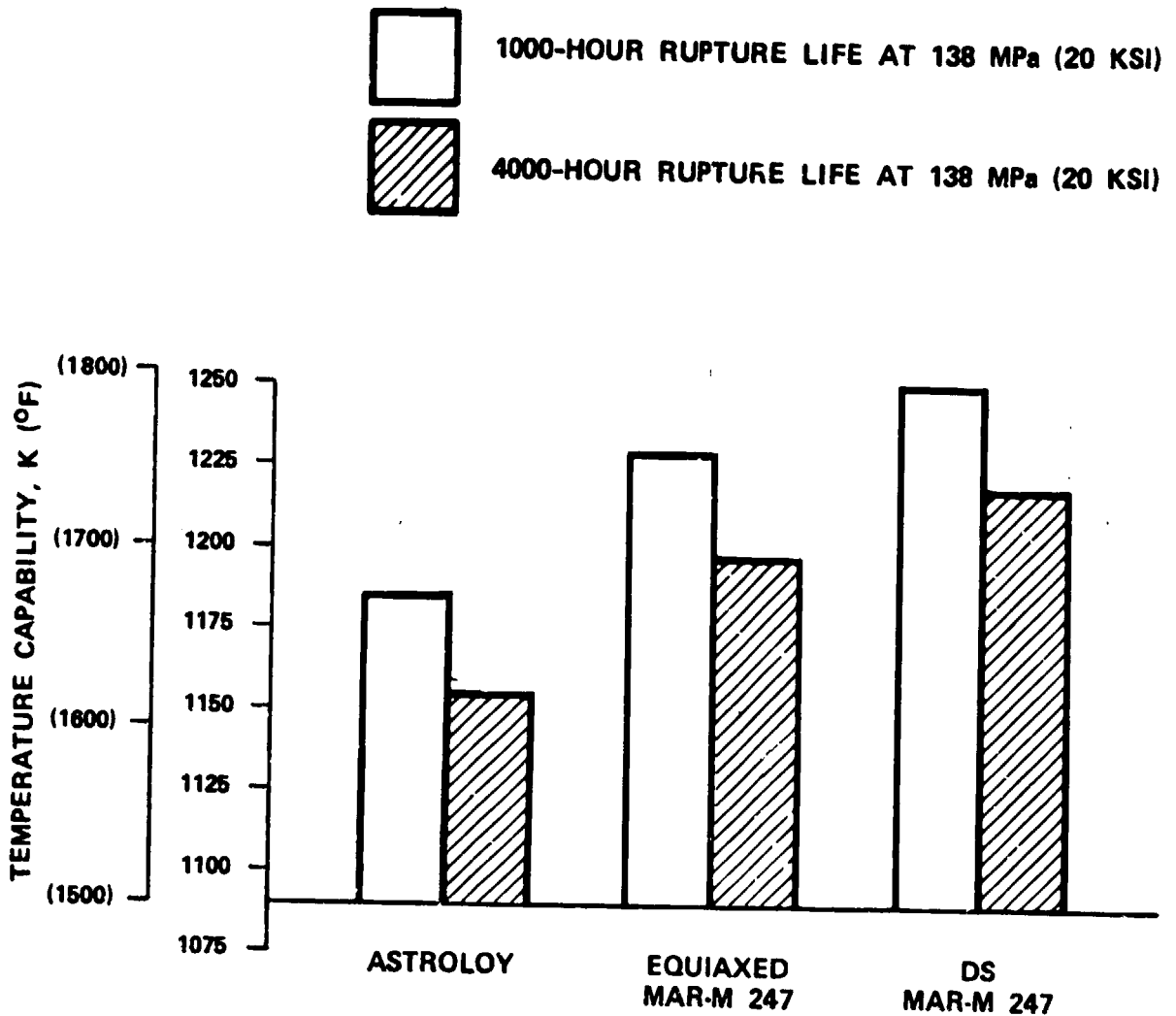


Figure 34. Stress-Rupture Capabilities of Candidate Turbine Superalloys.

thickness at 1366K (2000°F) (19), the projected vane hot-spot temperature. However, by 1987, it is expected that the lives of protective coatings will be increased by a factor of four. Consequently, the life of a 0.102-mm (0.004-in.) coating should be about 4000 hours.

4.5.1.3 Overtemperature Capability

The capability of the stator assembly to withstand brief overtemperature conditions is dependent on the incipient melting temperature of the superalloy. Table III indicates that incipient melting points of the candidate superalloys are in the range of 1505 to 1603K (2250 to 2425°F). Thus, all alloy candidates have overtemperature capabilities well above the proposed design requirements.

TABLE III. OVERTEMPERATURE CAPABILITIES OF CANDIDATE STATOR MATERIALS

Alloy	Incipient Melting Temperature, K (°F)
Mar-M 247	1505 (2250)
NASAIR 100	1603 (2425)
MA6000E	1569 (2365)

4.5.1.4 Thermal Fatigue

Studies of thermal-fatigue cracking of DS superalloys have indicated that resistance to thermal-fatigue crack initiation and propagation is increased as the elastic modulus is decreased (20,21).

Elastic moduli of the candidate alloys are listed in Table IV. This table indicates that DS Mar-M 247 and SC NASAIR 100, with the crystallographic axis oriented parallel to the vane axis, are preferable from an elastic modulus standpoint.

TABLE IV. ELASTIC MODULI (ROOM TEMPERATURE)
OF CANDIDATE SUPERALLOYS

Alloy	Modulus	
	kPa	psi
Equiaxed Mar-M 247	212.36 x 10 ⁶	(30.8 x 10 ⁶)
DS Mar-M 247 (Longitudinal)	144.79 x 10 ⁶	(21.0 x 10 ⁶)
SC NASAIR 100 (Longitudinal [001])	144.79 x 10 ⁶	(21.0 x 10 ⁶)
MA6000E (Longitudinal)	202.71 x 10 ⁶	(29.4 x 10 ⁶)
SC Mar-M 200 [001]*	124.11 x 10 ⁶	(18 x 10 ⁶)
SC Mar-M 200 [110]*	220.63 x 10 ⁶	(32 x 10 ⁶)
SC Mar-M 200 [111]*	296.47 x 10 ⁶	(43 x 10 ⁶)

*Kear and Piearcy - Pratt & Whitney Aircraft, 1967

Although MA6000E has a high modulus parallel to the extrusion/rolling direction, it should be noted that initial thermal fatigue test results were comparable to DS and SC Mar-M 200 data(22). Based on these results, DS Mar-M 247, SC NASAIR 100, and MA6000E are all considered viable candidates for vane application. Oxidation resistance of the coating is expected to be life-limiting.

4.5.2 Sidewall

Since the sidewall will have biaxial stresses, the preferred material for this application is cast equiaxed Mar-M 247. Hot-spot conditions of 1366K (2000°F) indicate that oxidation resistance may be life-limiting for this application. It should also be noted that the impingement-cooled sidewall design may be complemented with the use of a thermal-barrier coating to reduce metal temperature and increase component life.

4.6 Recommended Variable Stator Concepts

After considering all aspects of each design, the full-vane rotation and minivane concepts were eliminated. The articulated

trailing-edge design was slightly more favored than the movable-sidewall design and was ultimately selected as the primary design candidate. However, in the March 27, 1980 Task I Review at NASA it was recommended that the local movable sidewall concept be retained for further investigation. This recommendation led to an add-on contract to the detailed stator substantiation phase for examination as an alternate candidate.

The fabrication method selected for the stator concepts consists of laminated vanes inserted and brazed into separate sidewalls. Depending on future engine design analysis, the sidewalls could be either continuous rings or two vane segments. The laminated vanes could be constructed from either equiaxed Mar-M 247 material or from DS Mar-M 247 (if the laminates can be oriented perpendicular to the flow direction to increase vane strength). If high-temperature integrity beyond Mar-M 247 capabilities is necessary, oxide dispersion-strengthened alloys (such as DS nickel) are alternate candidates. The sidewalls would be cast from equiaxed Mar-M 247. If the final stator-design cooling configurations were simple, conventional vane casting could be used for the articulated trailing-edge vane pieces as an alternate to laminates. An additional option is the use of thermal-barrier coatings, particularly in the sidewalls (where allowances can be made for coating thickness).

The turbine stator detailed mechanical-design substantiation was accomplished by ensuring that acceptable temperature levels and gradients were achieved. It should be noted that life prediction requiring 3-dimensional stress analysis, LCF calculations, and creep-deformation predictions were considered beyond the scope of the existing program. Preliminary design cooling configurations were established for the articulated trailing-edge vane, the movable sidewall vane, and the sidewalls. This included predicting metal temperatures and cooling flow-rate requirements at 60- and 100-percent engine power. All work was accomplished using a rotor-inlet temperature of 1644K (2500°F), which was later reduced for the final design. The cooling configurations for the vane and band were similar to that selected for the final design, and are discussed in Section 6. The final design demonstrated the feasibility of achieving satisfactory temperature distributions in a variable-area stator. However, cooling-flow usage at 60-percent power was quite high in the final design.

4.7 Turbine Rotor Materials Evaluation

The principal requirements for the radial-turbine materials system are:

- o High tensile strength in the hub;
- o Good biaxial-creep strength and thermal-fatigue strength in the rim; and
- o High creep strength in the inducer.

To meet these requirements a dual-alloy rotor is recommended.

A cooled, laminated radial turbine developed by Garrett successfully demonstrated the use of a laminated bonding technique. This technique was selected for development of the dual-alloy rotor blade ring. The rotor blade ring will be constructed from laminated Mar-M 247 sheets with DS inducer blade tips, while an AF 115 powder metal⁽²³⁾ (or similar high-tensile-strength material) will be used for the rotor disk. Candidate materials considered for the cooled rotor concept relative to an Astroloy baseline are shown in Figure 34.

The viability of this dual-alloy radial turbine approach was demonstrated by both Garrett and another engine manufacturer⁽²⁴⁾. A solid, dual-alloy (Mar-M 247/Astroloy) radial turbine rotor with DS blade tips is also being developed at Garrett with NASA/DOE sponsorship under Contract No. DEN 3-167. Figure 35 shows the tensile properties of the dual-alloy rotor hub materials.

4.8 Cooled Rotor Concept Aero/Mechanical Evaluation

Selection of a rotor concept was based primarily on mechanical considerations, since the goal was to maximize allowable tip speed while satisfying the required duty-cycle life. In addition, the magnitude and location of rotor internal-cooling flows would be similar for either a cast or laminated cooled rotor. No unique aerodynamic advantage was identified from the rotor concepts evaluated.

With uncooled blading previous Garrett experience in radial-turbine rotor design has shown that a practical limit of about 1422K (2100°F) exists for turbine rotor inlet temperatures. This limit reflected the use of materials with near-term applicability to the design. Rotor tip speeds beyond the current state-of-the-art, and life requirements consistent with program goals (1589 to 1644K (2400° to 2500°F) total inlet temperature) require substantial cooling flows and high thermal performance internal cooling geometry. Radial turbine configurations with no provision for inserted blades require either an integrally cast or laminated design. Prior Garrett experience with integrally cast turbines with cooled blading has been discouraging, due to the cooling complexity and casting yield. However, recent improvements in

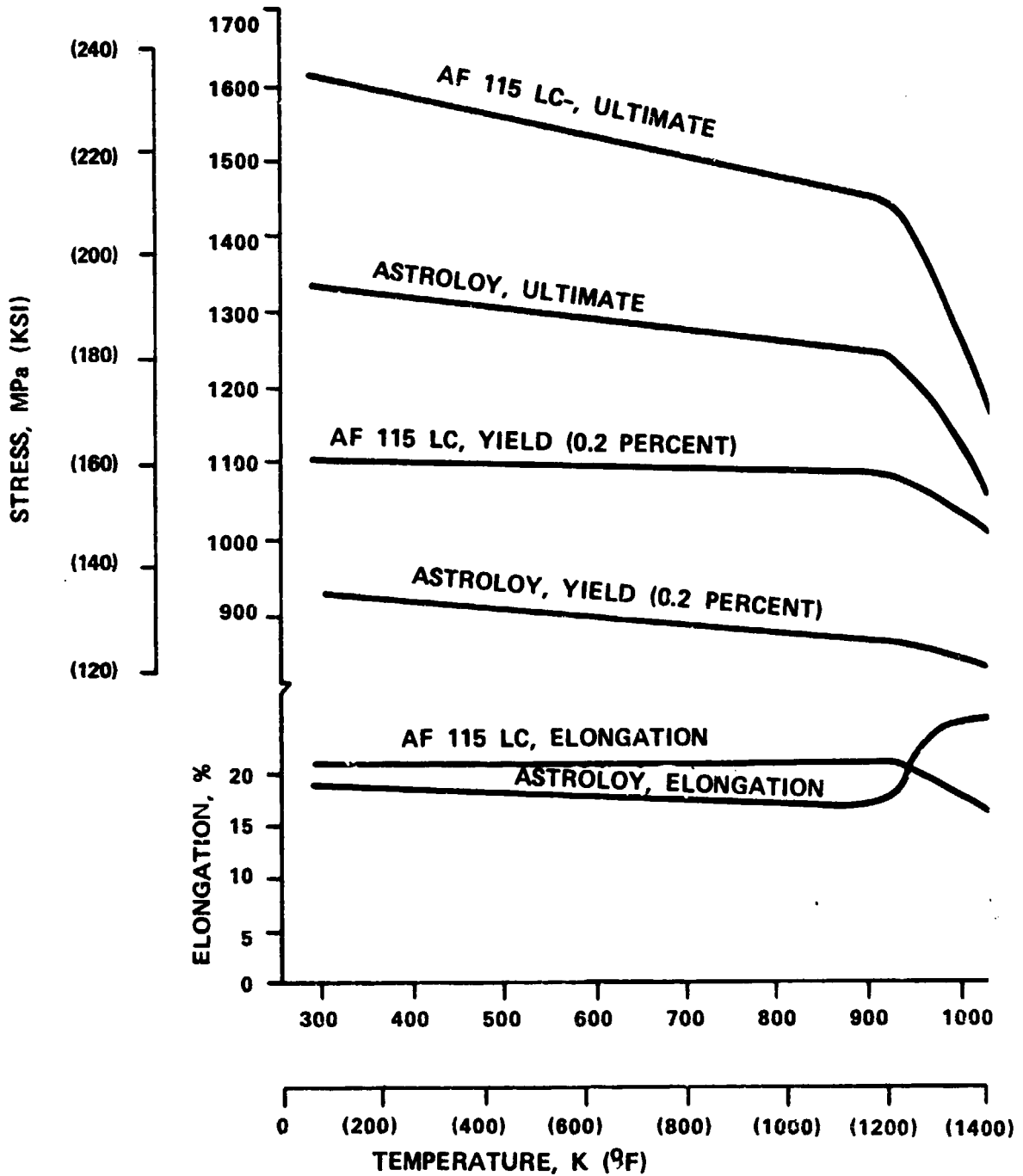


Figure 35. Tensile Properties of Hub Materials, Dual-Alloy Turbine Rotor.

casting technology have been promising in regards to the feasibility of such an approach. Laminated sheet technology has also been encouraging. Garrett, in cooperation with the U.S. Army, has designed a radial turbine that meets similar, but less ambitious goals.

With the increase in turbine inlet temperature experienced with conventionally cooled radial-turbine designs, the stress-rupture life in the inducer portion becomes a primary design restriction. The ability to reduce metal temperatures below currently attained values with added cooling flow is limited. Therefore, material property improvement is necessary. For a typical radial-turbine inducer stress, Figure 36 compares the potential metal-temperature increase (over an Astroloy baseline) for several alloys at a 4000-hour mission life. The temperature increase afforded by the selection of DS Mar-M 247 was deemed a realistic goal for the 1988 timeframe. However, both the cast or laminated approach would require a moderately aggressive manufacturing technology program of approximately equivalent effort to permit production within that timeframe.

An effort was made to compare the cooling-system complexity achieved with laminates to a cored casting. A typical laminated design with a high level of complexity is presented in Figure 37. This figure shows the USARTL turbine design previously completed at Garrett. Discussions were held with a casting vendor on the feasibility of achieving similar geometry features in a radial turbine by 1988. It is believed that time and expense, in conjunction with advanced casting technology such as the use of quartz-rod cores, could produce the radial design shown in Figure 38. The dimensions indicated are believed feasible, and would be also technically acceptable for a high-thermal-performance design. It is believed that there would be no discernible difference between the cooling effectiveness achievable with the laminated approach using current techniques and the cast blade ring yet to be developed. However, both approaches will necessitate improvements in material technology to reach the program total inlet temperature goals.

One possible method to produce laminates with the high rupture strength of a DS Mar-M 247 casting is to simply slice sheets from a bar of material with directional grains in the outermost region. This would provide tensile and fatigue properties in the disk bore region equivalent to those of an equiaxed casting. It is proposed that both these approaches (laminated and cored casting) be used to produce a rotor blade ring of material containing cooling passages. Two potential candidates for the powder-metal hub design are powdered Astroloy and AF 115. The powder metal hub

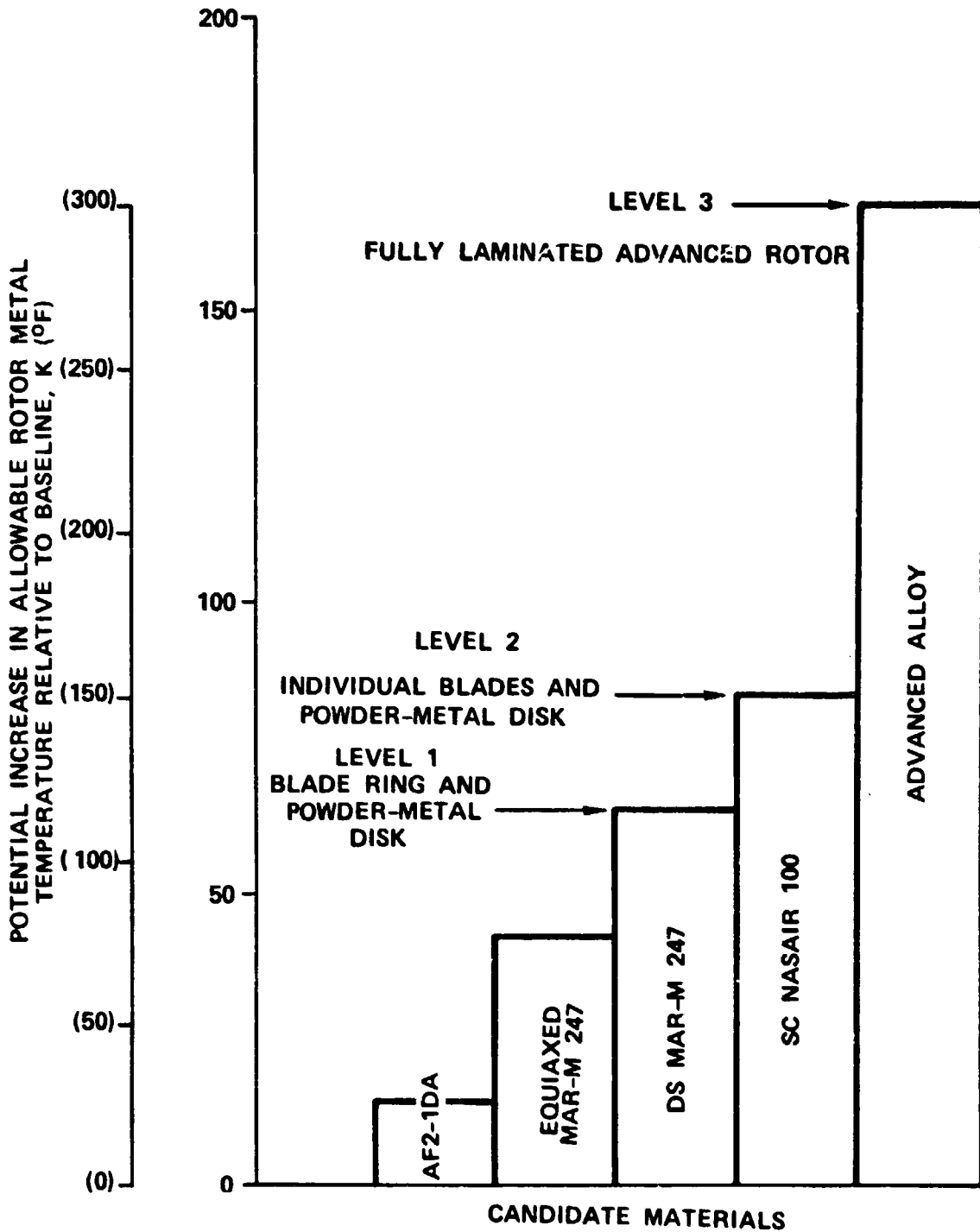


Figure 36. Comparison of 4000-Hour Mission Life and Density-Corrected Stresses at Inducer Tip at 640 m/s (2100 Ft/Sec).

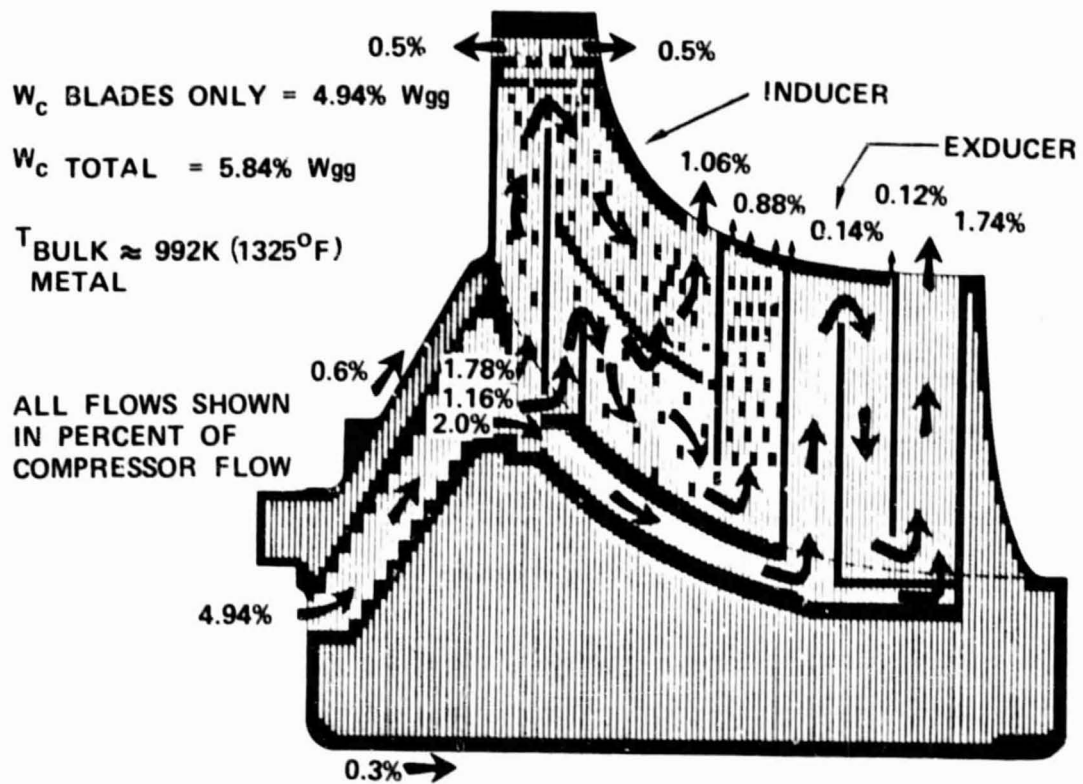
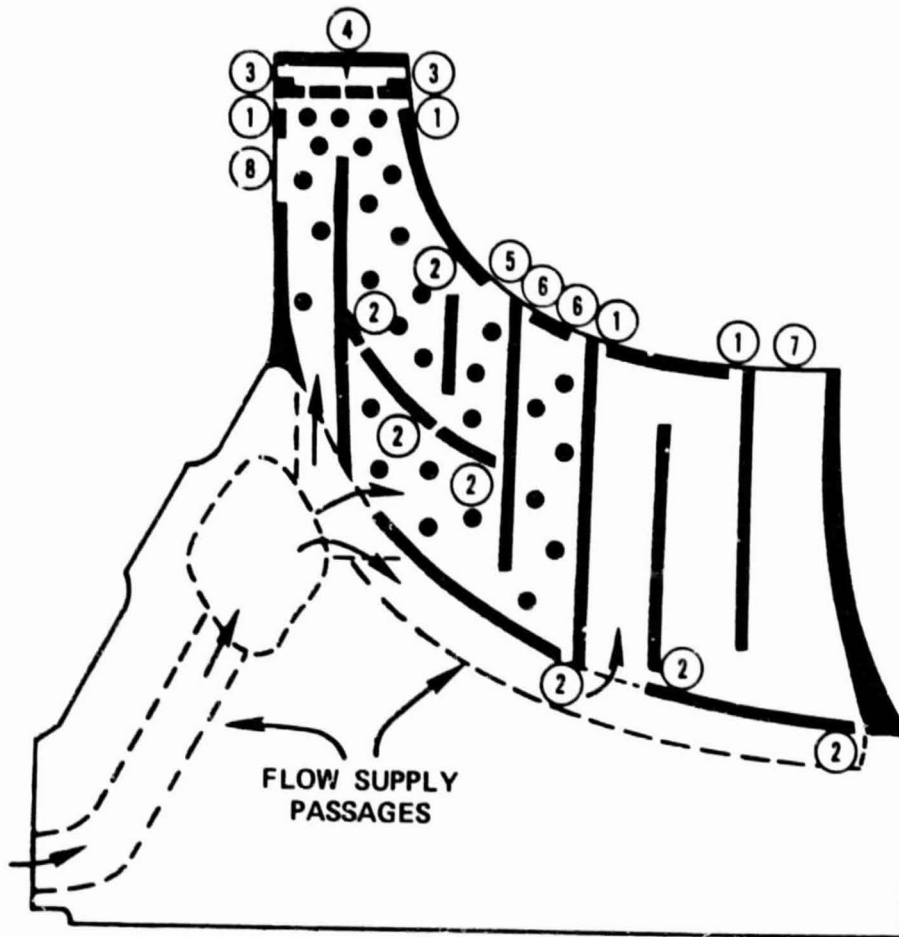


Figure 37. USARTL Cooled, Laminated Rotor Design.



NOTES:

APPROXIMATE SCALE = 2X

PASSAGE THICKNESS $\approx 0.064 - 0.076$ CM (0.025 - 0.030 IN.)

HOLE SIZES:

- 1 DUST HOLES $\approx 0.038 - 0.051$ CM (0.015 - 0.020 IN.) DIA.
- 2 DUST HOLES ≈ 0.076 (0.030 IN.) DIA.
- 3 LEADING-EDGE DISCHARGE $\approx 0.064 - 0.076$ CM (0.025 - 0.030 IN.) DIA.
- 4 IMPINGEMENTS HOLES $\approx 0.038 - 0.051$ CM (0.015 - 0.020 IN.) DIA.
- 5 INDUCER DISCHARGE SLOT $\approx 0.076 \times 0.254$ CM (0.030 x 0.100 IN.)
- 6 TIP DISCHARGE $\approx 0.076 \times 0.406$ CM (0.030 x 0.160 IN.) SLOT
- 7 TIP DISCHARGE $\approx 0.076 \times 0.102$ CM (0.030 x 0.040 IN.) SLOTS
- 8 CORE SUPPORT SLOT = VARIABLE WIDTH

PIN FINS:

≈ 0.063 CM (0.025 IN.) DIA; MINIMUM SPACING ≈ 0.152 CM (0.060 IN.)

Figure 38. Preliminary Cooled Radial Rotor Design.

would then be bonded to the blade ring using a hot-isostatic-pressing (HIP) process. A powder-metal hub with uniformly fine-grain structure would produce higher burst-margin capabilities and fatigue strength in high-stress regions.

4.9 Recommended Cooled Rotor Concept

The recommended cooled rotor concept is a dual-alloy laminated rotor. The rotor blade ring will be constructed from laminated Mar-M 247 sheets with DS inducer blade tips. An AF 115 powder metal (or other similar high-tensile-strength material) would be utilized for the rotor disk. Comparison between laminated and advanced cast DS Mar-M 247 blade rings showed approximately equal cooling-flow capabilities, development cost, and risk. Therefore, a clear choice between these two methods is not possible at this time. The laminated method was selected on the basis of cost effectiveness for the follow-on rotor test program.

The potential rotor-inlet temperature achievable using DS Mar-M 247 DS blades was evaluated using the internal cooling-flow geometry from the existing USARTL laminated rotor and the mission life defined for the cooled variable-area radial turbine. Table V shows that mission life decreases rapidly between 1533 to 1644K (2300 to 2500°F) rotor-inlet temperatures. On the basis of possible improvements to the USARTL inducer cooling-flow scheme (e.g., film cooling in the critical region), a maximum rotor-inlet temperature of 1589K (2400°F) is recommended to achieve the 4000-hour mission life goal. The recommended cooled rotor concept is presented in Figure 39.

TABLE V. EVALUATION OF COOLED ROTOR LIFE AS A FUNCTION OF ROTOR-INLET TEMPERATURE, DUTY CYCLE, AND TIP SPEED.

Configuration	Material	T_4 K (°F)	U_{t4} m/s ft/ sec	100-Percent- Power Life (hrs)	Mission Life (hrs)	Ratio of Mission Life/ Baseline Life
Baseline: USARTL Cooled Laminated Radial Turbine	Astroloy	1533 (2300)	573 (1880)	1691	8455	1.0
USARTL	DS Mar-M 247	1533 (2300)	573 (1880)	29,240	146,000	17.0
Variable-Area Radial Turbine		1533 (2300)	573 (1880)	4470	16,300	2.0
Variable-Area Radial Turbine		1533 (2300)	640 (2100)	1360	4910	0.6
Variable-Area Radial Turbine		1589* (2400)	640 (2100)	315	1130	0.13
Variable-Area Radial Turbine		1644 (2500)	640 (2100)	80	290	0.03

o For constant life, $T_{\text{metal DS Mar-M 247}} = T_{\text{metal Astroloy}} + 63.8\text{K (115°F)}$

o For 16:1 Cooled, Variable-Area Radial Turbine, life at 100-percent power = 0.28 x mission life

* Recommended maximum rotor-inlet temperature for cooled rotor

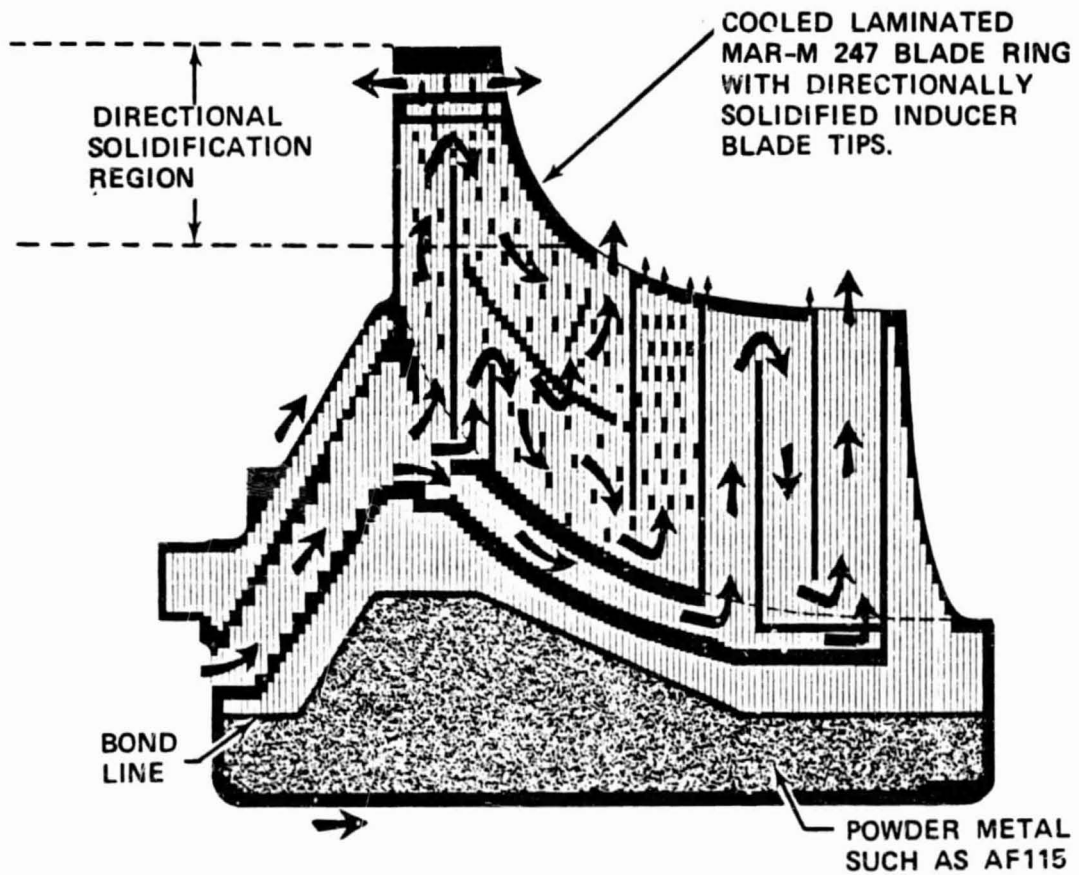


Figure 39. Recommended Cooled Rotor Concept.

5.0 TASK II - DETAILED PARAMETRIC STUDY

5.1 Selected Speed and Cycle Conditions

The objective of the detailed parametric study was the selection of the turbine stage configuration for the detailed design. The study consisted of examination of the effects of stage cooling flows, stator leakage, and rotor/exducer blockage on stage efficiency from 60- to 100-percent power for both cooled and uncooled turbine configurations.

The results of the Garrett Small Axial/Centrifugal Compressor Design Study (conducted for the NASA-Lewis Research Center under Contract No. NAS3-21621) were used to evaluate turbine/compressor rotational speed compatibility. For a 2.27 kg/s (5 lb/sec), 2-stage centrifugal compressor, the selected pressure ratio in the compressor study was 17:1 with a rotational speed of 5601 rad/s (53,486 rpm). The rotational speed selected for the turbine preliminary parametric study was 6964 rad/s (66,500 rpm) with a pressure ratio of 17:1. This speed was selected on the basis of a minimum specific speed of 0.468 (60.0) to maintain peak attainable efficiency. However, examination of the 17:1, two-stage, centrifugal-compressor efficiency characteristics showed a rapid decrease in performance as speed increased. It was determined that turbine specific speeds below 0.468 (60.0) were required to achieve optimum turbine/compressor rotational speed. The compressor and turbine efficiency characteristics as a function of rotational speed are presented in Figure 40. As shown in Figure 41, the efficiency product is relatively flat between 5550 rad/s (53,000 rpm) and 5969 rad/s (57,000 rpm), as shown in Figure 41. Therefore, a design rotational speed of 5969 rad/s (57,000 rpm) was selected for the detailed parametric study. This result, in conjunction with the preliminary parametric study and the stator and rotor concepts evaluation, resulted in the following cycle and turbine conditions for the detailed parametric study:

- o Cycle pressure ratio: 17:1;
- o Rotational speed: 5969 rad/s (57,000 rpm). (Although peak compressor/turbine efficiency occurred at 5760 rad/s (55,000 rpm), increasing the rotational speed to 5969 rad/s (57,000 rpm) had relatively little effect on efficiency;
- o Rotor inducer tip speed: 640 m/s (2100 ft/sec);
- o Maximum rotor-inlet temperature;
 - Cooled rotor = 1589K (2400°F);
 - Uncooled rotor = 1478K (2200°F);

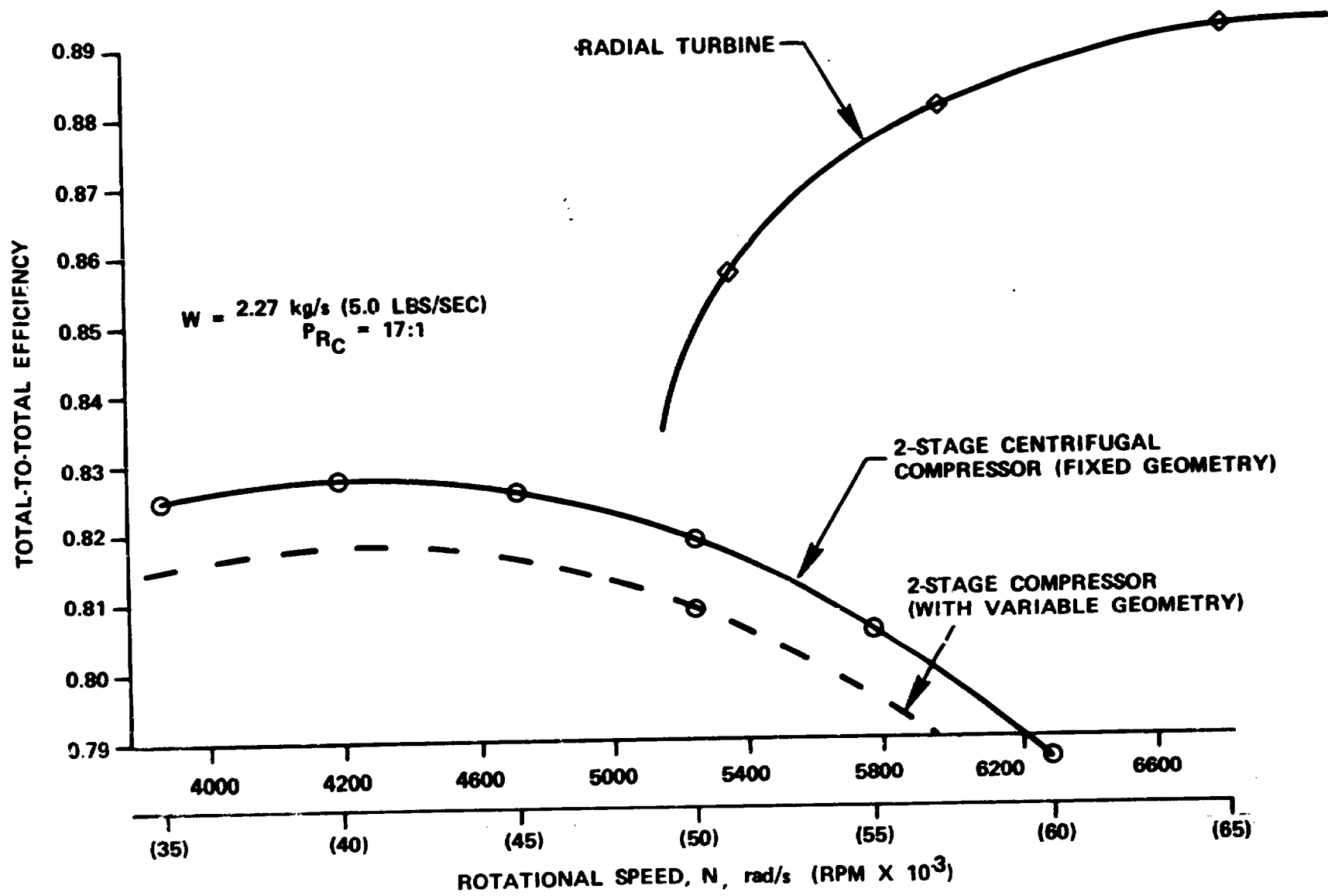


Figure 40. Cooled, Variable-Area Radial Turbine Compressor Speed Study.

$W = 2.27 \text{ kg/s (5.0 LR/SEC)}$

$P_{RC} = 17:1$

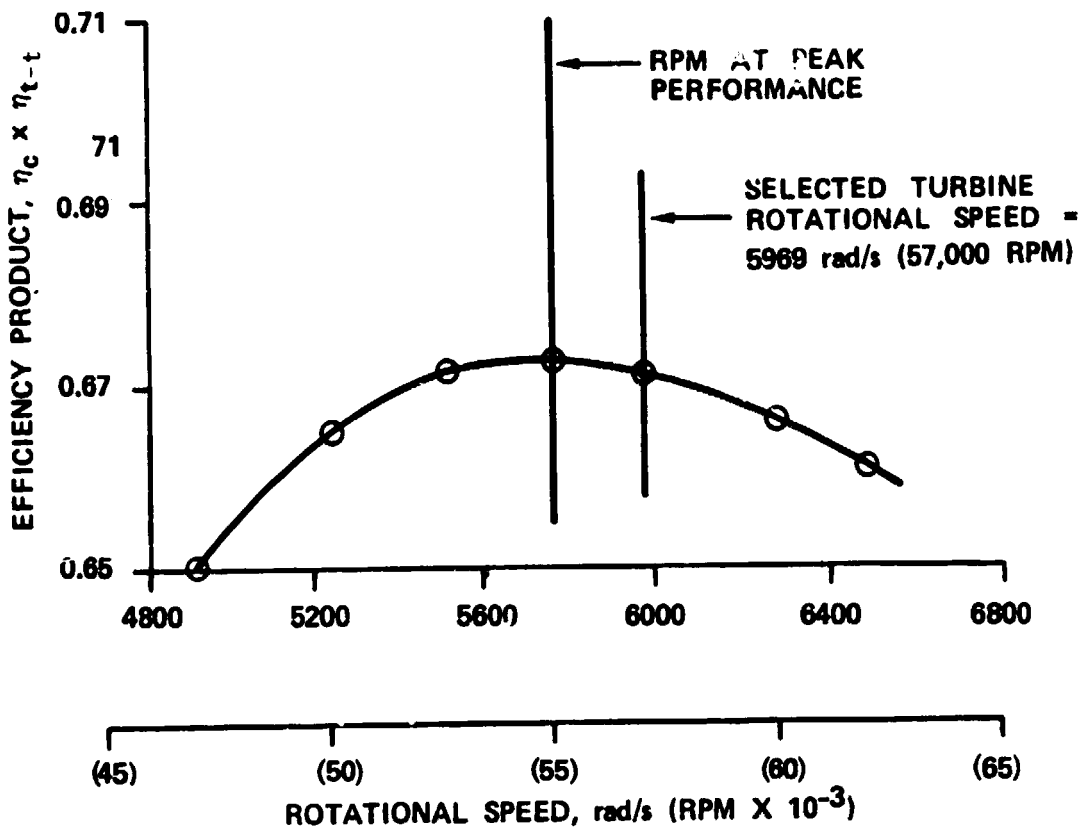


Figure 41. Compressor Turbine Efficiency Product Characteristics.

- o Variable-area stator: Articulated trailing-edge and locally movable sidewall configurations;
- o Cooled rotor: Laminated dual-alloy configuration;
- o Uncooled rotor: Dual-alloy configuration.

5.2 Effects of Stage Cooling Flows

A detailed schematic of the stage cooling flow circuits for the cooled variable-area radial turbine is presented in Figure 42. Since the effects of internal rotor-cooling flow on stage performance were not available, the cooling-flow model relied heavily on the results available from existing axial turbine concepts and from correlation with the tested effects of external radial rotor-cooling flow results. The situation with the stator was similar, except test results for trailing-edge discharge flow were available from the Model GT601 radial gas generator turbine.

At Garrett, the accounting procedure for cooling flows is to assume all stator primary and cooling flows are available to do work in the rotor, and the available rotor-inlet temperature is based on a primary and cooling-flow mixed value. Therefore, the 1589K (2400°F) inlet temperature established for the cooled, variable-area radial turbine is defined as a rotor inlet absolute mixed temperature ($T_{4,Mix}$). Conversely, rotor-cooling flow is assumed to do no work in the turbine and thus bypasses that stage. However, the rotor-cooling flow is available to do work in downstream stages. Thus, the cooled turbine efficiency defined in this manner is a hybrid between truly primary and thermodynamic efficiency. That is, the available energy of the stator cooling flow is accounted for in the isentropic expansion, but the rotor-cooling flow work is added or subtracted from the actual work of the rotor-inlet flow. On this basis, the expression for the cooled turbine efficiency becomes:

$$\eta_{T-T \text{ Cooled}} = \frac{W_{4,Mix} \Delta H_{4,Mix} + \sum W_i \Delta H_i}{(W_{4,Mix} \Delta H_{4,Mix})_{isen}} \quad (1)$$

where:

$$W_{4,Mix} = W_p + W_{V,EW} + W_{VI}$$

$$\Delta H_{4,Mix} = \frac{W_p \Delta H_p + W_{V,EW} \Delta H_{V,EW} + W_{VI} \Delta H_{VI}}{W_{4,Mix}}$$

$$W_{VI} = W_{V,PS} + W_{V,SS} + W_{V,TE}$$

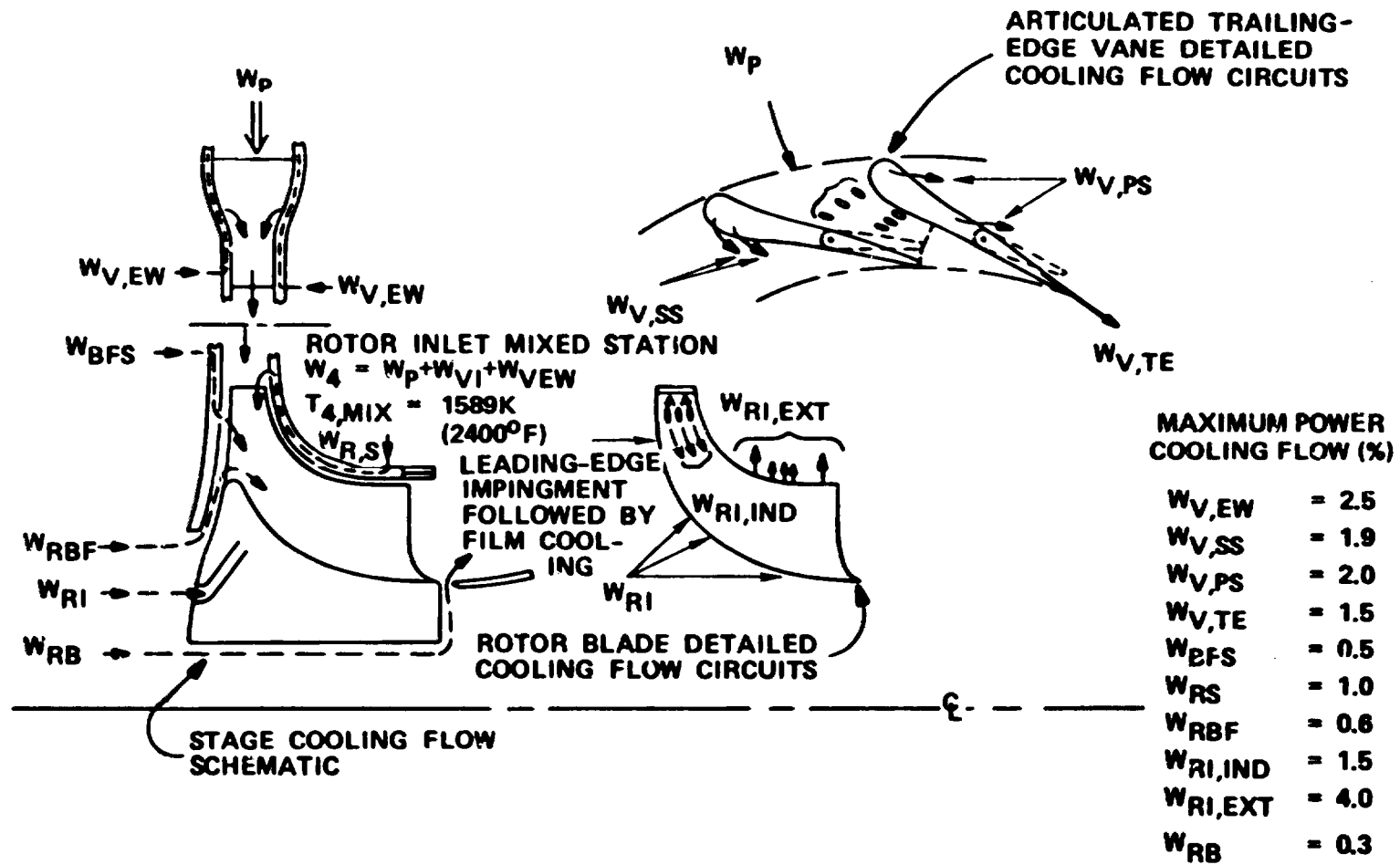


Figure 42. Turbine Cooling Flow Model for the Detailed Parametric Study.

$$\Sigma W_i \Delta H_i = W_{BFS} \Delta H_{BFS} + W_{RS} \Delta H_{RS} + W_{RBF} \Delta H_{RBF} \\ + W_{RB} \Delta H_{RB} + W_{RI} \Delta H_{RI}$$

A cooling-flow model was then established based on the following component evaluation:

- $W_{V,EW}$ - Vane sidewall impingement and film-cooling flow was estimated at 2.5 percent for 100-percent power, and 4.1 percent for 60-percent power. Although in-house test results from radial nozzle inlet veil cooling indicated no penalty, the location of the sidewall film-cooling discharge holes indicated the effect would be similar to vane leading-edge film-cooling flow. NASA test results indicated that film-cooling in the vane leading-edge region can be as high as 80-percent effective relative to the ideal kinetic energy at the vane exit. Therefore, vane sidewall-cooling flow was considered 80-percent effective.
- $W_{V,SS}$, $W_{V,PS}$ - Vane suction-side and pressure-side surface discharge cooling flows were considered to be 80-percent effective. (This was based on the discussion in the preceding paragraph.) The total cooling flow was estimated at 3.9 percent at 100-percent power, and 5.1 percent at 60-percent power.
- $W_{V,TE}$ - Vane trailing-edge cooling flow was considered 100-percent effective (based on in-house test results).
- W_{BFS} , W_{RS} - Rotor backface seal and shroud cooling flows enter the mainstream flow in the region of the rotor inducer, and are, on the average, 55-percent effective. The estimated cooling flow is 0.60 percent for the rotor backface seal, and 1.0 percent for the rotor shroud. Since a preliminary heat-transfer analysis was not performed for these regions, the estimated rates were assumed valid for all power settings.
- W_{RBF} - Rotor backface cooling flow prevents hot gas from recirculating on the back side of the rotor disk and enters the mainstream flow in the scallop saddle region. The detailed analysis of the Army laminated rotor showed that 0.6-percent cooling flow was required for this region. Test results conducted on the Model GTP305-2 radial rotor(7) indicated that, without preswirl, the pumping work required to achieve the scallop-saddle rotor speed was offset by the cooling flow expanding through the remaining portion of the rotor flow path. Since the cycle had bypassed this cooling flow and the

pumping penalty was offset, no additional penalties were incurred.

- o **WRI,IND** - Without preswirl, the rotor cooling flow in the inducer region is pumped to inducer tip speed. Except for location, this is also true for both the rotor backface flow (which must be pumped to scallop wheel speed) and rotor shroud and backface seal cooling flow (which enters the rotor in the inducer region). However, in terms of mainstream flow disturbance, the rotor inducer cooling flow was considered similar to the cooling flow entering the scallop region. Therefore, the rotor inducer cooling-flow pumping penalty was considered offset by expansion of the cooling flow through the rotor after discharging in the inducer region. Furthermore, since the cycle already bypassed this flow, no additional penalty was incurred.
- o **WRI,EXT** - Rotor internal cooling discharged into the exducer tip region - Based on axial turbine test results with tip discharge, the pumping penalty was again offset by a reduction in exducer clearance penalty.
- o **WRB** - Rotor bore cooling flow - Analysis of the Army cooled laminated rotor showed that a 0.30-percent cooling flow was required in this region. In addition to bypassing the rotor, a pumping penalty based on the rotor exit hub radius was applied to this cooling flow.

From the preceding considerations, the 100-percent power cooled turbine efficiency is expressed as:

$$\eta_{T-T \text{ Cooled}} = 0.9884 \frac{\Delta H_{4, \text{Mix}}}{\Delta H_{4, \text{Mix}} \text{ isen}} + \frac{W_{RS} \Delta H_{RS} + W_{BFS} \Delta H_{BFS}}{W_{4, \text{Mix}} \Delta H_{4, \text{Mix}} \text{ isen}} - \frac{W_{RB} U_{H5}^2}{W_{4, \text{Mix}} \Delta H_{4, \text{Mix}} \text{ isen}} \quad (2)$$

Using Garrett test data and the difference between the rotor-cooling flow assumed by the cycle and the estimated rotor-cooling flow, the penalty for rotor-shroud and backface-seal cooling flow was estimated at 0.6-percent efficiency. The final expression for the cooled turbine efficiency is:

$$\eta_{T-T \text{ Cooled}} = (0.9884) \left(\eta_{\text{Parametric Study}} \right) - 0.006$$

In general, the total penalty for all cooling flows was on the order of 2.0-points efficiency at 100-percent power. Cooling flows were then assumed to vary linearly to 50-percent power, and the cooled efficiency was varied accordingly.

5.3 Effects of Stator Leakage

Two stator sidewall leakage models were derived for the articulated trailing-edge configuration. Both models were based on the current Garrett model for axial nozzle leakage with full vane rotation. This was modified to account for leakage in the trailing-edge region alone. The axial turbine model related the performance decrement by a ratio of clearance area to nozzle throat area in the following manner:

$$\frac{\eta_L}{\eta} = 1 - \frac{A_{\text{Leakage}}}{A_{\text{Throat}}} \cdot K$$

The constant, K, was evaluated from test results. Applying the model to the full-vane rotation concept resulted in the characteristics shown in Figure 43, and illustrates why this concept was eliminated from consideration. For the articulated trailing-edge concept, no leakage occurred until the pivot point was reached (slightly downstream of the nozzle suction-surface throat point). The leakage area was no longer based on the annular leakage area at the vane trailing-edge, but was reduced by $\cos \alpha_{\text{pivot}}$. If all the tangential momentum generated up to the nozzle pivot point is assumed lost, the expression for the leakage model becomes (Model No. 1):

$$\eta_L/\eta = 1 - \frac{2\pi R_3 \cos \alpha_{\text{pivot}} \cdot 2C}{2\pi R_3 \cos \alpha_3 \cdot b_3}$$

$$\eta_L/\eta = 1 - \frac{\cos \alpha_{\text{pivot}} \cdot 2C}{\cos \alpha_3 \cdot b_3} \quad (5)$$

where:

α_{pivot} = Average stator angle at articulated pivot point

α_3 = Stator-exit angle

NOTE: α_{pivot} and α_3 are shown in Figure 78, Section 6.3.

Assuming α_{pivot} is equal to 1.13 radians (65 degrees) and α_3 is equal to 1.22 radians (70-degrees) leakage, Model No. 1 characteristics are as shown in Figure 43. These results show significant performance decrements--even with only 0.09-radian

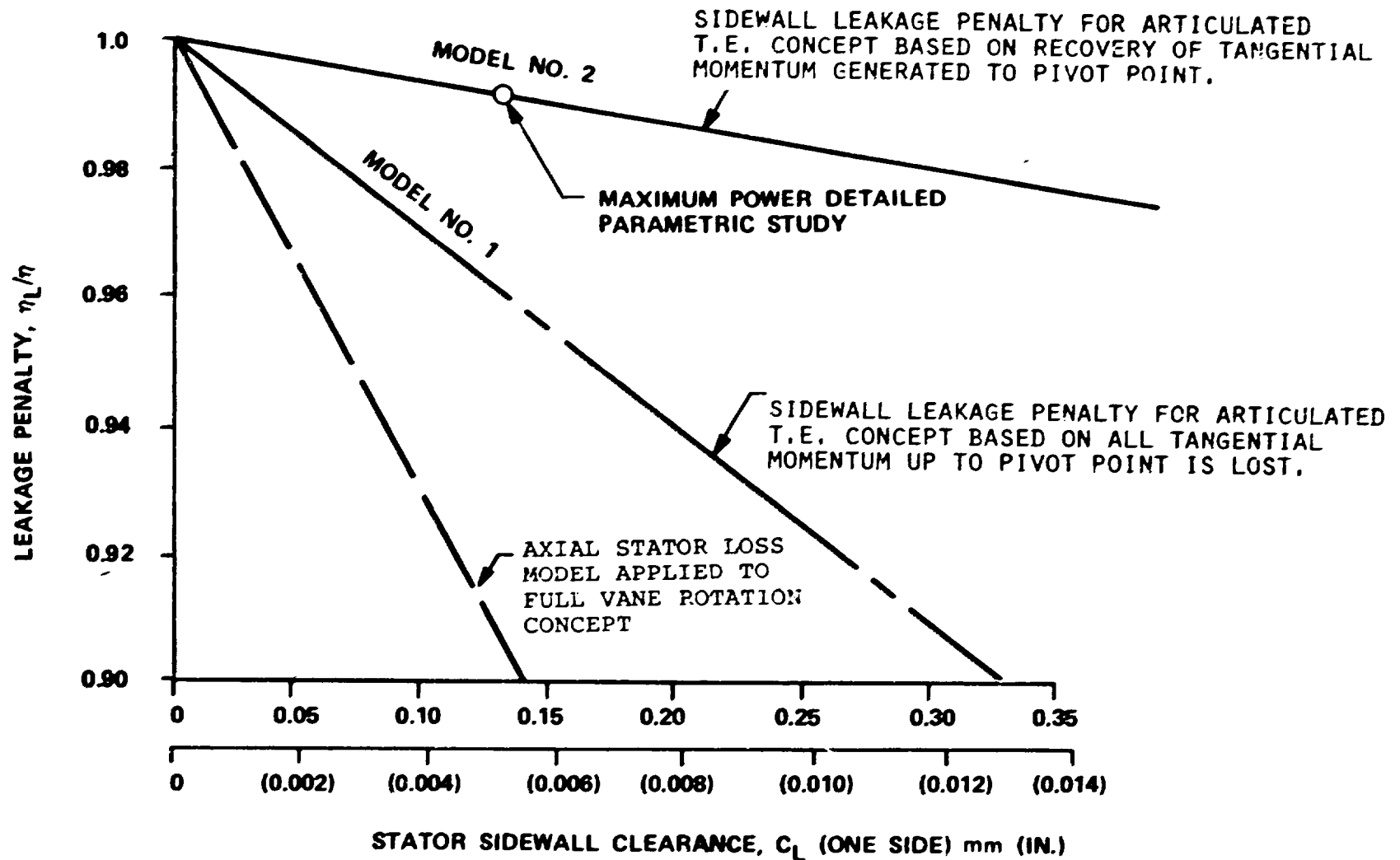


Figure 43. Articulated Trailing-Edge Nozzle, Sidewall Clearance Loss Models.

(5-degrees) downstream turning. If the tangential momentum is recovered, the performance decrement can then be approximated with the following expression (Model No. 2):

$$\eta_L/\eta \approx 1 - \frac{\cos \alpha_{\text{pivot}} \cdot 2C}{\cos \alpha_3 \cdot b_3} + \frac{\sin \alpha_{\text{pivot}} \cdot 2C}{\sin \alpha_3 \cdot b_3} \quad (6)$$

Stator sidewall leakage effects are presented in Figure 43, and are based on the pivot and exit angles assumed for Model No. 1. If a 0.013-cm (0.005-in.) sidewall clearance is selected for the maximum power point, the effect of stator leakage at part-power is as illustrated in Figure 44. With the sidewall clearance held constant, the reduction in performance at lower power levels is due to the increase in α_3 with a fixed α_{pivot} .

This effect can be minimized with a stator designed for 80-percent power. The articulated trailing-edge would then be required to actuate in both an open and closed mode, but the total excursion in each direction would be reduced by 50 percent. This approach was examined in the detailed design phase.

5.4 Cooled Rotor Aerodynamic Analysis

The performance model used for the detailed parametric study was updated to calculate the radial variation of flow properties inside the trailing-edge plane for a given minimum blade tip thickness, maximum allowable blade stress, and specified rotor exit mean work coefficient. This was achieved by solving the non-isentropic radial equilibrium equation for the specified rotor exit hub and shroud radii. The primary results of the solution included the rotor exit blockage, relative total pressure loss due to the blockage, and radial relative velocity distribution.

The maximum power results for the cooled 1589K (2400°F) rotor configuration are presented in Figures 45 through 47 for rotor inlet-blade angles of 0, 0.17, and 0.35 radian (0, 10, and 20 degrees), and a radius ratio of 0.65. The following parameters were held constant during the analysis:

- o Stator exit angle: $\alpha_3 = 1.31$ radians (75.0 degrees) specified at the rotor-inlet station - A higher stator exit angle (compared to the preliminary study) was required to achieve reasonable rotor inlet blade heights with the lower shaft speed of 5969 rad/s (57,000 rpm). However, the stator vane loading and trailing-edge blockage were maintained at constant values by adjusting the vane number and radii chord;
- o Rotor blade number: 14;

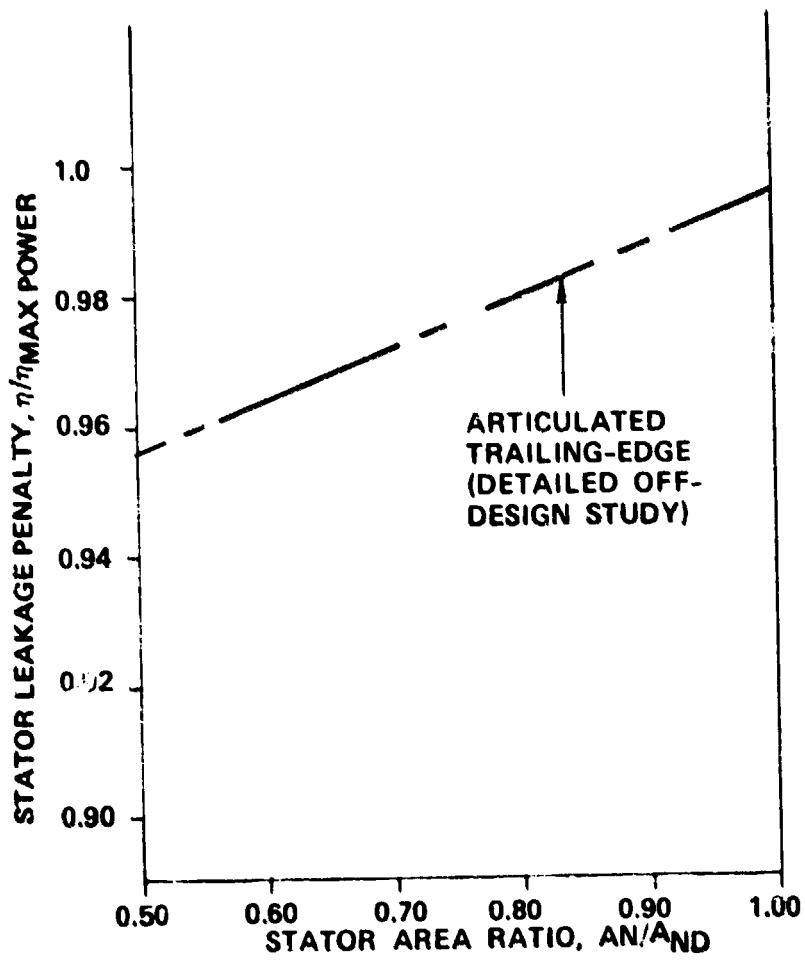
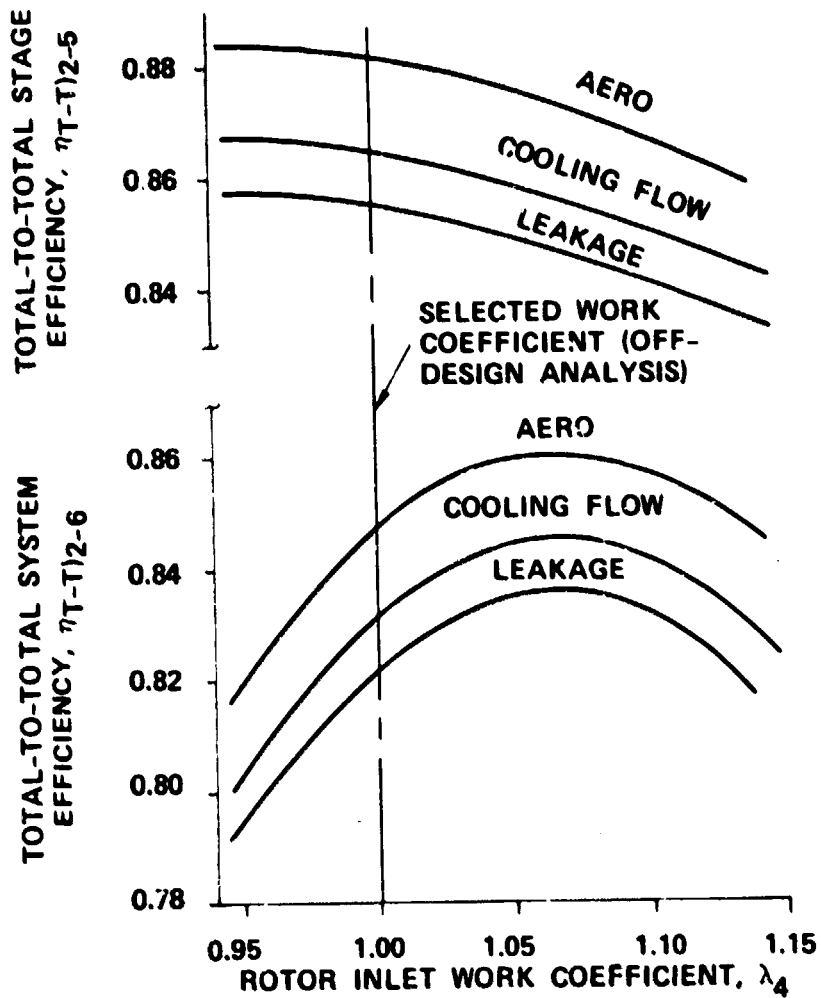
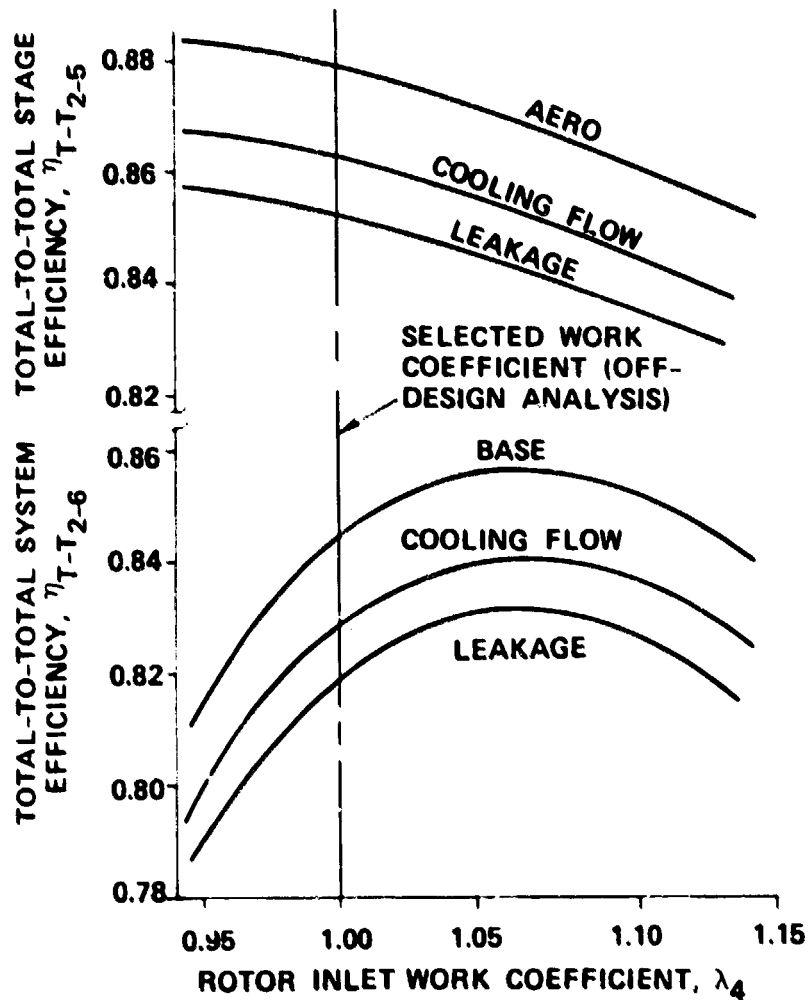


Figure 44. Effect of Stator Leakage on Off-Design Performance.



- $T_4 = 1589\text{K (2400}^\circ\text{F)}$
- $N = 5969 \text{ rad/s (57,000 RPM)}$
- $U_{T_4} = 640 \text{ m/s (2100 FT/SEC)}$
- $N_B = 14$
- $R/R = 0.65$
- $A_5 = 77.4 \text{ cm}^2 (12.0 \text{ IN.}^2)$

Figure 45. Detailed Parametric Study, $\beta_B = 0$ Radian (0°), Maximum Power Condition.



- $T_4 = 1589\text{K} (2400^\circ\text{F})$
- $N = 5969 \text{ rad/s} (57,000 \text{ RPM})$
- $U_{T_4} = 640 \text{ m/s} (2100 \text{ FT/SEC})$
- $N_B = 14$
- $R/R = 0.65$
- $A_3 = 77.4 \text{ cm}^2 (12.0 \text{ IN}^2)$

Figure 46. Detailed Parametric Study, $\beta_B = 0.17$ radian (10°), Maximum Power Condition.

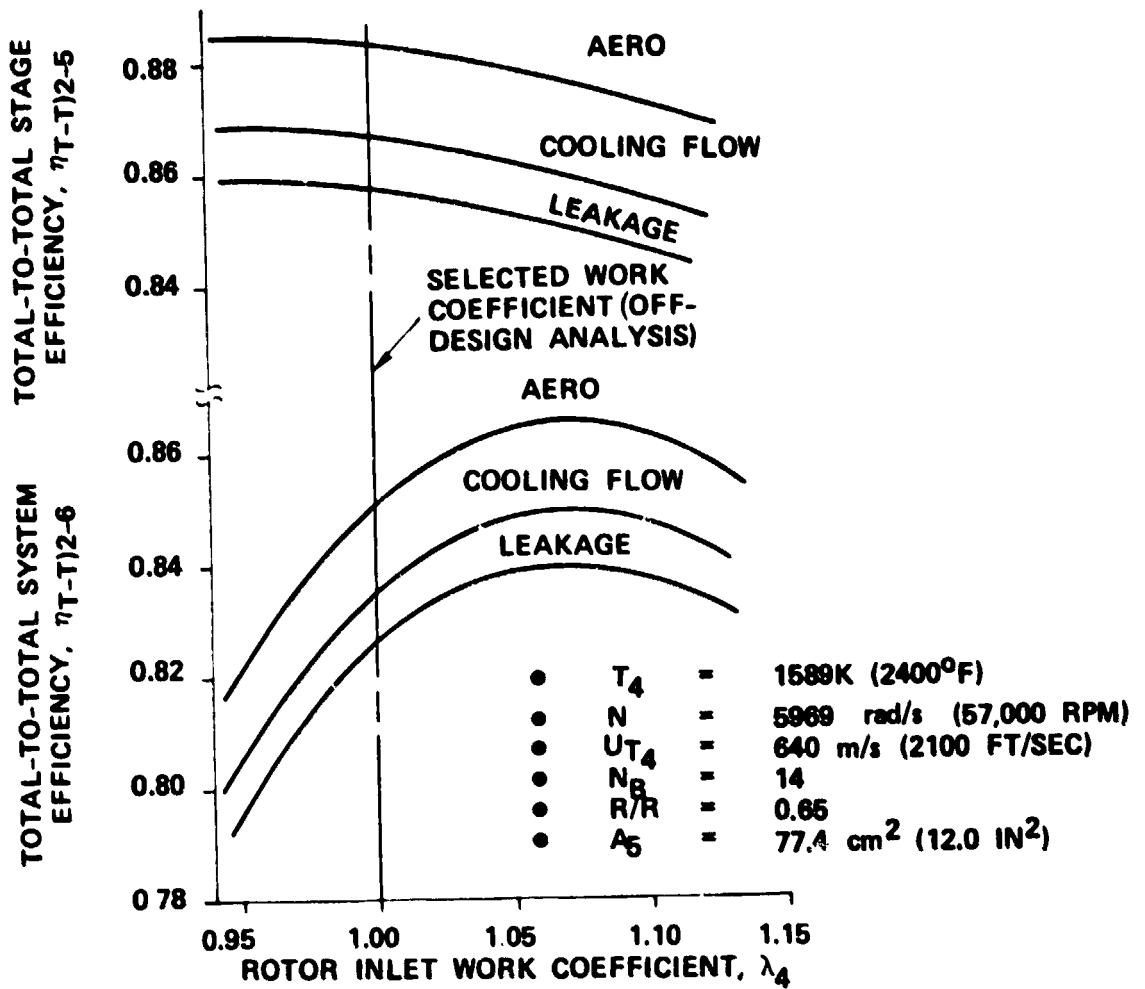


Figure 47. Detailed Parametric Study,
 $\beta_B = 0.35$ radian (20°)
 Maximum Power Condition.

- o Rotor-exit area: 77.4 cm^2 (12.0 in^2) - For lower radius ratios, this value resulted in higher performance levels when compared to larger rotor-exit areas;
- o Rotor exducer tip-to-inducer tip radius ratio: 0.65 - The effect of this radius ratio was examined in details during the off-design study.

The results shown in Figures 45 through 47 were similar to the preliminary parametric analysis results, except that the effects of stage-cooling flows and stator leakage significantly deteriorated stage and system performance. At the maximum power point, increasing the rotor-inlet blade angle from 0 to 0.35 radian (0 to 20 degrees) increased overall efficiency by approximately 0.9 point. Thus, 3-dimensional rotor blading alone could not recover the performance decrements incurred with cooling and leakage. However, 3-dimensional rotor blading, in conjunction with a judicious radius-ratio selection, resulted in optimum overall duty-cycle performance.

As shown previously, selecting the rotor-inlet work coefficient at peak system performance over-penalized the performance at lower power settings. Therefore, the selected design-point inlet work coefficients were based on a design point corresponding to approximately -0.52 radian (-30.0 degrees) exit swirl angle. Under these conditions, the rotor inlet work coefficient was 1.0 for radius ratios of 0.65 and 0.70 compared to 1.04 for a radius ratio of 0.60. The rotor flow-path geometry for the three rotor radius ratios are presented in Figure 48.

The results of the off-design study are presented in Figures 49 through 53 for 50- to 100-percent power based on the following effects:

- o System efficiency;
- o Rotor inlet relative temperature;
- o Interstage duct total pressure loss;
- o Stage reaction;
- o Rotor exit absolute swirl angle;
- o Rotor exit absolute critical velocity ratio;
- o Rotor reaction effects;
- o Reynolds number effects;
- o Cooling flow effects;
- o Leakage flow effects.

In general, the results show that below 60-percent power, performance deteriorates rapidly. Therefore, limiting the variable geometry to 60-percent flow is recommended. These figures also show that overall performance between 60- and 100-percent power is maximized by increasing the duct loss at high power (where the incidence effects are low), and minimizes duct loss at 60 percent (where incidence loss is relatively high). This

$P_{RC} = 17:1$
 $T_4 = 1589\text{K} (2400^\circ\text{F})$
 $N = 5969 \text{ rad/s} (57,000 \text{ RPM})$
 $U_{T_4} = 640 \text{ m/s} (2100 \text{ FT/SEC})$

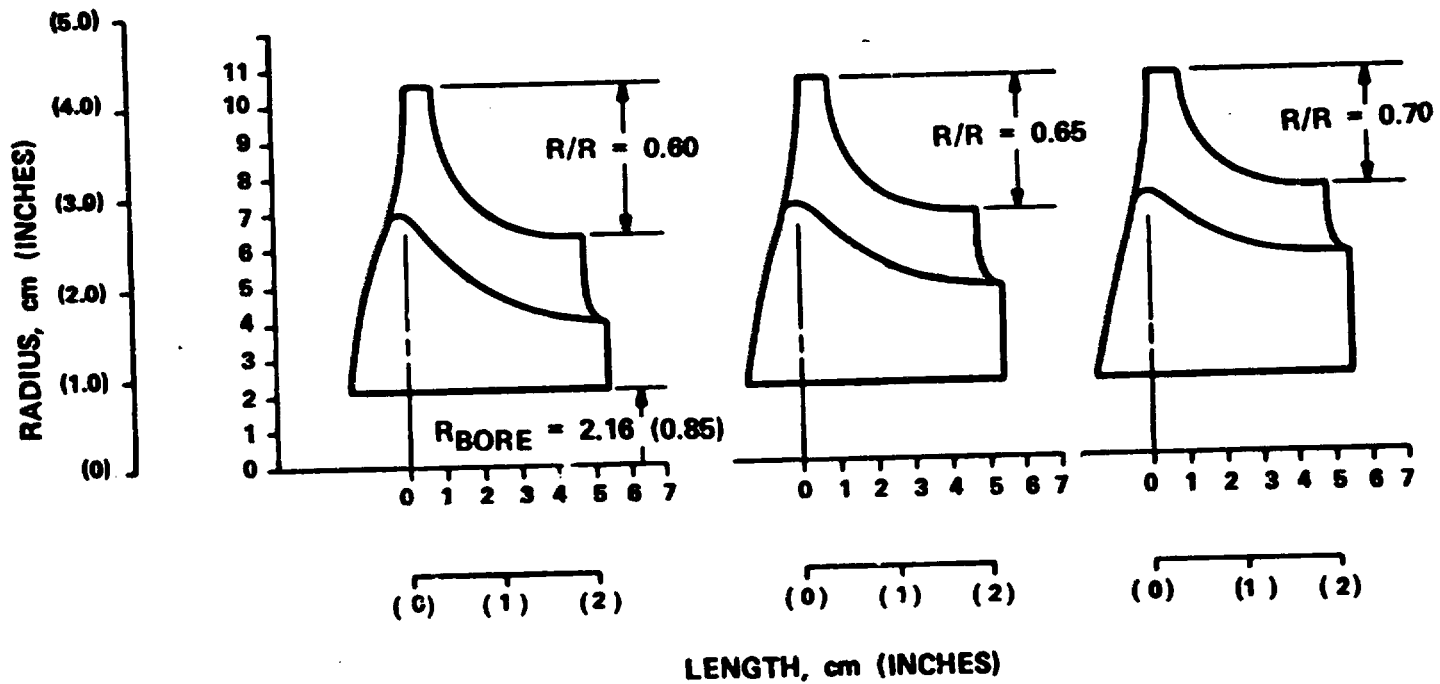


Figure 48. Cooled Rotor Configurations from Detailed Parametric Study.

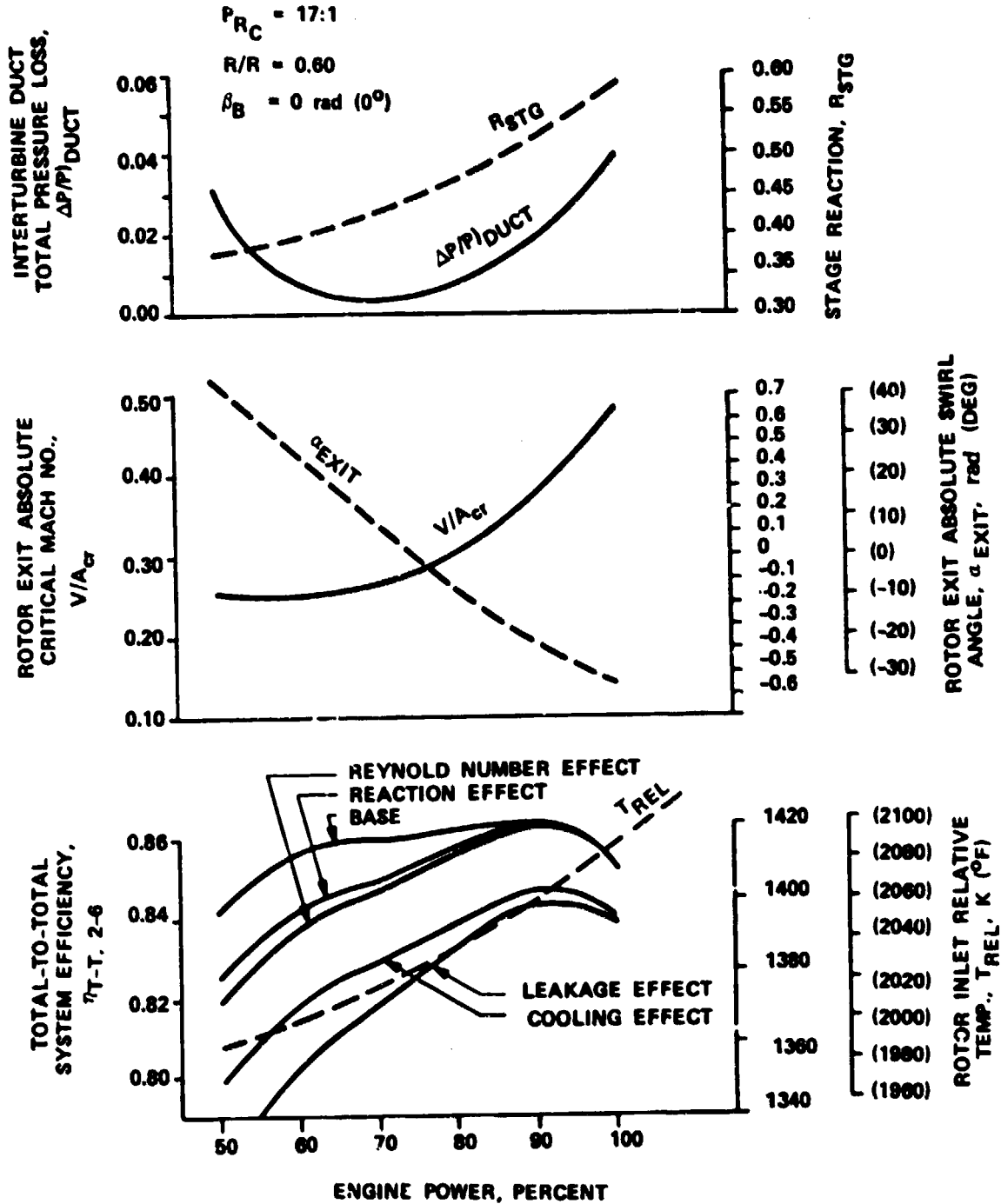


Figure 49. Off-Design Turbine Characteristics with $\lambda_4 = 1.04$, 1589K (2400°F), 5969 rad/s (57,00 RPM), and 640 m/s (2100 Ft/Sec), $R/R = 0.60$, $\beta_B = 0 \text{ rad } (0^\circ)$.

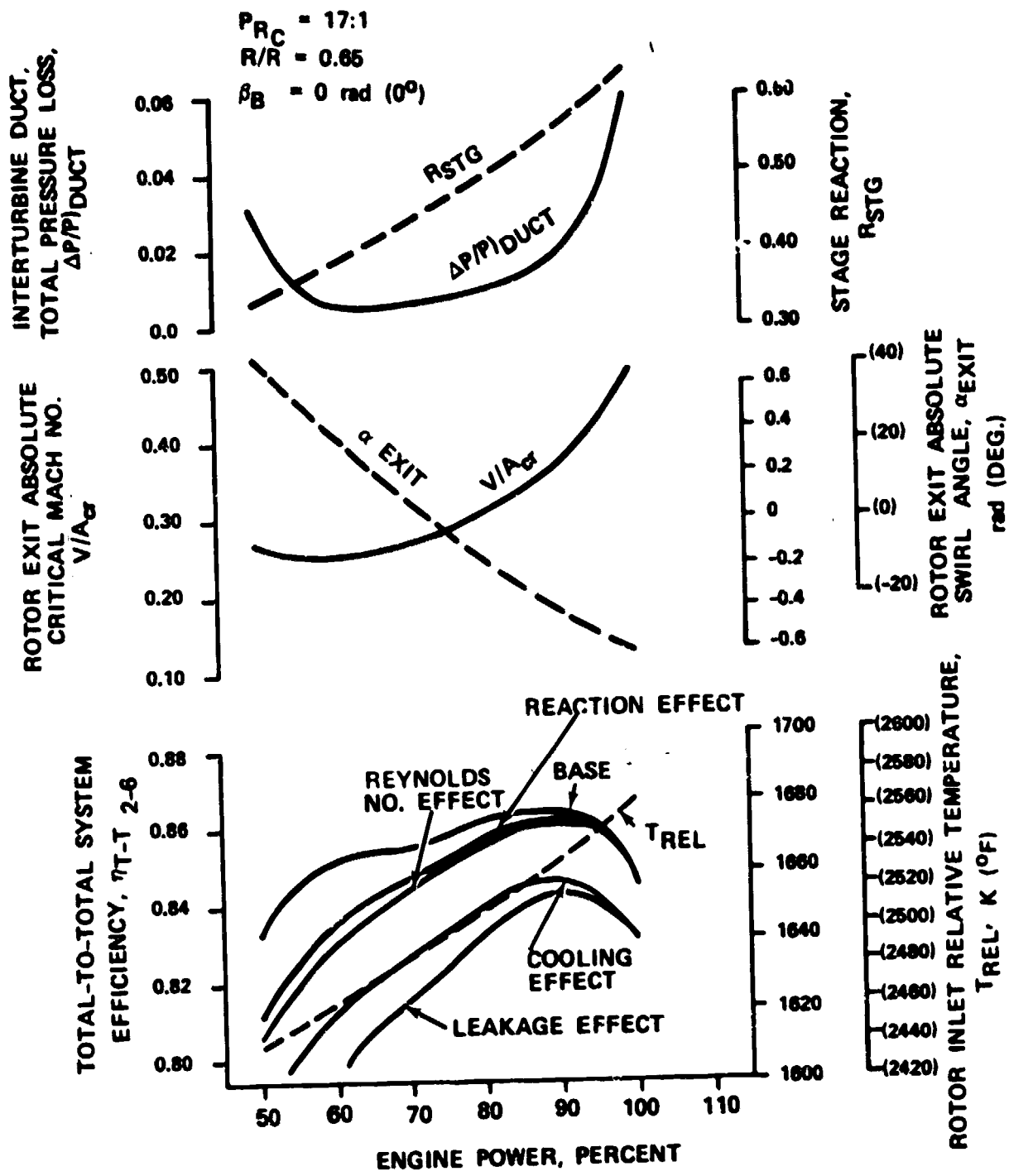


Figure 50. Off-Design Turbine Characteristics with $\lambda_4 = 1.0$, 1589K (2400°F), 5969 rad/s (57,000 RPM), and 40 m/s (2100 Ft/Sec). $R/R = 0.65$, $\beta_B = 0 \text{ rad } (0^\circ)$.

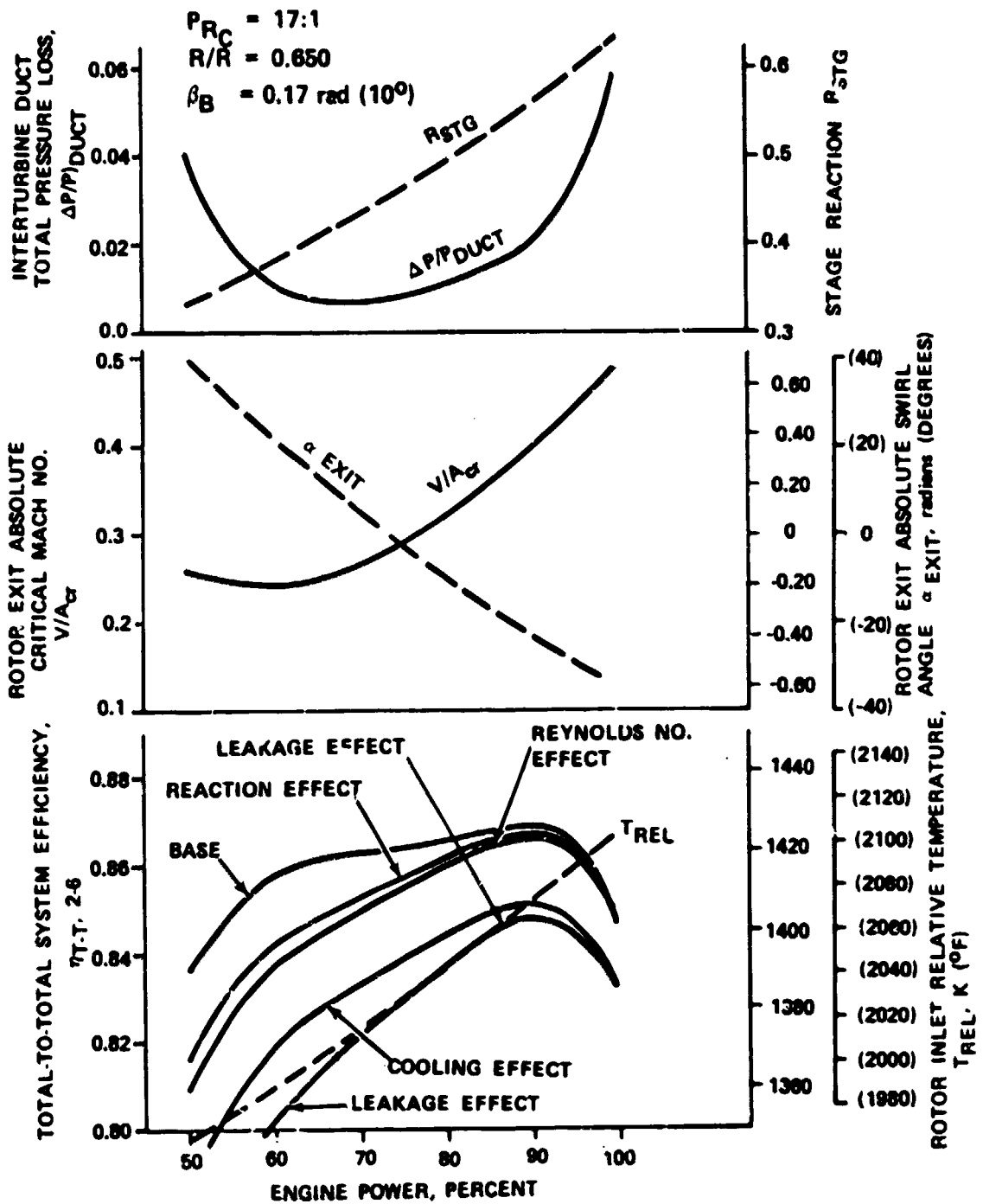


Figure 51. Off-Design Turbine Characteristics with $\lambda_1 = 1.0$, 1589K (2400°F), 5969 rad/s (57,000 RPM), and 640 m/s (2100 Ft/Sec), $R/R = 0.65$, $\beta_B = 0.17 \text{ rad } (10^\circ)$.

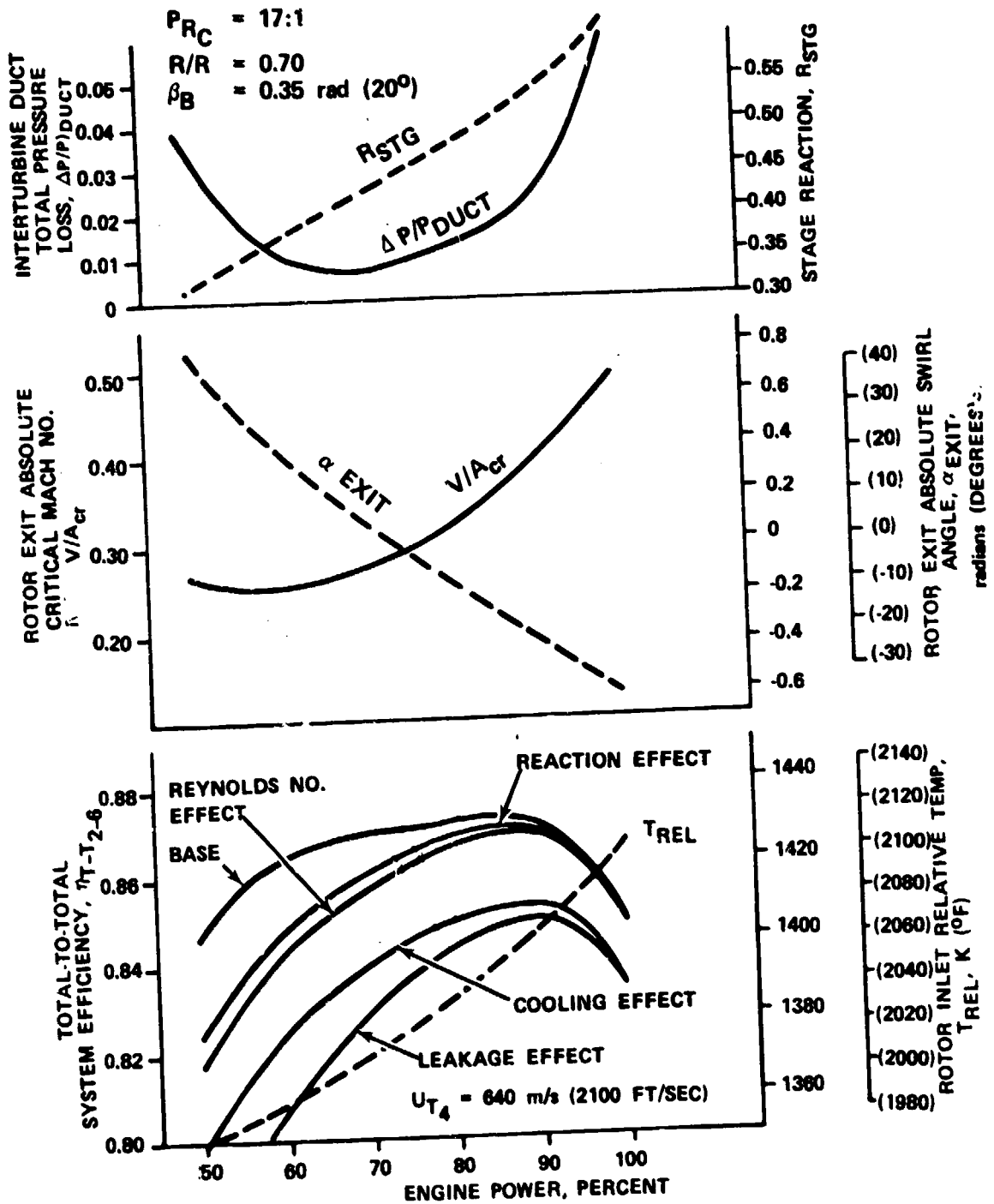


Figure 52. Off-Design Turbine Characteristics With $\lambda_4=1.0$, 1589K (2400°F), 5969 rad/s (57,000 RPM) and 640 m/s (2100 ft/sec), $R/R=0.65$, $\beta_B=0.35 \text{ rad } (20^\circ)$.

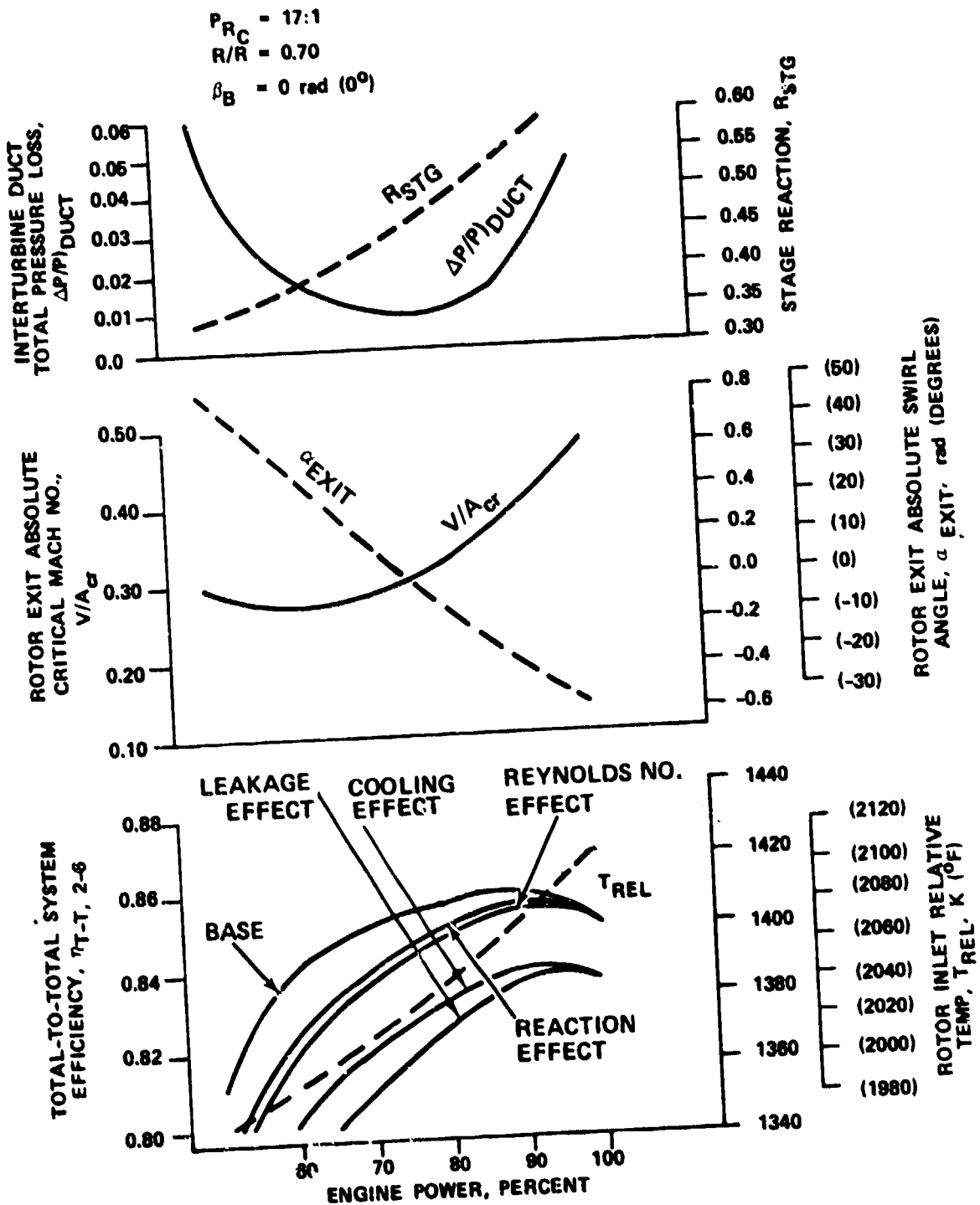


Figure 53. Off-Design Turbine Characteristics with $\lambda_4 = 1.0$, $1589K$ ($2400^\circ F$), 5969 rad/s ($57,000 \text{ RPM}$) and 640 m/s (2100 Ft/Sec). $R/R = 0.70$, $\beta_B = 0 \text{ rad } (0^\circ)$.

results in a relatively flat performance characteristic (especially with the higher rotor inlet blade angles), except for a rapid decrease in rotor reaction at lower power levels.

5.5 Uncooled Rotor Aerodynamic Evaluation

A detailed parametric study and off-design analysis was conducted for an uncooled/rotor configuration at 1478K (2200°F). The results are presented in Figures 54 and 55, and are based on the same tip speed and rotational speed used for the 1589K (2400°F) cooled rotor. The selected rotor flow path is presented in Figure 56. The performance characteristics shown in Figure 55 are similar to the 1589K (2400°F) case. Note that cooling-flow penalties were not evaluated because early mechanical analyses indicated that extremely high blade-thickness taper ratios would be required in the inducer region to meet the 4000-hour mission life. These ratios would severely limit the rotor-burst margin.

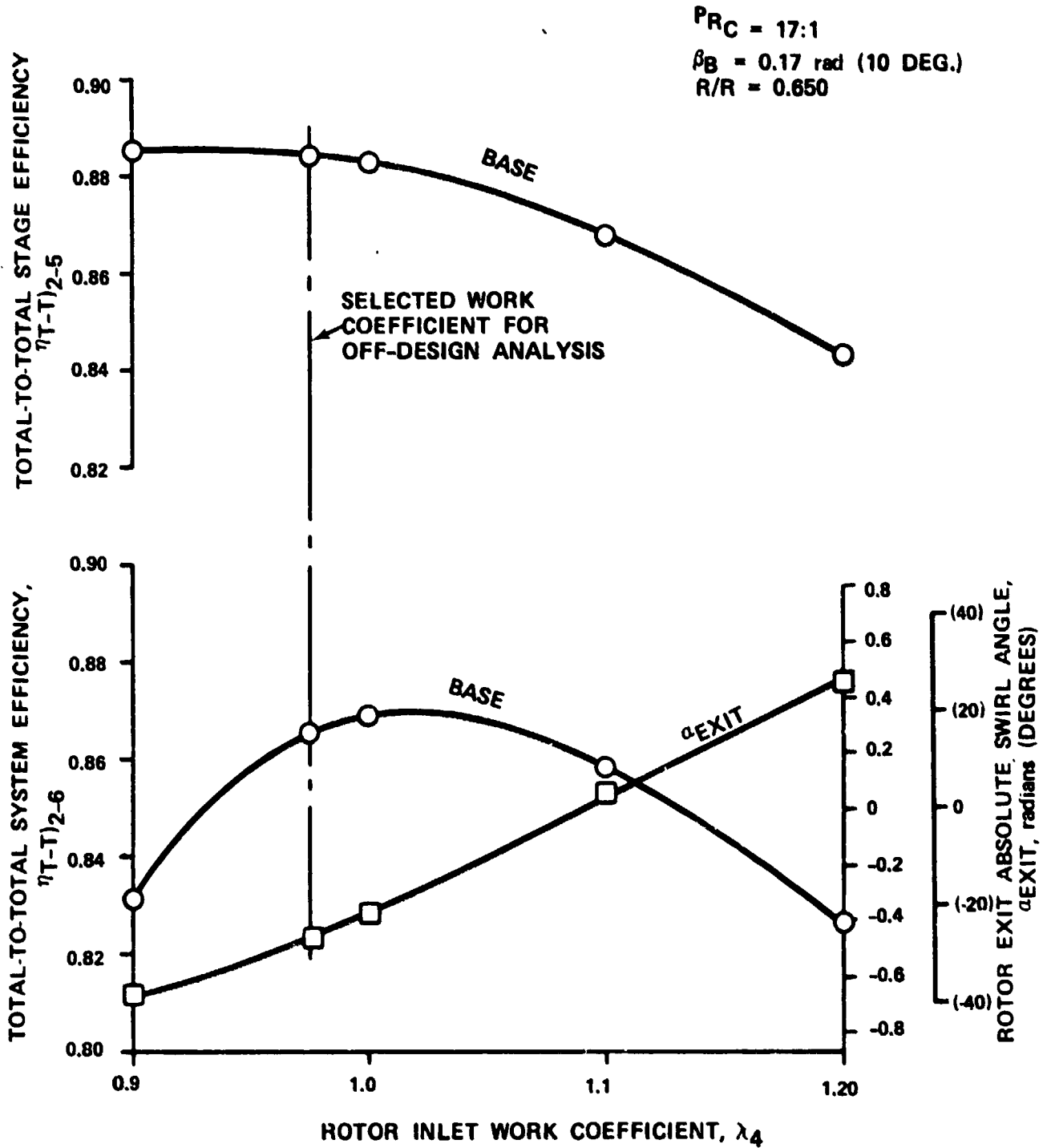


Figure 54. Detailed Parametric Study for Uncooled Rotor with 14 Blades at Maximum Power, 5969 rad/s (57,000 RPM), 1478K (2200 F), and 640 m/s (2100 Ft/Sec).

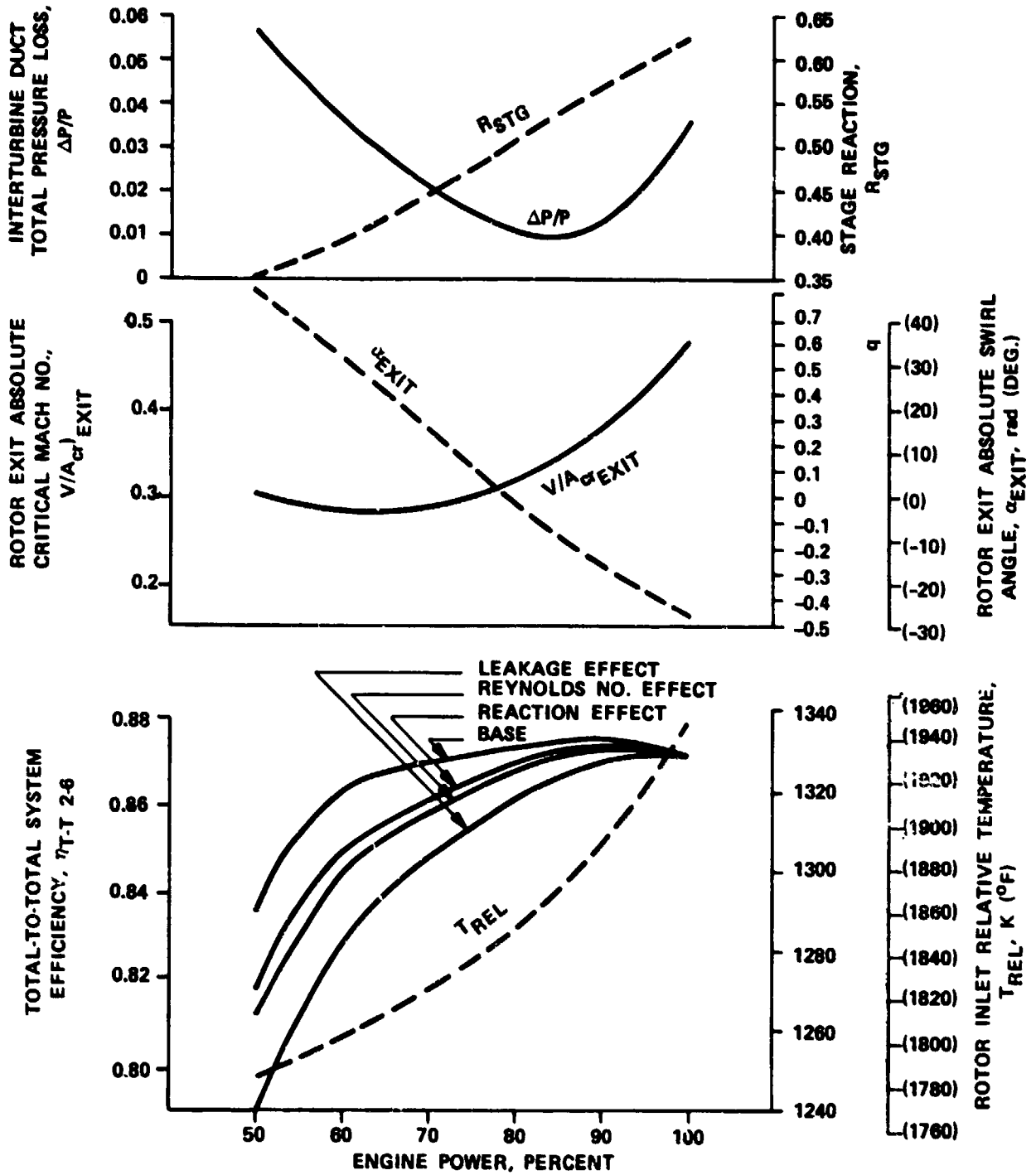


Figure 55. Off-Design Analysis for Uncooled Rotor at 1478K (2200 F), $\beta_B = 0.17$ rad (0), $\lambda_4 = 0.975$, $R/R = 0.65$, $\gamma = 1.5$, 640 m/s (2100 Ft/Sec), and 5969 rad/s (57,000 RPM).

- $T_4 = 1478\text{K}$ (2200°F)
- $N = 5969$ rad/s (57,000 RPM)
- $U_{T_4} = 640$ m/s (2100 FT/SEC)
- $R/R = 0.650$
- $A_5 = 77.4$ cm² (12.0 IN.²)
- $\lambda_4 = 0.975$

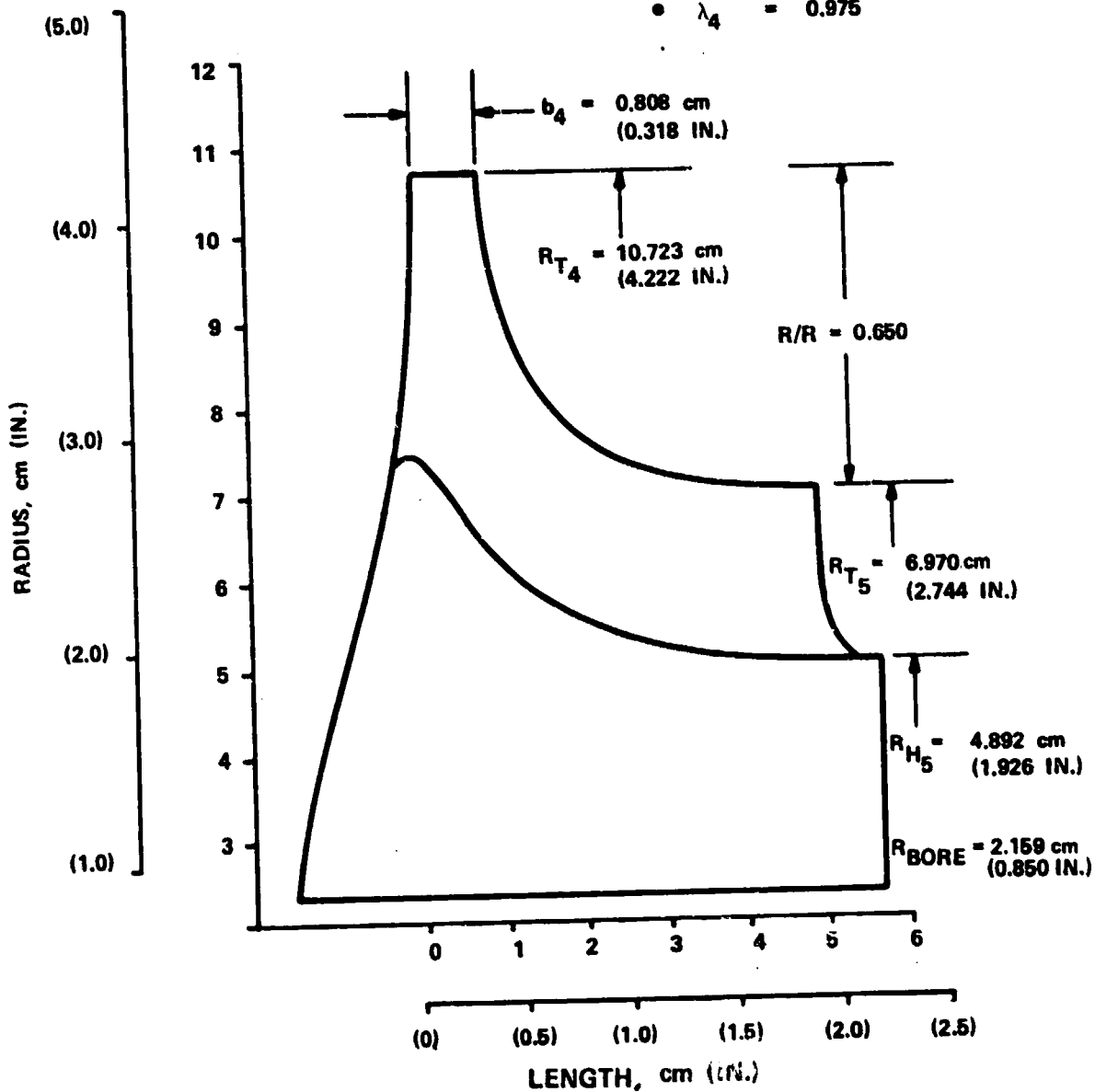


Figure 56. Uncooled Rotor Configuration.

5.6 Uncooled Rotor Mechanical Analysis

A mechanical feasibility evaluation of the uncooled rotor design was conducted with the following analyses:

- o A 2-dimensional thermal analysis;
- o A 1-dimensional stress-rupture analysis;
- o A 2-dimensional finite-element stress analysis.

The 2-dimensional thermal analysis computed the temperature distribution in the blade based on a rotor-inlet temperature of 1478K (2200°F). For the stress-rupture analysis, a temperature distribution and duty cycle life requirement of 4000 hours were used to calculate the taper ratio for the blade. Figures 57 and 58 show the temperature and thickness distributions resulting from these analyses. Based on this taper ratio, a 2-dimensional finite-element model was established. A rotor flow path was based on the detailed parameter and off-design analysis (Figure 56). Figure 59 illustrates the 2-dimensional finite-element model for the uncooled rotor.

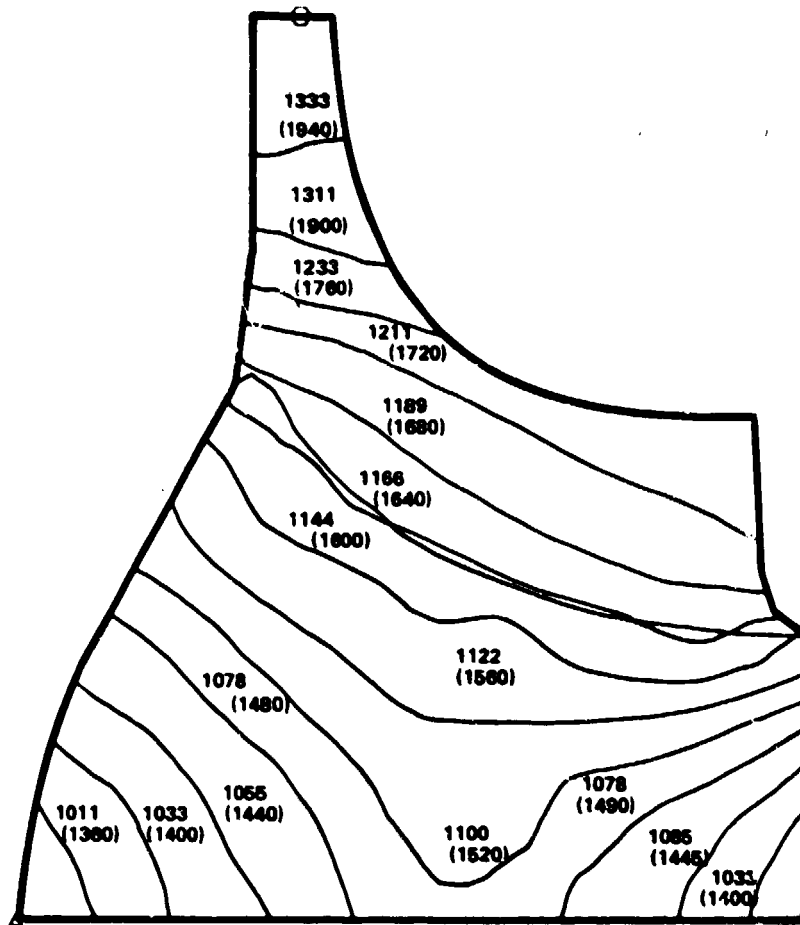
This rotor configuration was based on the dual-alloy approach, using a DS Mar-M 247 blade ring, with a powder-metal Astroloy hub. Table VI summarizes the stress levels and burst margins that occurred in the mechanical analysis for the disk at different conditions. The inadequate burst margin that resulted was sufficient justification for eliminating the uncooled rotor from consideration. Acceptable burst margin levels (125 percent) could be achieved only by reducing the inlet temperature below 1478K (2200°F) and by further reducing the blade thickness.

5.7 Cooled Rotor Mechanical Analysis

5.7.1 Influence of Radius Ratio on Rotor Stresses

During the preliminary design definition, aerodynamic and mechanical parametric studies were conducted concurrently to optimize flow-path geometry. Since the decision to proceed with a cooled rotor concept had not yet been made, the initial effort was conducted using uncooled hub geometries and solid blades. In addition, the basic influences of flow-path size on blade and hub stresses were similar for both cooled and uncooled turbines.

An initial 2-dimensional stress analysis was performed on the two rotors from the preliminary parametric study. The rotors represent two different flow paths that were primarily defined by the radius ratio difference from inducer tip-to-exducer tip at the same cycle conditions. The basic assumptions used for this study were:



TEMPERATURE, K (°F)

Figure 57. Mode Temperature Distribution, Uncooled Rotor.

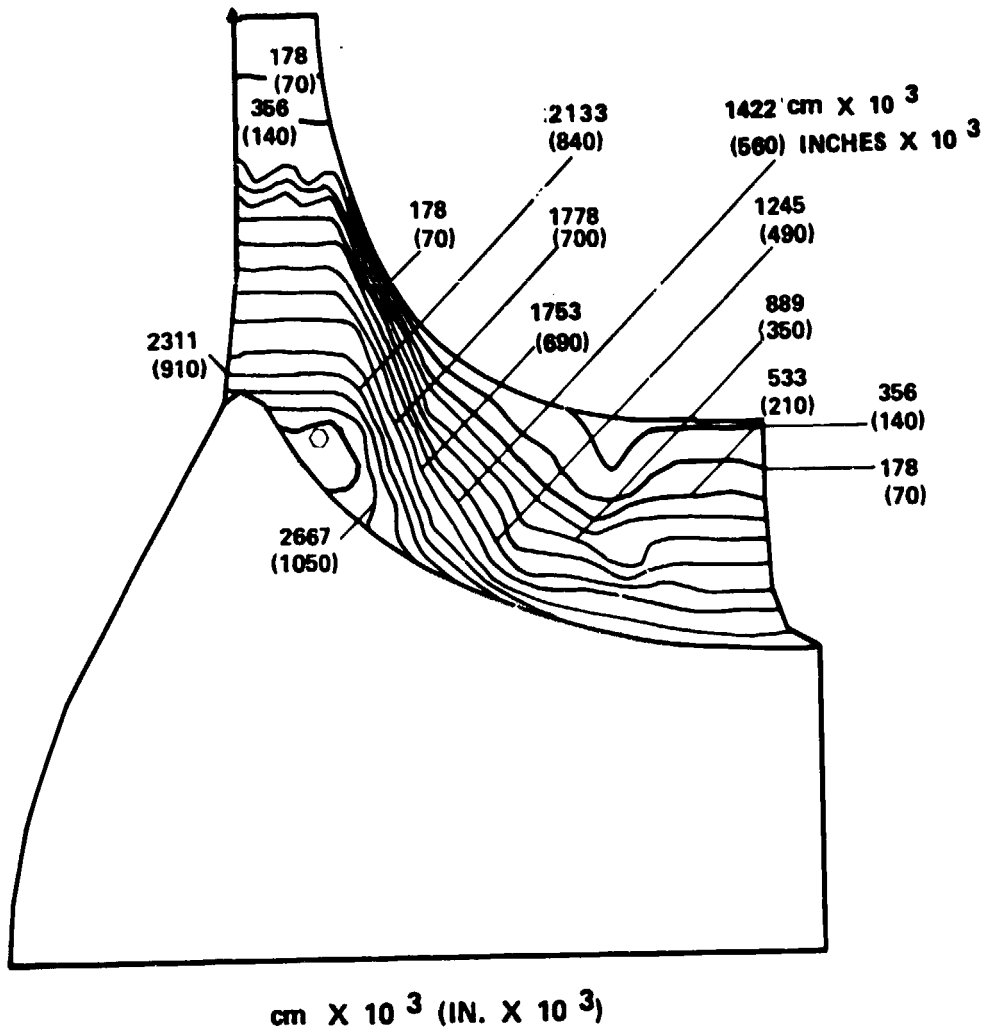


Figure 58. Normal Thickness Distribution, Uncooled Rotor.

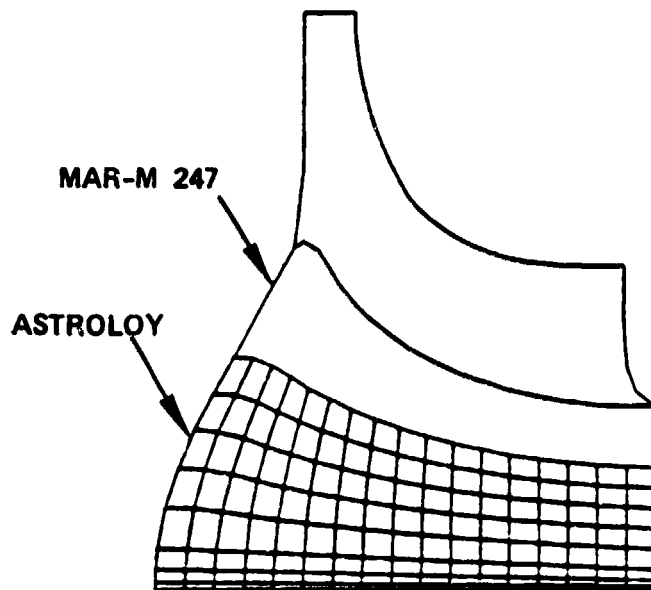
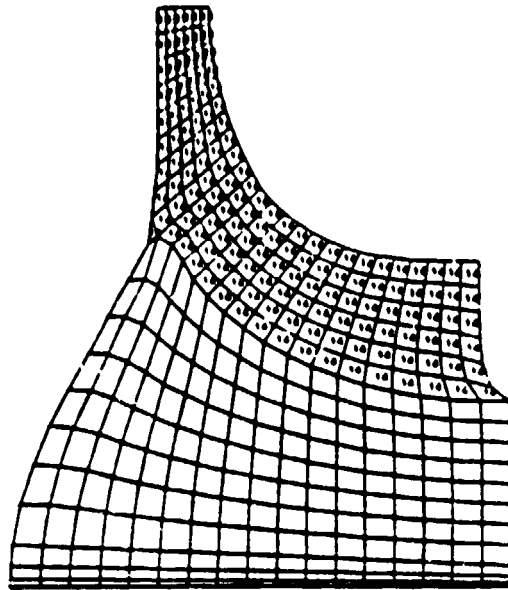


Figure 59. Uncooled 1478K (2200°F) Rotor,
2-Dimensional Finite-Element Model.

TABLE VI. MECHANICAL ANALYSES OF UNCOOLED ROTOR DISK.

*Blades	σ_T max MPa (KSI)	σ_R max. (Bond Line) MPa (KSI)	σ_T avg. MPa (KSI)	Burst Margin Ratio	Astroloy -3 UTS MPa (KSI)
No Blade 294K (70°F)	921.1 (133.6)	196.5 (28.5)	558.5 (81.0)	1.38	1247.61 (180.95)
10 Blades 294K (70°F)	1190.0 (172.6)	361.3 (52.4)	748.1 (108.5)	1.19	1247.61 (180.95)
14 Blades 294K (70°F)	1303.1 (189.0)	424.0 (61.5)	823.9 (119.5)	1.13	1247.61 (180.95)
14 Blades Max. power	1385.8 (201.0)	425.4 (61.7)	822.5 (119.3)	0.95	869.43* (126.1*)

*The property at average temperature.

- o Uniform temperature
- o Rotational speed = 6807 rad/s (65,000 rpm);
- o Inducer tip speed = 640 m/s (2100 ft/sec);
- o Monoform rotor;
- o Material density = 7.916×10^{-3} kg/cm³ (0.286 lb/in.³);
- o 14 blades;
- o Bore diameter = 4.32 cm (1.70 in.);

The distribution of disk tangential stress for the two configurations is presented in Figure 60. The peak effective stress was 981.1 MPa (142.3 ksi) for the low-radius ratio rotor and 1163.8 MPa (168.6 ksi) for the high-radius ratio rotor. The results shown in these figures are for cold rotation only; if thermal gradients were imposed, the bore stresses would increase significantly. Experience with earlier radial turbine designs has indicated that the high-radius ratio design could be adversely affected by these gradients. For the purpose of this analysis, a typical thickness distribution as a function of radius was selected for the blade and was used for both turbine geometries. This thickness distribution is shown in Figure 61 using the low-radius-ratio design. The absolute suitability of this distribution for this case was not critical, since a separate analysis indicated that only 6.0 percent of the peak bore stress was attributable to the loading by the 14 blades.

By comparing these two configurations, it is apparent that the smaller radius ratio reduced rotor-hub stresses despite the presence of larger airfoils. The axisymmetric hub material near the flow path contributed more toward peak bore-stress magnitude than did the blades.

5.7.2 Incorporation of Cooled, Dual-Alloy Configuration

An extensive study of the effects of incorporating blade cooling-supply passages in the turbine rotor hub was conducted. This study analyzed the effects of using a dual-alloy rotor configuration. As discussed earlier, the dual-alloy, powder-metal hub possessed a higher tensile strength and low-cycle-fatigue (LCF) capability than the conventionally cast material. This was an important factor in attaining the ambitious performance goals of the program.

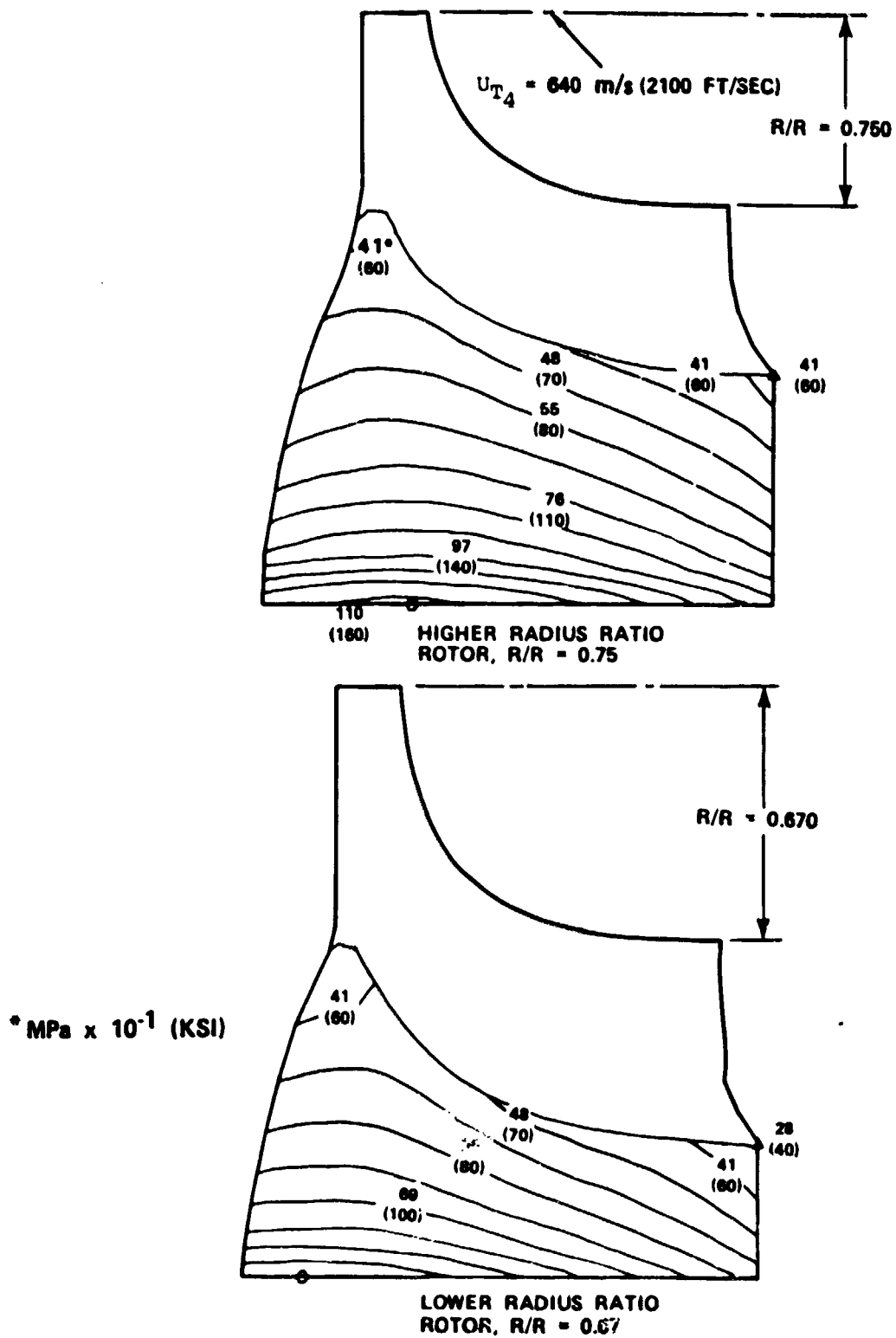
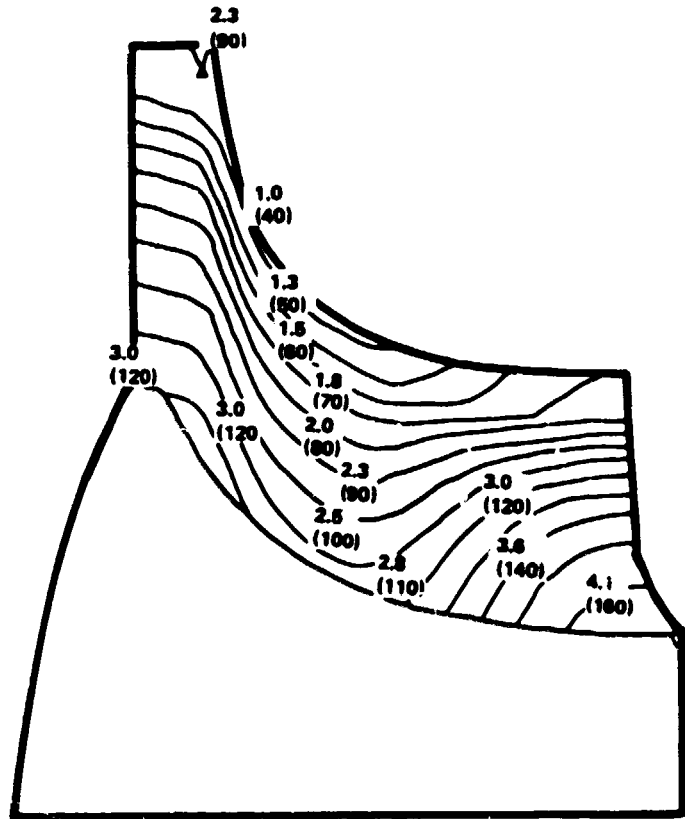


Figure 60. Effect of Rotor Flow Path on Tangential Disk Stress.



MILLIMETERS (INCHES x 10³)

Figure 61. Thickness Distribution for 0.67-Radius-Ratio Configuration.

A preliminary radius-ratio analysis indicated the advantages of a lower radius ratio. Hence, a 0.65-radius-ratio value was ultimately selected as a baseline for the study. Several model variations were produced during this study; all were for a single flow path, with the following parameters assumed:

- o Exducer tip-to-inducer tip radius ratio = 0.65;
- o Inducer tip radius - 10.723 cm (4.222 in.);
- o $N = 5969$ rad/s (57,000 rpm);
- o Tip speed = 640 m/s (2100 ft/sec);
- o Radial blading;
- o $T_4 = 1589\text{K}$ (2400°F);
- o Coolant inlet temperature = 717.8K (832.3°F).

The blade thickness was determined by a blade metal temperature field based on anticipated cooling performance, boundary conditions, and previous Garrett design experience. The total blade thickness distribution for adequate stress rupture life was then computed assuming minimum material properties similar to those of DS Mar-M 247. After the blade thickness distribution was established (Figure 62), a series of models were studied to determine the effects of using a dual-alloy rotor disk and the addition of cooling supply passages.

The geometry selected had no rotor-backface web between blades and no T-section, since it was determined that the web could not be adequately cooled in the predicted environment. Optimization of the disk contour and scallop region geometry was performed on the baseline geometry using previous radial turbine design experience.

The baseline model, A, is shown in Figure 63. This model was a single-alloy rotor using DS Mar-M 247 cast material for the inducer. Even at room temperature, this rotor had inadequate hub strength, but was included for comparison with the dual-alloy models.

The dual-alloy models used Mar-M 247 blade section material. Low-carbon, powder-metal Astroloy "C" properties were used for the disk. This latter material exhibits high strengths and ductility at the temperature levels encountered in the cooled rotor hub. Other suitable powder-metal alloys included AF2-1DA and a relatively new material, AF115. If higher tensile strength or fatigue properties are achieved with these alloys, they could easily be substituted in the design.

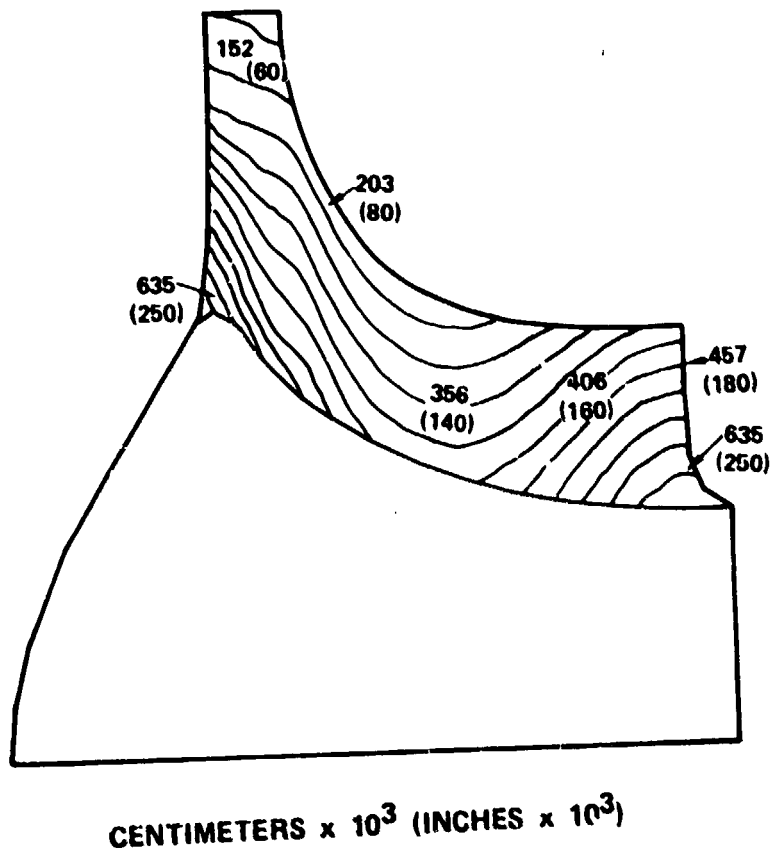
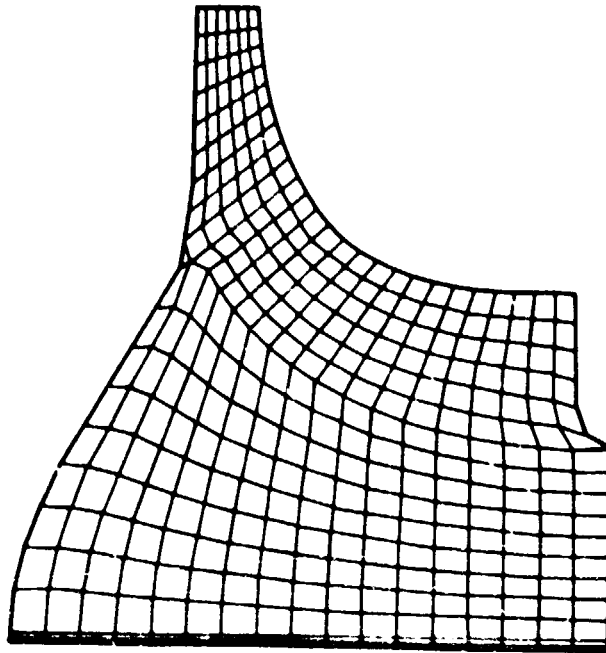
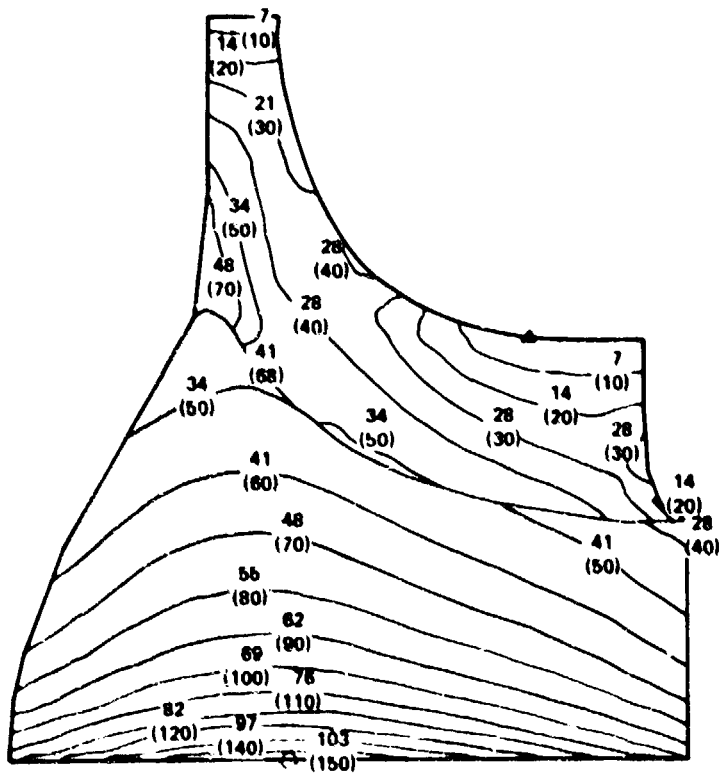


Figure 62. Normal Blade Wall Thickness, Dual-Alloy Geometry Study.



MATERIAL ELEMENT



TANGENTIAL STRESS, MPa X 10⁻¹ (KSI)

MODEL A

Figure 63. Single-Alloy Solid Rotor at Room Temperature.

Initially, a dual-alloy bondline was placed in a position that allowed easy insertion of a large cooling-supply passage in the outer material region. The solid rotor version, B1, is included in Figure 64 to illustrate the gains achieved over the single-alloy, solid rotor configuration. Astroloy showed a lower density than Mar-M 247, and thus lowered the average tangential and peak effective stress in the disk. The average ultimate strength was considerably increased over the single-alloy rotor configuration. This resulted in a higher burst ratio and fatigue life for the dual-alloy rotor. Model B2 (Figure 64) shows the effects of adding a cooling passage.

It was determined that internal cooling passages were needed in the final rotor design and that the rotor must be capable of withstanding both steady-state and transient-temperature conditions. Model B3 (Figure 65) shows a temperature field imposed on the rotor. This temperature field was derived from cooling requirement predictions for overall design life and from previous experience with cooled radial turbines. Both of these changes decreased the mechanical feasibility of this particular rotor. Table VII shows that with a temperature field, the burst margin for Model B3 was only 13 percent. This number was derived from a modified burst criteria that emphasized the load bearing capability of the inner material of a dual-alloy rotor. Normal turbine design constraints at Garrett require a burst margin of 25 percent with a 0.85 burst factor.

Additional analyses were then performed representing rotors where the dual-alloy bondline was moved progressively outward until a position was reached that still allowed the insertion of a cooling passage. This model was considered to be an only slightly more optimistic design concept, since the blades were still too thin to meet stress-rupture life requirements. Also, the cooling passages were slightly smaller than necessary from a flow standpoint. Several versions of Model D are presented showing the stress effects of various aspects of the rotor geometry.

Models D1 and D2 (Figure 66) illustrate the impact of blade loading, which was higher than in the previous models. This was due to the blade thickness requirements incurred by the temperature and life goals of the rotor. The higher placement of the bondline lowered the stresses and increased the average strength. This was expected, but the major improvement in stress level over Model B2 appeared as a result of the smaller cooling passage of Model D4 (Figure 67).

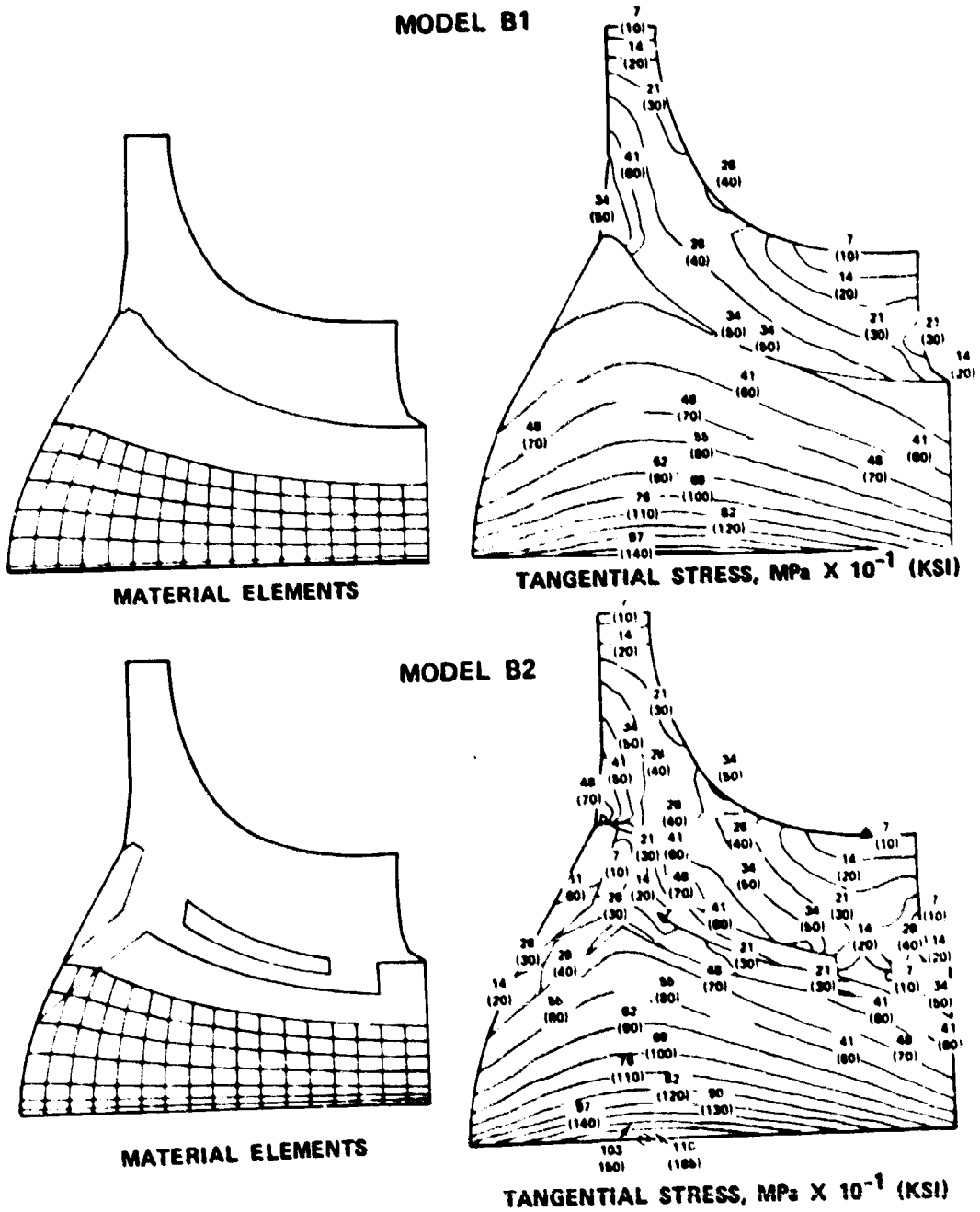
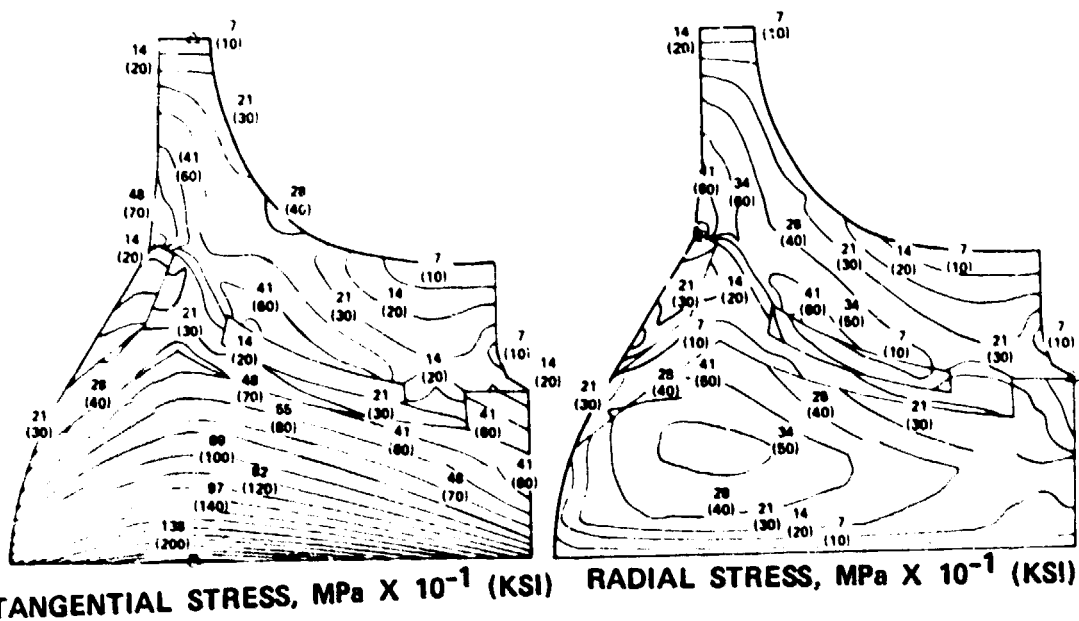
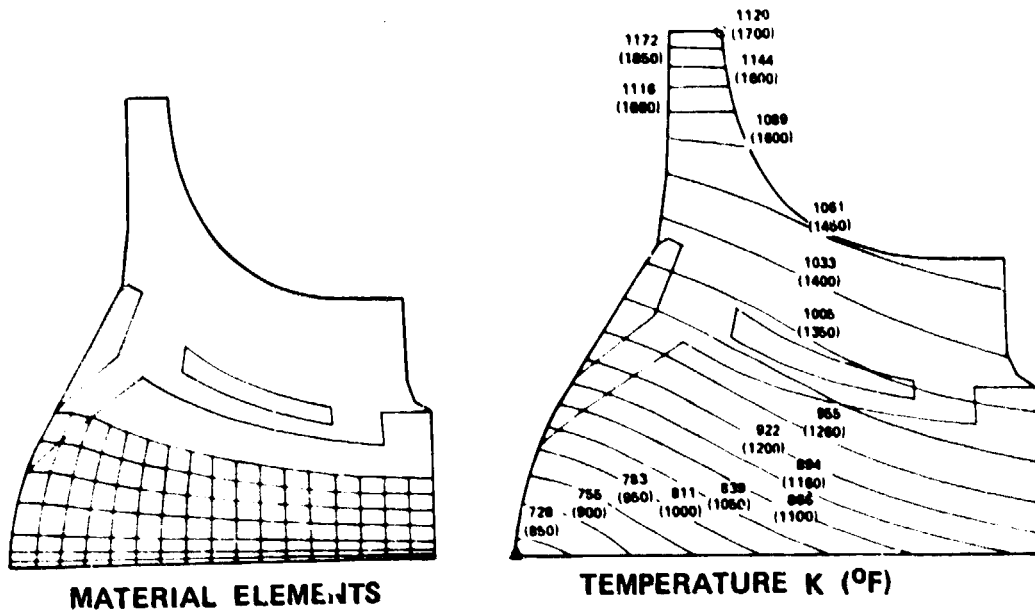


Figure 64. Dual-Alloy Rotor With and Without Full-Cooling Passage at Room Temperature.



MODEL B3

Figure 65. Dual-Alloy Solid Rotor With Full-Cooling Passage at Maximum Temperature.

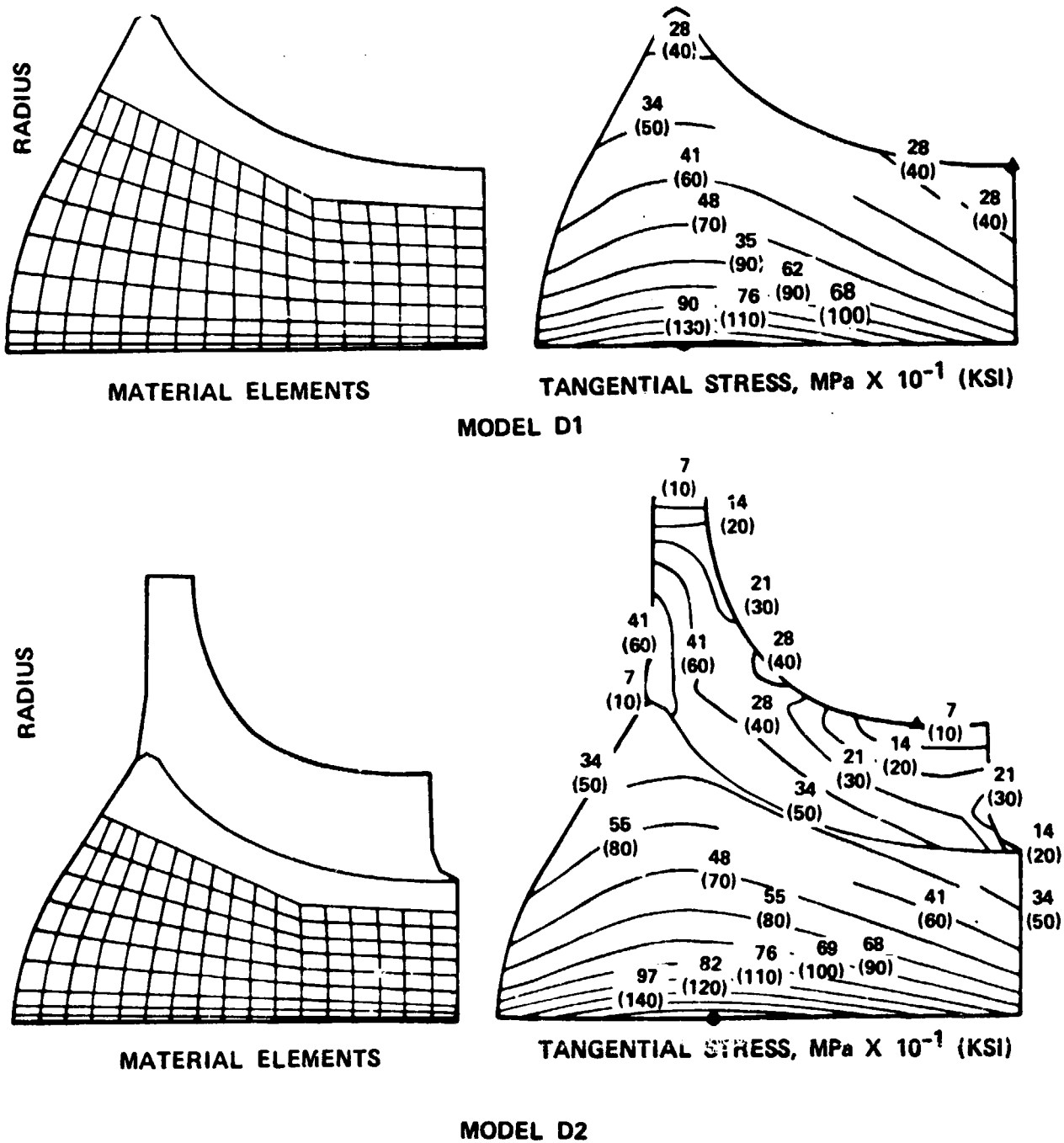
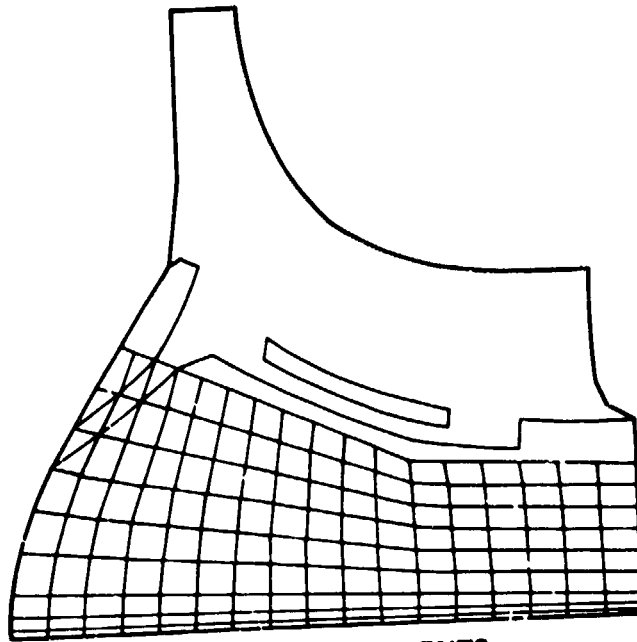
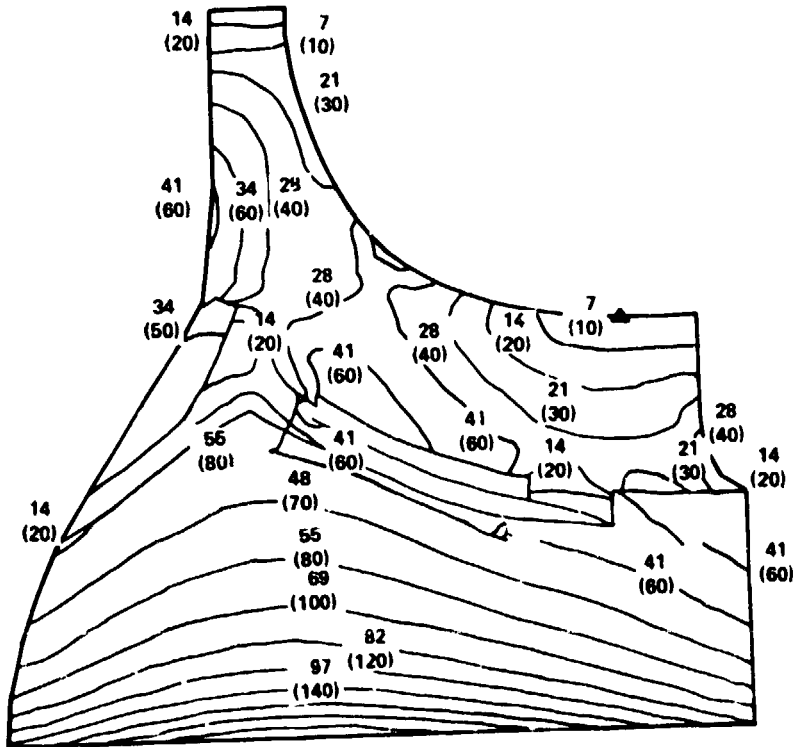


Figure 66. Dual-Alloy Solid Rotor with Bondline at Largest Practical Radius, Room Temperature.



MATERIAL ELEMENTS



TANGENTIAL STRESS, MPa X 10⁻¹ (KSI)

Figure 67. Dual-Alloy Solid Rotor with Bondline at Largest Radius and With Full-Cooling Passage, Room Temperature.

Figure 68 presents the model D configuration with the imposed steady-state maximum power temperature distribution. The modified burst ratio and the bore fatigue life are marginal for this flow path with a radius ratio of 0.65.

A comparison summary of the progression from a solid, uncooled monofrom cast rotor to a preliminary optimized geometry is shown in Table VII. The average tangential stress and average ultimate strength are area- or volume-weighted averages that take into consideration both cast- and powder-metal portions of the rotor axisymmetric regions. The average tangential stress in the powder-metal region of the hub, as determined by integration of the finite-element stress results, was used to determine the modified burst ratio. This ratio was intentionally conservative, since it focused on higher stress portions of the rotor.

5.7.3 Optimum Rotor Selection

Aerodynamically, the lower blade exducer tip-to-inducer tip radius ratios were superior at lower power settings. Even though several disadvantages (greater cooled blade-surface area, limited space available for a powder-metal disk, and low radius ratio designs) existed, higher burst margins and lower peak bore stresses were attained. After careful screening, two candidates were selected with radius ratios of 0.60 and 0.65, respectively. A 2-dimensional, finite-element analysis was used for the final design selection. The results of this analysis are shown in Figure 69.

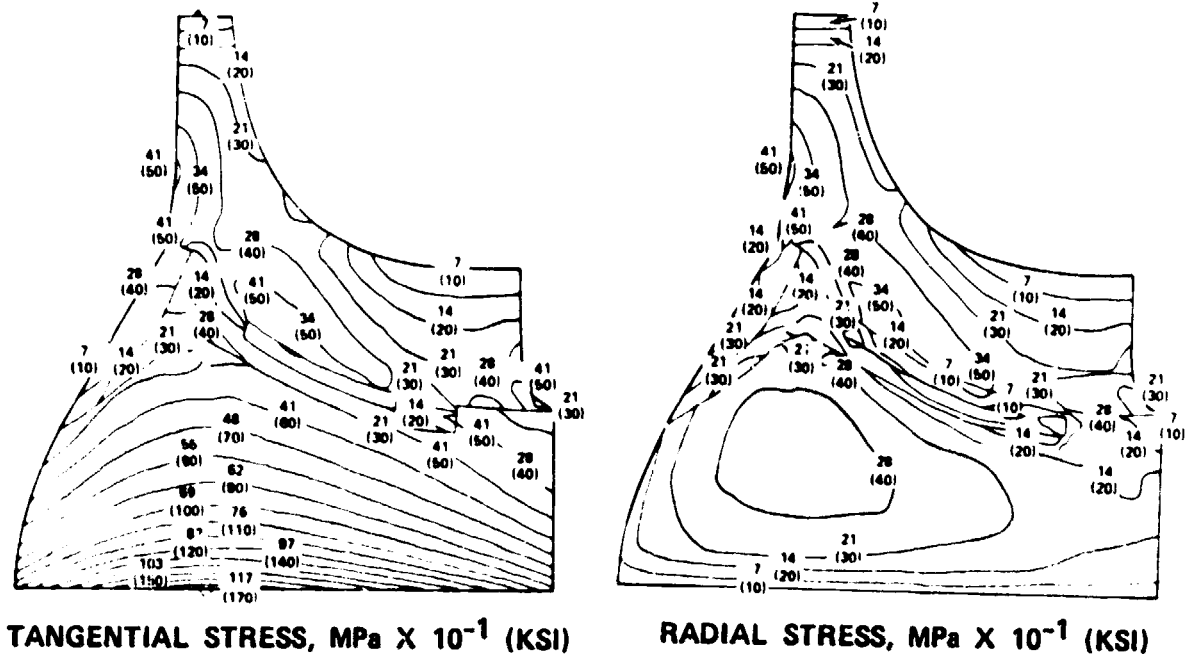
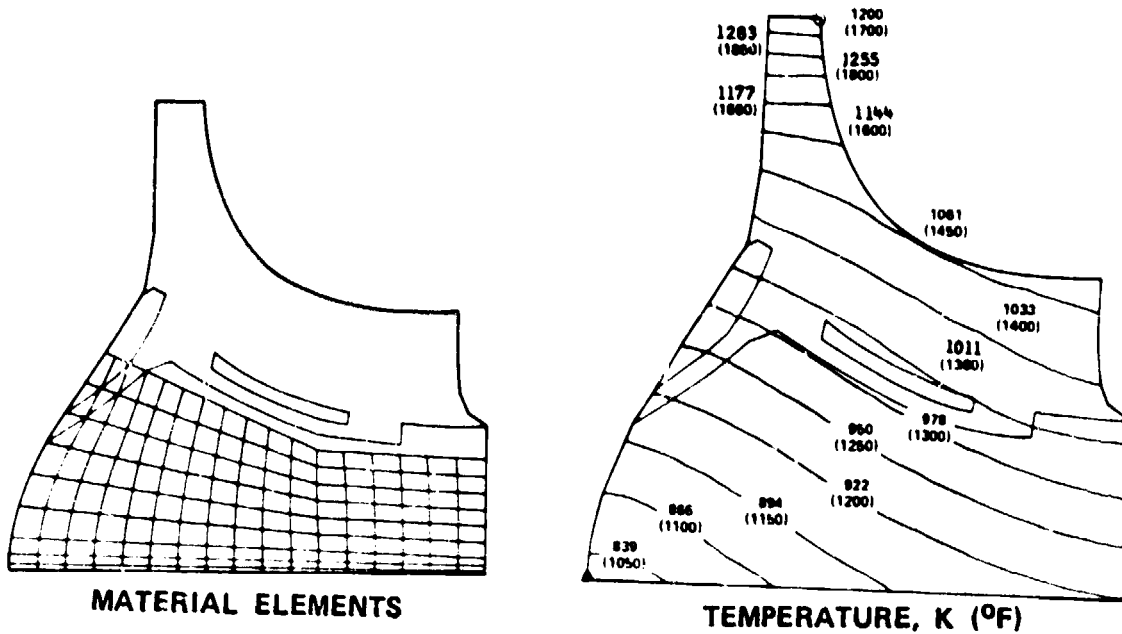
The following parameters were used in the final configuration selection:

- o Airfoil Cooling

- The 0.65 radius-ratio airfoil is smaller in size than the 0.60 radius-ratio airfoil with 13-percent less surface area to cool. This airfoil has a lower aspect ratio inducer. Consequently, significant improvements in cooling flow-distribution are possible.

- o Airfoil Vibration

- The 0.60 radius-ratio airfoil inducer and exducer height were increased by 66 and 69 percent, respectively over the 0.65 radius ratio design. The resultant lower frequencies increased the potential high-cycle-fatigue (HCF) problems.

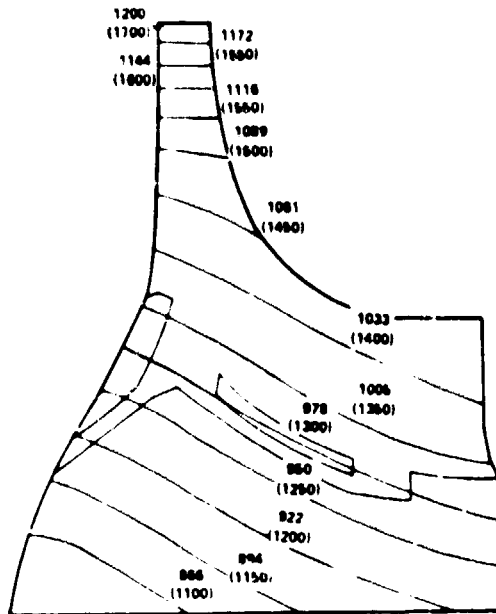


MODEL D4

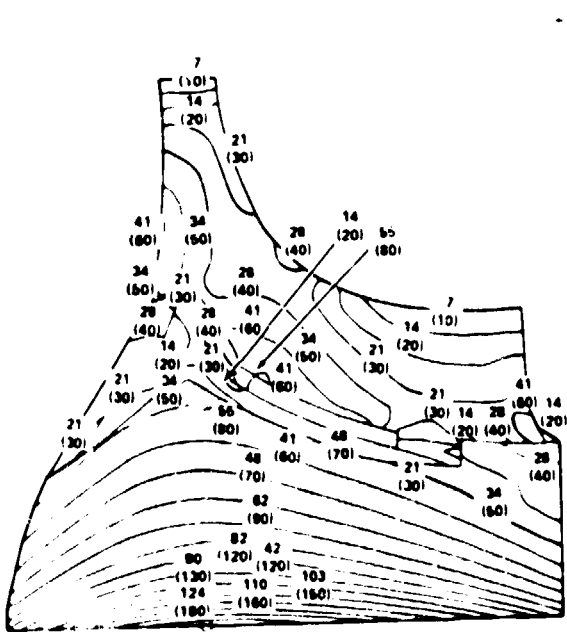
Figure 68. Dual-Alloy Rotor, Highest Bondline Radius, Full-Cooling Passage, Maximum Power Temperature.

TABLE VII. COMPARISON OF MECHANICAL PROPERTIES FOR COOLED-ROTOR MODELS.

Model	Avg. Tang. Stress MPa (ksi)	Avg. Ult. Strength MPa (ksi)	Modified Burst Margin Ratio	Peak Effective Stress MPa (ksi)	Temp. Field K (°F)	Comment
A	599.8 (87.0)	937.7 (136.0)	---	1105.9 (160.4)	294 (70)	Single-alloy, solid rotor
B1	583.3 (84.6)	1126.6 (163.4)	---	1057.7 (153.4)	294 (70)	Dual-alloy, solid rotor
B2	688.8 (99.9)	1152.1 (167.1)	---	1209.3 (175.4)	294 (70)	Full coolant passage
B3	688.8 (99.9)	1125.9 (163.3)	1.129	1516.2 (219.9)	Yes	Temp. field imposed
D1	494.36 (71.7)	1186.6 (172.1)	1.406	933.6 (135.4)	294 (70)	Model D2 with blades removed
D2	575.7 (83.5)	1186.6 (172.1)	1.310	1042.5 (151.2)	294 (70)	Dual-alloy solid rotor highest bond-line
D4	630.9 (91.5)	1206.6 (175.0)	1.267	1114.9 (161.7)	294 (70)	Full coolant passage
D5	630.9 (91.5)	1139.7 (165.3)	1.222	1306.6 (189.5)	Yes	Temp. field imposed

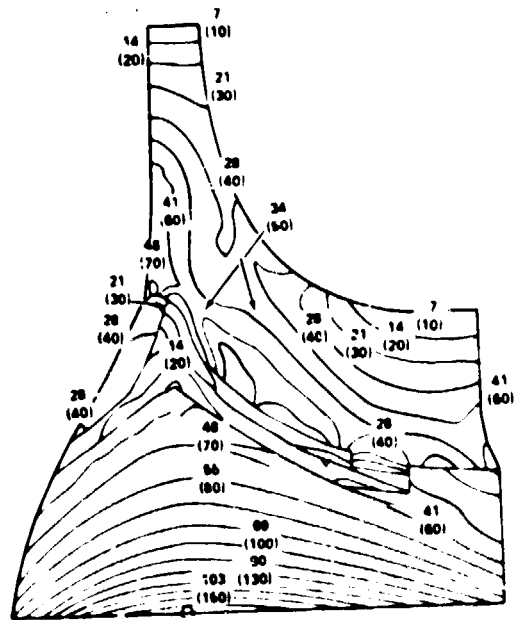


TEMPERATURE K (°F)



EQUIVALENT STRESS, MPa X 10⁻¹ (KSI)

RADIUS RATIO = 0.65



EQUIVALENT STRESS, MPa X 10⁻¹ (KSI)

RADIUS RATIO = 0.60

Figure 69. Assumed Temperatures and Equivalent Stresses.

o Airfoil Stress

- The ability to have nonradial blading without excessive bending stresses was enhanced by the shorter inducer of the 0.65-radius-ratio airfoil. A tall inducer implied substantial taper to reduce centrifugal stresses. This eroded any thickness margin that could be used to increase section modulus and reduce bending stress.
- Thicker blading near the scallop region could be detrimental to aerodynamic performance. The taller the inducer, the greater the blockage near the scallop due to reduced radius and greater airfoil thickness, and the greater the optimized stress level.

o Rotor-Hub Burst Margin

- The small cooling passage used for both the 0.60- and 0.65-radius ratios allowed adequate air distribution to the exducer and provided for the highest bondline achieved in the stress model. The final design is likely to have larger cooling passages and thicker blades that would incur higher stresses. The smaller 0.60-radius-ratio hub would be affected more by these design adjustments than the 0.65-radius ratio hub. It is anticipated that the small advantages observed with the 0.60-radius ratio hub would be insignificant.

o Hub LCF Life

- Hub LCF life decreases with an increase in peak stress. The 0.65-radius-ratio rotor, compared to the 0.60-radius ratio rotor, showed a 7.5-percent increase in peak stress. Both showed high peak stress levels that could present difficulties in achieving fatigue life goals.

In conclusion, the 0.65-radius-ratio flow path favored all aspects of the blade design, while the 0.60-radius ratio favored bore LCF life with a slightly higher burst margin. Since improved bore LCF life can be achieved by reducing bore diameter, the 0.65-radius-ratio configuration was selected for use in the final design.

5.8 Selected Stage Configuration

The system performance at 60-percent power is presented in Figure 70 as a function of rotor exducer tip-to-inducer tip radius ratio and inlet blade angle. On this basis, the aerodynamic benefits of minimizing radius ratio were consistent with the 0.65-radius-ratio selected from mechanical analysis.

The 3-dimensional (nonradial) rotor blade appeared ideally suited for the variable flow capacity engine, since rotor inlet incidence continually increased as power decreased from 100 to 60 percent. For the present duty cycle and life requirements, a 0.35-radian (20-degree) inlet blade angle was considered a high risk. Therefore, a 0.17-radian (10-degree) rotor inlet angle was selected for the detailed design. The stage meridional flow path and the 100-percent power 1-dimensional vector diagram for the selected configuration are presented in Figures 71 and 72, respectively. The aero/thermodynamic conditions and geometric stage characteristics that will be used for the detailed stator and cooled rotor design are presented in Table VIII.

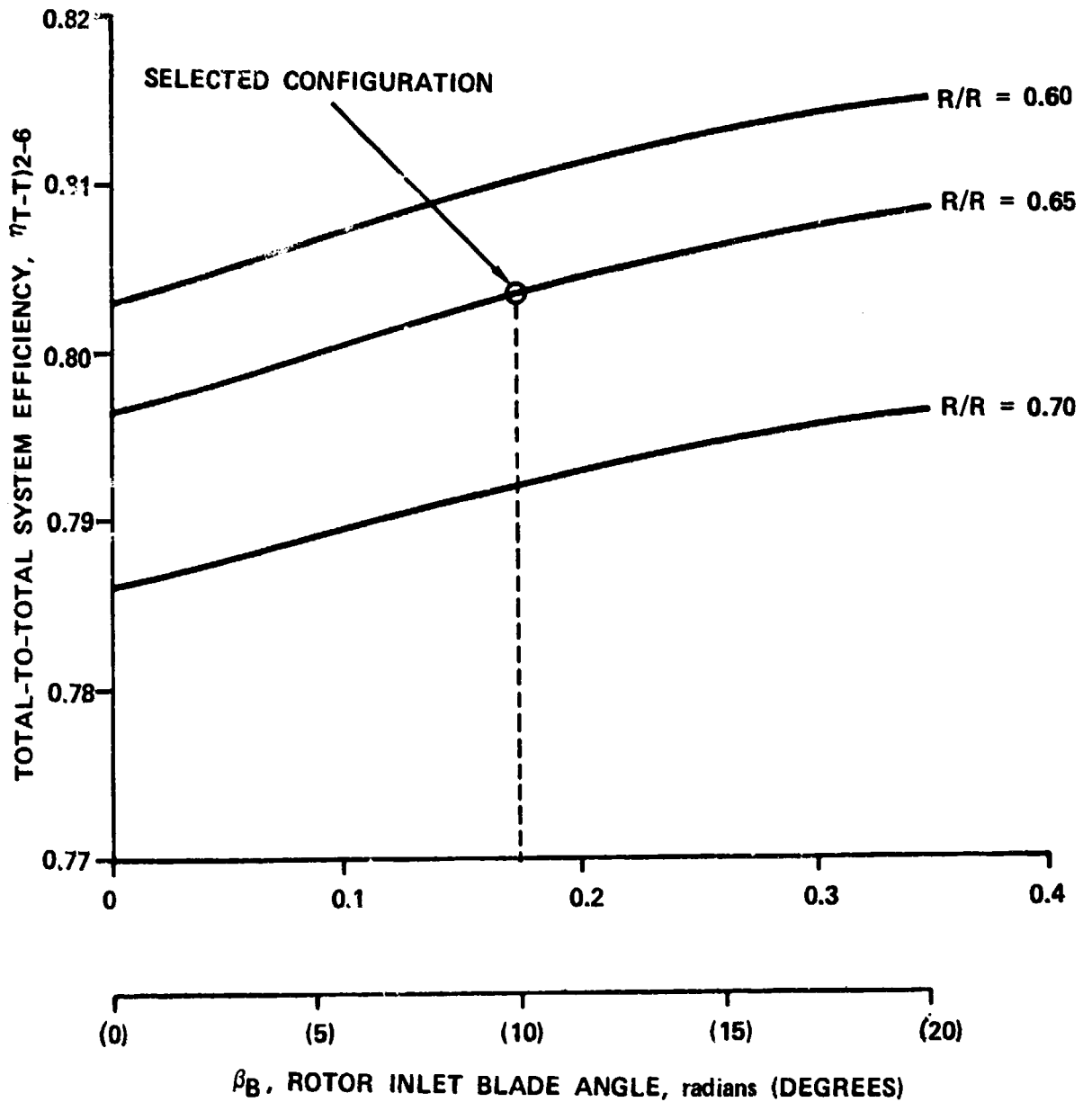


Figure 70. Effects of Radius Ratio and Inlet Blade Angle on System Performance at 60-Percent Power.

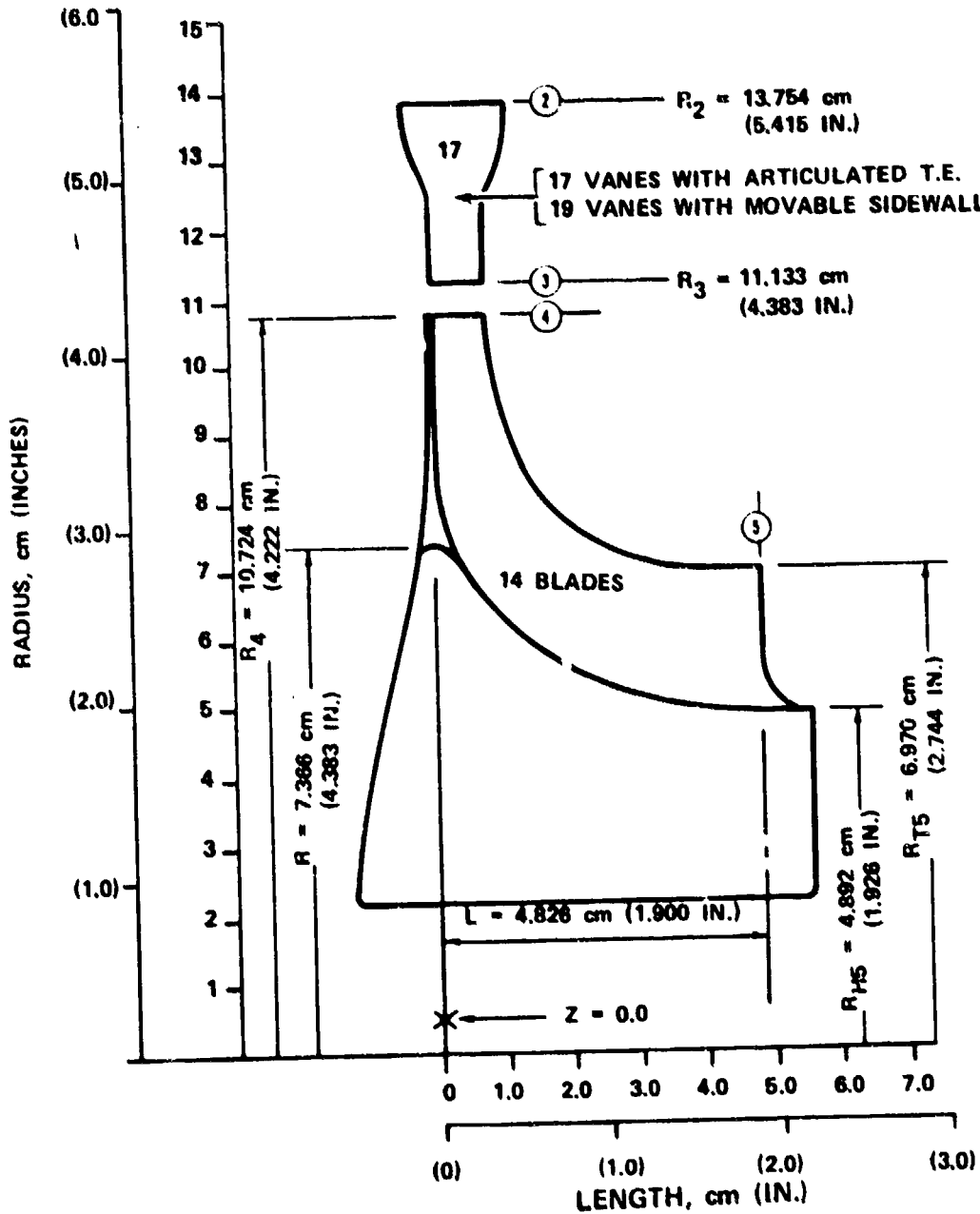


Figure 71. Selected Cooled Rotor, Meridional Flow Path
 at 1589K (2400°F), U_{T4} of 640 m/s (2100
 Ft/Sec) and 5969 rad/s (57,000 RPM).

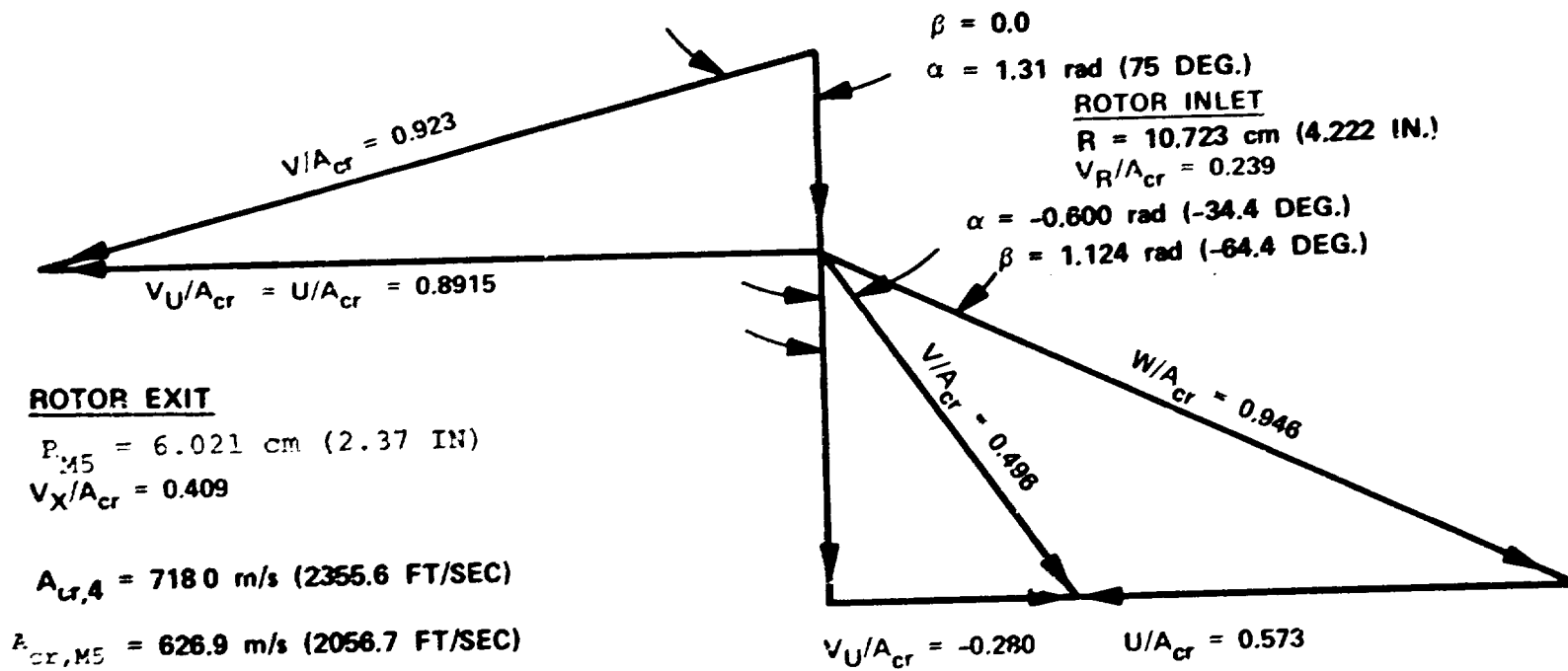


Figure 72. 1-Dimensional Vector Diagram for Selected Cooled-Stage Configuration, 100-Percent Power

TABLE VIII. SELECTED COOLED, VARIABLE-AREA RADIAL TURBINE STAGE CHARACTERISTICS.

Specific Stage Work, $\Delta H_m _{4-5}$	472.72 kJ/kg (203.27 Btu/lbm)
Stage Corrected Work, $\Delta H_{T/N} _{4-5}$	85.74 kJ/kg (36.87 Btu/lbm)
Compressor Discharge Temp, T_c	728.6K (851.8°F)
Compressor Discharge Pressure, P_c	1722.3 kPa (249.8 psia)
Mass Flow, \dot{W}	2.15 kg/s (4.73 lbm/sec)
Compressor Pressure Ratio, P_{r_c}	17:1
Rotor Inlet Mixed Temperature, T_4	1588.7K (2400°F)
Inlet Corrected Flow, $\dot{W}/\sqrt{\delta} _4$	0.3084 kg/s (0.680 lbm/sec)
Stage Total-to-Total Pressure Ratio, $P_{R_{T-T}} _{2-5}$	0.945
Stage Inlet Total Pressure, P_{T2}	1654.7 kPa (240.0 psia)
Inducer Tip Speed, U_{T4}	640 m/s (2100 ft/sec)
Rotor Inlet Blade Angle, β_B	0.1745 rad (10 degrees)
Rotational Speed, N	5969 rad/s (57,000 rpm)
*Stage Work Coefficient, λ_{STG}	1.154
*Rotor Inlet Work Coefficient, λ_4	1.000
*Rotor Exit Mean Work Coefficient, λ_{m_5}	-0.489
*Specific Speed, N_s	0.424 non-dimensionalized (54.64 rpm FT ^{3/4} /SEC ^{1/2})
*Reynolds Number, R_s	3.734×10^5
*Stage Reaction, R_{STG}	0.638
Exducer Tip-to-Inducer Tip Radius Ratio, R_{T5}/R_{T4}	0.650
Exducer Hub-to-Exducer Tip Radius Ratio, R_{H5}/R_{T5}	0.456
Rotor Exit Annular Area, A_5	77.4 cm ² (12.0 in. ²)
Number of Rotor Blades, N_B	14.0
Number of Vanes with Articulated Trailing-Edge ($N_{V_{ATE}}$)	17.0
Number of Vanes with Movable Sidewall, ($N_{V_{MSW}}$)	19.0
Rotor Exit Mean Swirl Angle, α_{M_5}	-0.6098 rad (-34.44 deg)
*Rotor Exit Mean Critical Velocity Ratio, V/A_{cr5}	0.496

*Values at 100-Percent Power

6.0 TASKS III AND IV - VARIABLE-AREA STATOR AERODYNAMIC AND MECHANICAL DESIGN

6.1 Detailed Aerodynamic Design Procedure

During the conceptual evaluation phase of the program (Task I), the four leading variable-area stator concepts were reduced to two: an articulated trailing-edge and a locally movable sidewall. Due to a lack of previous aerodynamic and mechanical experience with these concepts, it was concluded that a detailed design of each concept would be required before a final design could be recommended.

The detailed aerodynamic evaluation of the two variable-area stator concepts was based on a 2-phased numerical procedure. First, a preliminary evaluation of the flow pattern and the vane loading was obtained using the Katsanis stream-function approach⁽²⁵⁾. The stator geometry was simulated using the Katsanis 2-dimensional model. This analysis was an economical design tool for eliminating deficient configurations from those investigated during the detailed design phase. The stator geometrical configurations selected through this process were then used as an input in the second phase of the numerical analysis. In this phase, the stator flow field was analyzed on a 3-dimensional basis using a finite-element approach. The two solutions were then compared to verify the conclusions and justify the decisions made in the first phase.

6.2 Articulated Trailing-Edge Stator - Detailed Aerodynamic Design

Figure 73 is a schematic diagram of the articulated trailing-edge concept. Depending on the selected design point, the vane trailing-edge is rotated around the pivot point to either increase or decrease the cross-flow area. Since this rotation affects flow turning (and subsequently vane loading), it was important to examine the stator performance associated with different power settings once the design point was selected. The design-point power setting was based on a qualitative estimate of potential leakage, which appeared to be a major drawback of this mechanism.

The vane was first designed at the 100-percent power level with parallel sidewalls. The profile for this configuration is shown in Figure 74 for both the 60- and 100-percent power settings. The vane loadings for these settings were obtained through Katsanis blade-to-blade flow analysis, and are shown in Figure 75. As shown, considerable diffusion was associated with the excessive turning on the vane pressure-side and the reversed curvature along the suction-side at the 100-percent power level. Conversely, the vane performance at the 60-percent power level is characterized by

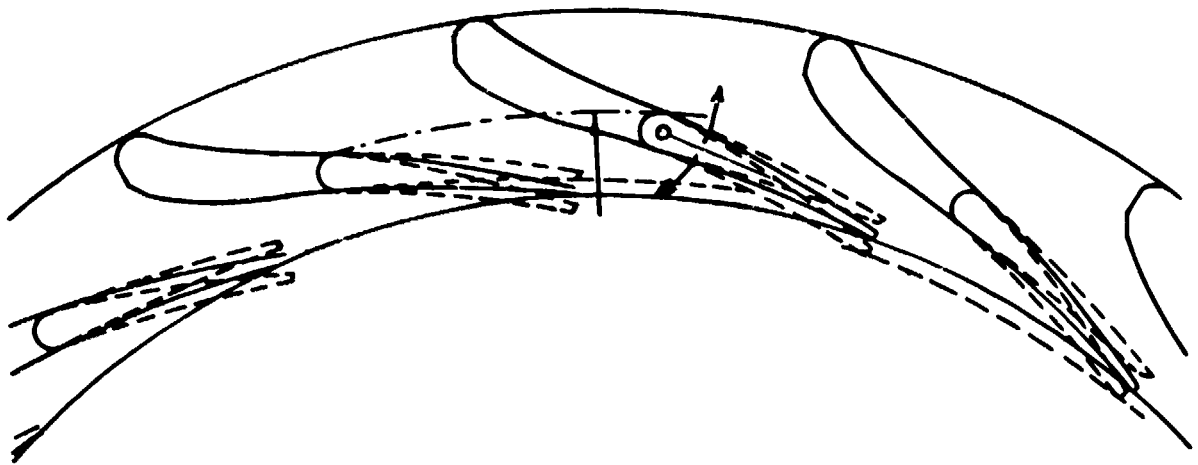


Figure 73. Articulated Trailing-Edge Vane Concept.

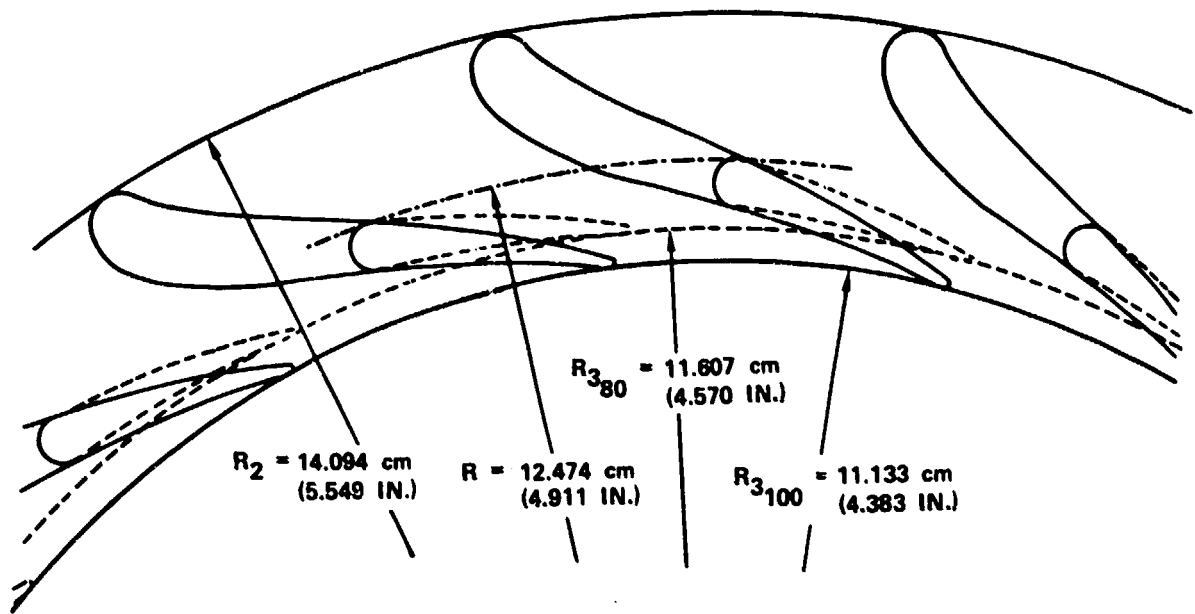


Figure 74. Articulated Trailing-Edge at 100-Percent Power Design Point (Rotated Closed at 60-Percent Flow).

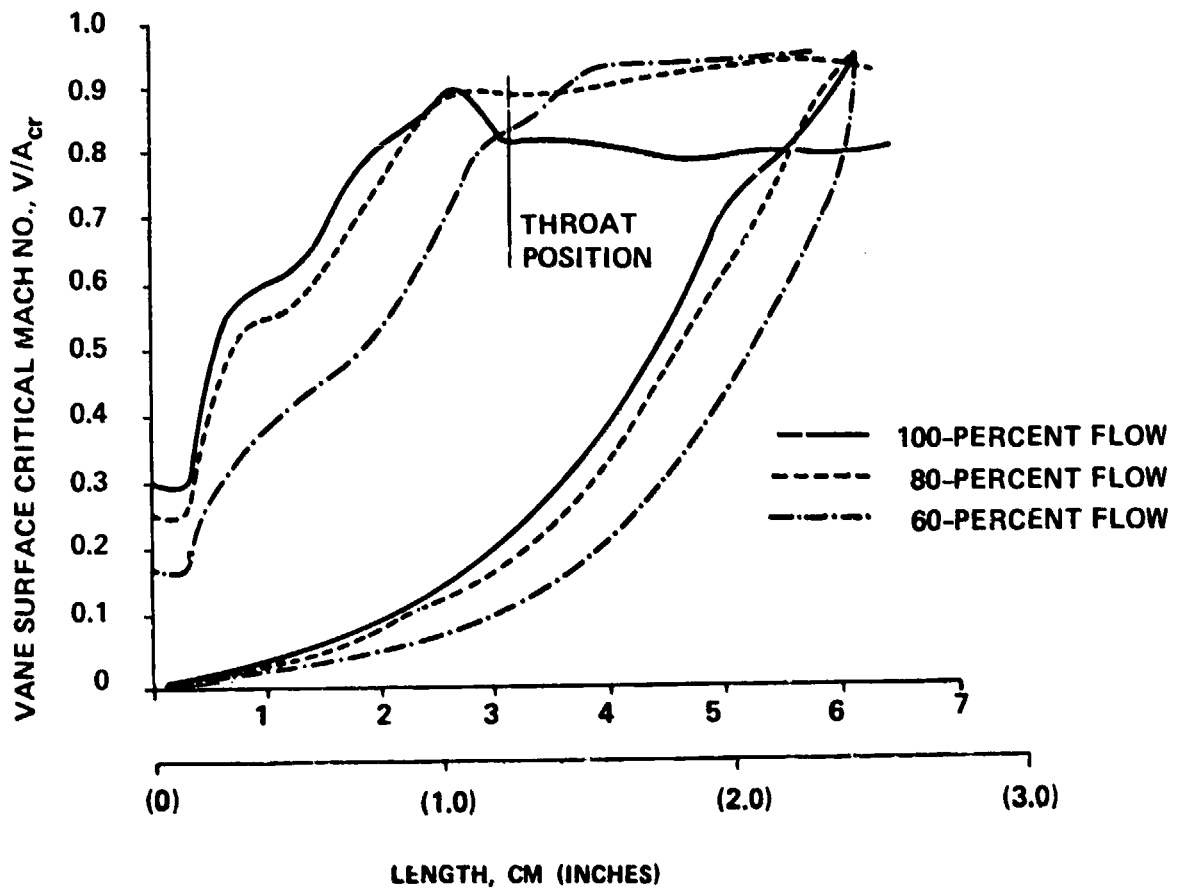


Figure 75. Articulated Trailing-Edge Configuration, Vane Velocity Distributions for 100-Percent Power Design Point (Stream-Function Solutions).

a significant increase in loading near the trailing-edge, which could lead to leakage problems.

Using the same parallel sidewall configuration, a 60-percent power design point was then considered (Figure 76). The basic problem incurred with this case was a relatively low loading of the vane leading edge, followed by a rapid increase in loading downstream (Figure 77). Again, the 100-percent power setting was associated with substantial diffusion over the suction side.

When the design point was shifted to 80-percent, satisfactory stator performance was achieved, and this power level was selected for the final configuration. The final vane profile is shown in Figure 78. This figure also shows the details of the trailing-edge in the two extreme power settings of 60- and 100-percent. Contoured sidewalls were selected for this design, as shown in the meridional view (Figure 79). This reduced the curvature at the stator inlet and minimized the inlet velocity gradients. The vane loadings at all three power levels are shown in Figure 80. This figure demonstrates that a more uniform loading over the required power spectrum is achieved in this case. Again, the diffusion incurred on the suction side at the 100-percent power level appeared to be unavoidable. However, this effect was comparatively reduced at the selected 80-percent design point.

6.3 Detailed Aerodynamic Design of the Movable Sidewall Stator

Although the articulated trailing-edge configuration was the primary candidate for a variable area stator, a locally movable sidewall mechanism was also studied. The advantages offered by this concept were primarily mechanical. For this configuration the stator vanes were single, stationary units. This provides more flexibility in the internal cooling flow design and improves structural support for the entire stator assembly. Moreover, if the sidewall seals were located outside the flow path, this would allow employment of a higher performance seal arrangement that could also be used for external cooling purposes. However, this design incurred high stator-exit dump losses at low power levels that were a major drawback in this case.

The simplest configuration in the movable-sidewall category was a purely translating sidewall mechanism. This configuration is shown in Figure 81. The abrupt enlargement at the movable sidewall exit in this configuration severely affects the loss levels at the rotor inlet, and consequently, stage efficiency. This was established from previous Garrett in-house rig test program using a symmetrical reduction in stator passage width. The program showed that a reduction of approximately 4 points in efficiency results from a 30-percent reduction in nozzle passage width, (with no sidewall leakage).

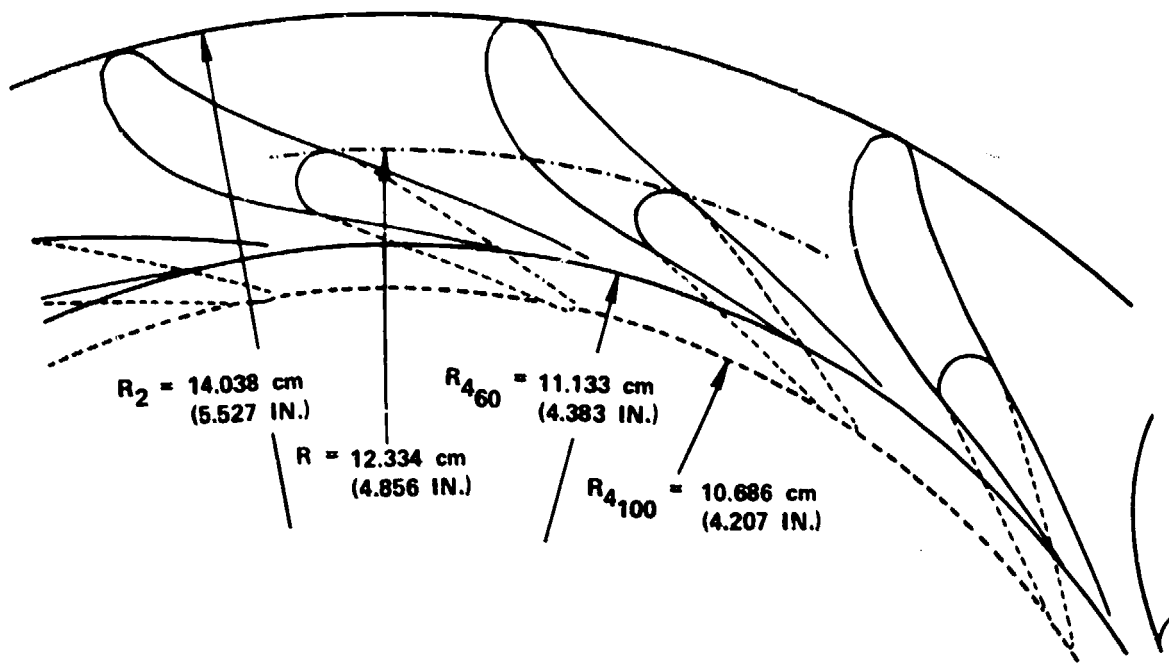


Figure 76. Articulated Trailing-Edge, 60-Percent Power Design Point (Rotated Open at 100-Percent Flow).

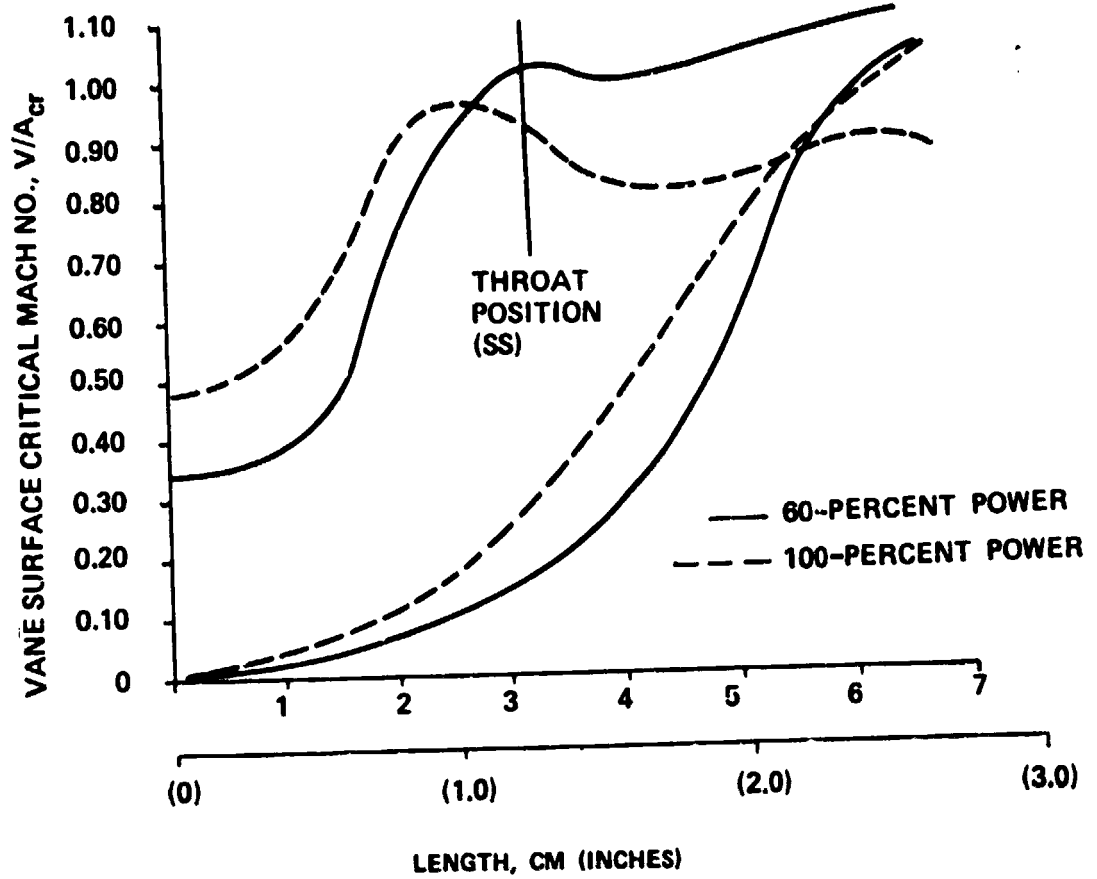


Figure 77. Articulated Trailing-Edge Configuration, Vane Velocity Distribution for 60-Percent Power Design Point (Stream Function Solution).

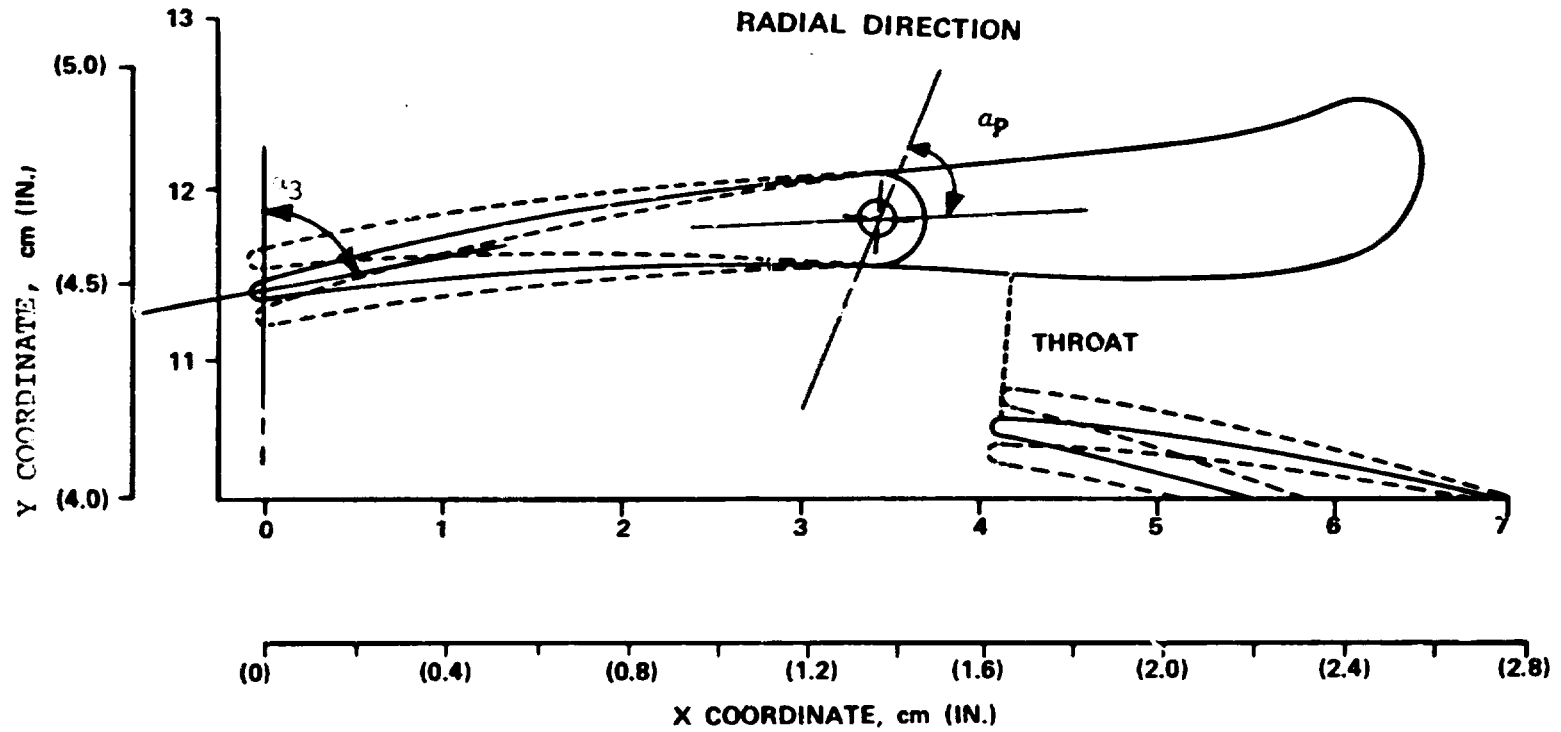


Figure 78. Final Articulated Trailing-Edge 17 Vane Profile Design for 80-Percent Power Design Point.

ALL UNITS ARE IN cm (IN.)

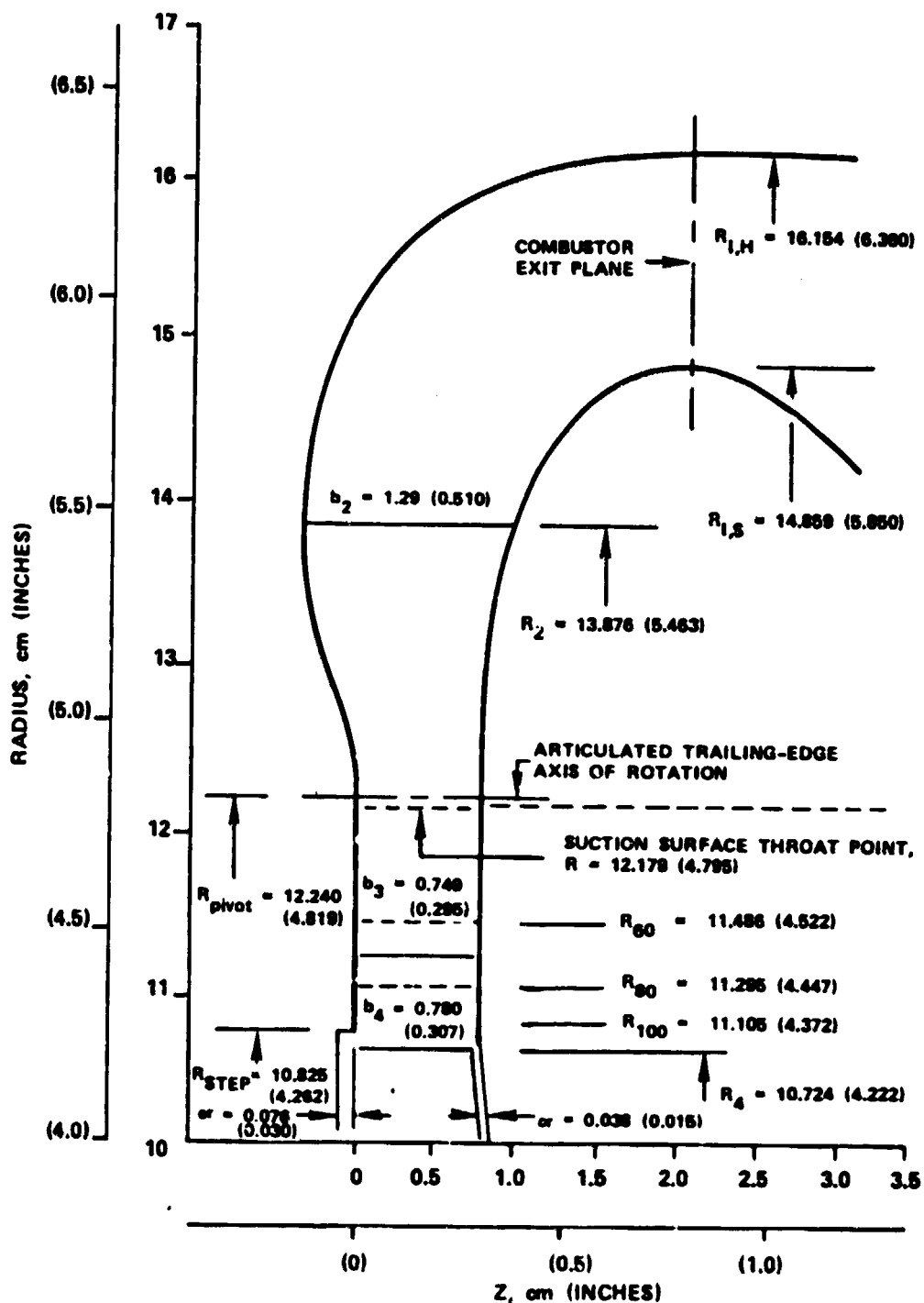


Figure 79. Articulated Trailing-Edge Concept, Final Stator, Inlet Meridional Geometry.

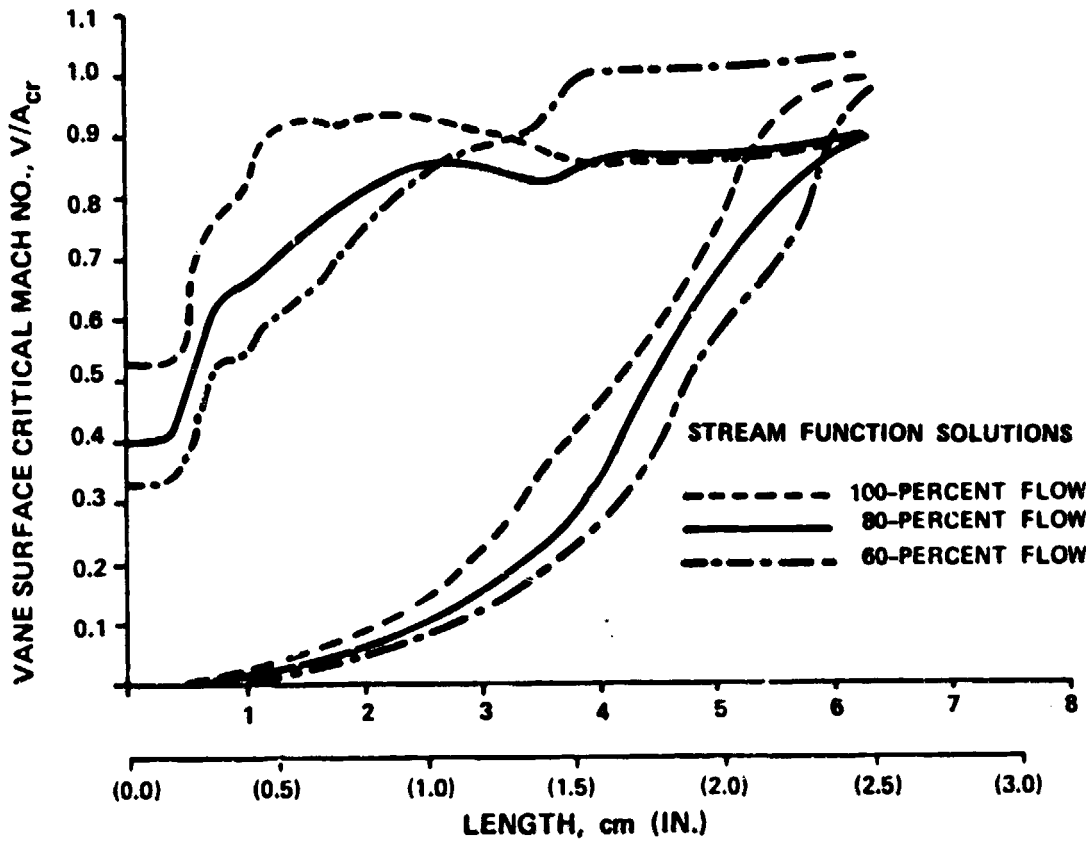


Figure 80. Vane Velocity Distribution for Final Articulated Trailing-Edge Stator Design (17 Vanes).

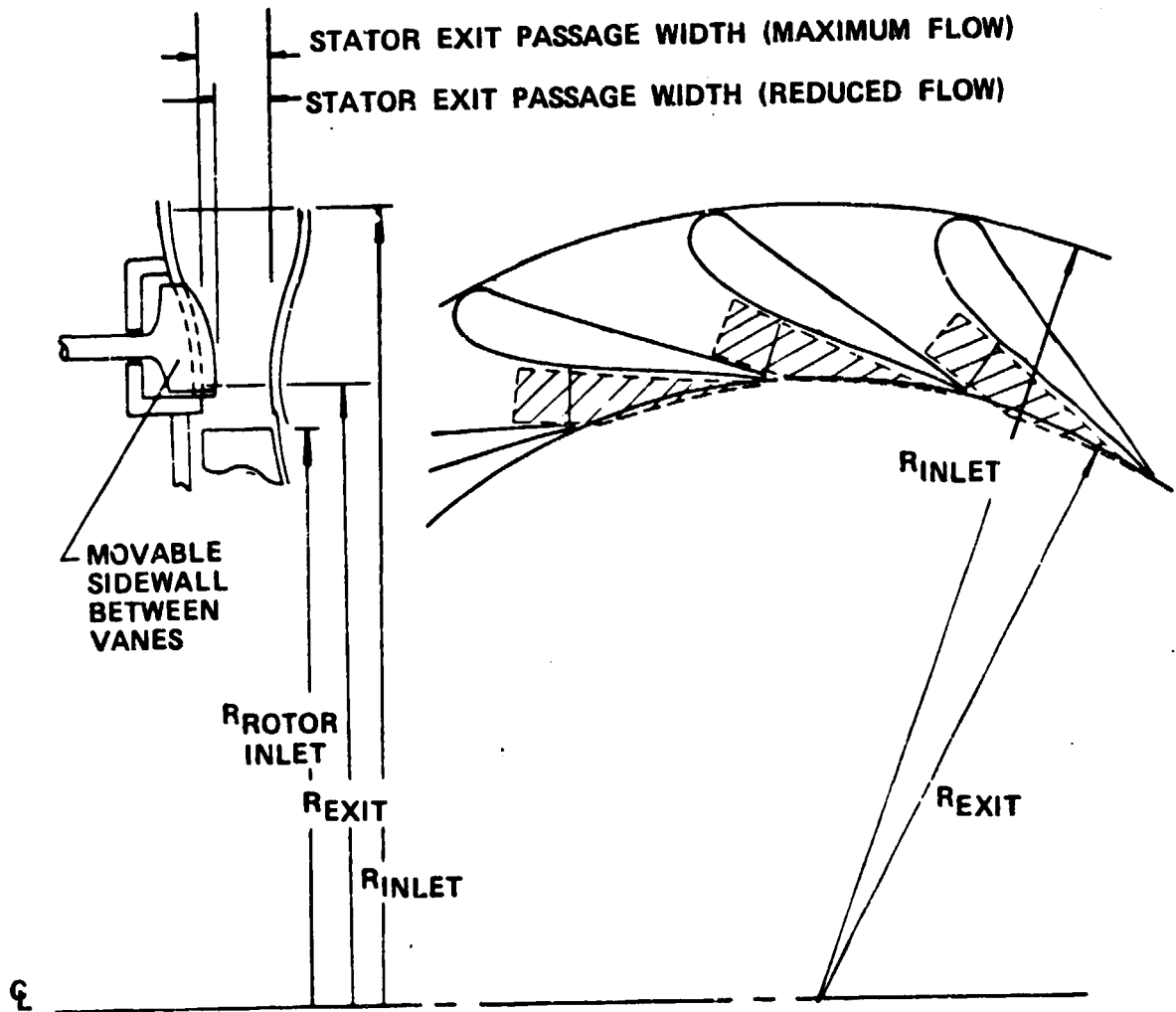


Figure 81. Movable Sidewall Original Configuration.

Two alternate approaches to the conventional translating sidewall have since been investigated by Garrett. The first approach is defined as a purely rotating (pivotal) sidewall mechanism and is shown in Figure 82. This figure shows a blade-to-blade view of a typical flow passage, as well as the rectangular segment over which the rotating insert contacts the stator flow. Also shown is a section in a plane parallel to the stream-wise edges of the insert and perpendicular to the pivotal axis. This section depicts the sidewall movable segment at the extreme high- and low-power level positions. The second approach investigated was a rotating-translating sidewall mechanism (Figure 83). As the term implies, change in the cross-flow area is now achieved through a combination of insert rotation and translation. In this mechanism, a line contact between the insert and sidewall is maintained over the entire power range at the insert front and rear edges. Examination of Figures 82 and 83 reveals that the stator exit sudden expansion is replaced by a smooth ramp in the vaneless space. Clearly, the rotating-translating sidewall configuration offers smoother transition in the passage width upstream from the throat. Therefore, this mechanism appears to maintain a more desirable flow behavior in this region.

Several important aspects were revealed in the preliminary geometric and aerodynamic analysis of the two configurations. In both cases, the sides of the movable segment were parallel. This was required to avoid binding during actuation. In addition, to minimize gaps between the vane and the movable segment, the vane contour was made straight over the region where the insert extends. This required a local thickness increase, as well as relatively high wedge angles at the trailing-edge (Figure 84). These configurations also required an increase in vaneless space to avoid rotor-tip interference.

The vane configuration shown in Figure 84 corresponds to the optimized profile. This configuration was the result of a detailed analytical study in which loadings corresponding to different blade geometries were evaluated. A Katsanis stream-function flow analysis was again used to obtain the blade loading for each iteration. The passage width was simulated in the program input data by using an average value at the different radial locations in both the vaned- and unvaned-stator portions. The objectives were to minimize the velocity peaks along the vane surface and to obtain a monotonically accelerating channel.

Figure 85 shows the vane loading at both the 100- and 60-percent power levels. As indicated on the figure, the power reduction was achieved through a purely rotating and a rotating-translating sidewall mechanism. This figure shows that despite the irregular geometry in the 60-percent flow configuration, the flow is continuously accelerated in both cases. However, the purely rotating sidewall option incurred a slight local diffusion

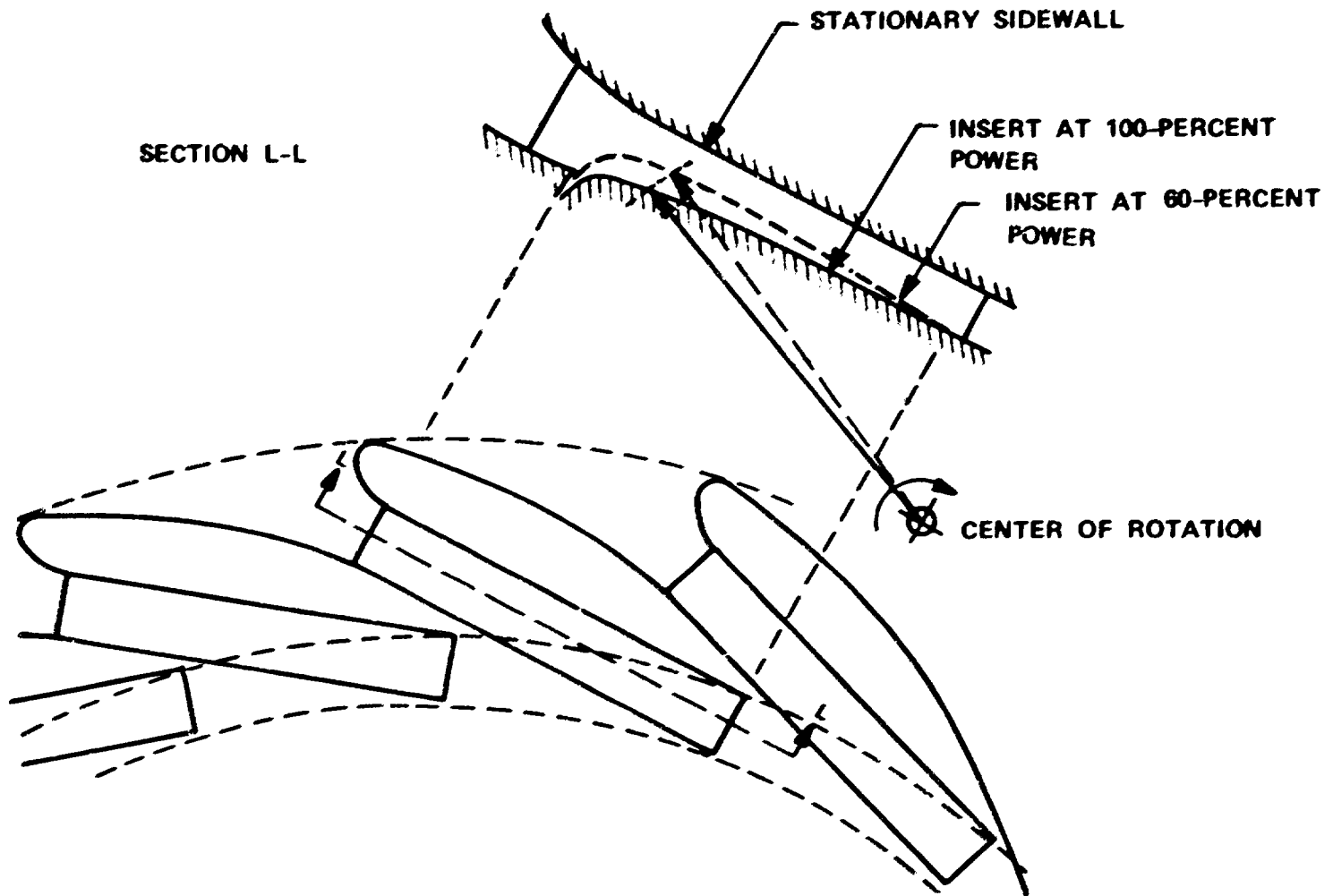


Figure 82. Movable Sidewall Configuration (Purely Rotating Insert) Schematic Diagram.

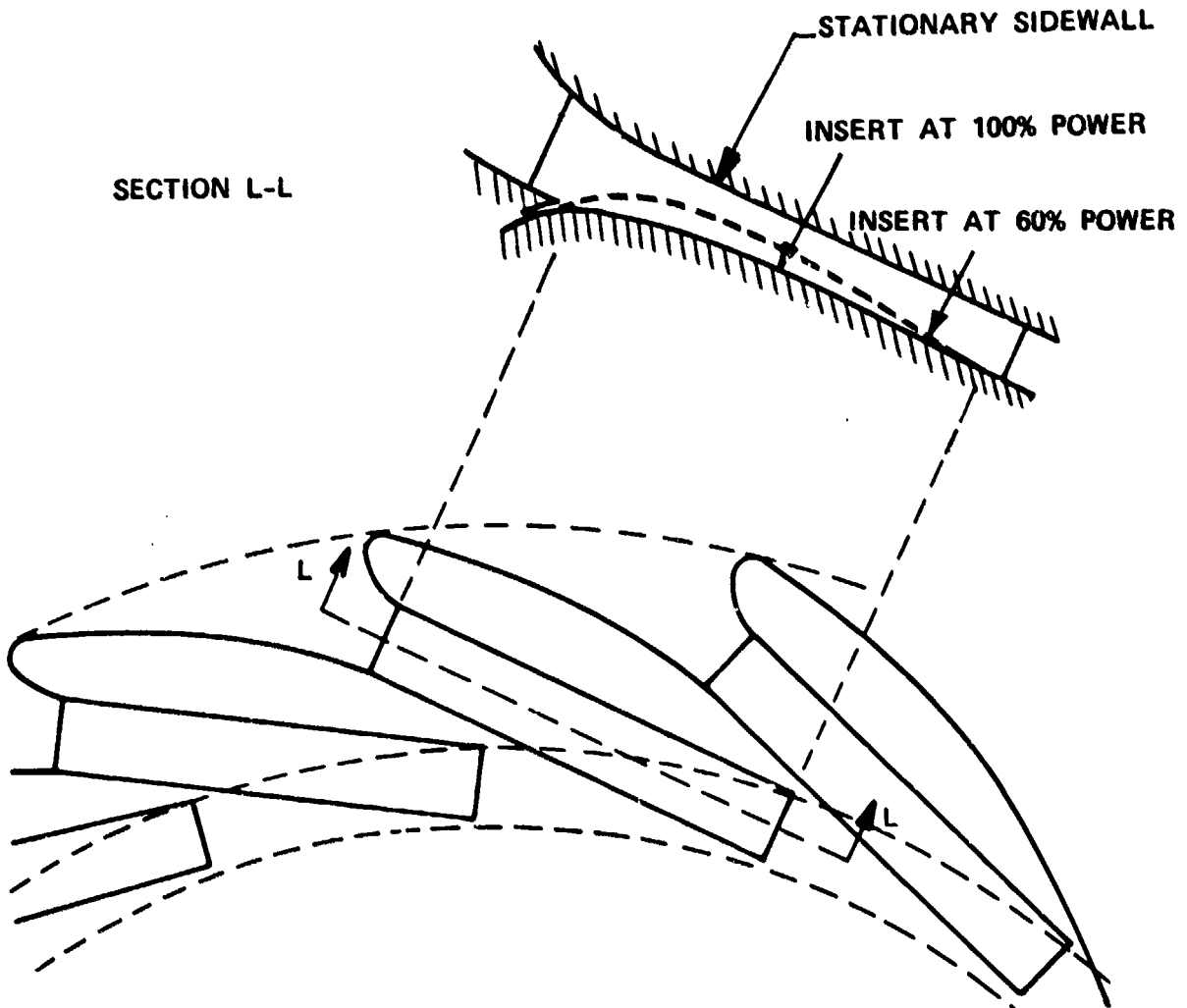


Figure 83. Movable Sidewall Configuration (Rotating-Translating Insert), Schematic Diagram.

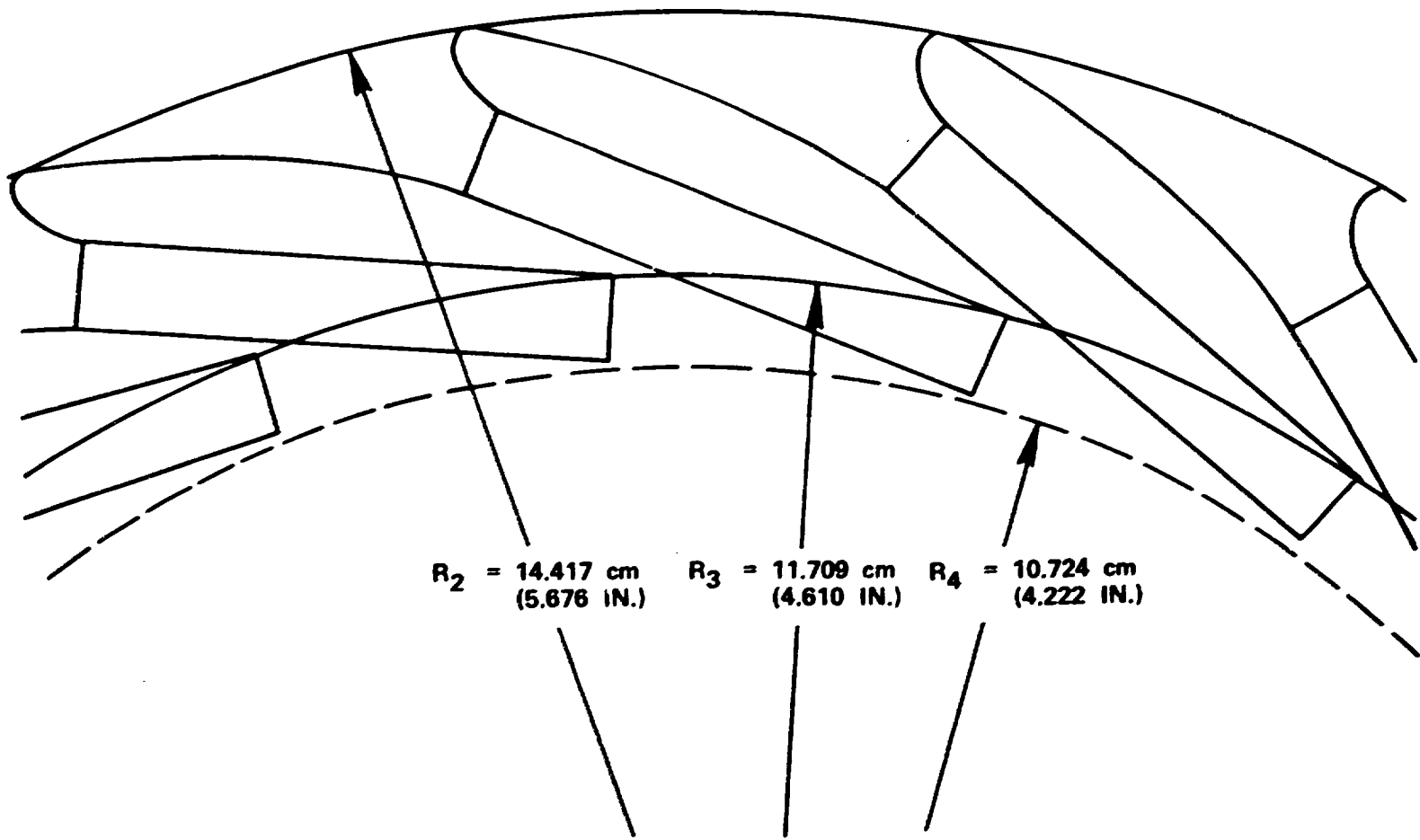


Figure 84. Final Vane Profile, Movable Sidewall Concept.

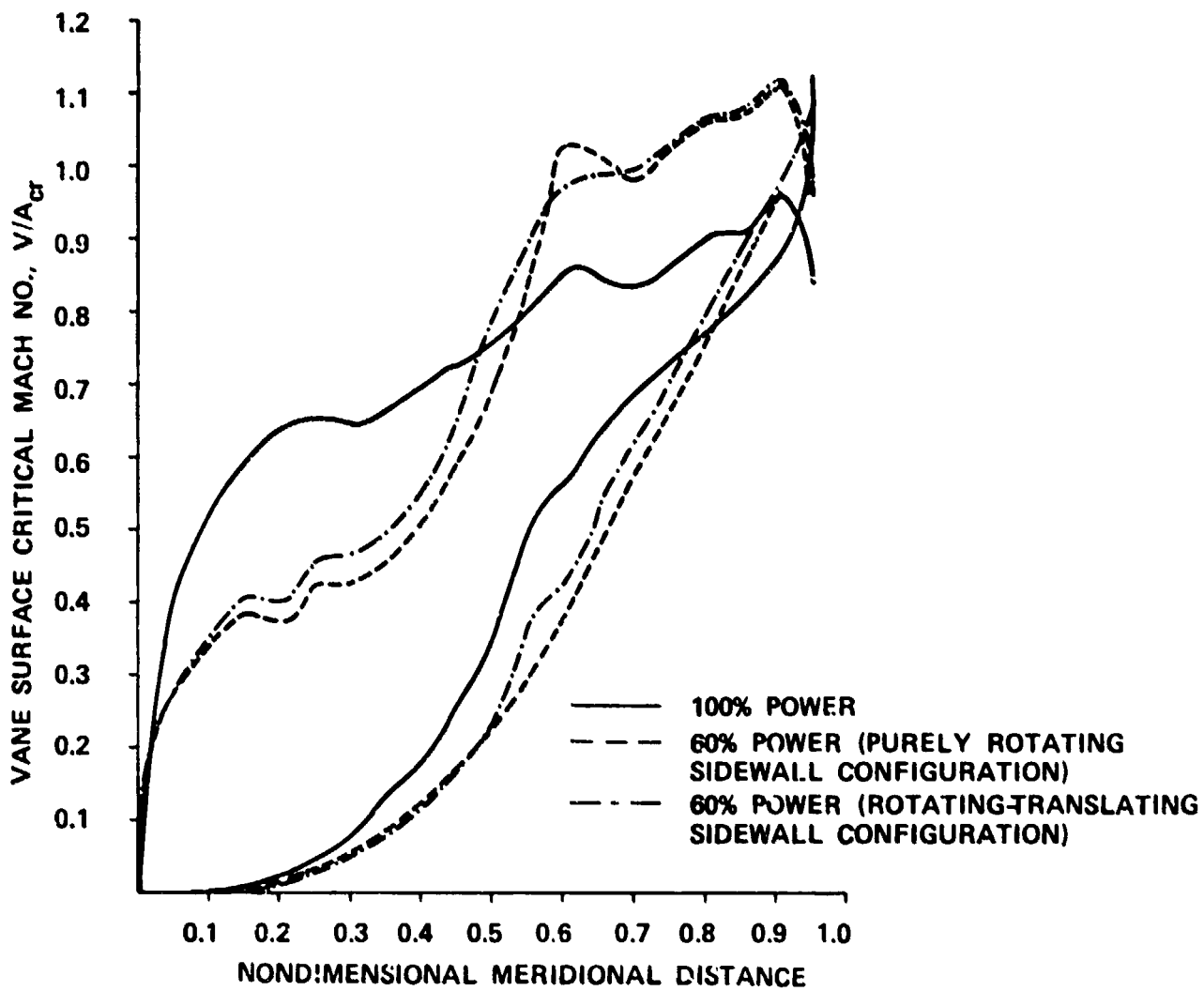


Figure 85. Movable Sidewall Stator Vane Velocities with 19 Vanes (Stream-Function Solution).

on the vane suction side when compared with the rotating-translating sidewall option. Nevertheless, the closeness of the loading characteristics in both cases makes selection of one mechanism over the other difficult. The final vane design parameters for both the articulated trailing-edge and locally movable sidewall variable-area stator concepts are presented in Table IX. A more accurate description of the flow field for both cases was obtained through a 3-dimensional, finite-element flow analysis, in which the geometrical details of these configurations were rigorously simulated.

6.4 Stator Flow Field - 3-Dimensional, Finite-Element Analysis

The stator flow field that corresponded to each stator configuration was first analyzed using the blade-to-blade, stream-function approach developed by Katsanis. This approach is based on the use of a finite-differencing method to solve the flow-governing equations along the blade-to-blade stream surface and assumes an irrotational flow. Thus formulated, this approach does not provide a rigorous basis for handling a 3-dimensional flow region. This disadvantage was a source of uncertainty -- particularly in cases where the stator sidewalls were geometrically complicated, 3-dimensional surfaces (such as the locally movable sidewall configuration). Furthermore, an external constraint in the form of a specified flow exit angle is required by the Katsanis approach to yield a unique solution. This angle is not generally known in advance and the correct value can be evaluated only through a trial-and-error process.

To overcome the geometrical and analytical difficulties involved in handling flow fields in 3-dimensional passages of turbomachines, Garrett has developed a finite-element approach particularly suitable for this problem. This approach combines the numerical advantages inherent in the finite-element technique with simplicity in specifying the flow exit conditions.

6.4.1 Background

The finite-element method is a process through which a continuum with infinite degrees of freedom can be approximated by an assemblage of subregions called elements. In each element, a finite number of discrete field variables are utilized as degrees of freedom. Each of these subregions interconnects with others in a way similar to discrete structural assemblies. Within each element, an approximate solution is constructed in terms of a number of unknown parameters. The latter consists of the field variable nodal values and may include derivatives and/or other characteristic variables. A set of algebraic equations is then derived on an element basis, in accordance with an integral statement of the

TABLE IX. FINAL VANE DESIGN FOR SELECTED VARIABLE-AREA STATOR CONCEPTS.

Design Parameters	Articulated Trailing-Edge Concept (800 Power Design Point)	Rotating-Translating Movable Sidewall Concept (1000 Power Design Point)
Number of Vanes, N_V	17	19
Inlet Radius, R_2 , cm (In.)	13.876 (5.463)	14.417 (5.676)
Exit Radius, R_3 , cm (In.)	11.295 (4.447)	11.709 (4.610)
Inlet Flow Angle, α_2 , radians (Degrees)	0	0
Exit Flow Angle, α_3 , radians (Degrees)	1.366 (78.320)	1.307 (74.900)
Inlet Vane Angle, α_{2V} , radians (Degrees)	0.175 (10.000)	0.244 (14.000)
Exit Vane Angle, α_{3V} , radians (Degrees)	1.333 (76.390)	1.262 (72.320)
Radial Chord, C_R , cm (In.)	2.580 (1.016)	2.708 (1.066)
Leading-Edge Thickness, T_{N_2} , cm (In.)	0.737 (0.290)	0.533 (0.210)
Trailing-Edge Thickness, T_{N_3} , cm (In.)	0.102 (0.040)	0.102 (0.040)
Trailing-Edge Tangential Thickness, T_T , cm (In.)	0.432 (0.170)	0.335 (0.132)
Trailing-Edge Spacing, S_{P_3} , cm (In.)	4.178 (1.644)	3.871 (1.524)
Trailing-Edge Tangential Blockage, (T_T/S_{P_3}) , cm (In.)	0.264 (0.104)	0.220 (0.087)
Maximum Vane Thickness, $T_{N_{MAX}}$, cm (In.)	0.826 (0.325)	0.826 (0.325)
Throat Dimension, "O", cm (In.)	0.823 (0.324)	0.909 (0.358)
Inlet Passage Width (b_2), cm (In.)	1.295 (0.510)	1.295 (0.510)
Exit Passage Width (b_3), cm (In.)	0.749 (0.295)	0.749 (0.295)
Critical Mach No., $V/A_{cr,3}$ (Outside Trailing-Edge)	0.960	0.843

problem under consideration. The final system of equations is obtained by "patching" the elements together in such a way that contributions involving the same parameter are properly added.

The foremost advantage offered by the finite-element method is its efficiency in handling regions with geometrically irregular boundaries. These usually are problems where the field variable gradients are high and often require a grid of varying mesh size. This requirement is not easily handled through conventional finite-difference methods, since complicated schemes⁽²⁶⁾ are often involved. However, the finite-element analysis can proceed using arbitrarily constructed subdomains with, if desired, different order approximate solutions. These can be properly placed in the domain of interest to reflect the anticipated gradients of the field variable. Another advantage of the finite-element method is the flexibility and simplicity of specifying arbitrary boundary conditions along curved boundaries.

The application of the finite-element method to problems of potential fluid flow has been reported in several references^(27,28). In the two-dimensional flow problems, either a stream-function or a velocity-potential formulation is adopted. The governing equation respectively reflects the law of mass conservation or the irrotationality condition. A different set of boundary conditions is associated with each case. In general, each set can be a basis for selecting one formulation over the other in terms of the solution accuracy and the rate of convergence⁽²⁸⁾. Three-dimensional applications of the method have also been reported by, among others, Prince⁽²⁹⁾ and Laskaris⁽³⁰⁾.

6.4.2 Analysis and Program Description

The finite-element flow analysis developed by Garrett is applicable to the transonic flow field in the blade-to-blade channel of the radial stator. This analysis is based on the assumption of a steady, inviscid, and shockless flow with localized supersonic regions. The analysis follows Galerkin's weighted-residual approach⁽³¹⁾ combined with linear tetrahedral elements. With the velocity potential as the primary field variable, the flow-governing equation is linearized in each iteration using the density field obtained from the preceding iteration until convergence is achieved. This approach is numerically stable over a range of Mach numbers, that extends to slightly transonic flow regimes. The circulation around the blade is introduced in the finite-element formulation as a field variable to be evaluated in the final solution process. As a result, a unique distribution of the flow exit angle is obtained that is not necessarily uniform. At this point, the analysis deviates from conventional analyses in which the exit angle is externally imposed a priori. A detailed description of this analysis is available^(32,33).

A finite-element discretization model is generated in the program as part of the computational process (Figure 86). The characteristics of the generated model can be controlled by the input parameters and provides a geometrical description of the stator blade and sidewalls for each case, as well as the desired number of blade-to-blade, inlet-to-exit, and sidewall-to-sidewall stations.

6.4.3 Application of the Finite-Element Flow Analysis to the Variable Geometry Stator

The finite-element analysis described in the preceding paragraphs was used to investigate the inviscid flow field in the two variable-area radial stator concepts (i.e., the articulated trailing-edge and the locally movable sidewall configurations). The results were then compared to those obtained through the Katsanis analysis. For each case considered, a 3-dimensional, finite-element model was established using four layers of elements between the stator sidewalls. Figures 87 and 88 show the articulated trailing-edge, and Figures 89 through 91 show the locally movable sidewall configurations. At the 50-percent power setting, the locally movable sidewall becomes a 3-dimensional surface. To illustrate the change in the sidewall spacing in this case, different sections in the flow passage are shown in the last two figures. These sections were taken along the dotted lines, as indicated in the X-Y views of the finite-element models. The rectangular region of the sidewall, which is the X-Y projection of the rotating and rotating-translating inserts is also shown. The contours of the stator axial widths are within this rectangle and are plotted in Figures 92 and 93. These figures further illustrate the reduction of the passage axial width, when compared to 0.7407-cm (0.2916-in.) design value in the vaneless stator portion, and an average value of 0.94 cm (0.37-in.) upstream of the insert. Figure 94 shows the blade-to-blade view in each stator configuration along with the station designation used for the purpose of discussing the numerical results later in this section.

After comparing the finite-element results with those obtained with the Katsanis analysis, the flow exit angle in the latter analysis was corrected to the average value obtained in the finite-element solution and the 2-dimensional program rerun. This established a nearly unified basis for comparison. More importantly, in cases where the exit angles were significantly different from the values obtained in the finite-element solution, the Katsanis analysis was repeated to verify the conclusions drawn in the preliminary design step (where approximate values were used).

Results of the finite-element analysis for the articulated trailing-edge configuration are shown in Figures 95 and 96. The final Katsanis loading corresponding to the 100-percent power setting is shown in Figure 95 for comparison. Since the sidewalls

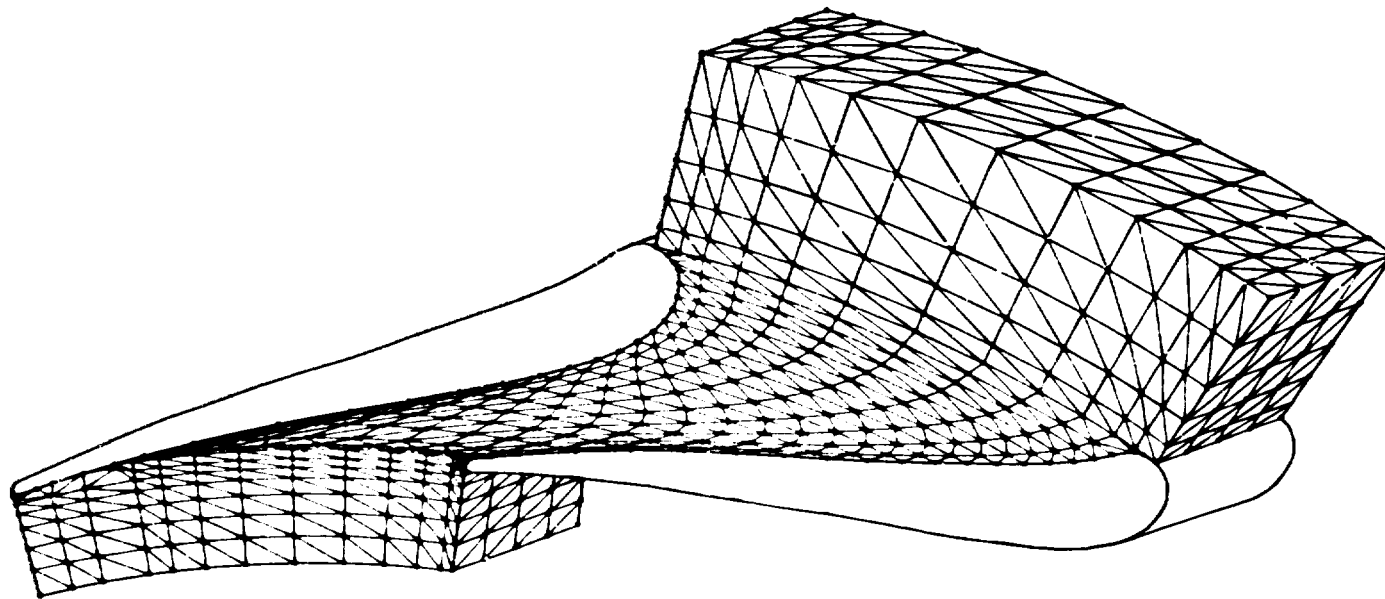


Figure 86. Stator Finite-Element Analysis Discretization Model.

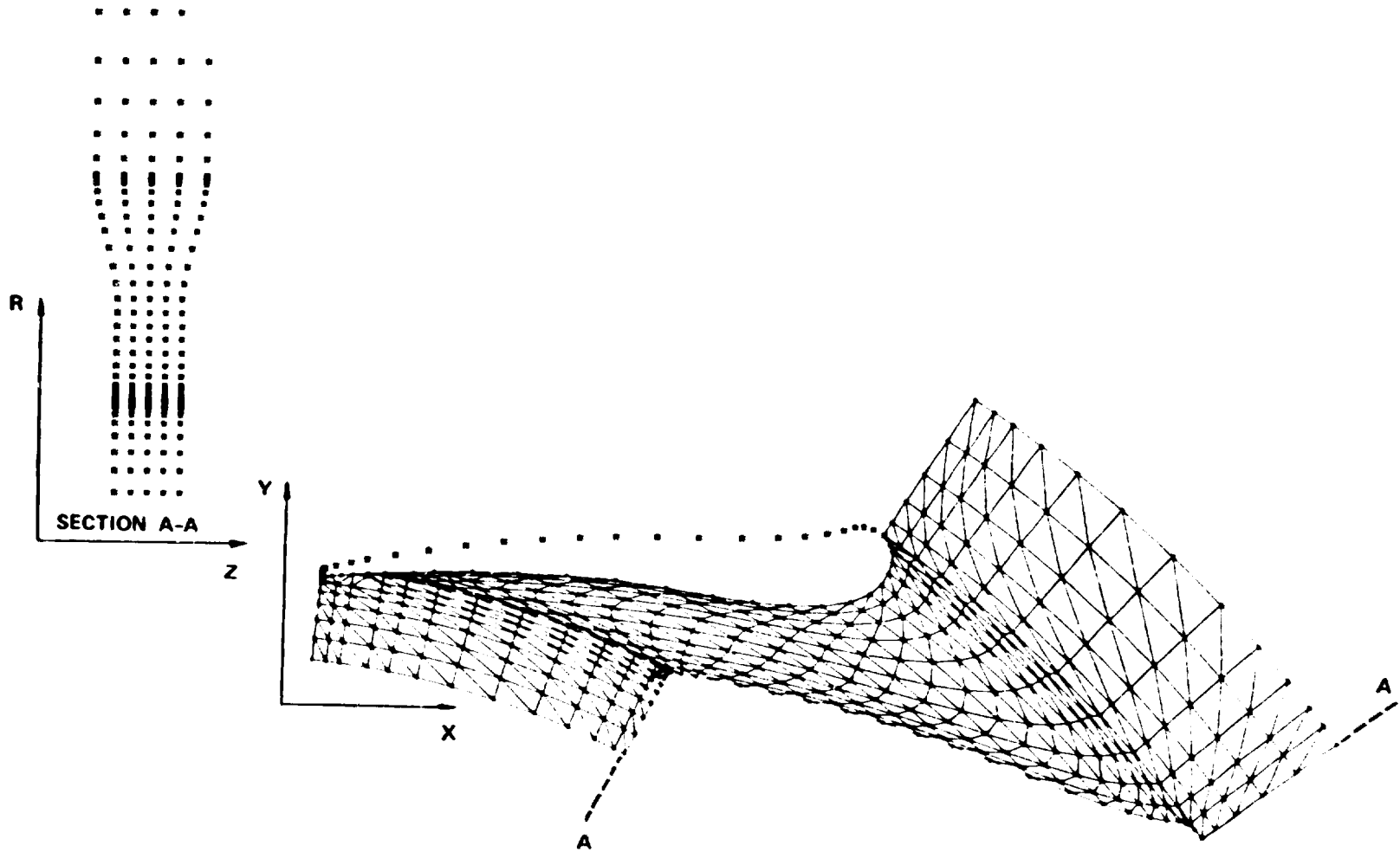


Figure 87. Articulated Trailing-Edge Configuration, 60-Percent Power Setting, 80-Percent Power Design Point.

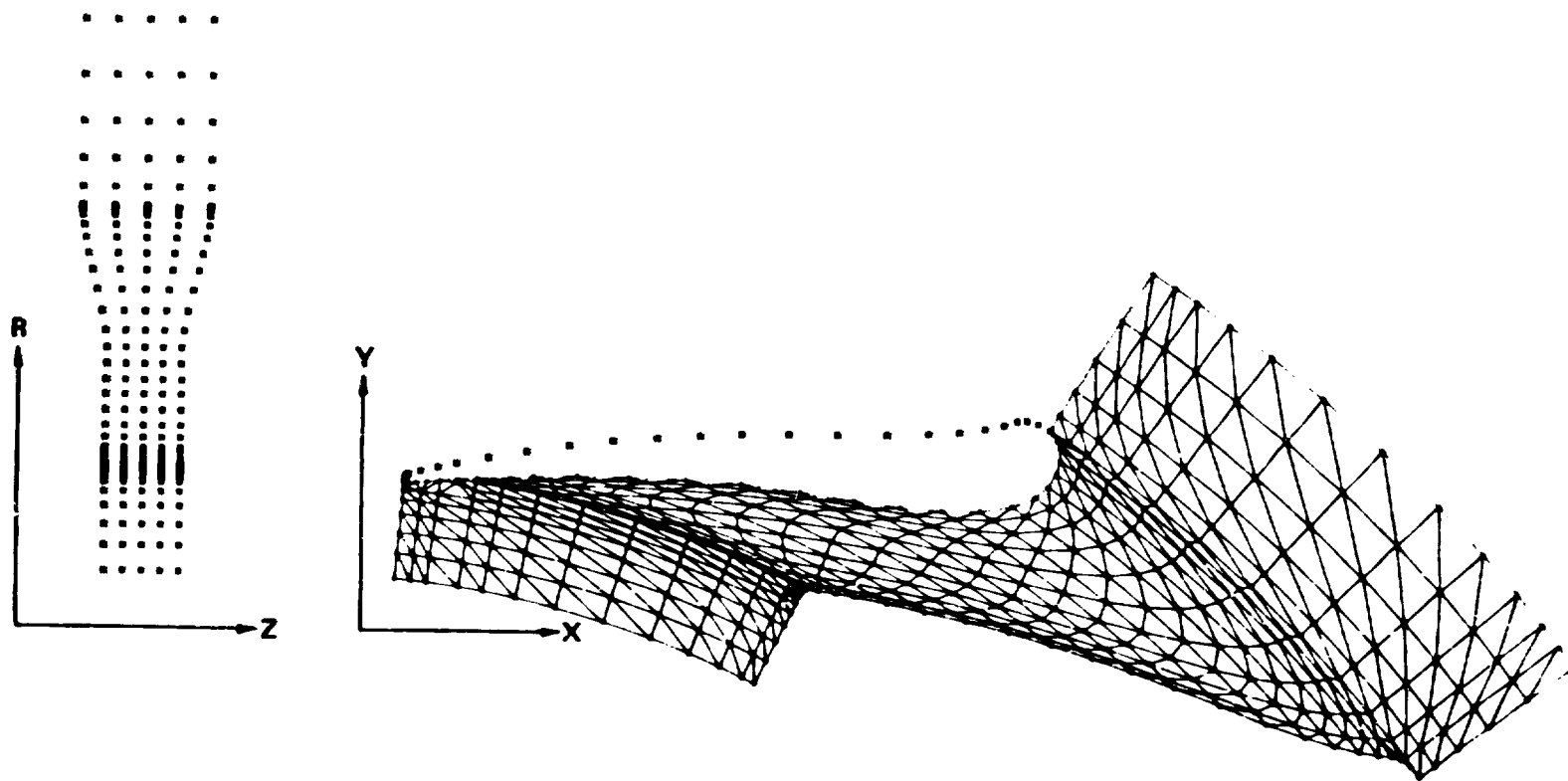


Figure 88. Articulated Trailing-Edge Configuration, 100-Percent Power Setting, at 80-Percent Power Design Point.

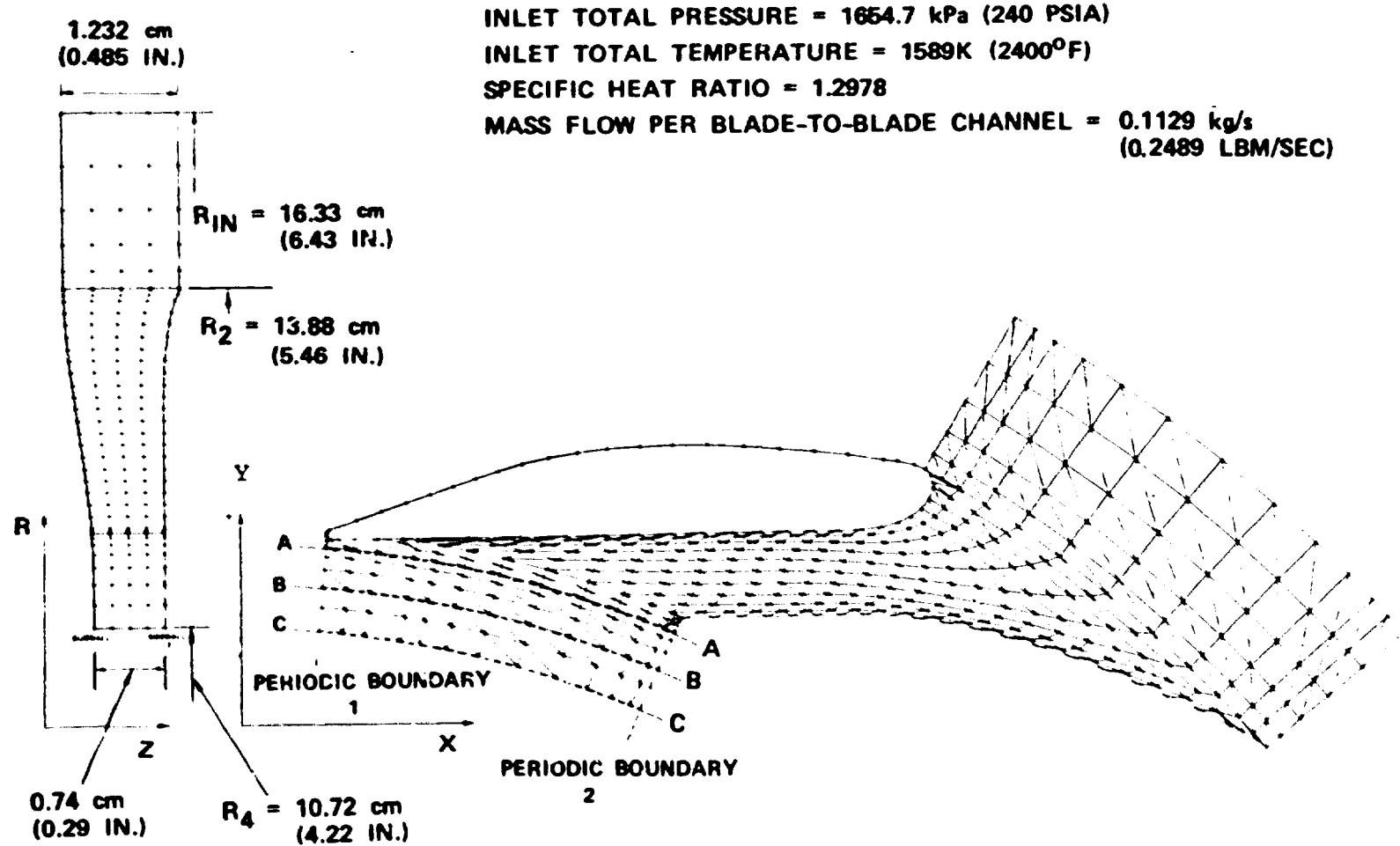


Figure 89. Finite-Element Model for Locally Movable Sidewall Configuration, 100-Percent Flow Geometry.

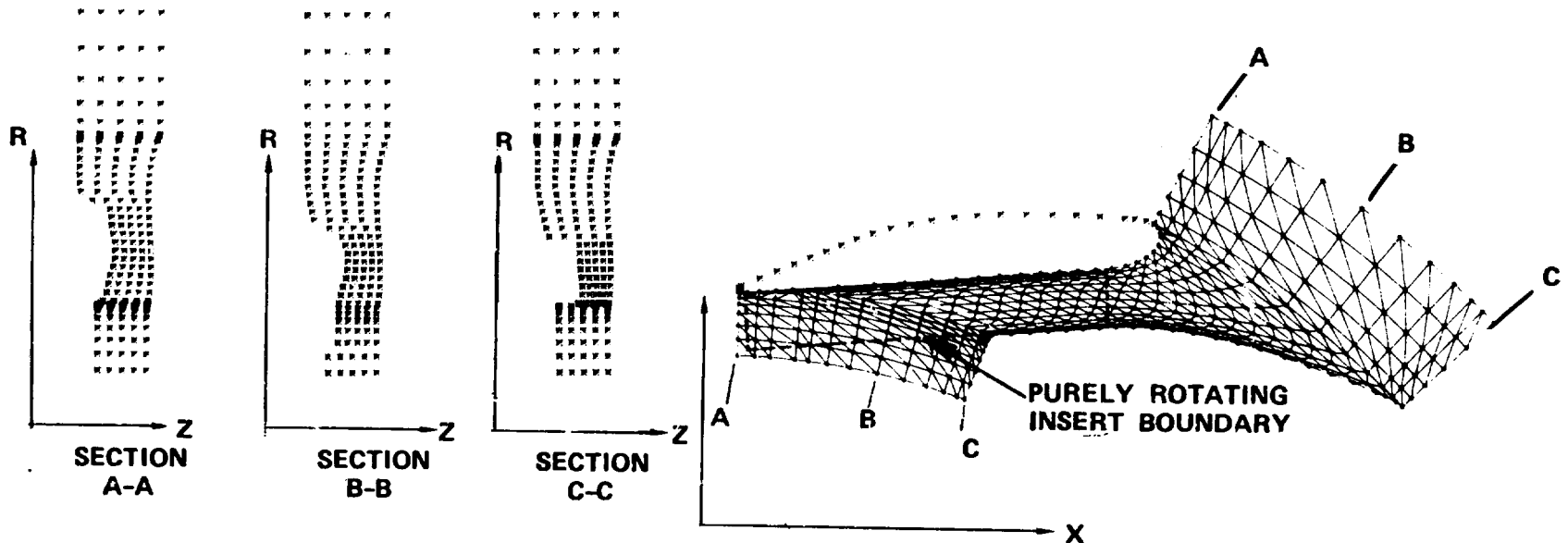


Figure 90. Finite-Element Model for Movable Sidewall Configuration, (Purely Rotating Insert) at 60-Percent Power Setting.

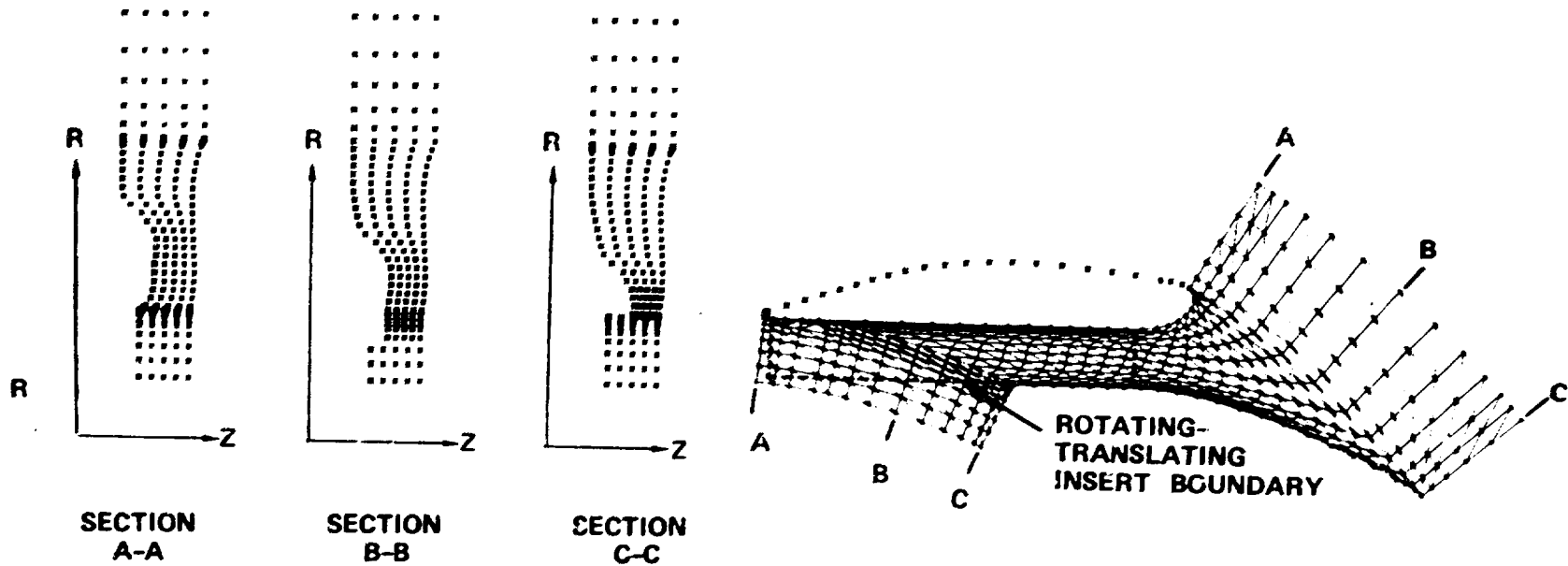


Figure 91. Finite-Element Model for Movable Sidewall Configuration, (Rotating-Translating Insert) at 60-Percent Power Setting

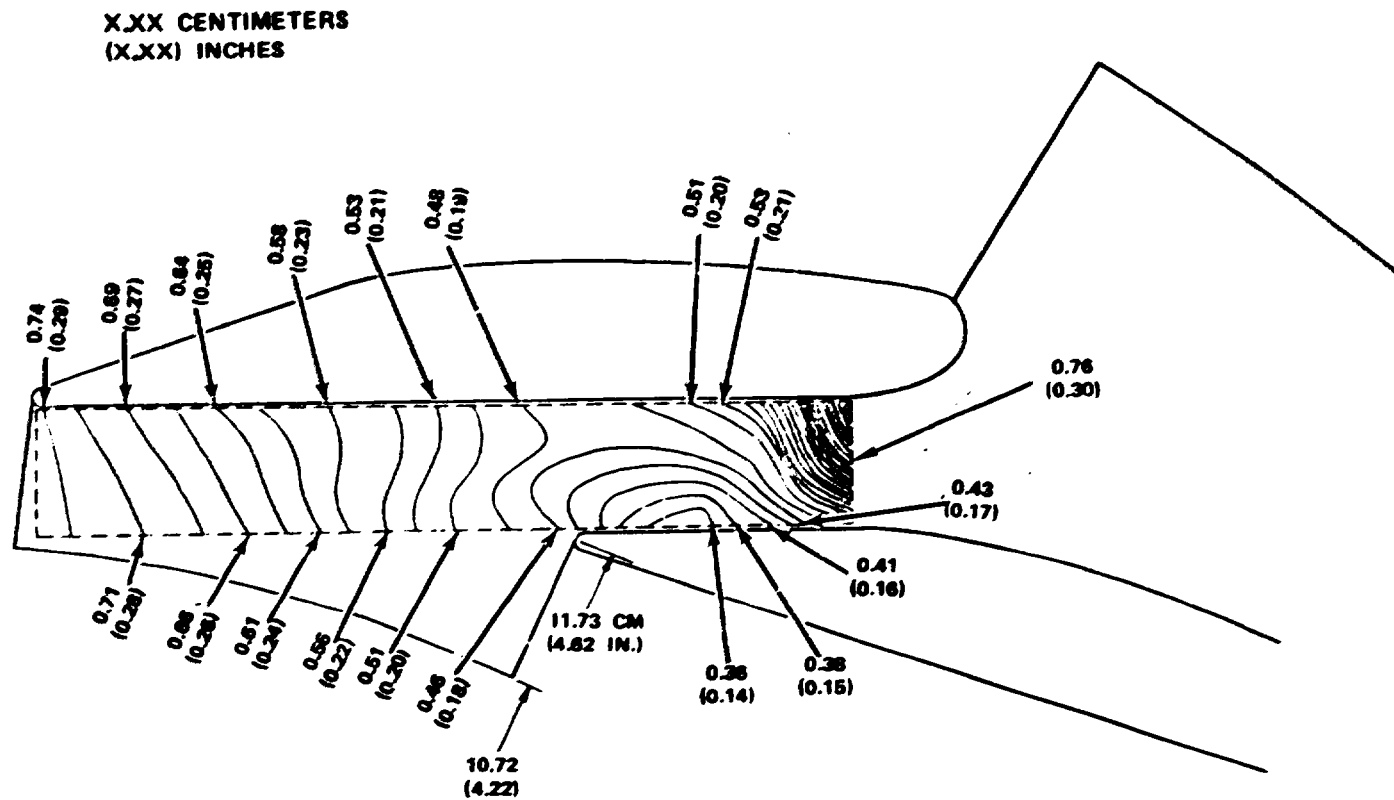


Figure 92. Contours of the Flow Passage Axial Width within the Purely Rotating Insert at 60-Percent Flow Setting.

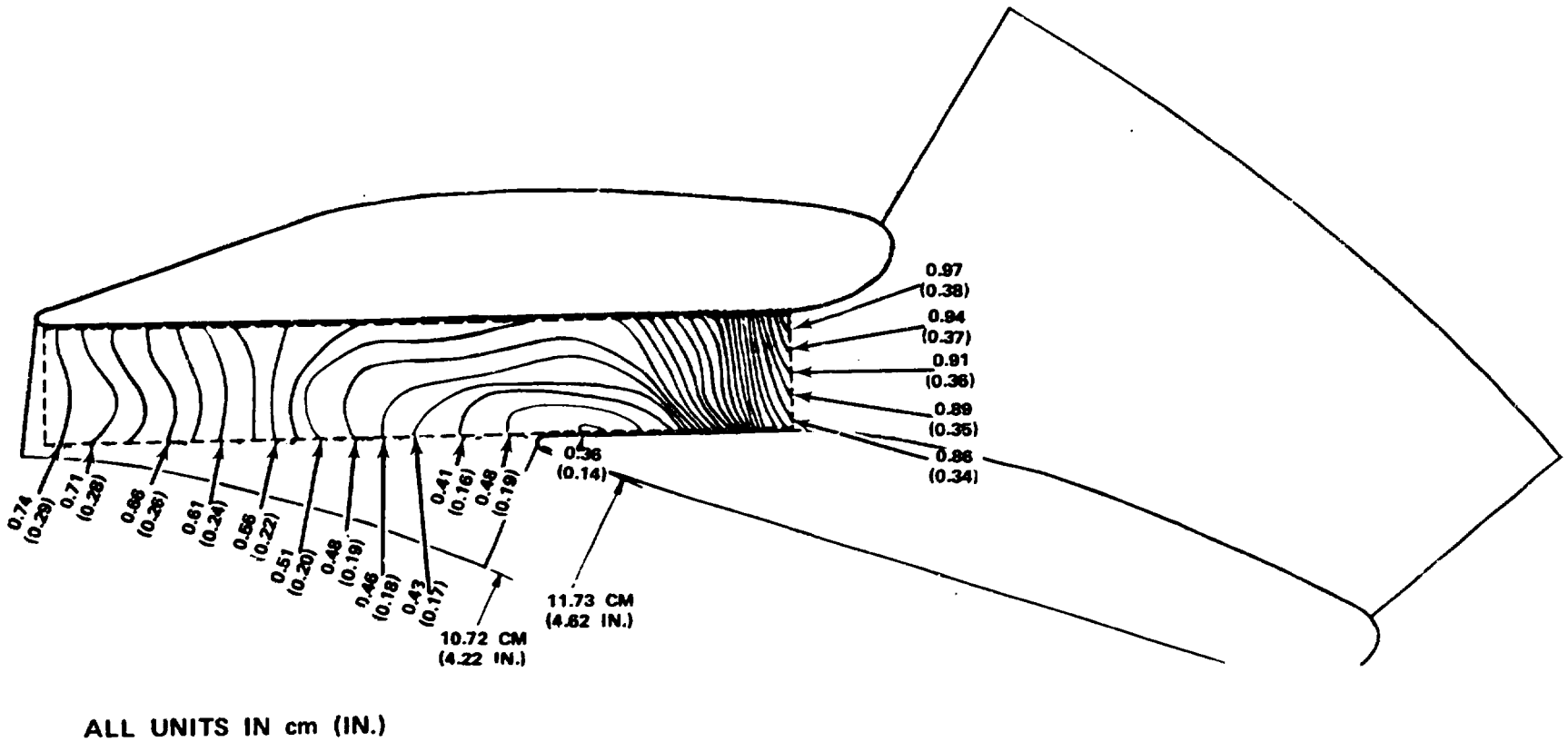
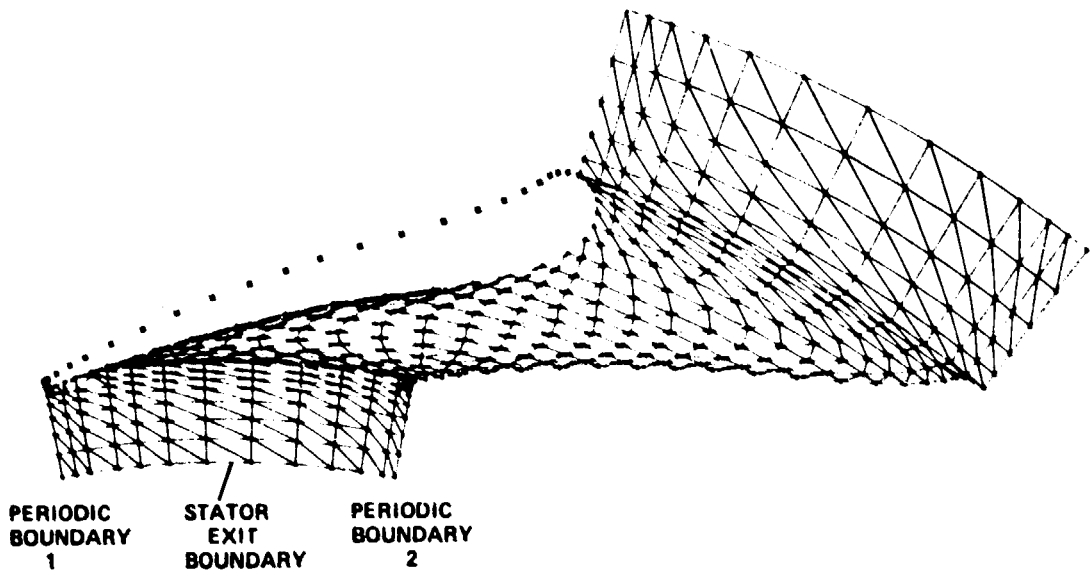
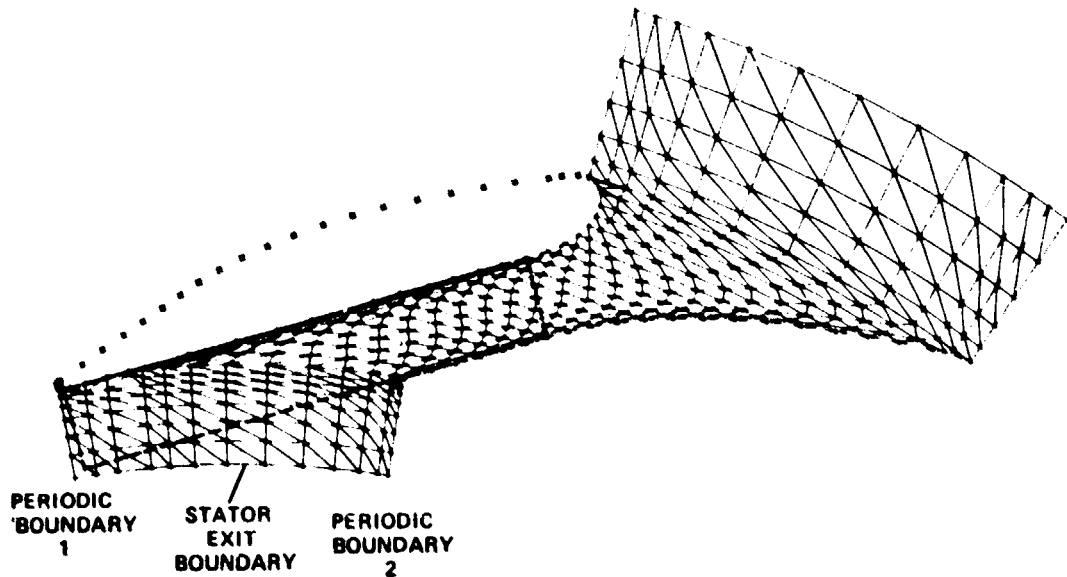


Figure 93. Contour of the Flow-Passage Axial Width within the Rotating/Translating Insert at 60-Percent Flow Setting.



ARTICULATED TRAILING-EDGE CONFIGURATION



MOVABLE SIDEWALL CONFIGURATION

Figure 94. Stator Geometry and Station Designation.

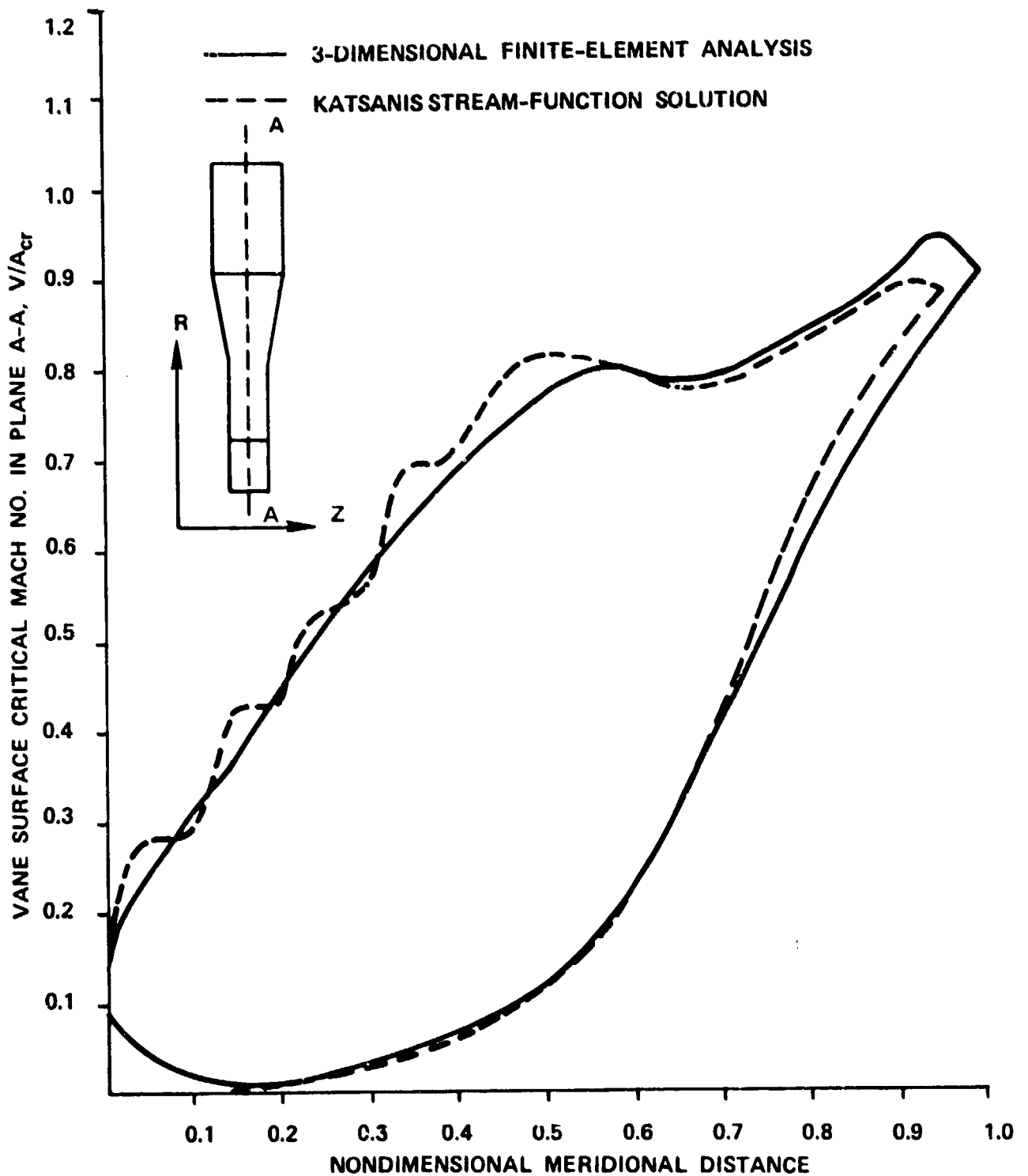


Figure 95. Articulated Trailing-Edge Configuration Vane Velocity Distribution for 100-Percent Power Setting (Design Point: 80-Percent Power).

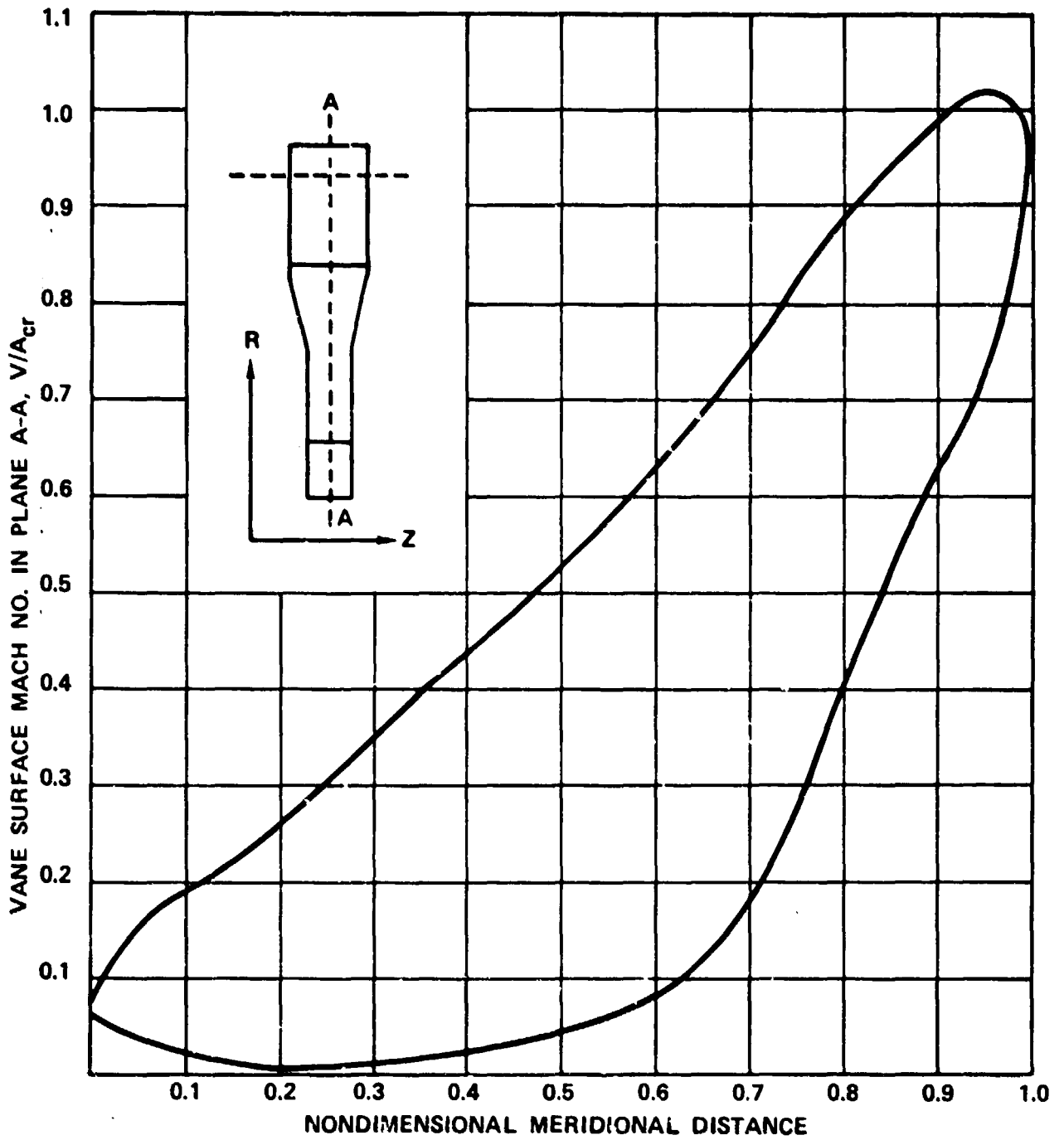


Figure 96. Articulated Trailing-Edge Configuration Vane Velocity Distribution for 60-Percent Power Setting (Design Point at 80-Percent Power), 3-Dimensional Finite-Element Analysis.

in this category are nearly parallel, good agreement is observed between the two sets of results shown in this figure. As shown in these figures, the 60-percent power setting is associated with relatively low velocity levels on the pressure side over 60 percent of the radial chord followed by a rapid increase over the downstream portion. The 100-percent power setting on the other hand, is characterized by a knee-shaped velocity curve in the vicinity of the throat point on the suction side. This is basically due to the reverse-curvature along the suction side in this region.

Vane loadings corresponding to the movable sidewall configuration are shown in Figures 97 through 99. The 60-percent power loadings at different axial locations for this configuration are shown in Figures 98 and 99, including both sidewalls and a midway station. These figures show that the flow is accelerating continuously (with the exception of a slight local diffusion over the vane suction-side in the purely rotating sidewall mechanism at the 60-percent power level). The flow behavior in the vaneless nozzle for the different geometries considered is shown in Figures 100, 101, and 102, respectively. The nondimensional velocity contours are plotted over the three concentric cylindrical surfaces which are indicated in Figure 89 by dotted lines between the two periodic boundaries. As shown in these figures, significant tangential gradients in the exit velocity are associated with the 60-percent power geometry -- particularly in the case of the rotating-translating sidewall option. The circumferential distributions of the flow angle and the critical velocity ratio at the stator exit station (station C-C, Figure 89) and midway between the two sidewalls are shown in Figure 103 for all the stator configurations considered. This figure shows that the high tangential gradients of the flow exit angle are associated with the movable sidewall configuration, a characteristic that is conceptually undesirable at the rotor inlet station.

6.5 Detailed Aerodynamic Design Conclusions

The variable-geometry stator flow analysis is basically a problem where the solution domain falls in the 3-dimensional category. This is particularly true for those configurations where locally movable sidewalls are incorporated. The numerical design procedure adopted for the present study took this problem into account, while providing fast, low-cost answers in the early stage of the detailed design task where a large number of vane and sidewall shapes were considered for comparison. In this stage, the stator geometry was reduced to a 2-dimensional region in the flow analysis and the Katsanis stream function approach was utilized.

The objectives of the second phase of the detailed stator design were to account for the flow 3-dimensionality and to verify the results of the first phase. Ideally, this procedure should be

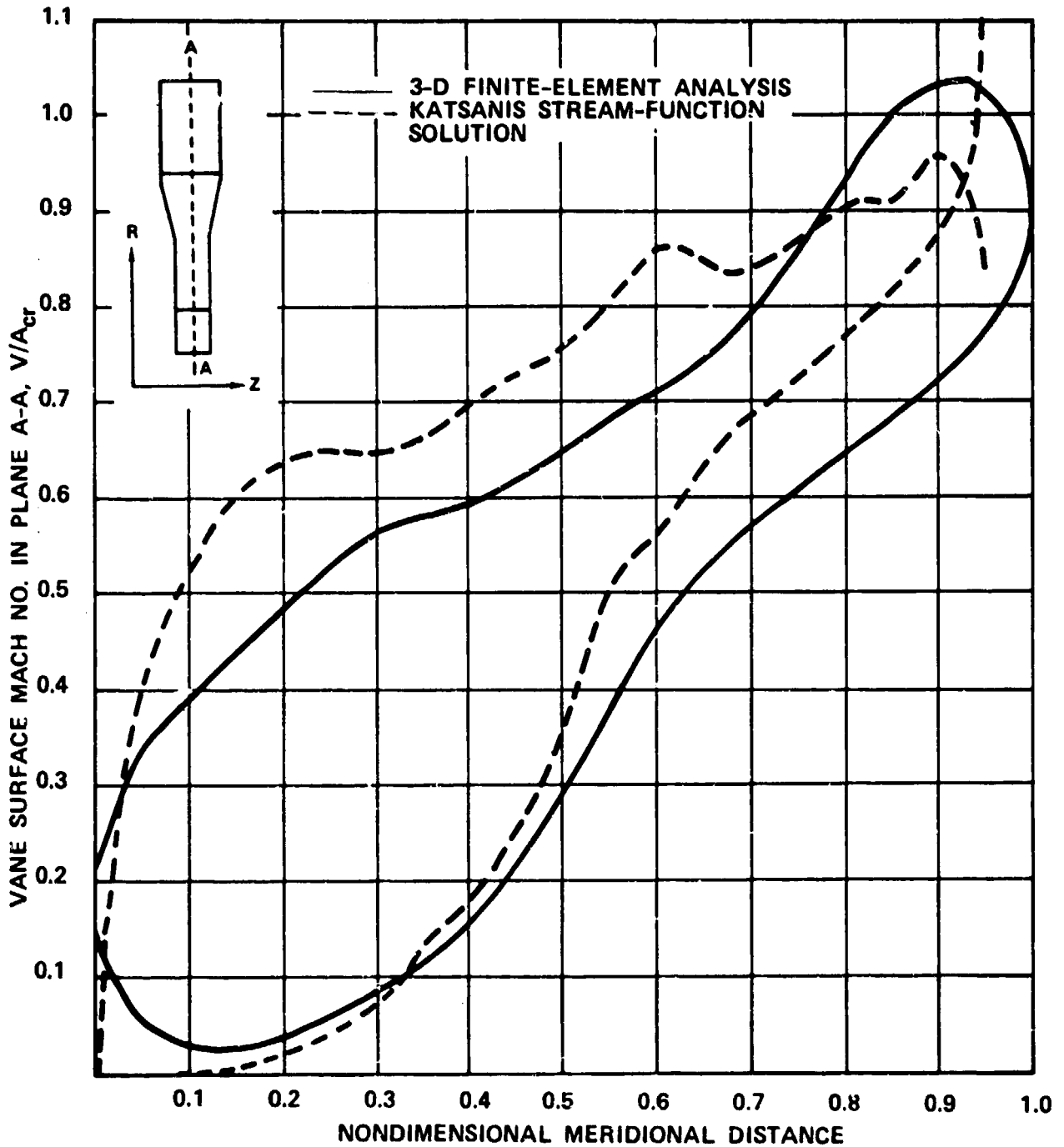


Figure 97. Movable Sidewall Configuration Vane Velocity Distribution for 100-Percent Power.

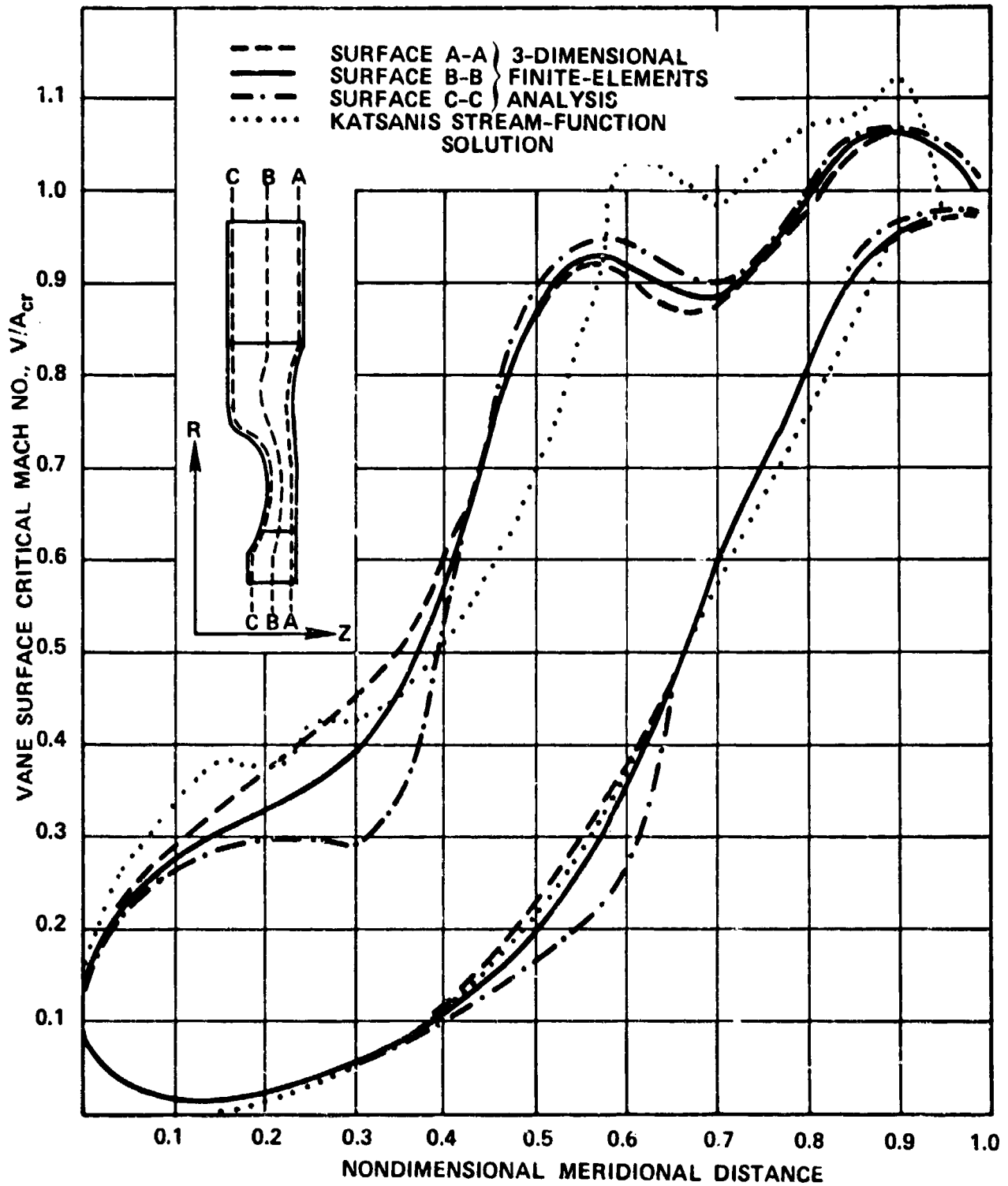


Figure 98. Purely Rotating Sidewall Configuration Vane Velocity Distribution for 60-Percent Power.

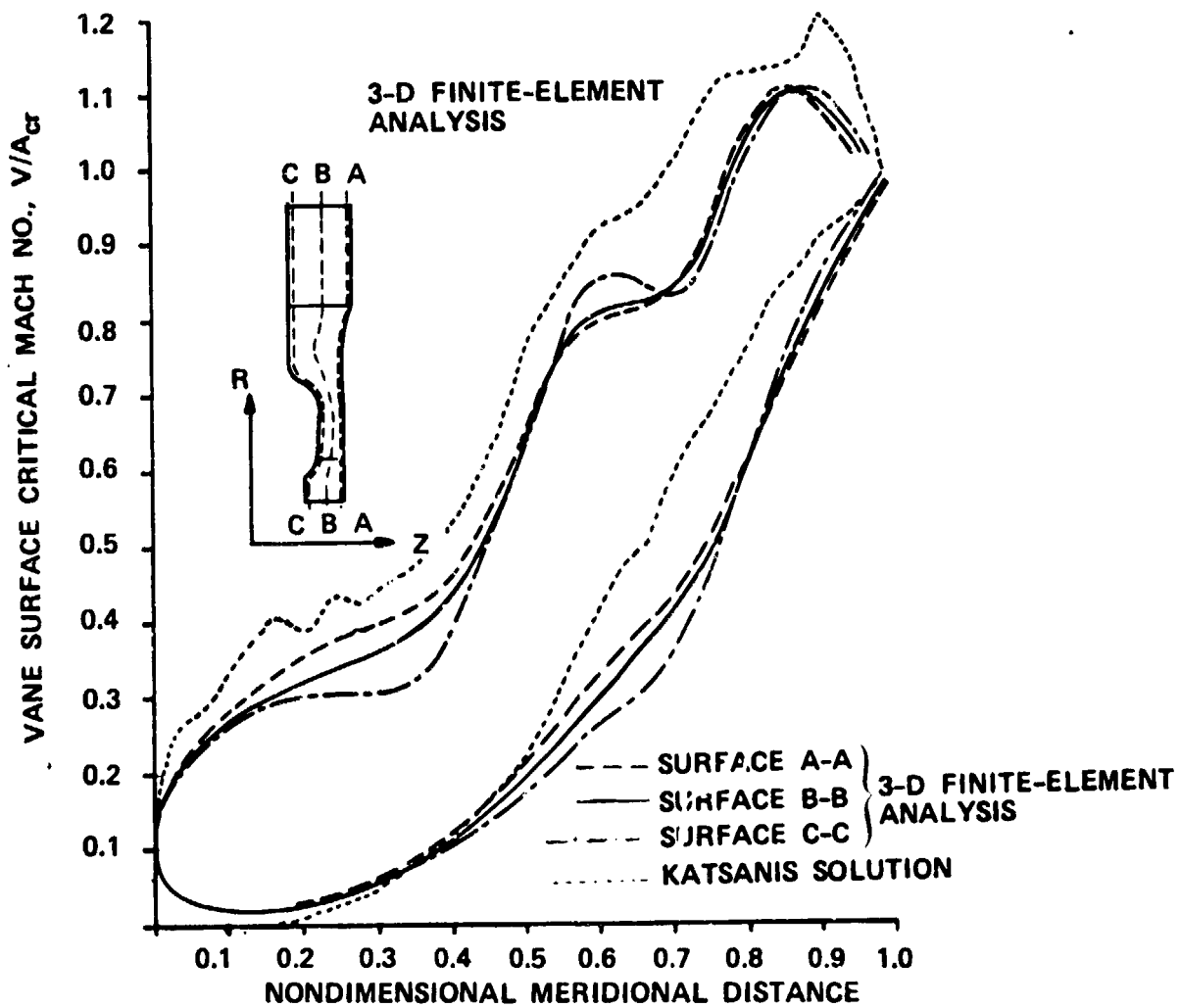


Figure 99. Rotating-Translating Movable Sidewall Configuration, Vane Velocity Distribution for 60-Percent Power Setting.

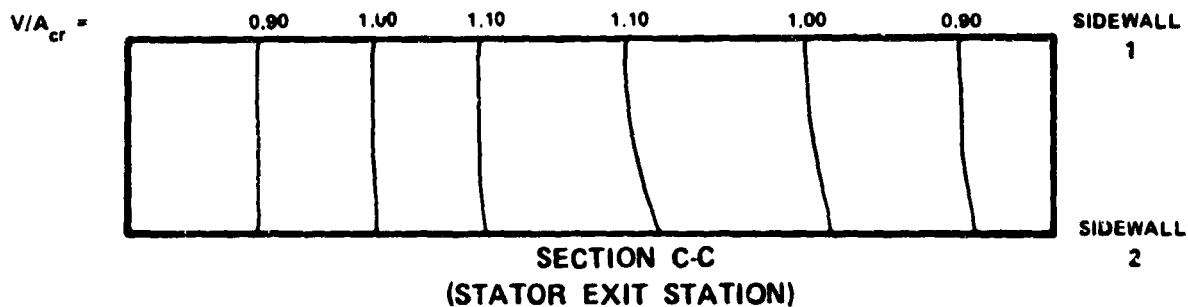
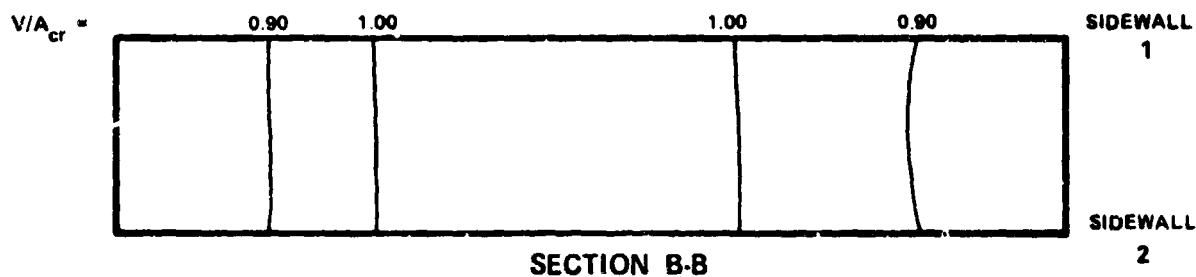
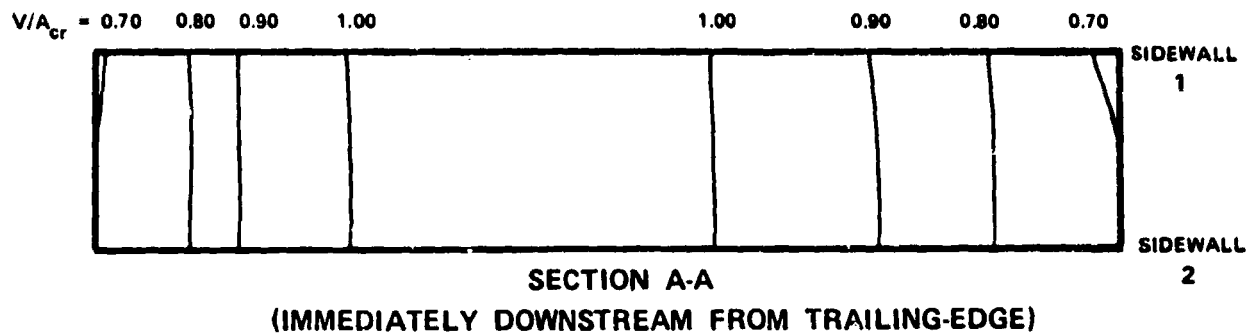


Figure 100. Movable Sidewall Configuration, Critical Mach No. Contours in the Vaneless Nozzle for 100-Percent Power Setting (3-Dimensional Finite-Element Analysis).

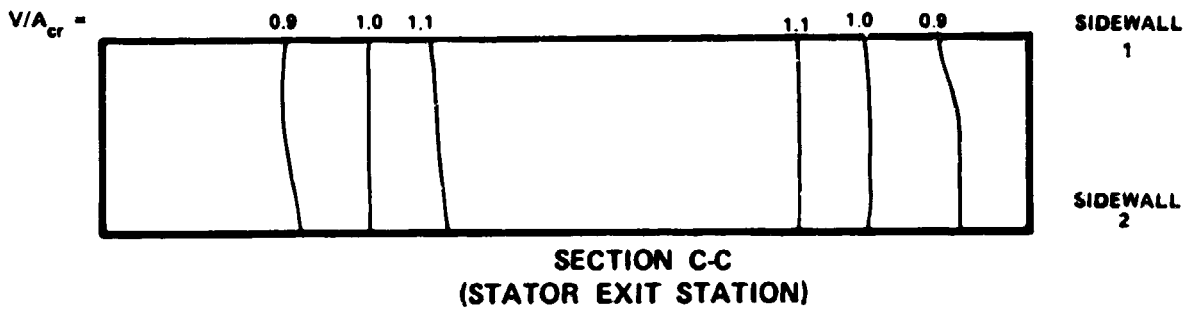
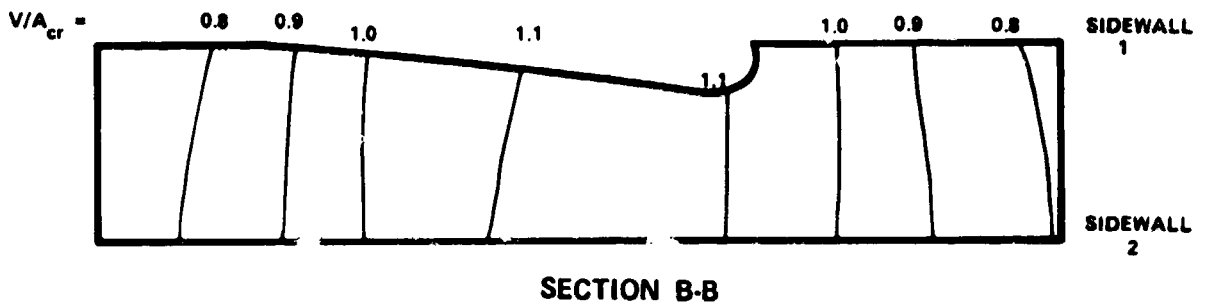
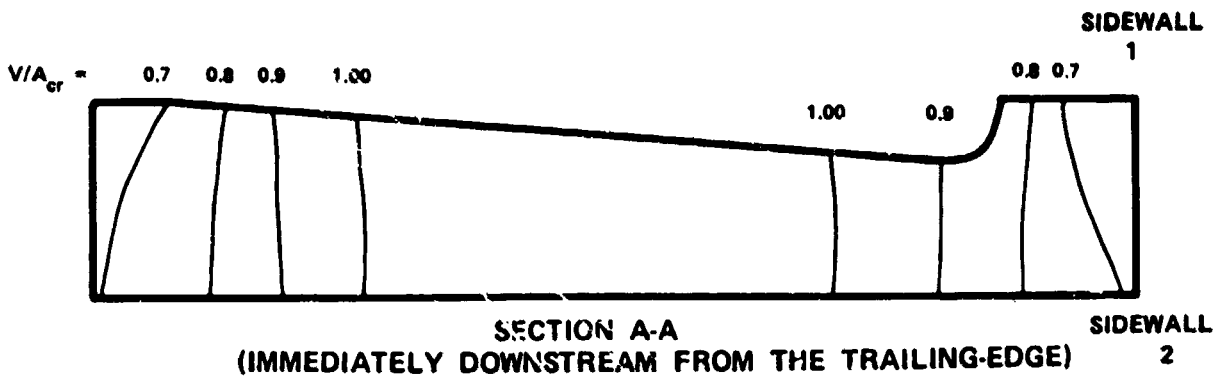


Figure 101. Purely Rotating Sidewall Configuration, Critical Mach No. Contours in the Vaneless Nozzle for 60-Percent Power Setting (3-Dimensional Finite-Element Analysis).

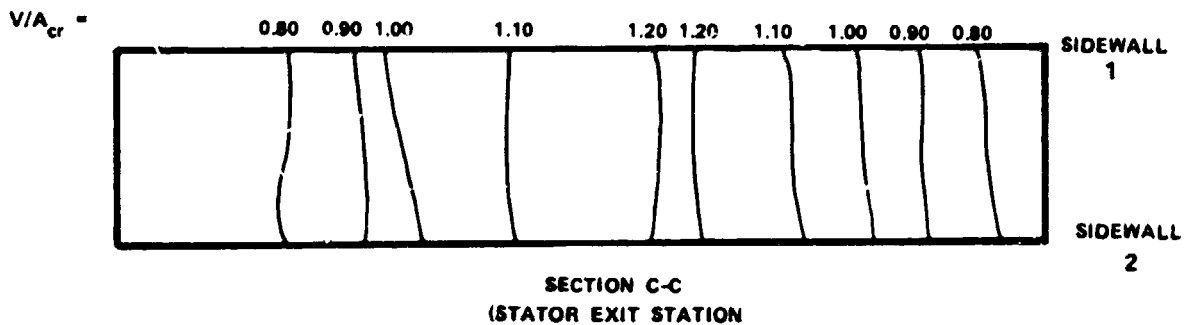
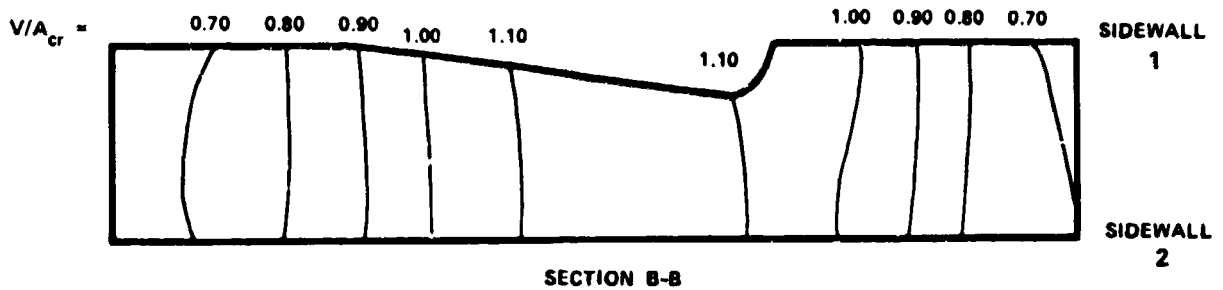
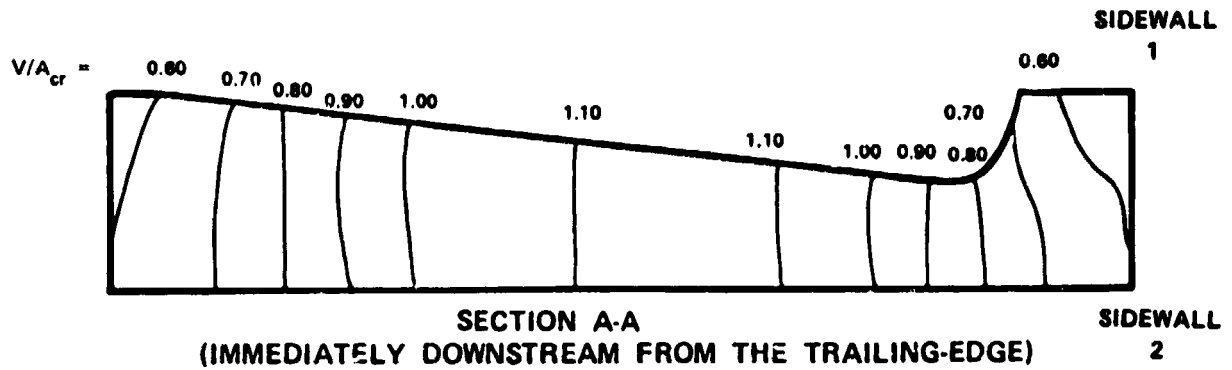


Figure 102. Rotating-Translating Sidewall Configuration, Critical Mach No. Contours in the Vaneless Nozzle for 60-Percent Power Setting (3-Dimensional Finite-Element Analysis).

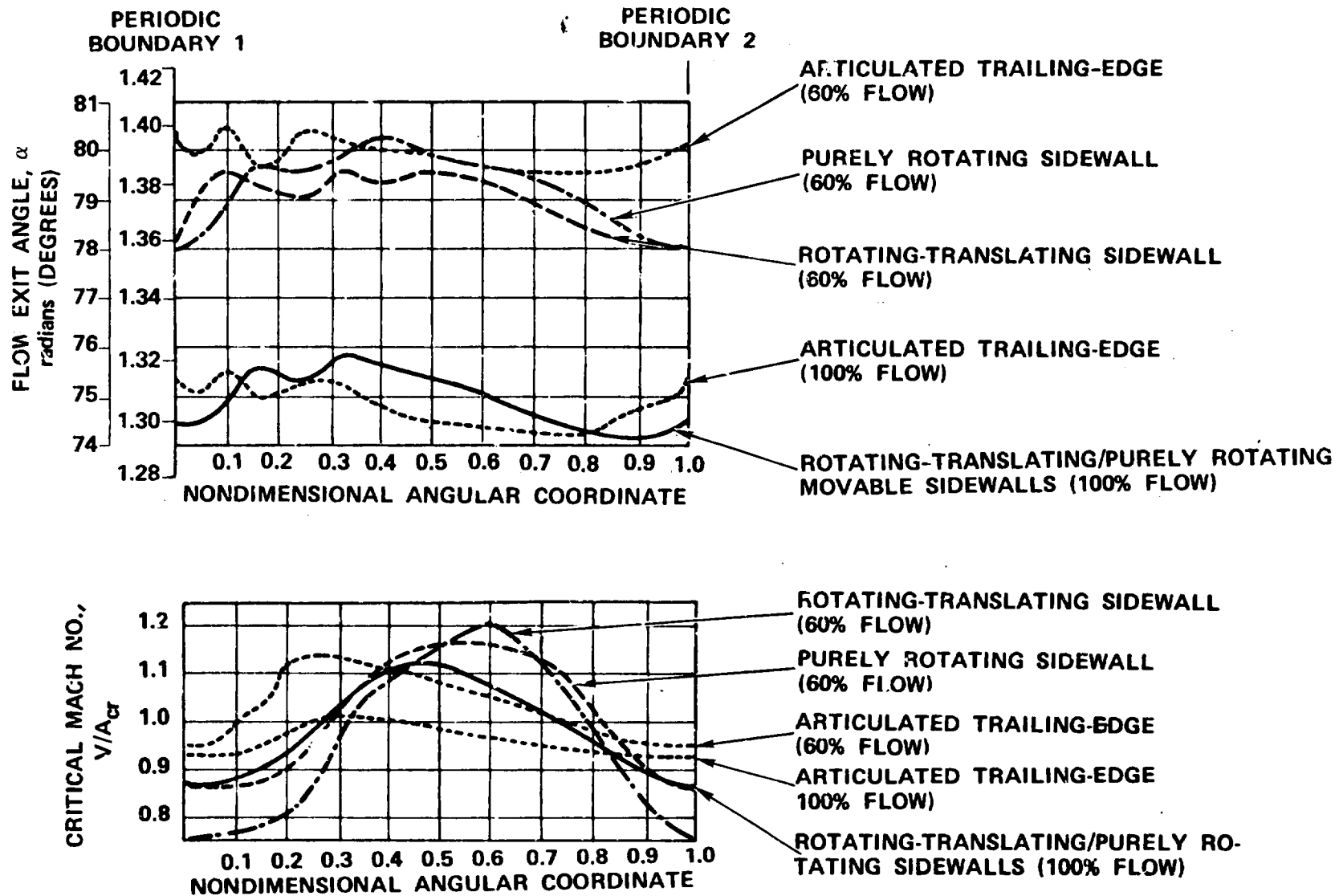


Figure 103. Comparison of Flow Properties at Stator Exit Station (Three Dimensional Finite Element Analysis).

iterative, in the sense that the 3-dimensional results can lead to reconsideration of some configurations that were not considered in the first phase. However, this was unnecessary for this program, because of the careful geometry selection used in the first phase in conjunction with an accurate projection of 3-dimensional effects.

Each stator configuration appeared to attain peak performance at a different power level. With the design point at the 80-percent power setting, the vane loading at 100-percent power in the articulated trailing-edge configuration is characterized by local diffusion over the suction-side, downstream from the throat point. At the 60-percent power setting, desirable loading characteristics are generally achieved with the flow constantly accelerated on both the suction- and pressure-side, and moderate trailing-edge loading. However, opposite conclusions can be drawn for the movable sidewall configuration. The major drawback to this configuration is the losses associated with the stator exit dump at low power settings. The relatively high tangential gradients at the stator exit-rotor inlet station represents an additional disadvantage for this configuration.

Selection of an optimum configuration for the variable area stator is based not only on aerodynamic evaluation, but also on mechanical and cooling considerations. While the articulated trailing-edge configuration appears to offer slightly better aerodynamic performance in a global sense, the movable sidewall option offers considerable mechanical and cooling advantages. Incorporation of a rotating-translating insert in the movable sidewall option provides better performance from an aerodynamic standpoint while maintaining similar mechanical and cooling advantages.

6.6 Articulated Trailing-Edge Stator - Mechanical Substantiation

6.6.1 Mechanical Description

The preliminary conceptual analysis (Task I) identified the articulated trailing-edge stator as the primary candidate for achieving variable geometry for this program. The stator configuration shown in Figure 78 was ultimately selected as a result of parametric analysis and final aerodynamic-design studies. For this concept, the trailing-edge was rotated about the axis by the controlled actuation linkage movement attached to a hollow hinged pin that penetrated the forward sidewall. The trailing edge was confined to the portion of the stator channel with parallel sidewalls, so that adequate sealing could be obtained at all power conditions.

The stem portion of the hinged pin had a 0.317-cm (0.125-in.) inside diameter that allowed cooling flow to enter the trailing edge. The 0.102-cm (0.040-in.) thick walls provided adequate rigidity and strength to withstand aerodynamic loading. For the final design cooling-flow rate through the stem, a pressure loss of about 6.9 MPa (1.0 psi) was predicted for a supply pressure of 1717 KPa (249 psia). Hence, the pressure drop was insignificant. The highest aerodynamic loading on the trailing-edge occurred at the 60-percent power condition. In this worst case, the torsional-stress level was calculated at less than 69 MPa (10 ksi) and is only a small percentage of the NASAIR-100 material yield strength at predicted temperatures.

Figure 78 shows the long radial span of the vane and also the varying trailing-edge radius from the 60- to 100-percent power settings. The vane and sidewall surface area to be cooled is significant and, in general, the need for cooling at these temperature levels is considerable.

6.6.2 Impact of Cycle Conditions on Stator Design

The cycle-point selection for the final design employed a 17:1-cycle pressure ratio, a physical compressor inlet-mass flow of 2.3 kg/s (5.0 lbm/sec), and a turbine-rotor inlet temperature of 1589K (2400°F). A fixed rotor inlet temperature was used to control engine power output in the cycle analysis, with the resultant stator-inlet temperature computed from this temperature. The mainstream mass flow and injected-coolant mass flow from the vane and sidewalls mix to produce the desired cycle value of enthalpy at the rotor inlet. As the utilized cooling flow increases, the stator-inlet mainstream gas temperature also increases. This compensates for the lower temperature of injected coolant and the gas flow removed from the flow path. However, this increases the need for cooling to maintain appropriate metal temperatures. Obtaining

the correct rotor-inlet temperature raised the stator-inlet temperature to high levels (Figure 104). The impact of stator coolant on inlet-gas temperature was plotted for both an average and a hot-streak condition using a combustor pattern factor of 0.20. It is a standard practice to design vanes to withstand the maximum hot-streak temperature that exists in the combustor. This pattern factor is defined as:

$$PF = \frac{T_{\text{gas max}} - T_{\text{gas avg}}}{T_{\text{gas avg}} - T_{\text{combustor in}}}$$

Since the amount of cooling required for mechanical integrity of the stator was not known at the outset of the design, the process of computing stator inlet temperature was iterative. Preliminary cooling-flow design values were used in the final design process. Using these values, the stator-inlet temperature design values shown in Figure 104 were reached. The values were 1844K (2860°F) at 100-percent power and 1897K (2955°F) at 60-percent power. Total cooling-flow usage in the final design configuration was slightly greater than that assumed for establishing these gas temperatures. This did not justify further iterations on inlet temperature for design substantiation.

6.6.3 Stator Aerodynamic Boundary Conditions

The aerodynamic boundary condition trends observed for the final design solutions were similar to those reached in the preliminary design investigations. The velocity diagrams (Figures 105 and 106) from the aerodynamic analyses were for 100-percent and 60-percent power, respectively. As with any radial inflow turbine design, the inlet velocities to the stator were quite low and remained so in the passage, particularly on the pressure side, where low values extended along the initial 40-percent of the surface length. With a fixed geometry vane in a conventional cycle, low velocities at part-power condition would not be a concern from a heat-transfer standpoint. This is because the need for providing adequate cooling flow is reduced in proportion to turbine temperature. With this design, the stator pressure-side velocities at 60-percent power were quite low. However, coolant still had to be driven through the vane, since the inlet temperature was even higher at this condition. The low velocity did not produce sufficient static pressure drop from the coolant supply level to drive a film-cooling design on the pressure-side (normally used at these temperatures).

This problem is also addressed in Figure 107, showing the vane-surface static pressures at 60- and 100-percent power from the loading diagrams. This allowed an available pressure drop of

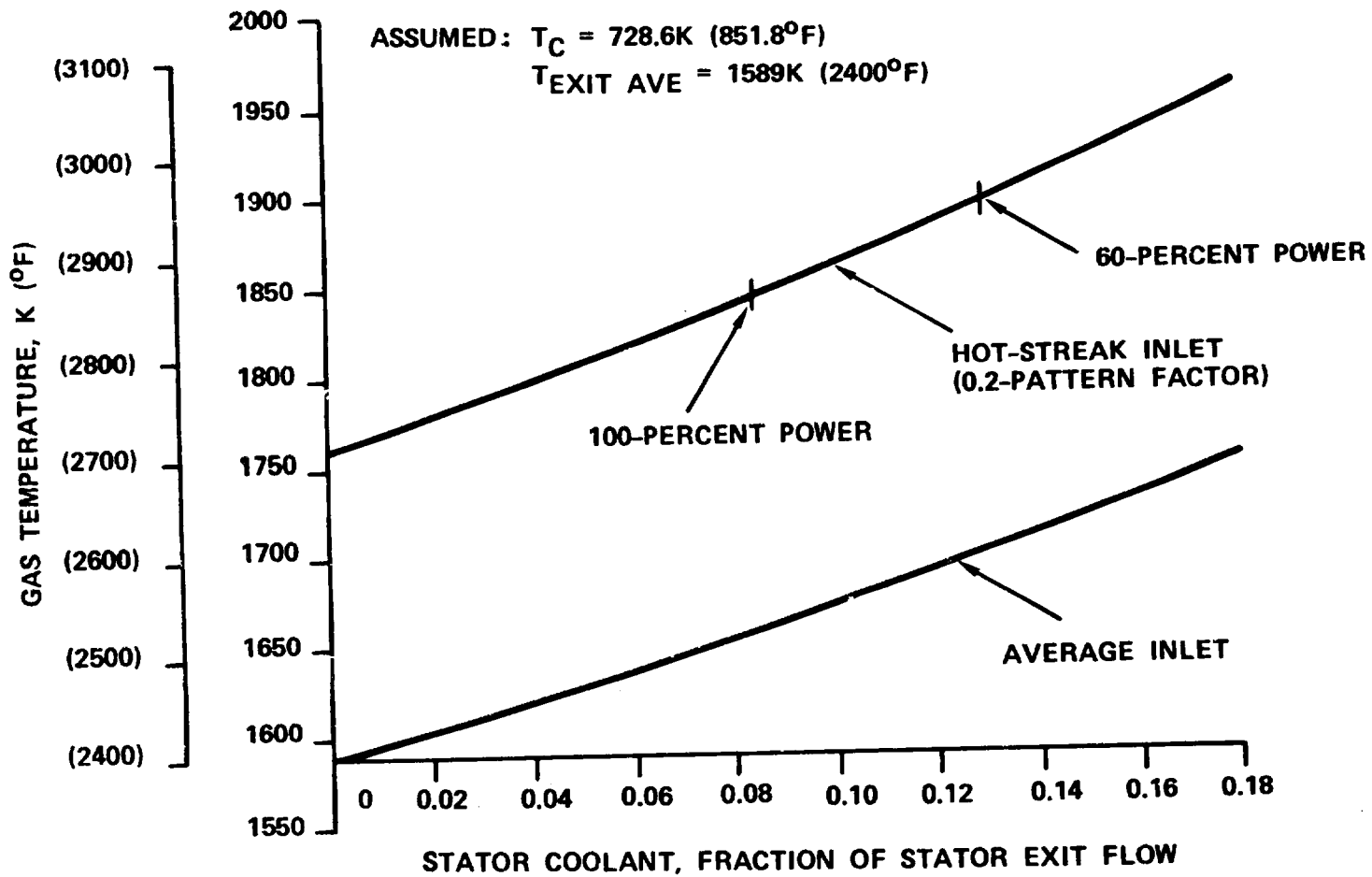


Figure 104. Inlet Gas Temperature Versus Coolant-Added, Variable-Area Stator.

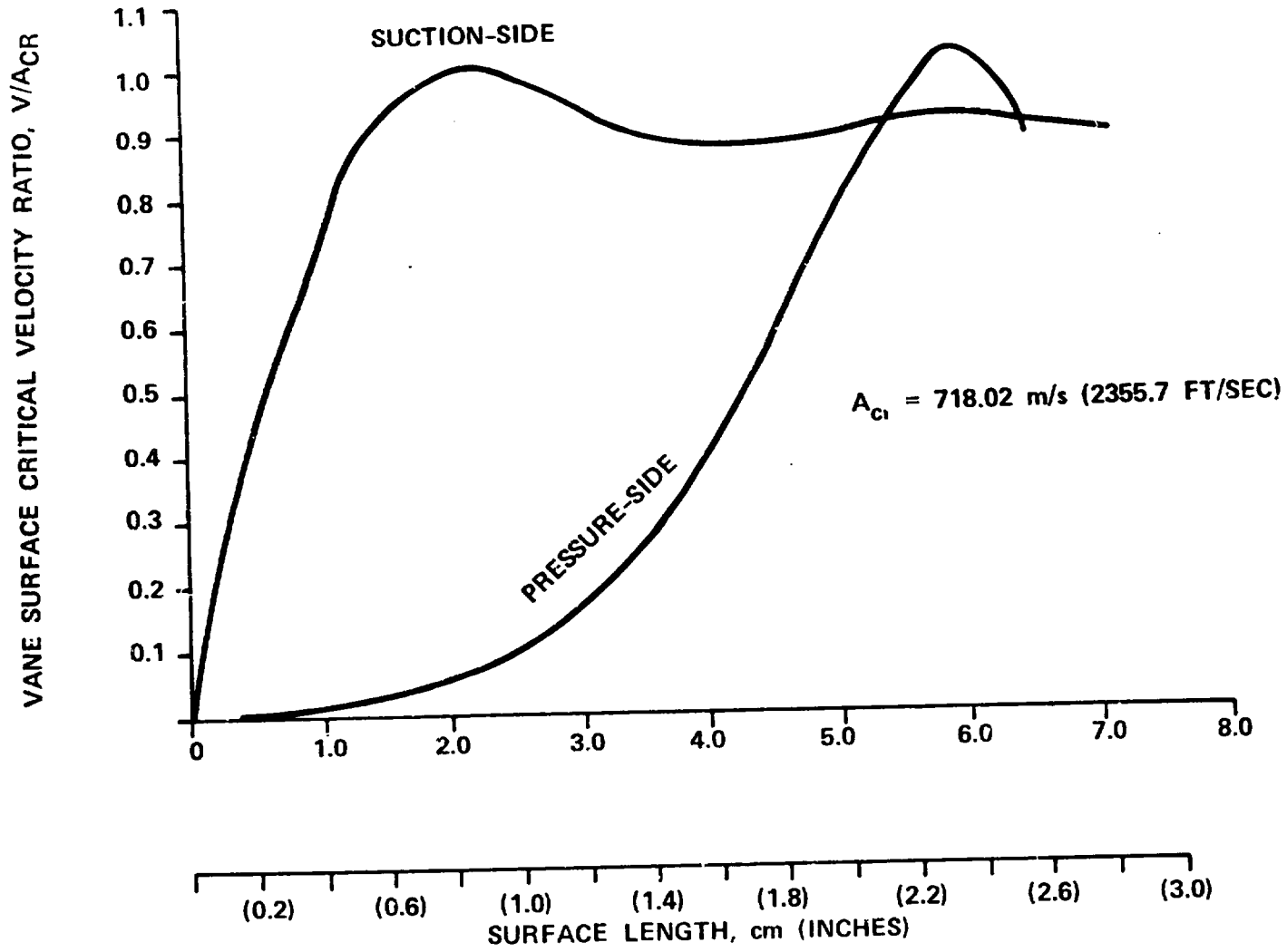


Figure 105. Articulated Trailing-Edge Stator Vane Velocities at 100-Percent Power, Katsanis Solution.

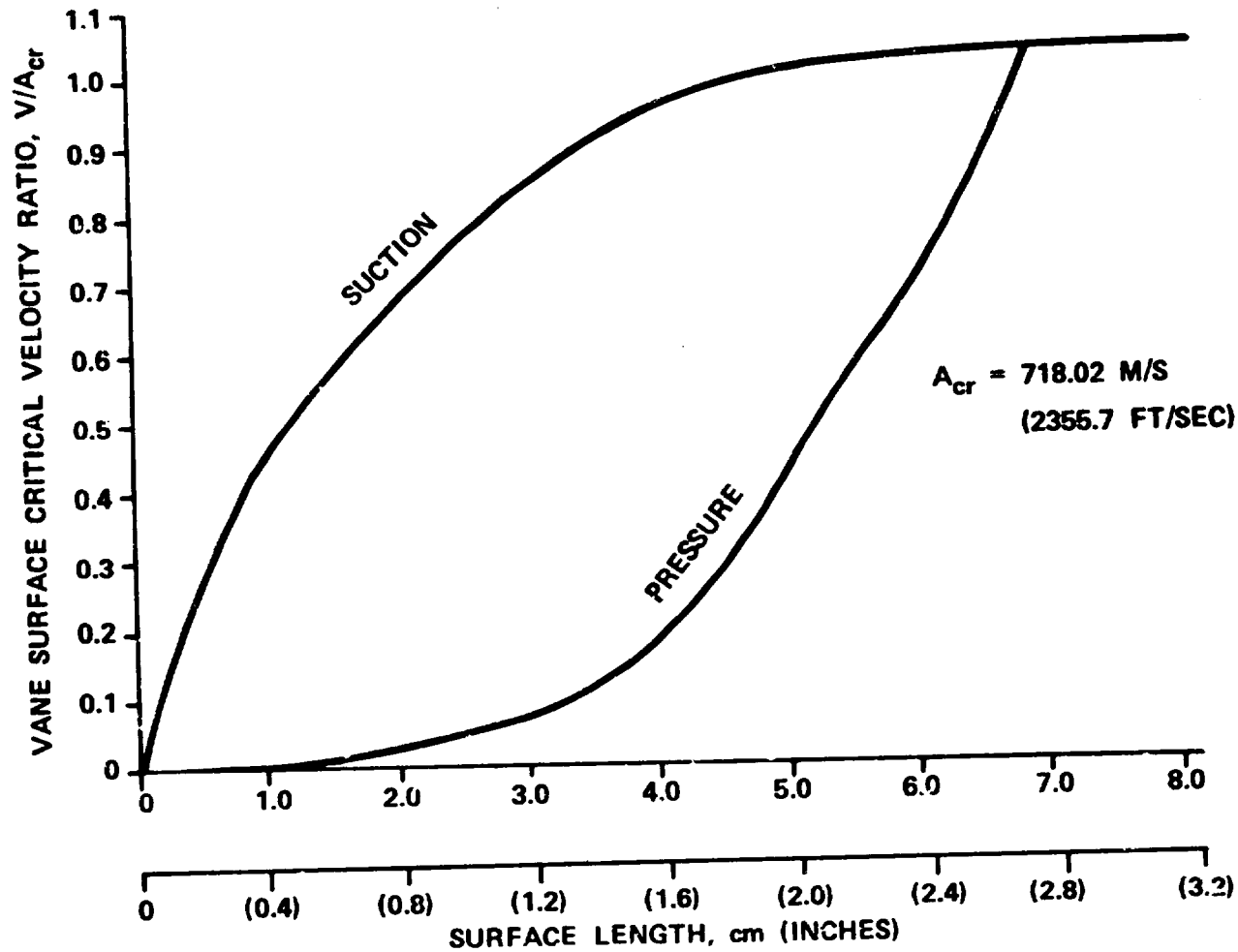


Figure 106. Articulated Trailing-Edge Stator Vane Velocities at 60-Percent Power.

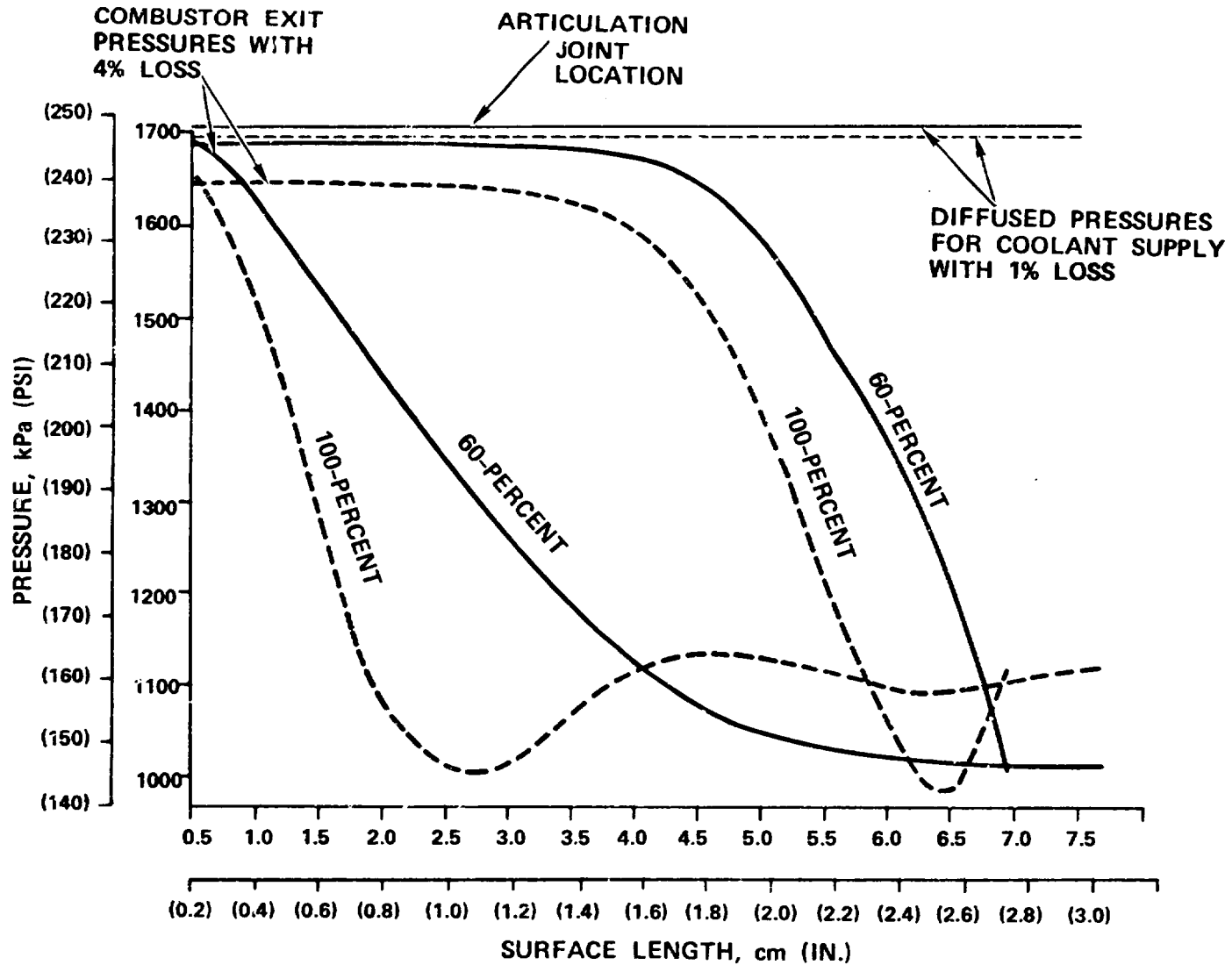


Figure 107. Articulated Trailing-Edge Stator Vane Static Pressure Distribution.

about 51.7 kPa (7.5 psia) at 100-percent power forward of the articulation joint, to drive a film-cooling design on the pressure side. However, this pressure drop decreased to less than 20.68 kPa (3.0 psia) at 60-percent power, and did not allow adequate pressure-side film cooling of the forward portion of the vane. This design was subsequently dropped from consideration. Suction-side film injection was ultimately selected for the configuration since the injection points allowed adequate pressure (Figure 107). These points were located as far forward of the throat as possible.

Using aerodynamic velocities and stage inlet conditions, turbulent heat-transfer coefficients were calculated on both the suction- and pressure-sides of the vane. A standard Garrett computer method for airfoil heat-transfer was used and did not include effects from film cooling on the suction-side. Figures 108 and 109 respectively show the resulting values for the suction- and pressure-side surfaces at both 60- and 100-percent power. It should be noted that at the 100-percent power condition, greater heat-transfer coefficients existed on the forward portion of both surfaces. At the 60-percent power condition heat-transfer coefficient was predominant on the rear portion. This is further illustrated in Figure 110, showing heat-flux computation on the trailing-edge for a constant wall temperature.

6.6.4 Vane-Cooling Circuit Design

The major problems that existed with the design of the forward stationary portion of the vane-cooling circuit were adequate cooling of the vane pressure side without external film and creating a passage to the suction-side for coolant discharge that would not interfere with fresh coolant supply. A wall average metal temperature of 1255K (1800°F) was selected in the belief that DS Mar-M 247 would provide this capability. This was a small step in temperature beyond existing values produced with more conventional alloys.

The final design employed the cooling configuration shown in Figure 111. Cooling air entered the vane through an unobstructed central supply region and then split into two paths. A large portion of the cooling air was transmitted into the nose region of the vane through three rows of impingement holes. This cooling air then exited the vane through suction-side film holes. The impingement holes were 0.038-cm (0.015-in.) in diameter, with a total of thirteen holes with 8 diameter and 6 diameter spacings. A total of six 0.071-cm (0.028-in.) diameter film cooling holes were located across the vane span. Leading-edge and impingement-wall thicknesses were 0.127 cm (0.050-in.). Smaller amounts of cooling air scrubbed the inner surface of the pressure-sidewall moving aft. This air then crossed to the suction-side, upstream

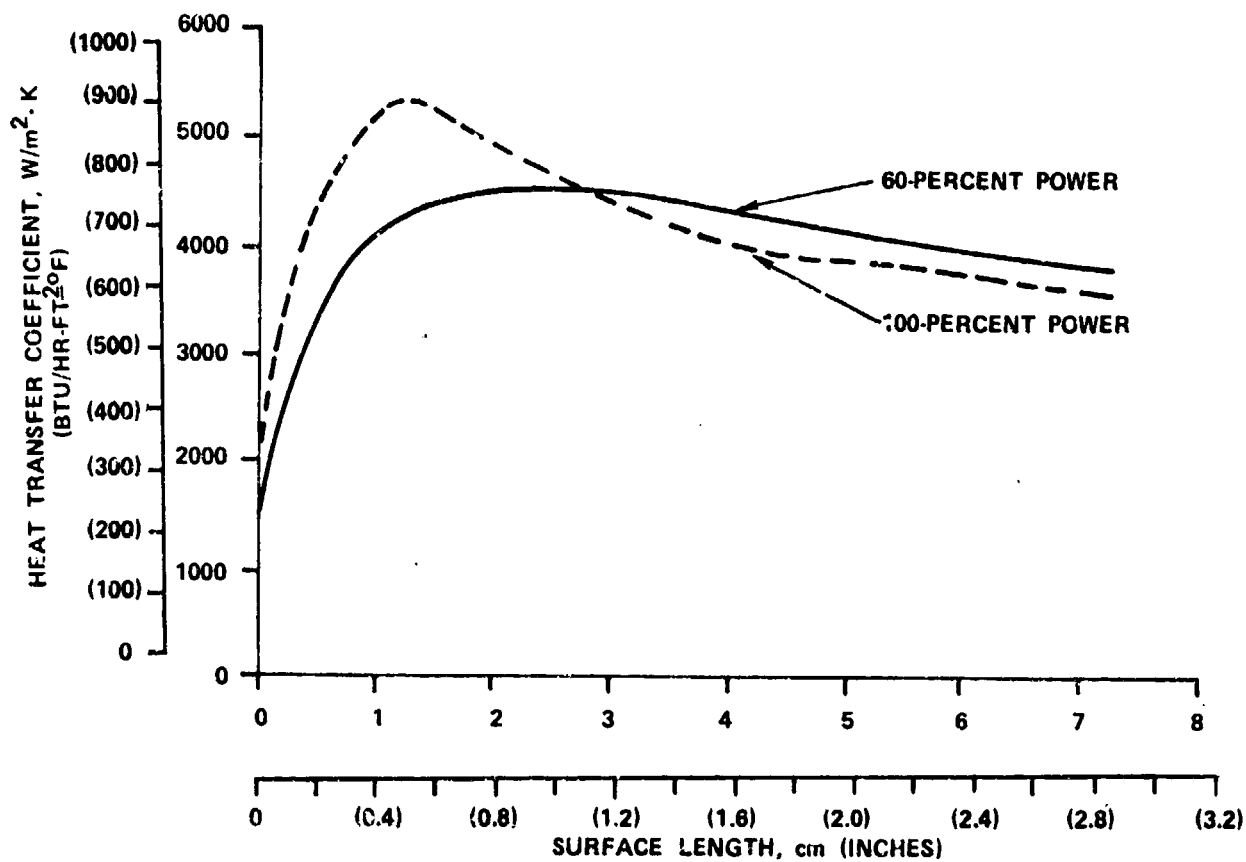


Figure 108. Articulated Trailing-Edge Stator Vane, Suction-Side Surface Heat-Transfer Coefficients.

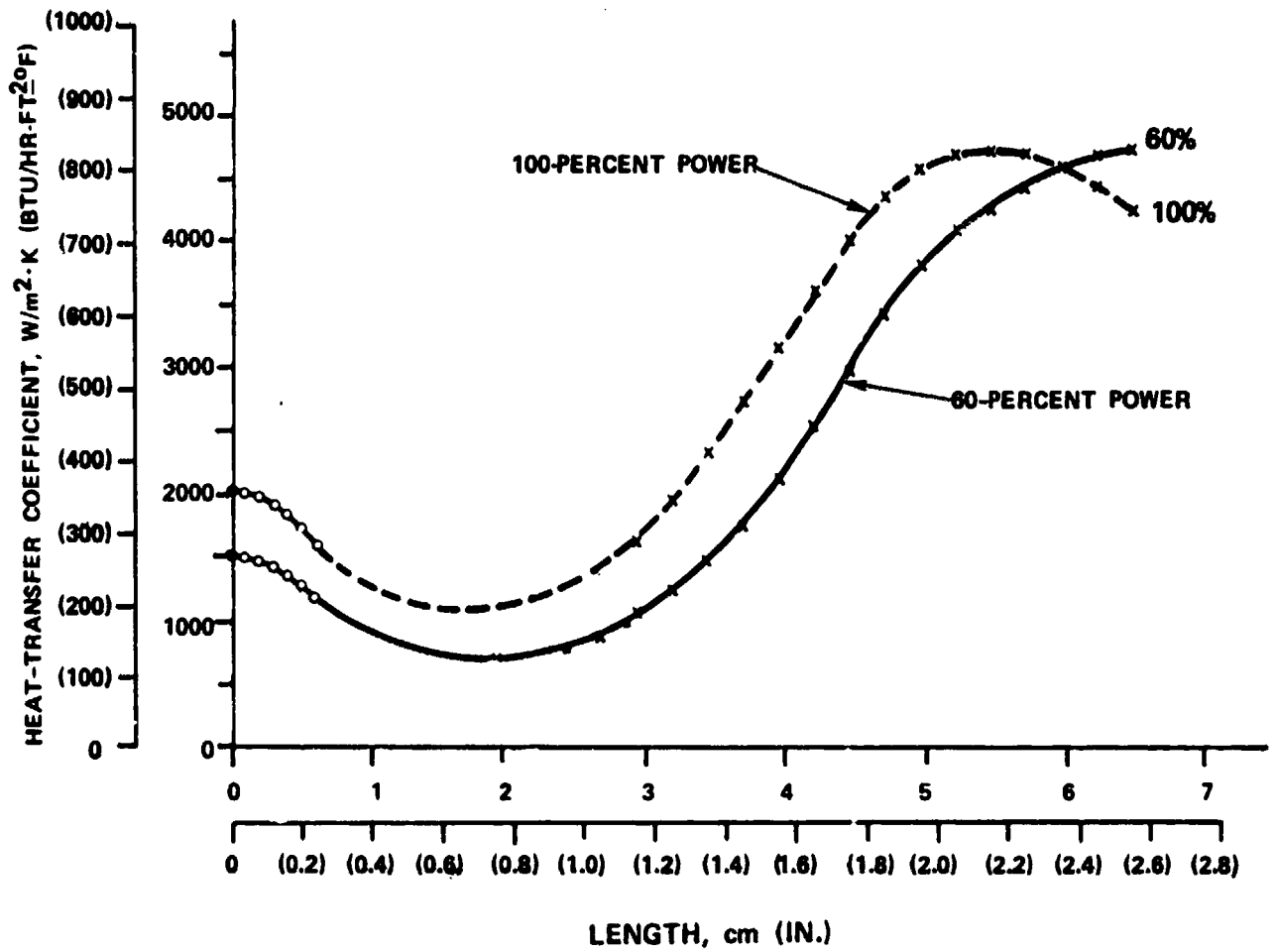


Figure 109. Articulated Trailing-Edge Stator Vane, Pressure-Side Surface Heat-Transfer Coefficients.

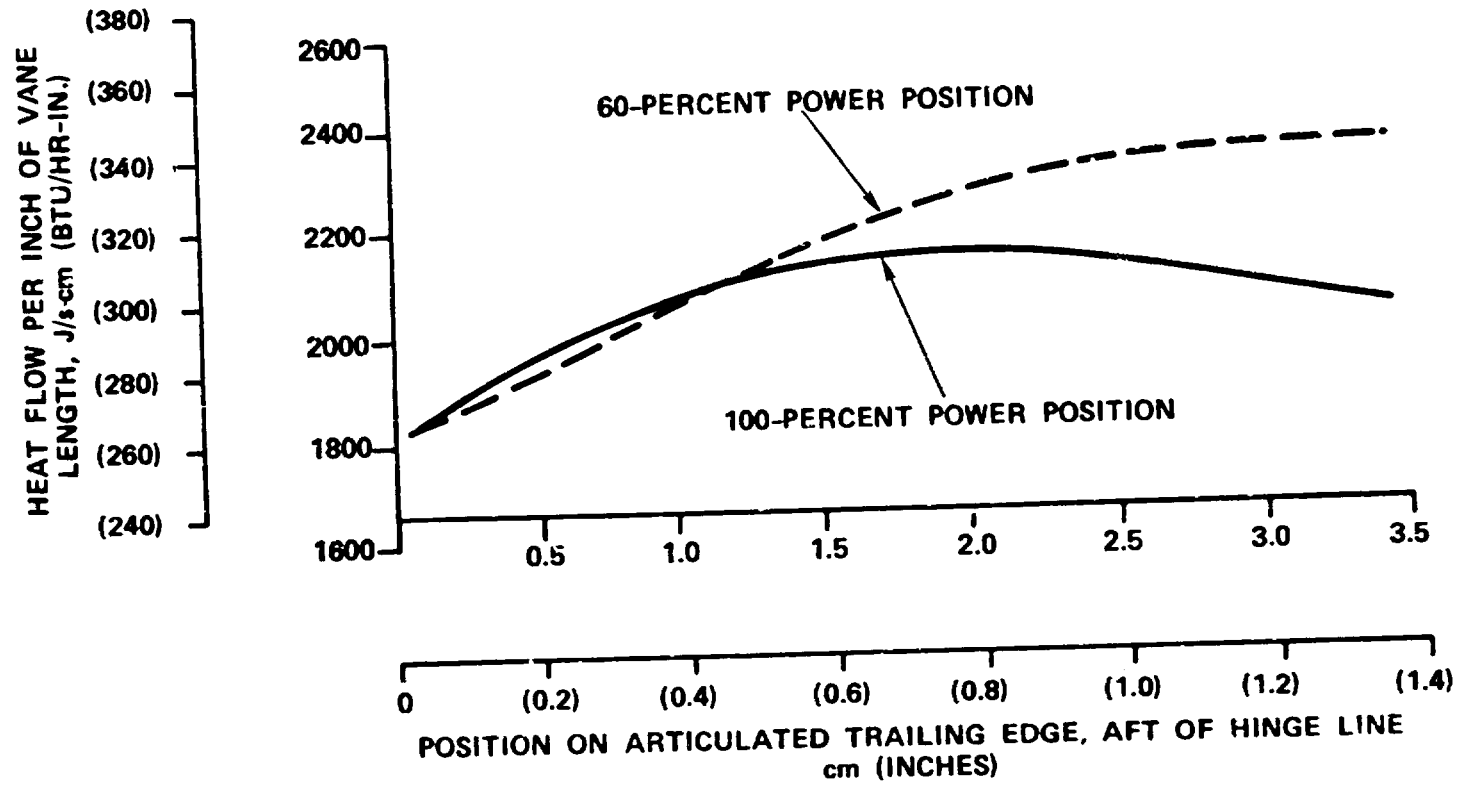


Figure 110. Thermal Loading on Articulated Trailing-Edge (No Film Cooling).

of the articulation point, and ducted forward along the suction-side inner wall. Pin-fin arrays of 0.08-cm (0.03-in.) dimensional pins of varying densities were positioned around this path with all passage heights set at 0.102 cm (0.040 in.). The air was then metered through two 0.064-cm (0.025-in.) holes. This metering dropped the pressure prior to film-hole discharge such that necessary mass velocities for film cooling were reached. A total of five 0.045-cm (0.018-in.) film holes that flared to 0.071-cm (0.028 in.) at the outer surface were used.

The vane nose heat-transfer problem was not as severe as in the case of an axial vane, since approach velocities are lower. The internal heat-transfer rates at the vane nose ranged from an average of 8511.7 W/M²·K (1500 Btu/hr.-ft²·°F) for 100-percent power to about 6242.2 W/M²·K (1100 Btu/hr.-ft²·°F) at 60-percent power. The higher gas temperatures at 60-percent power were more restrictive, and it was apparent that metal temperatures at full-power were substantially lower (Figure 111). Wall temperature differences of 28K (50°F) on the leading edge were not severe. For this design, the vane nose region flow corresponded to 1.79 percent at 100-percent power, and 2.01 percent at 60-percent power. However, a severe sidewall heat-transfer problem existed on the pressure side at 100-percent power. Since this condition controlled the flow geometry, higher wall temperatures were experienced. On the suction-side, a severe 60-percent power condition existed caused by the shift in film-hole discharge static pressure that reduced the cooling flow rate. Due to heat pickup, the reduced physical flow rate--even at higher percentage values--produced a noticeable effect on the suction-side downstream passage. Optimization beyond that achieved may be possible, since a sufficient pressure drop exists for supplying more cooling flow to this passage, if desired. The sidewall region core flow was 0.73-percent at 100-percent power, and 0.85-percent at 60-percent power.

Vane trailing-edge cooling was a challenge, due to the very high external heat-transfer coefficients and large surface area. In addition, cooling-flow passage area was limited due to the narrow shape and the length of the vane. In fact, the final design was pressure-drop limited at the trailing-edge. A straight-through flow path was utilized (Figure 112), with coolant supplied from the stem and then exited toward the trailing-edge.

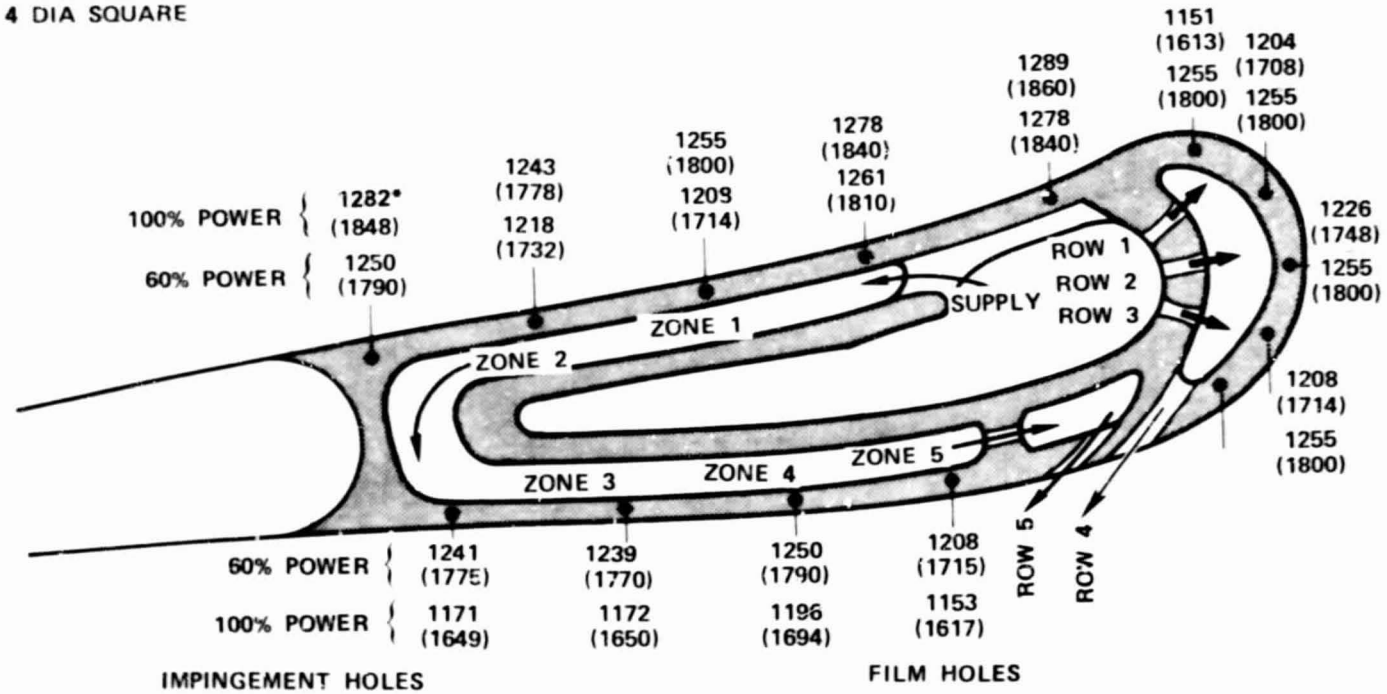
In the upstream portion of the trailing-edge, heavy cross ribs were placed between the suction- and pressure-sidewalls for flow acceleration and to reduce side-to-side temperature difference caused by heat cross-conduction. Passage height in this area was controlled by the 0.102-cm (0.040-in.) thick outer walls and the overall vane thickness.

PIN-FIN SPACINGS

ZONE 1 = 6 DIA SQUARE
 ZONE 2 = 5 DIA SQUARE
 ZONE 3 = 3 DIA SQUARE
 ZONE 4 = 3 DIA SQUARE
 ZONE 5 = 4 DIA SQUARE

ROW 4 W_C = 1.79% AT 60-PERCENT POWER
 2.01% AT 100-PERCENT POWER

ROW 5 W_C = 0.73% AT 60-PERCENT POWER
 0.85% AT 100-PERCENT POWER



ROW 1 = 4 HOLES: 0.038-CM (0.015 IN) DIA
 ROW 2 = 4 HOLES: 0.038-CM (0.015 IN) DIA
 ROW 3 = 5 HOLES: 0.038-CM (0.015 IN) DIA

ROW 4 - 6 HOLES: 0.071 CM (0.028 IN) DIA
 ROW 5 - 5 HOLES: 0.045 CM (0.018 IN) INNER DIA
 0.071 CM (0.028 IN) OUTER DIA

*TEMPERATURES K(°F)

Figure 111. Articulated Trailing-Edge Stator Vane Forward Section, Cooling Configuration.

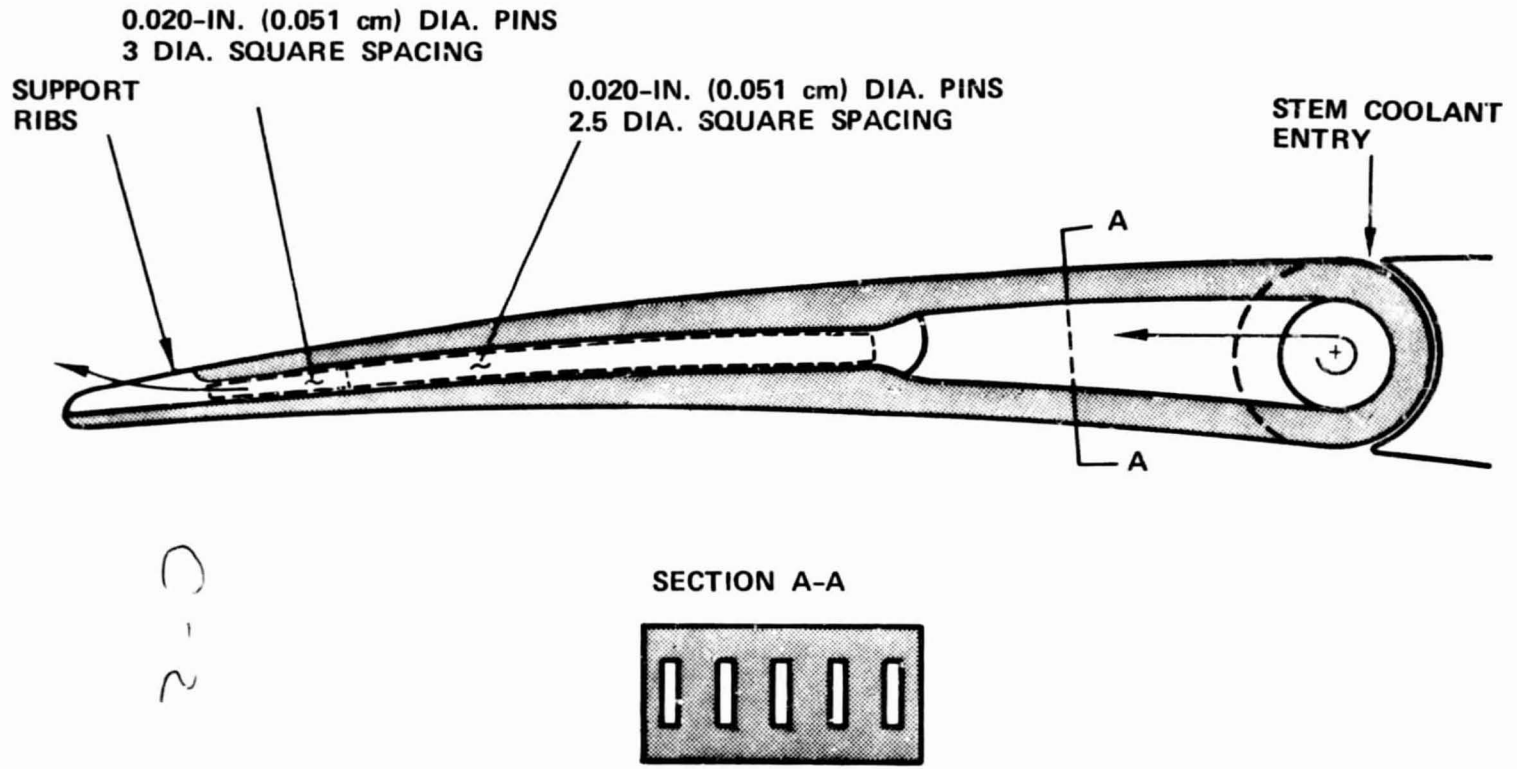


Figure 112. Articulated Trailing-Edge Stator Vane Cooling Configuration.

With the increased coolant temperatures that existed in the midregion, it was necessary to decrease the passage height to 0.102 cm (0.040 in.). Thicker walls and pin fins of 0.051-cm (0.020-in.) diameter were packed into a dense array of 6.4-cm (2.5-in.) diameter square spacing. As shown in Figure 113, this array allowed control of suction-sidewall temperatures, but was not sufficient to achieve the required 1255K (1800°F) temperature on the pressure-sidewall.

Near the trailing-edge cooling-flow discharge slot, the pressure- and suction-sidewalls tapered to a 0.051-cm (0.020-in.) thickness, and the passage converged to 0.051-cm (0.020-in.) in height. The pin-fin array density opened to a 3-diameter spacing, with no exit restriction. This prevented "choking" of the cooling flow rate. No metering orifice was included, but the major pressure drop was uniform in the last section of passage.

The peak metal temperature of 1366K (2000°F) was slightly exceeded at the hot-spot design condition. However, the major concern was that a relatively large section of the pressure-side exceeded 1311K (1900°F). Temperature relief could be achieved through another design iteration that would increase the trailing-edge thickness and thus allow higher cooling-flow usage. Another consideration would be small amounts of film cooling using air injected just downstream of the articulation joint. Either approach could be evaluated in the component detailed final design phase.

The cooling flow used in the trailing-edge consisted of 1.9-percent core flow at 100-percent power. The same physical flow corresponded to 3.17 percent at 60-percent power.

Figure 114 presents a vane cooling flow usage summary and distribution. Totals of 4.4 percent at 100-percent and 6.0 percent at 60-percent power were required with the articulated trailing-edge configuration.

6.6.5 Sidewall Cooling Design

Sidewall cooling of a radial turbine stator operating at high temperature levels is inherently more difficult to achieve since more cooling air is required than required with an axial stator design. This results from the basic geometries employed. The large radial position of the in-flow stator in the engine results in larger area sidewall rings, with relation to other turbine cooled surfaces. In this particular stator design, the vanes were long and slender, and required a significant amount of cooling flow for the resultant surface area (Figure 114). However, the sidewall area-to-vane area ratio for this design was 1.7. The articulated trailing-edge covering the sidewall requires cooling flow since it is alternately covered and uncovered when power level

$W_C = 1.9 \text{ PERCENT @ 100-PERCENT POWER}$
 $3.17 \text{ PERCENT @ 60-PERCENT POWER}$

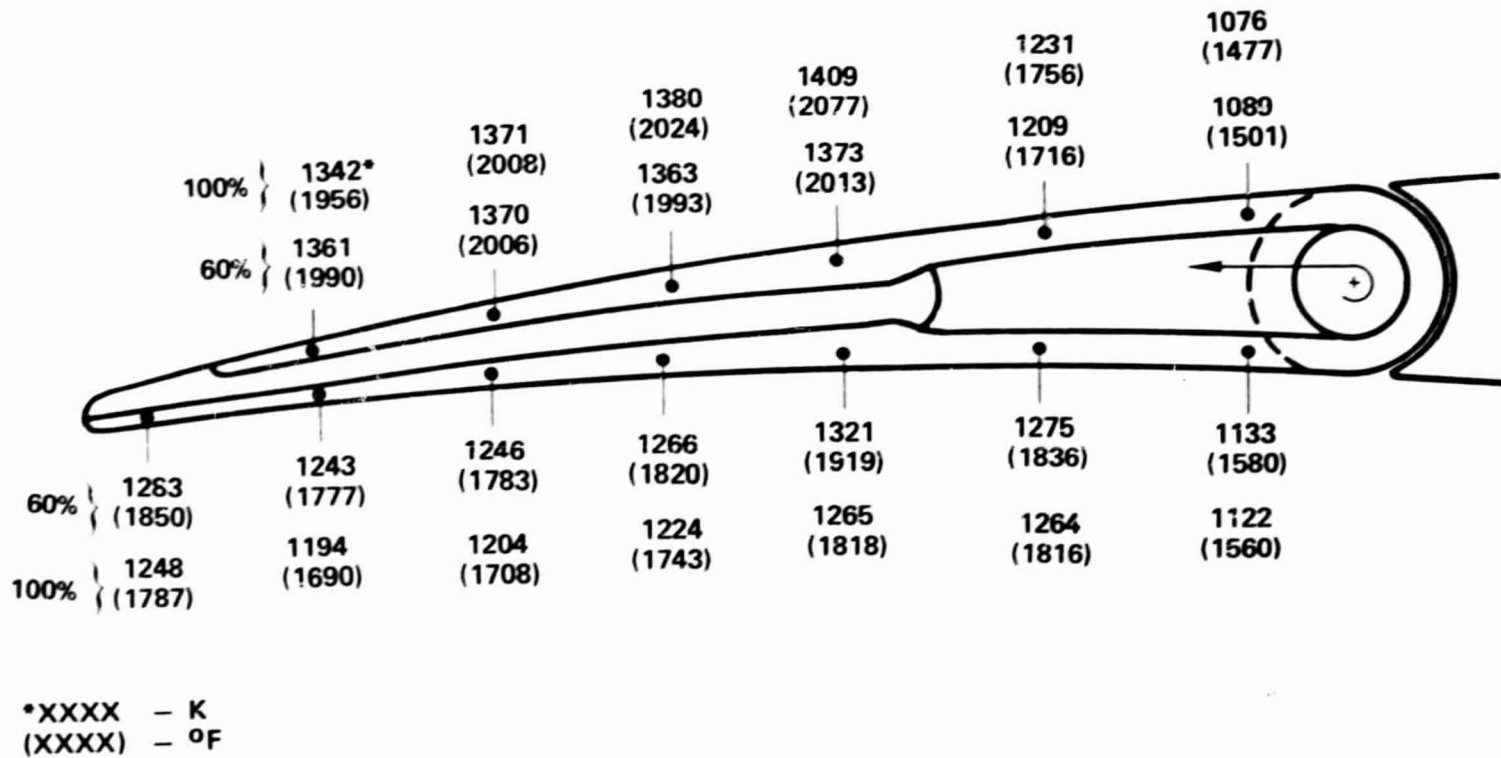


Figure 113. Articulated Trailing-Edge Stator Vane.

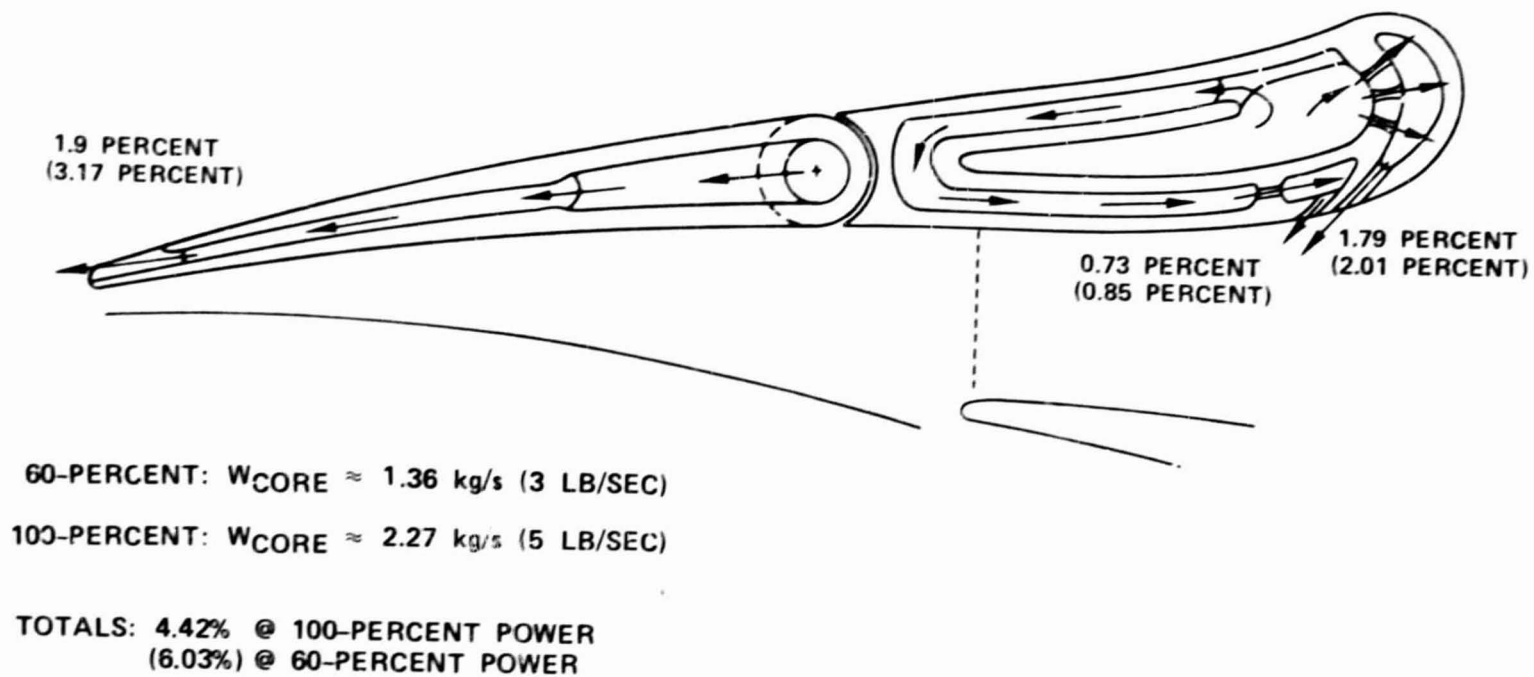


Figure 114. Articulated Trailing-Edge Stator Vane Cooling Flow Summary.

changes. It is believed that some benefit is achieved through this partial vane coverage, so that a slight decrease in local cooling flow is warranted.

The stationary sidewalls are easily accessible on the rear surface in a typical stator design. This allows employment of an efficient cooling scheme that uses square-array impingement from behind, coupled with hot-side film cooling.

All mechanical design details associated with the support method used for the stator and its influence on the cooling geometry of the sidewalls were beyond the scope of this program. As such, the design reflected no complications of this sort. An uncomplicated stator design was analyzed that used a cast sidewall section (or fabricated ring) with ribs located on the cold side to which a sheet metal impingement plate could be brazed. The ribs and local standoffs controlled the impingement-plate spacing from the sidewall back surface. These ribs divided the cooled surface between the vanes into zones. This zoning concept was selected because of static pressure gradients that existed on the flow-path side (where the flow is discharged). Additionally, this zoning allowed for different cooling intensities that corresponded to various gas-path conditions.

Figure 115 presents this stator cooling design viewed from the sidewall hot side. The stator back side was divided into five zones by ribs (represented in this figure by dashed lines). Two rows of film cooling holes were positioned at the center portion of the sidewall. These holes were staggered with respect to the flow streamlines. Different groups of holes in each row were fed with coolant from the five different zones on the back side. For example, Zone 1 fed four film holes in the first row, while Zone 2 fed only one. All the impingement holes were 0.038-cm (0.015 in.) in diameter, with the same dimensional plate thickness. The film holes were all 0.051 cm (0.020 in.) in diameter and were positioned at shallow angles [0.52 radian (~30 degrees)] with the surface. The film-hole positions were established by the position of static pressure isobars on the sidewall surface for both the 60- and 100-percent power conditions. These positions were carefully established to ensure a balanced air supply for proper film cooling to each hole within a zone. The primary pressure drops were across the film holes and, hence, metered the flow. The number of impingement holes in each zone was adjusted to supply enough flow for uniform film cooling.

It was assumed that upstream coolant from the final combustor slots would provide a film effectiveness of 0.20 at the sidewall leading edge, with appropriate depreciation through the channel. The sidewalls were designed to achieve a 1255K (1800°F) metal temperature level. Local hot spots that result during component

IMPINGEMENT HOLE 0.038 cm (0.015 IN.) DIA. COOLING FLOW TOTALS = 4.9% AT 100-PERCENT POWER
 = 5.9% AT 60-PERCENT POWER

ZONE 1 = 21 HOLES
 ZONE 2 = 5 HOLES
 ZONE 3 = 9 HOLES
 ZONE 4 = 9 HOLES
 ZONE 5 = 14 HOLES

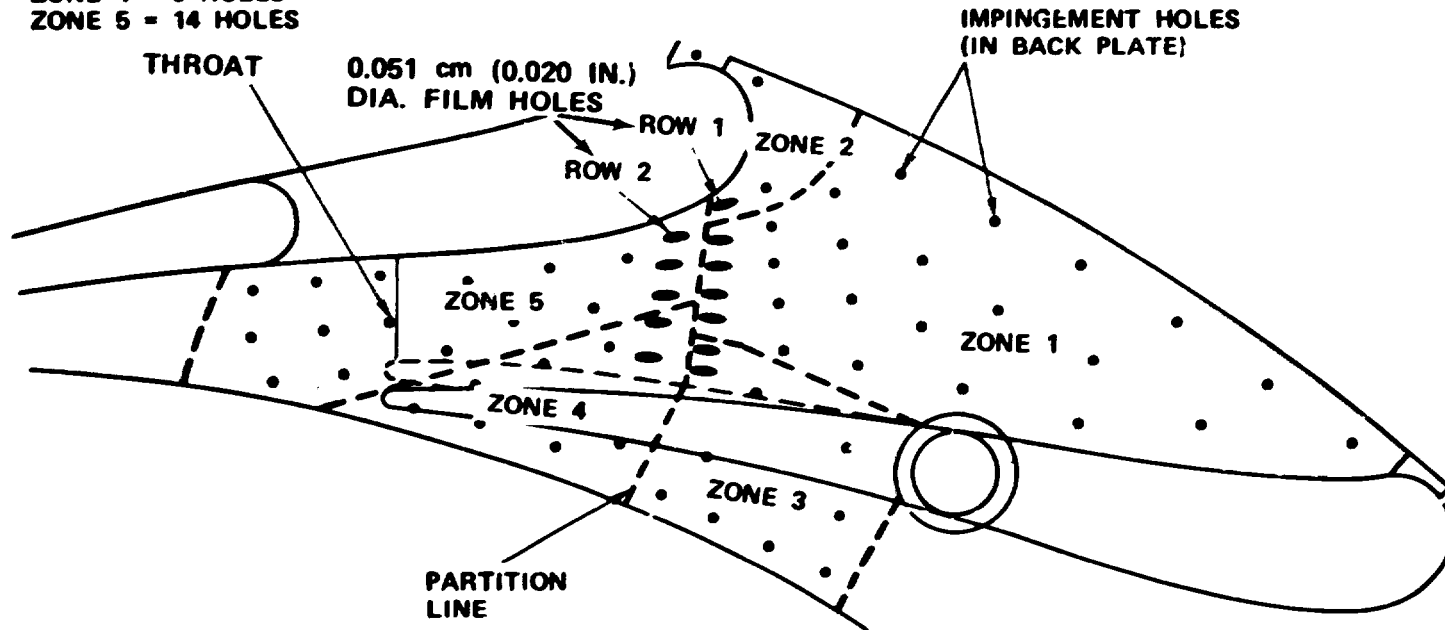


Figure 115. Articulated Trailing-Edge Stator Sidewall Viewed from Flow-Path Side.

testing could be corrected by increasing or moving the impingement holes. The 100-percent power condition presented the most severe design constraint on the forward region of the sidewall, while the 60-percent power condition presented severe design constraints in the downstream region. Forward and rear sidewalls were identical in cooling configuration. For both sidewalls, the total cooling flow usage was 4.9-percent core flow at 100-percent power, and 5.9-percent core flow at 60-percent power. As noted, these flows were as high -- or higher -- than those experienced for the vane. This is not typical for axial stators at high temperatures.

6.7 Movable Sidewall Stator - Mechanical Substantiation

6.7.1 Mechanical Description

The mechanical substantiation of the cooled, movable sidewall stator was based on the selected cycle conditions established for the articulated trailing-edge variable stator concept. The optimized 100-percent power vector diagram established for the articulated trailing-edge design was also used for this configuration. The mechanical design of the articulated trailing-edge vane and sidewalls -- particularly the cooling configuration definition with metal temperature predictions -- was performed beyond the substantiation level. Because of this, extensive understanding of inherent variable stator design difficulties was obtained. Most of the boundary condition behavior that influenced the thermal design of the movable sidewall stator was similar to that of the articulated trailing-edge design. Therefore, the movable sidewall stator study was not extensive and focused primarily on areas where differences might occur.

The baseline movable sidewall design, which employed a translating sidewall section, is shown schematically in Figure 116. An engine turbine-section conceptual layout was also made (Figure 117). Construction of the stationary portions of the sidewalls for the baseline and alternate approaches to this concept are predicted to be identical to those of the articulated trailing-edge design. These stationary portions would be fabricated from cast Mar-M 247 pieces (or a continuous ring), with sheet-metal impingement plates brazed onto the ribs with standoffs located on the rear surface. The cooling configuration would be zoned to provide for a flow distribution proportional to hot-side, heat-transfer rate variations. However, exact details of the zoning design were not studied. The movable sidewall section will be constructed in a similar fashion and zoned to provide a cooling-flow distribution suitable for all power conditions. An alternate design approach using laminated sheets could also be used for the movable sidewall section. This would provide additional flexibility, if required.

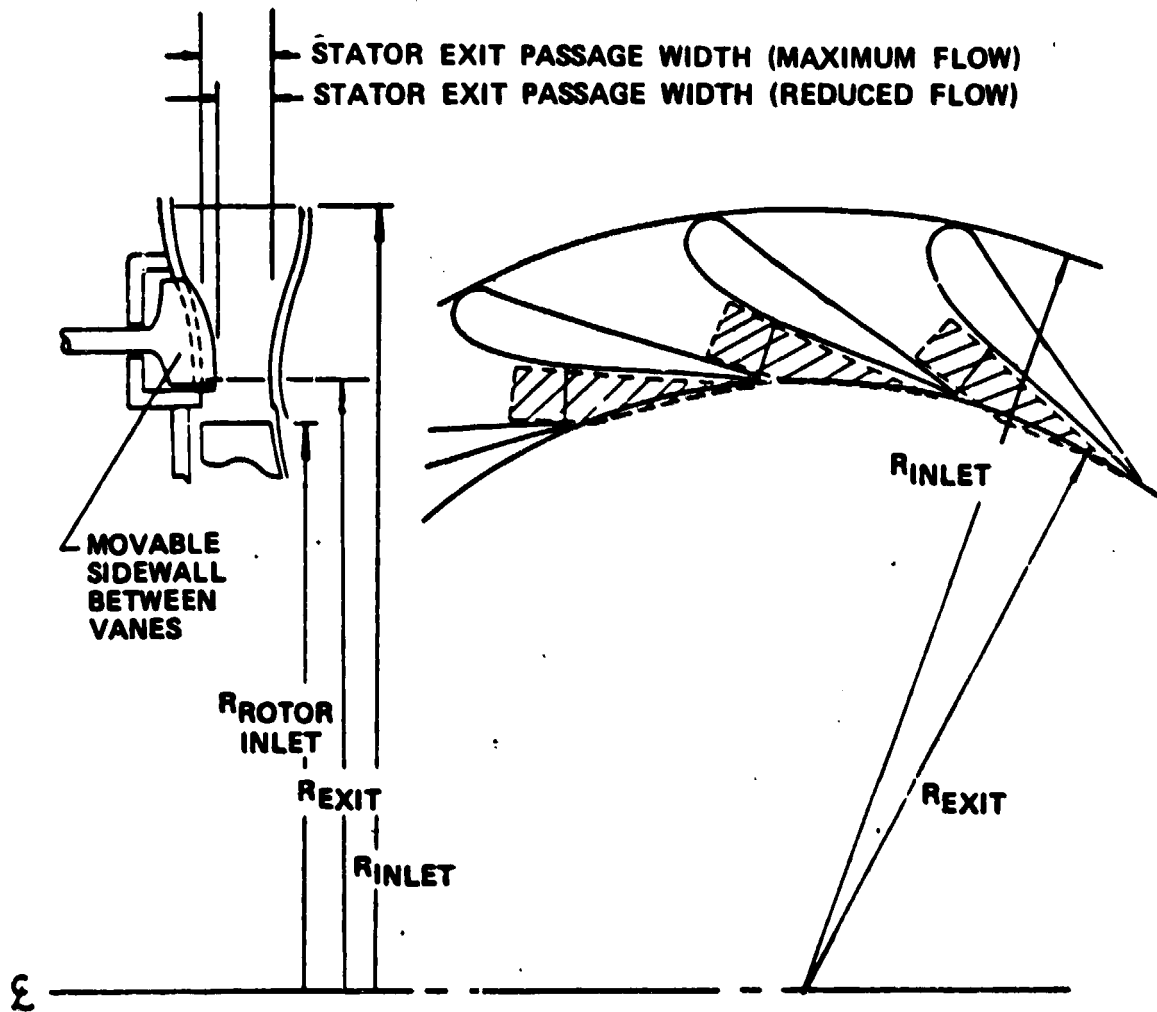
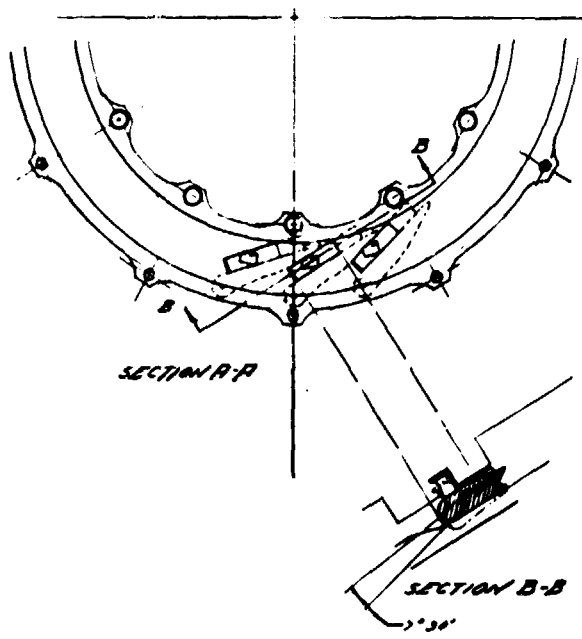
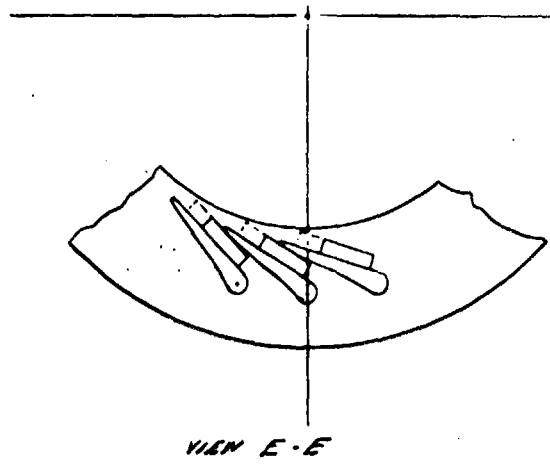
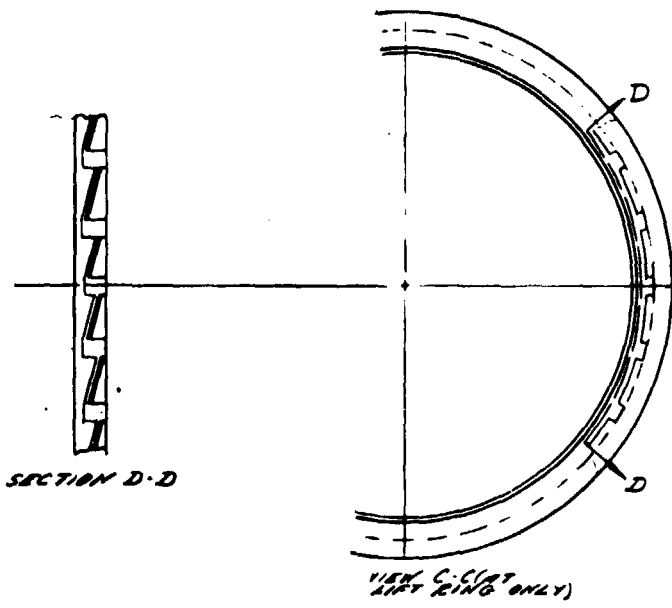


Figure 116. Movable Sidewall - Baseline Configuration.

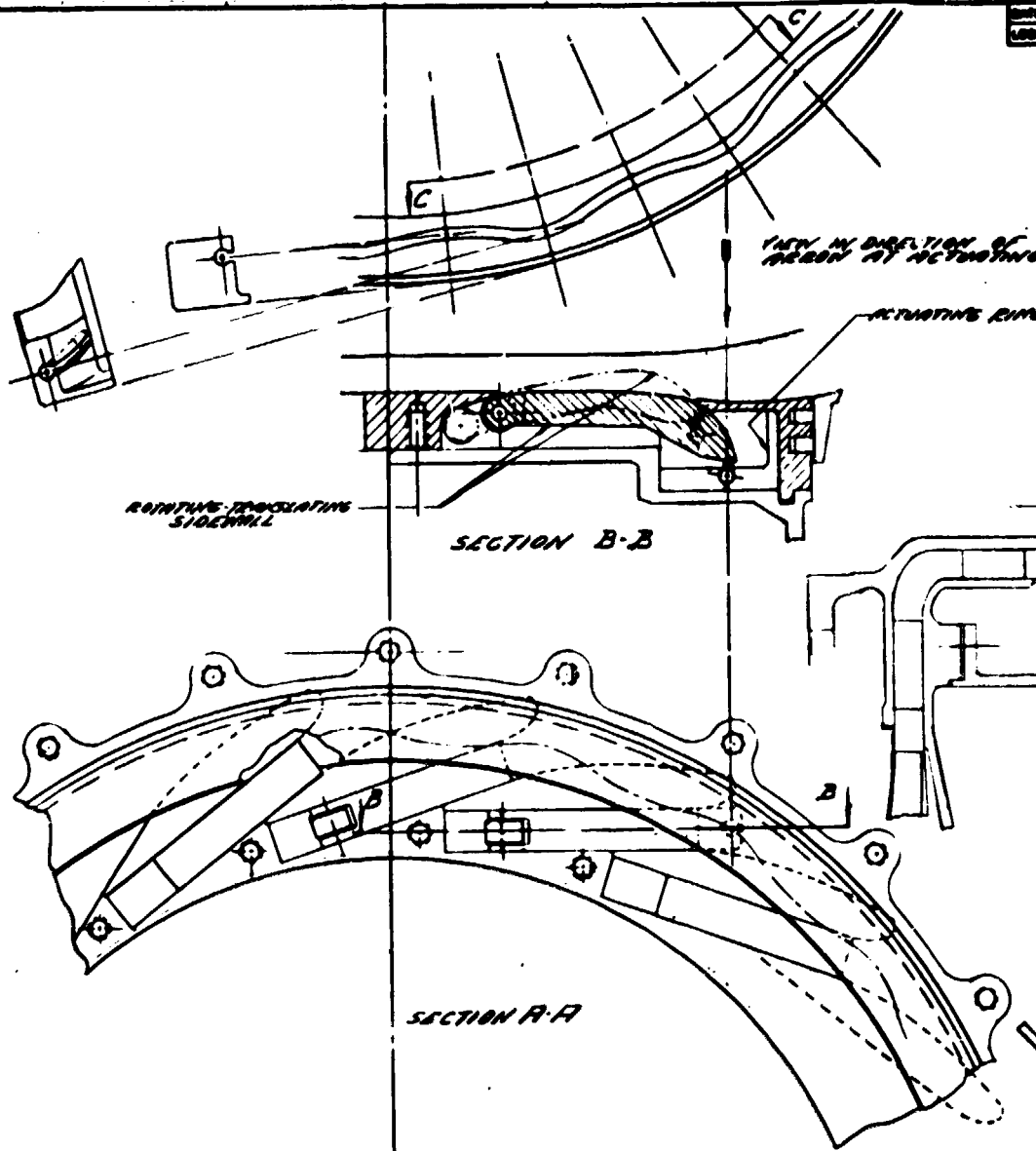


ROLLOUT FRAME

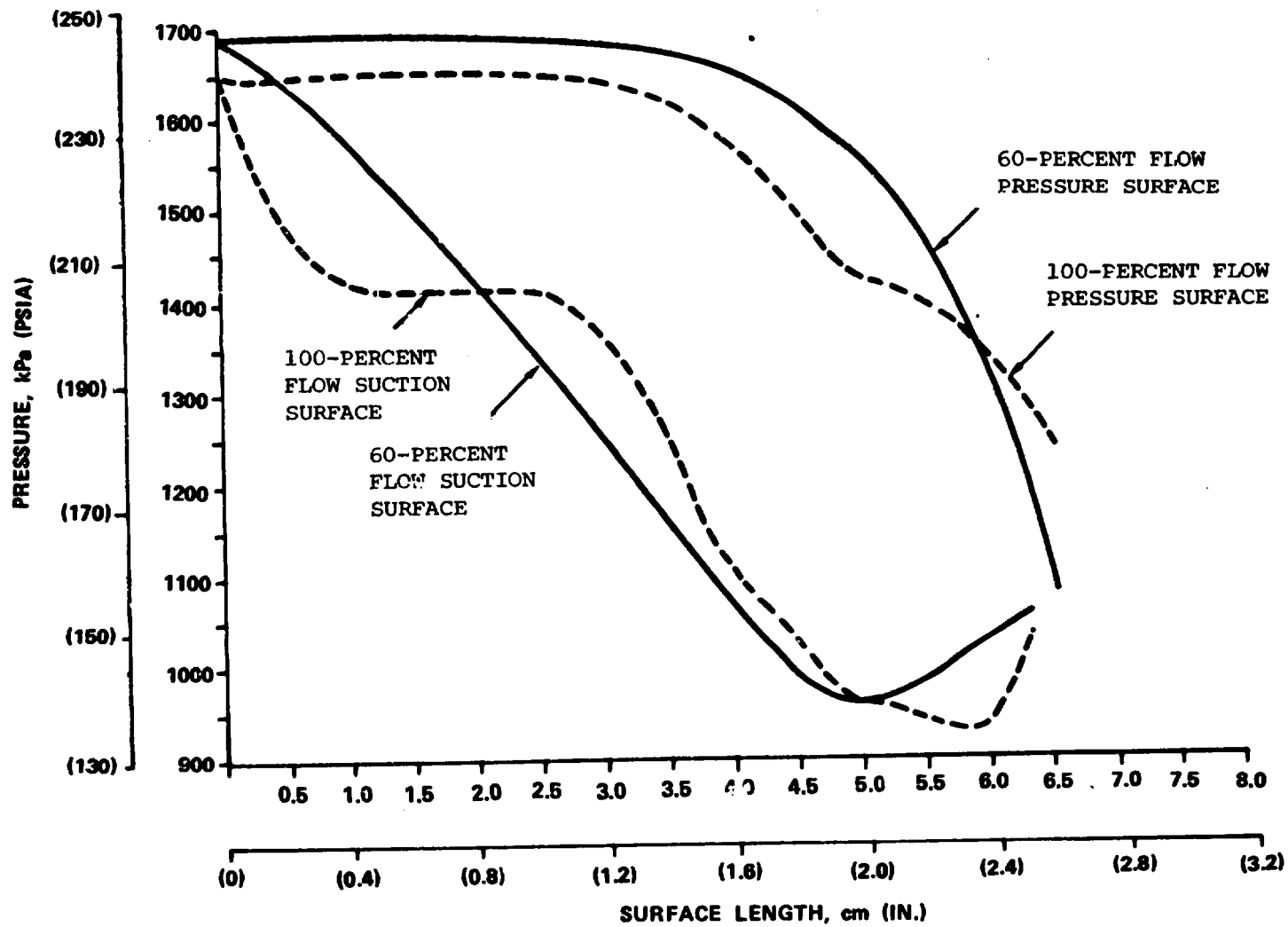
Two alternate conceptual stator mechanical design layouts were considered during the study. One design has a variable sidewall with a rotating and pivoting stator insert. The stator inserts are radially supported at the pivot and axially positioned by a rotating lift ring (view C-C in Figure 118). Rotation of the lift ring moves the stator insert into the stator throat (section B-B in Figure 118), thus reducing the flow area. The stator inserts and lift ring were built into a sealed plenum that controls the cooling-air supply to the inserts. The use of parallel sidewalls on the stator insert will provide close dimensional control between the inserts and the stator sidewall, thus minimizing leakage.

Figure 118 shows the variable sidewall concept with a rotating-translating stator insert. This concept is similar to the rotating-pivoting approach, in that the stator inserts and an actuating ring are also built into a sealed plenum to provide control over the cooling-air supply. However, the actuating ring (section B-B) has a machined groove with a 3-dimensional cam shape, with both a lift motion (view C-C) that axially positions the stator insert, and a translating (sliding) motion that allows radial positioning of the insert. For conceptual purposes, a roller is shown supporting the opposite end of the stator insert. However, to facilitate sealing, a sliding contact surface may be preferable.

The aerodynamic analysis of the movable sidewall stator vane resulted in loading diagrams that showed both similarities and differences to the articulated trailing-edge final design. The velocities produced static pressures on the vane suction- and pressure-side surfaces at 60-percent and 100-percent power, as illustrated in Figure 119. At the 60-percent power condition, the pressure distribution was quite similar to that occurring on the primary stator design (Figure 107). The only noticeable difference in behavior was a deceleration in flow and a rise in static pressure approaching the suction-side trailing edge -- a behavior that had little impact on the cooling design. The 100-percent power suction- and pressure-side static pressures fell off in steps towards the trailing-edge and behaved differently than the articulated trailing-edge, 100-percent power pressures. It should be noted that the continuing presence of high static pressures on the forward half of the pressure-side surface precluded film-cooling discharge in this region. Also, on the suction-side surface [at about 2.03-cm (0.80-in.) surface distance], a region existed where pressure is the same at both 60- and 100-percent power. This cooling discharge location provided a relatively constant cooling-circuit pressure drop and flow rate and ensured small metal temperature swings from one condition to another. Figures 119 and 107 show that the aft region on both suction-side and pressure-side surfaces have smaller 60- to 100-percent power



FOLDOUT FRAME



185 Figure 119. Rotating-translating Sidewall Concept, Surface Static Pressure Distribution

pressure changes than with the articulated trailing-edge. This could also facilitate improved usage of cooling air.

The velocity solution utilized standard Garrett computer tools to derive solutions for turbulent heat-transfer coefficients on the airfoil surface. Results for both surfaces are shown in Figure 120 at 100- and 60-percent power conditions. The suction-side surface heat-transfer coefficients are comparable to those of the articulated trailing-edge design (Figure 108). The levels are similar, with the only exception being a reduction in the suction gill region heat-transfer rate in the movable sidewall design at both power conditions -- particularly at the 100-percent power condition. It is anticipated that suction-side internal cooling geometry and flow rate will be similar in the two vanes and will produce similar metal temperature results. The pressure-side surface heat-transfer coefficients, when compared with Figure 109, were noticeably lower behind the stagnation cylinder region and rose to similar levels approaching the trailing-edge. For the movable sidewall stator, identical pressure-side heat-transfer coefficients levels existed at 60-percent and 100-percent power for a major portion of the surface, that facilitated cooling-flow rate optimization.

The vane cooling configuration selected for the preliminary design concept is shown in Figure 121. It is apparent from Figure 119 that film discharge on the pressure-side forward region is not achievable due to the lack of preswirl potential, and is not warranted because of low gas-side heat-transfer at this location. Further improvements could be made by moving the suction-side, leading-edge impingement discharge point further aft, to take advantage of the pressure equalization at 50- and 100-percent power.

Figure 122 shows the final movable sidewall vane design, including the proposed cooling configuration. Problems were incurred in the location of vane coolant-discharge. This was due to the movable sidewall coverage of the vane suction-side surface, and to a lesser extent, to the pressure-side surface (at 60-percent power). To take advantage of the pressure cross-over point, leading-edge impingement cooling-flow discharge was moved as far aft in the gill region as possible. This location is about 1.78 cm (0.70 in.) from the stagnation point (Figure 119). Complete optimization of the location is not possible, due to the presence of the movable sidewall. Also, an overlap problem could occur if the discharge was moved further downstream of the vane. Since pressure-surface film coolant was discharged as far aft as possible, this potential problem was not incurred. The trailing-edge discharge of suction-side coolant was compatible with the unique geometry problem of the movable sidewall design. At point 'A' in Figure 122, the sidewall height on the pressure surface was 0.41 cm (0.16 in.) above the suction-side surface on the same vane

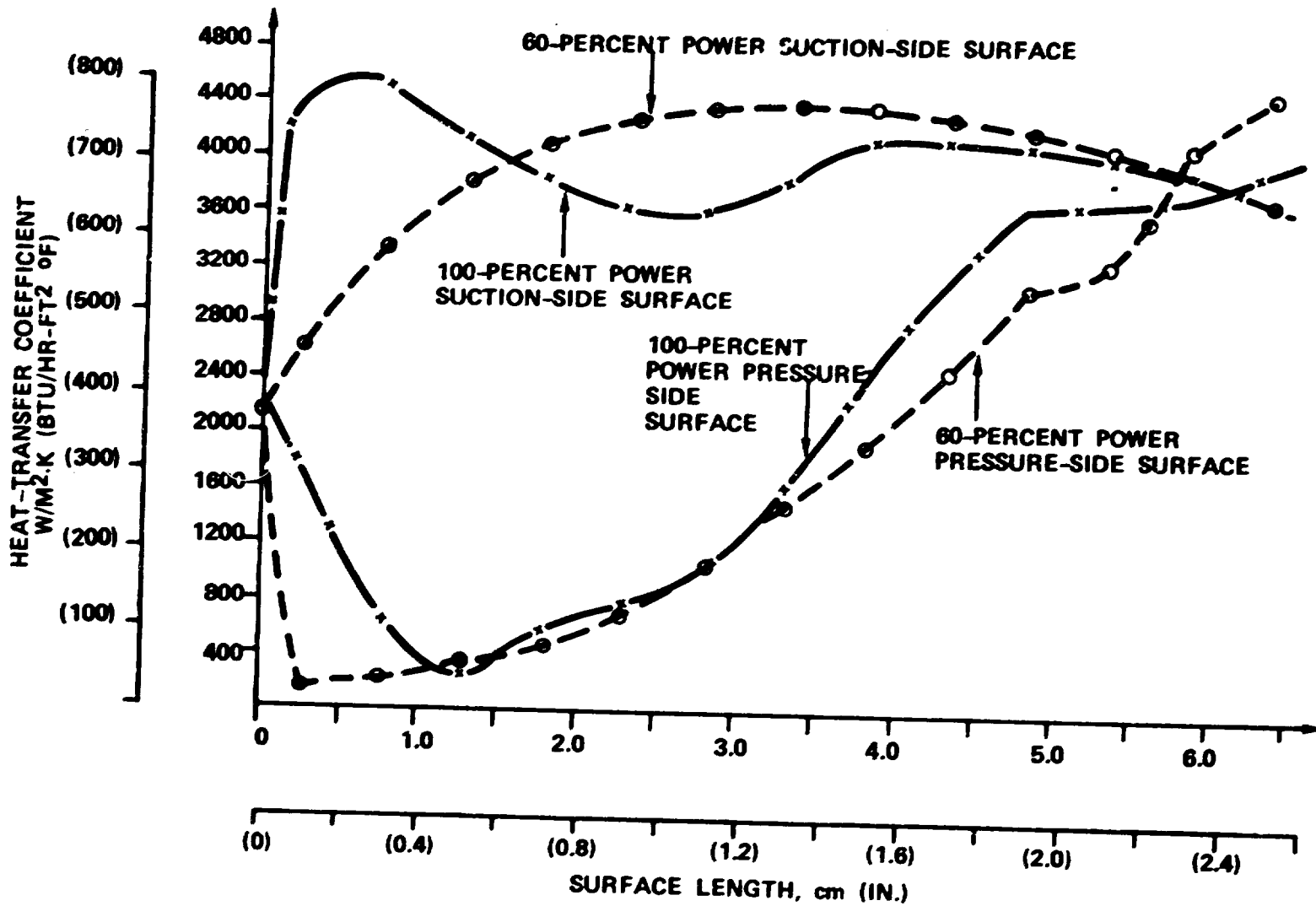
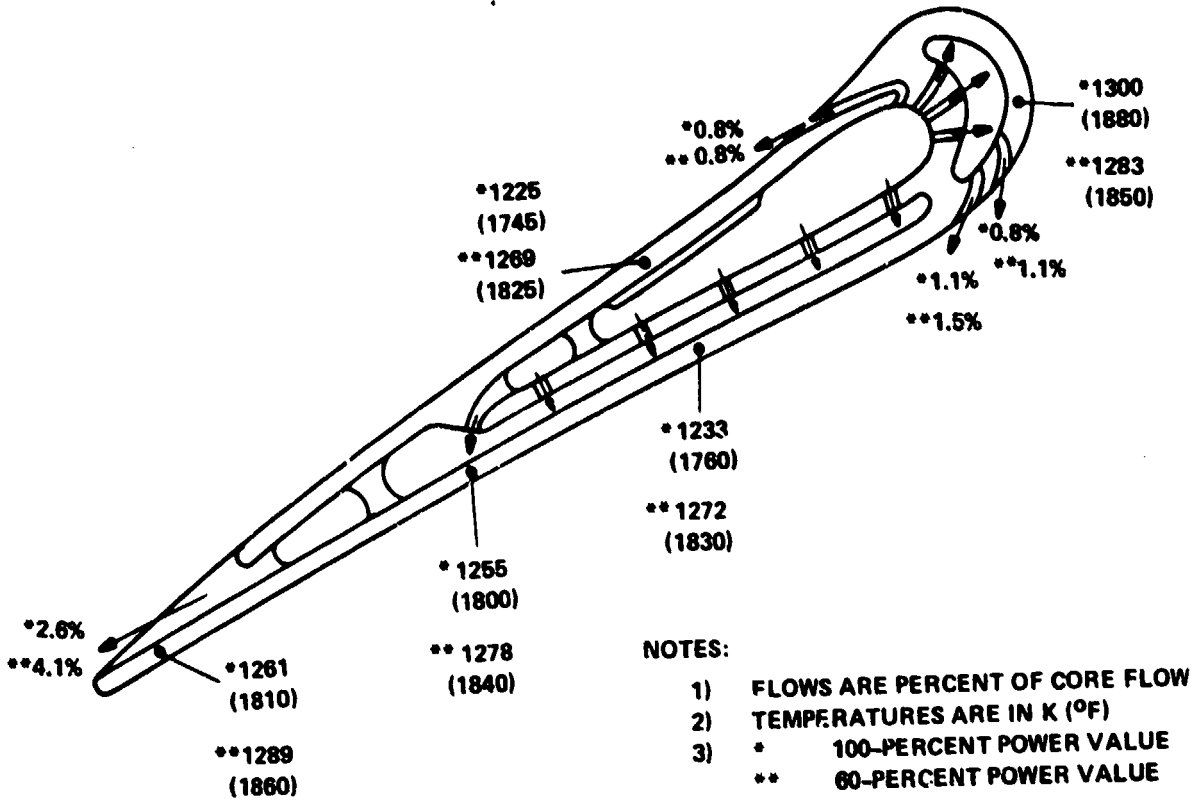


Figure 120. Rotating-translating Sidewall Concept, Heat Transfer Coefficients



$T_4 = 1644\text{K} (2500^\circ\text{F})$
 $T_{\text{GAS}} = 1939\text{K} (3030^\circ\text{F})$ FOR 0.2% FLOW
 $T_{\text{COOL}} = 744\text{K} (880^\circ\text{F})$

100-PERCENT POWER

$T_{\text{BULK}} = 1255\text{K} (1800^\circ\text{F})$
 $W_G = 2.27 \text{ kg/s} (5 \text{ LB/SEC})$
 $W_C = 5.3\% W_G$

60-PERCENT POWER

$T_{\text{BULK}} = 1278\text{K} (1840^\circ\text{F})$
 $W_G = 1.36 \text{ kg/s} (3 \text{ LB/SEC})$
 $W_C = 7.5\% W_G$

Figure 121. A Preliminary Concept for the Movable Sidewall Vane .

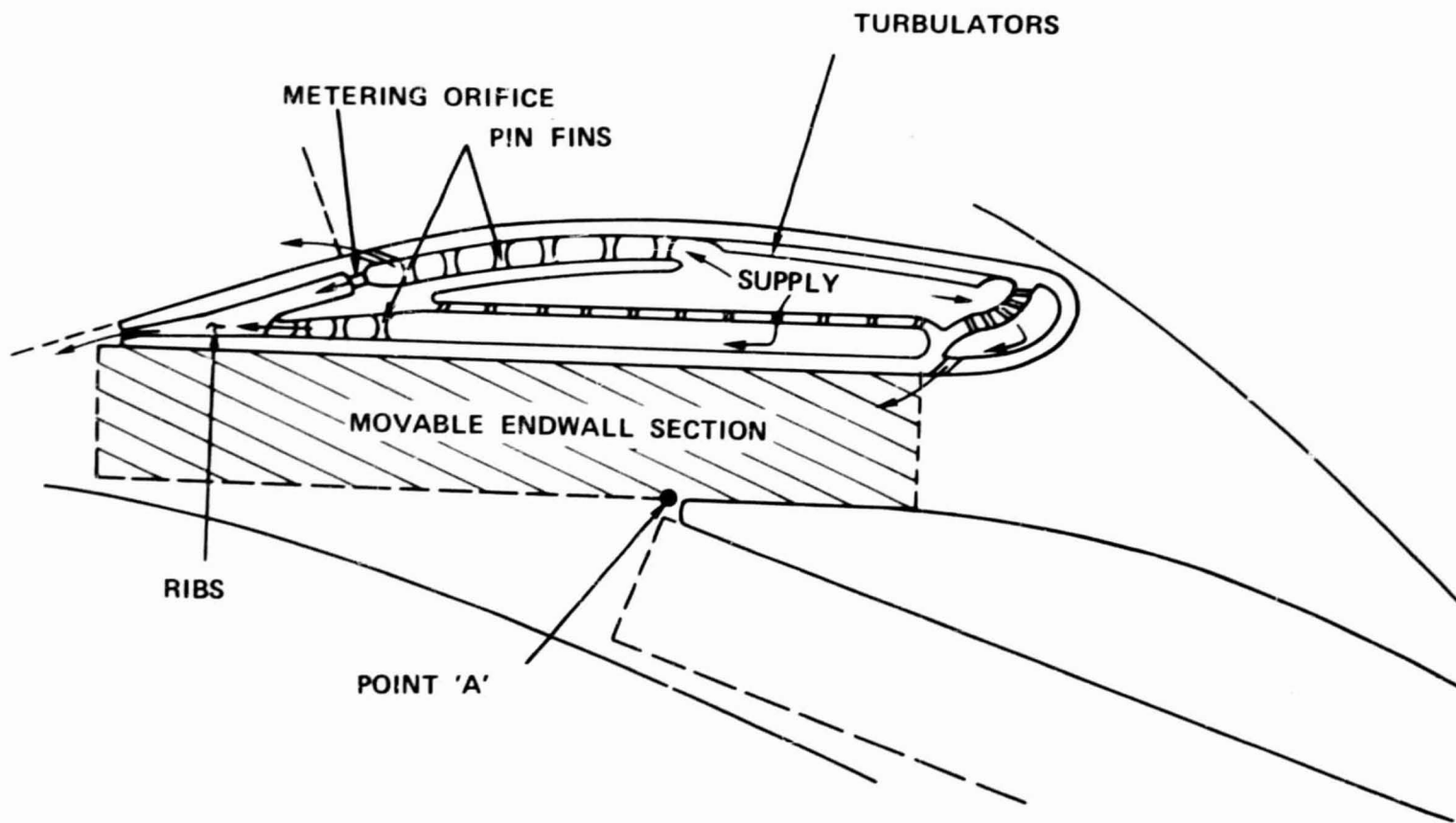


Figure 122. Movable Sidewall Configuration Showing Vane Cooling.

at the 60-percent power condition. The adjacent movable sidewall height tapered back to zero at this location. It is anticipated that the trailing-edge coolant-flow discharge will aid in the deflection of main flow from this blockage for part of the vane span and will fill in the wake generated by the 0.152-cm (0.060-in.) thick trailing-edge over the remainder of the vane span.

Cooling air was supplied to the central cavity of the vanes through the sidewalls. Turbulators were located on the pressure-side forward section and provided sufficient cooling at this wall, since gas-side heat-transfer at this location was low. As in the articulated trailing-edge vane design, impingement was used on both the leading-edge and the suction-side to provide high internal cooling rates in these critical areas. Pin-fin arrays were used as shown with spacing tailored to meet augmentation demands. Upstream of the trailing-edge discharge point, ribs accelerated the coolant, and provided increased surface area for effective cooling of both vane surfaces. In general, the vane was thick enough to provide adequate flow area for near optimum cooling flow distribution. Figure 123 presents the predicted cooling-flow distribution necessary to produce an average metal temperature of 1255K (1800°F) and to hold peak values below 1366K (2000°F). The articulated trailing-edge design showed problems with excessive temperatures. This was due to flow-rate limitations caused by the slender vane profile. However, this design should not incur the same limitations, due to its more advantageous shape. Moreover, no large swings in metal temperature occurred at the exposed portion of the leading-edge region at 60-percent power, since the coolant circuit held a constant physical flow rate. The 6.8-percent total coolant usage in the vane at 60-percent power was greater than that of the articulated trailing-edge vane. This resulted in a more constant metal temperature in this portion of the vane.

The portion of the vane covered by the movable sidewall the will have significantly lower temperatures at 60-percent power and could result in thermal-fatigue problems. However, the extent of this problem was not predictable within the scope of the program.

The sidewall cooling problems were similar to those experienced with the articulated trailing-edge stator sidewalls. The mainstream static pressures on the sidewalls are presented in Figure 124 for a midchannel streamline. Film-cooling flow discharge was restricted to a region at or downstream of the movable insert leading-edge. This resulted in a unique solution to the film-cooling problem. The leading edge of the insert was not sealed and was sized as a film-cooling slot. This provided a 2.5-percent core flow at 100-percent power with a pressure drop as shown on Figure 124 of 248 kPa (36 psia) minus impingement circuit drop on

100% W_{CORE} ≈ 2.27 kg/s (5 LB/SEC)
60% W_{CORE} ≈ 1.36 kg/s (3 LB/SEC)

TOTALS: 4.4% @ 100-PERCENT POWER
(6.8%) @ 60-PERCENT POWER

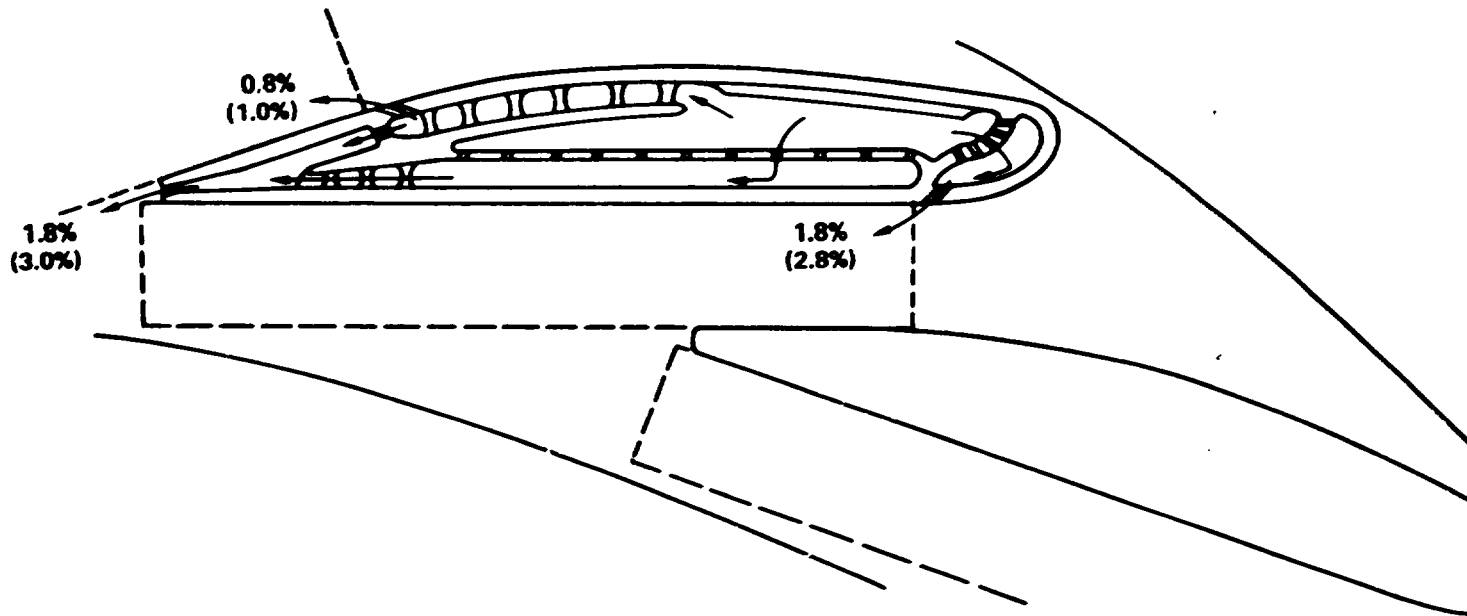


Figure 123. Movable Sidewall Configuration Vane, Flow Distribution.

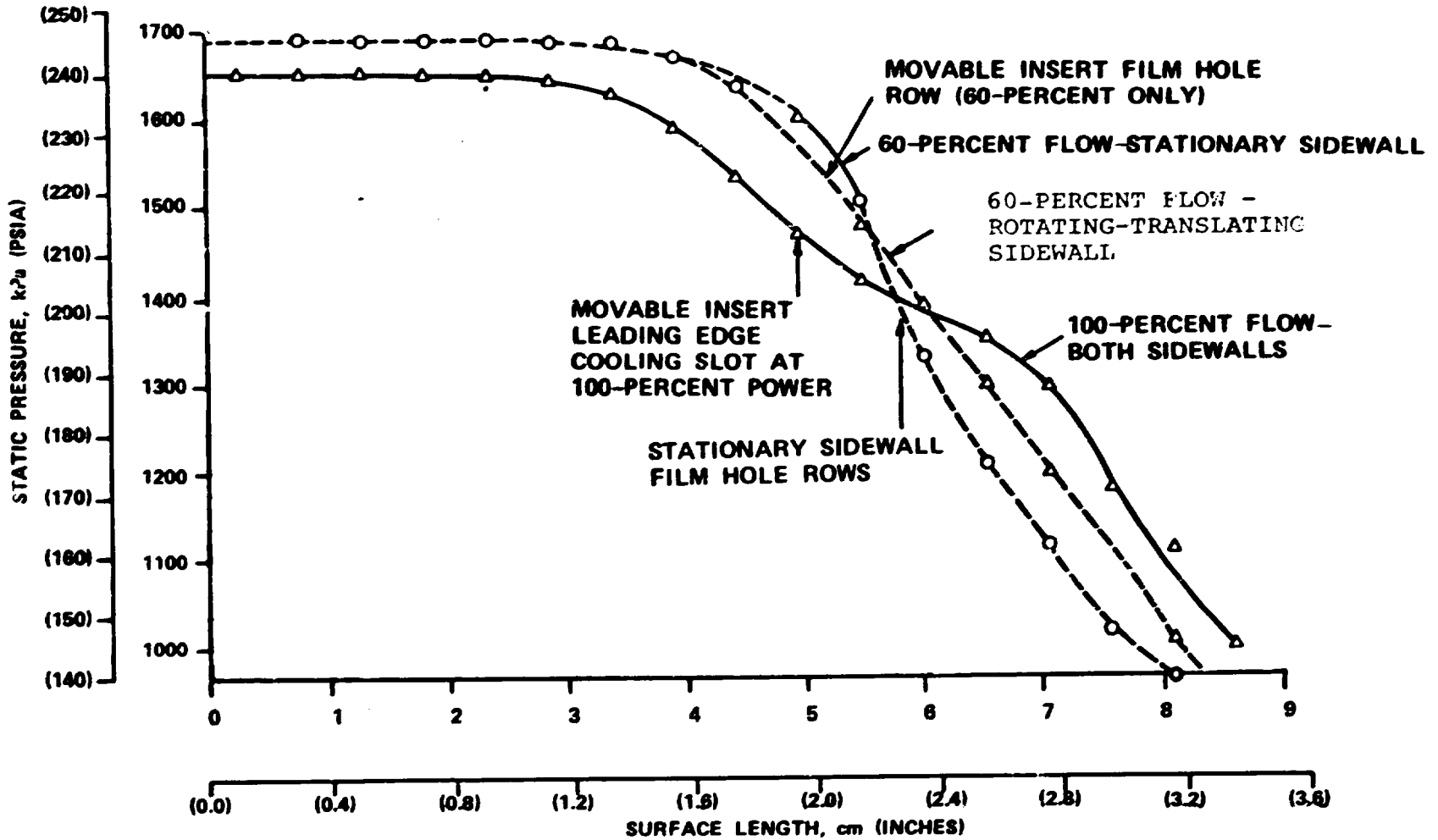


Figure 124. Static Pressure Distribution Along the Midchannel Streamline of the Rotating-translating Sidewall Stator

the rear of the sidewall. Forward stationary sidewall cooling was the same as the articulated trailing-edge stator cooling and allowed an upstream effectiveness of 0.20 and provided rear-side impingement. About 50-percent of the 2.5-percent core flow that exited this slot came from upstream. The other 50-percent came from cooling the movable insert exposed surface internally using an impingement method. This core flow was ducted forward to the slot. A section of the sidewall downstream of the vane trailing-edge was cooled with the additional 0.5-percent core flow.

At 60-percent power, the available pressure drop at the insert leading-edge was reduced. To supplement this flow and to hold a constant physical flow, film-cooling holes were added to the insert. These holes are exposed only with downstream rotation of the sidewall insert. At 100-percent power, the holes are covered and are positioned behind a close-fitting seal on the back side of the sidewall. In this condition, no cooling flow exists. The holes were sized to provide exits for insert impingement coolant and to maintain the same total physical flow. At 60-percent power, the coolant exiting the leading-edge slot enters from the upstream portion of the sidewall. This is illustrated in Figure 125. The stationary aft sidewall has two rows of film holes located as shown on Figure 124 and uses the same 3.0-percent total flow at maximum power. Therefore, the total flow from both sidewalls was 6.0 percent at 100-percent power and 10.0 percent at 60-percent power. With the sidewall heat-transfer coefficients shown in Figure 126, the selected flow rates produced the desired 1255K (1800°F) temperature level on both sidewalls.

TOTAL SIDEWALL FLOW = 6.0-PERCENT 2.27 kg/s (5 LB/SEC CORE) AT 100-PERCENT CORE FLOW
 [10.0-PERCENT 1.36 kg/s (3 LB/SEC CORE)] AT 60-PERCENT CORE FLOW

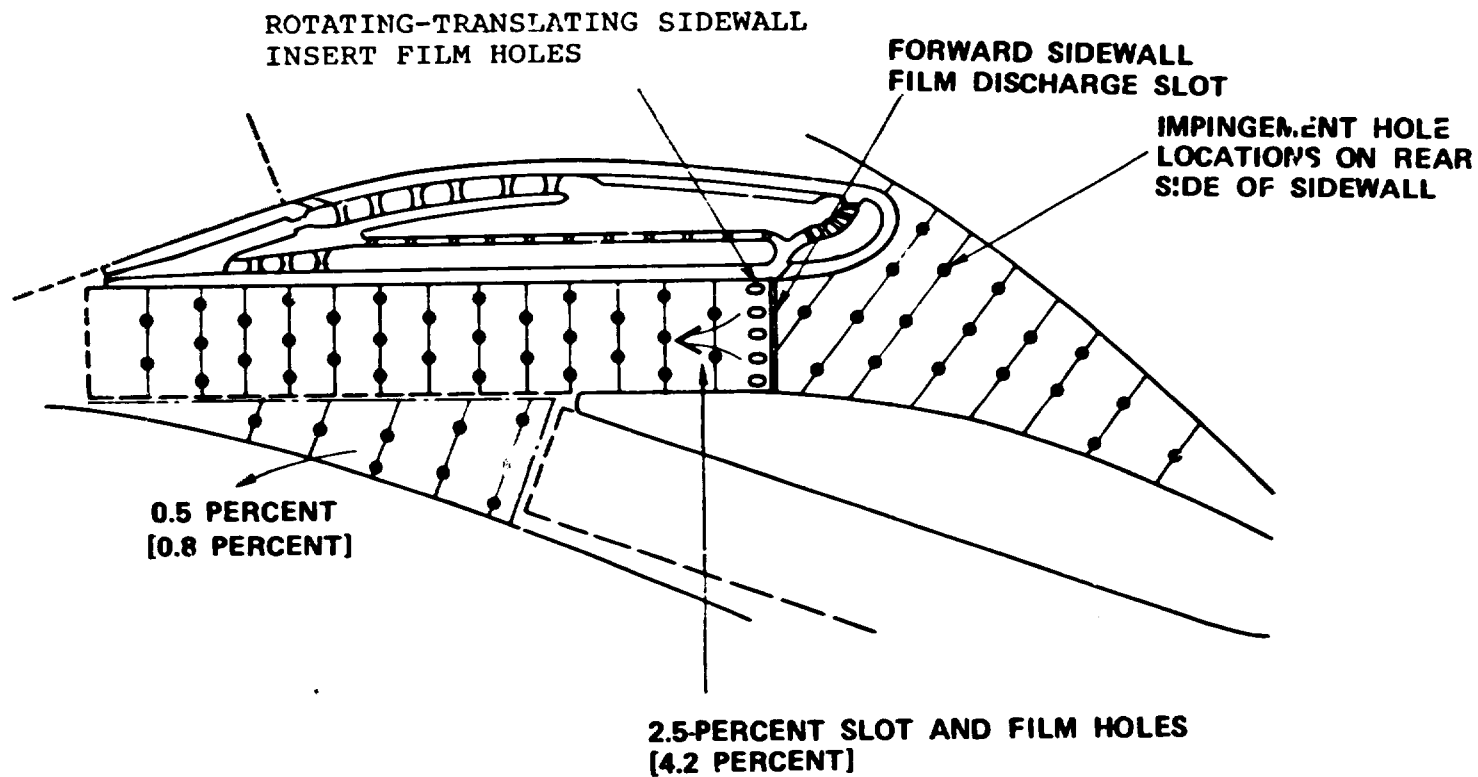


Figure 125. Rotating-translating Sidewall Configuration Cooling, Forward Sidewall at 60-percent Power.

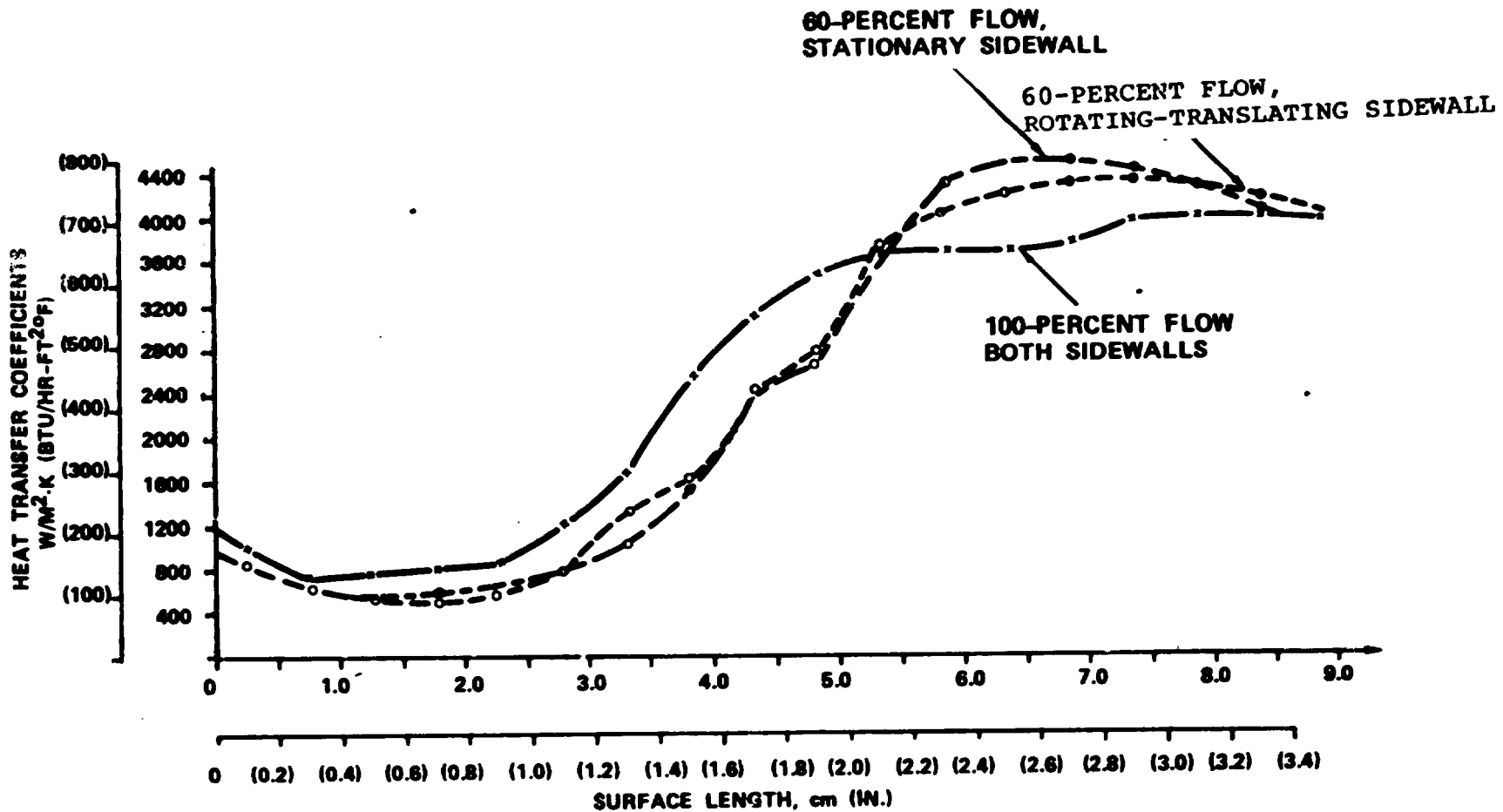


Figure 126. Rotating-Translating Movable Sidewall Stator, Heat Transfer Coefficients Mid-Channel Streamline.

7.0 TASKS III AND IV - COOLED ROTOR DETAILED AERODYNAMIC DESIGN AND MECHANICAL SUBSTANTIATION

7.1 Cooled Rotor Detailed Aerodynamic Design

7.1.1 Rotor-Blade Geometry Definition

An optimized 3-dimensional vector diagram was used to establish the rotor inlet and exit flow-path dimensions. A preliminary estimate of the rotor hub and shroud contour was then defined from an analytical curve-fitting routine, with specified coordinates established from this diagram. A good initial estimate of the contours was obtained by adjusting the curve fit until a smooth meridional rotor area distribution was achieved. To complete the initial definition of the rotor geometry, a specific blade angle and thickness distribution was required. Since the selected rotor design was based on a 0.17-radian (10-degree) rotor inlet angle, initial estimates of the blade-angle distribution were based on previous nonradial rotor design experience. The main design objectives were to simultaneously optimize rotor velocity distributions and to minimize blade lean. Initial thickness distribution was based on the 2-dimensional, finite-element stress analysis. These quantities were input to a radial turbine geometry program along specified quasi-orthogonal station lines. The resultant data matrix was then curve-fit to define the total blade geometry. The geometry program is a modification of an existing centrifugal impeller geometry program that allows arbitrary blade definition. An advantage to this program is that the nodal-point spacing along the station lines could be used to define geometric streamlines for the internal flow analysis. Therefore, defining the rotor blade-angle distribution along streamlines is more meaningful from an aerodynamic standpoint. However, from a mechanical standpoint, defining blade thickness along the station lines is more meaningful. In addition, if unique localized blade thicknesses were required, the station lines could be closely spaced. This would provide accurate blade thickness definition. The rotor-blade angle distribution defined along the streamlines combined with the blade thickness definition along the station lines form unique nodal points that are input to the geometry program as a function of radial and axial length. Once the final blade geometry is defined, the required tooling section coordinates can be calculated. The radial rotor geometry program capabilities are illustrated in Figure 127.

7.1.2 Rotor Aerodynamic Flow Analysis

The manner in which the profile directs the gas flow from known inlet-to-known exit conditions (i.e., blade loading) was used as the criterion for determining aerodynamically acceptable blade profiles. Acceptable blade loadings were characterized by:

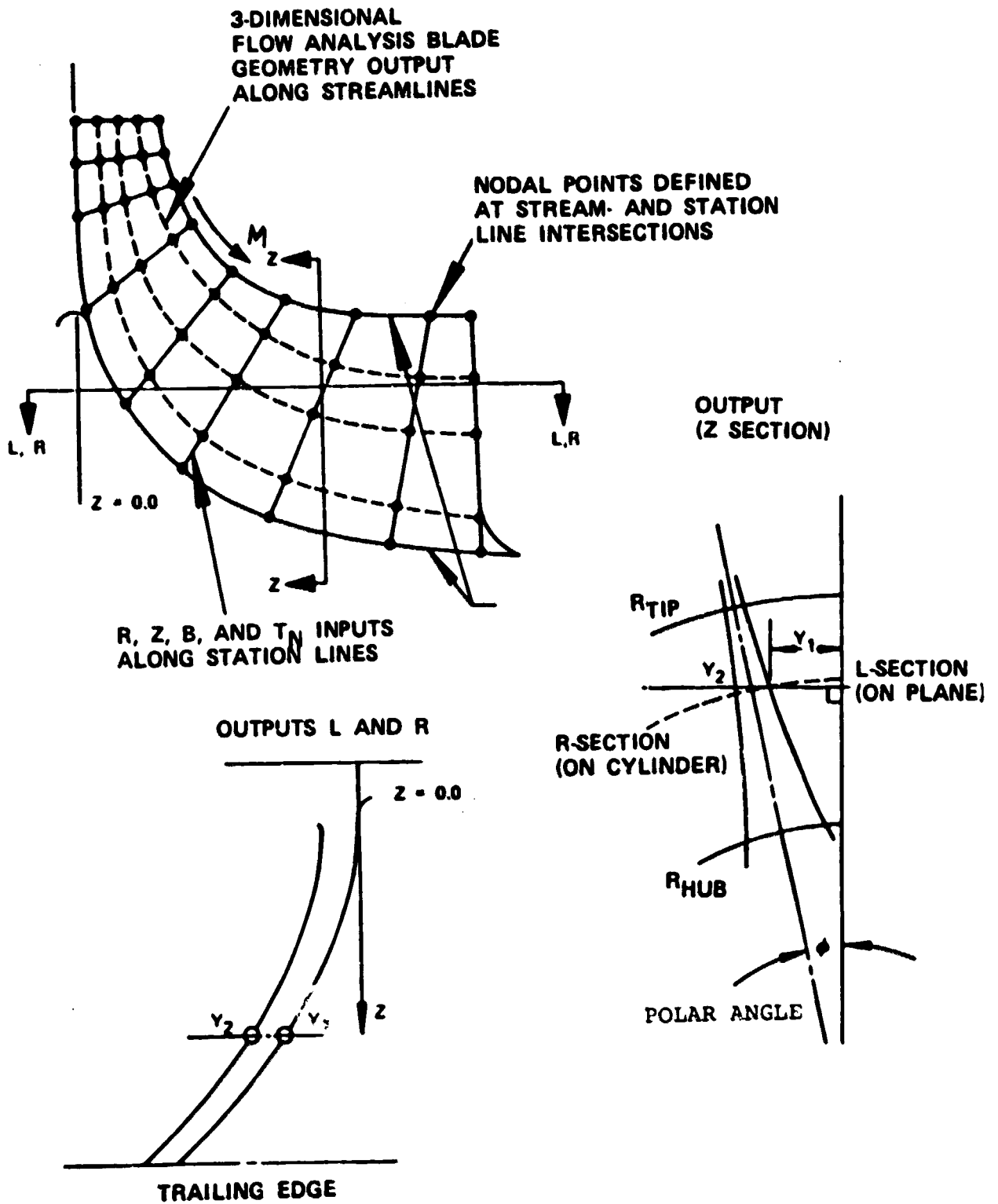


Figure 127. Radial Rotor Geometry Program.

- o High reaction from inlet to exit. This condition was initially established at the rotor meanline by maintaining 50-percent reaction in the 1-dimensional vector diagram optimization.
- o Monotonically increasing midchannel velocities along all streamlines.
- o Minimum suction-surface diffusion followed (when possible) by rapid acceleration.

To perform the internal flow analysis, the level and distribution of losses in the rotor had to be defined. Total stage-loss magnitude was determined from the efficiency analysis described earlier. The stator loss was estimated from stator reaction rig tests, with the remaining loss assigned to the rotor. Since rotor loss distribution in both the through-flow and radial directions was difficult to establish, the losses in the through-flow direction were assumed linear. For the radial direction, previous rotor-exit survey results showed that the radial loss characteristics for radial turbines exhibited certain similar characteristics. In the hub region the losses were low (due to lower loading level), then progressively increased to about 80 percent of the blade. Blade losses remained fairly uniform to the rotor tip. For the variable-area radial turbine, the radial-loss distribution was based on recent test data taken for the Garrett Model GTP305-2 Radial Turbine Program. This loss level was then adjusted to agree with the predicted performance level of the selected design.

The computer program for the rotor internal flow analysis solved the radial-equilibrium equation by satisfying the continuity, momentum, and energy equations in the meridional plane in a manner similar to that described in references (34,35). Blade surface velocities were computed from the local rate of change in moment of momentum, the condition of zero absolute vorticity, and linear velocities between suction- and pressure-side surfaces. Stanitz (36) showed that this method produced satisfactory results when compared with relaxation solutions of the potential flow equation. Numerous iterations between the geometry program and the internal flow analysis program were required to achieve satisfactory blade loading for each thickness distribution examined.

The final rotor flow-path configuration is presented in Figure 128. The final rotor blade-angle distribution for a 0.17-radian (10-degree) inlet blade angle is presented in Figure 129 as a function of percent meridional distance. Also shown are the locations at inlet and exit points, where flow deviations from the blade were assumed.

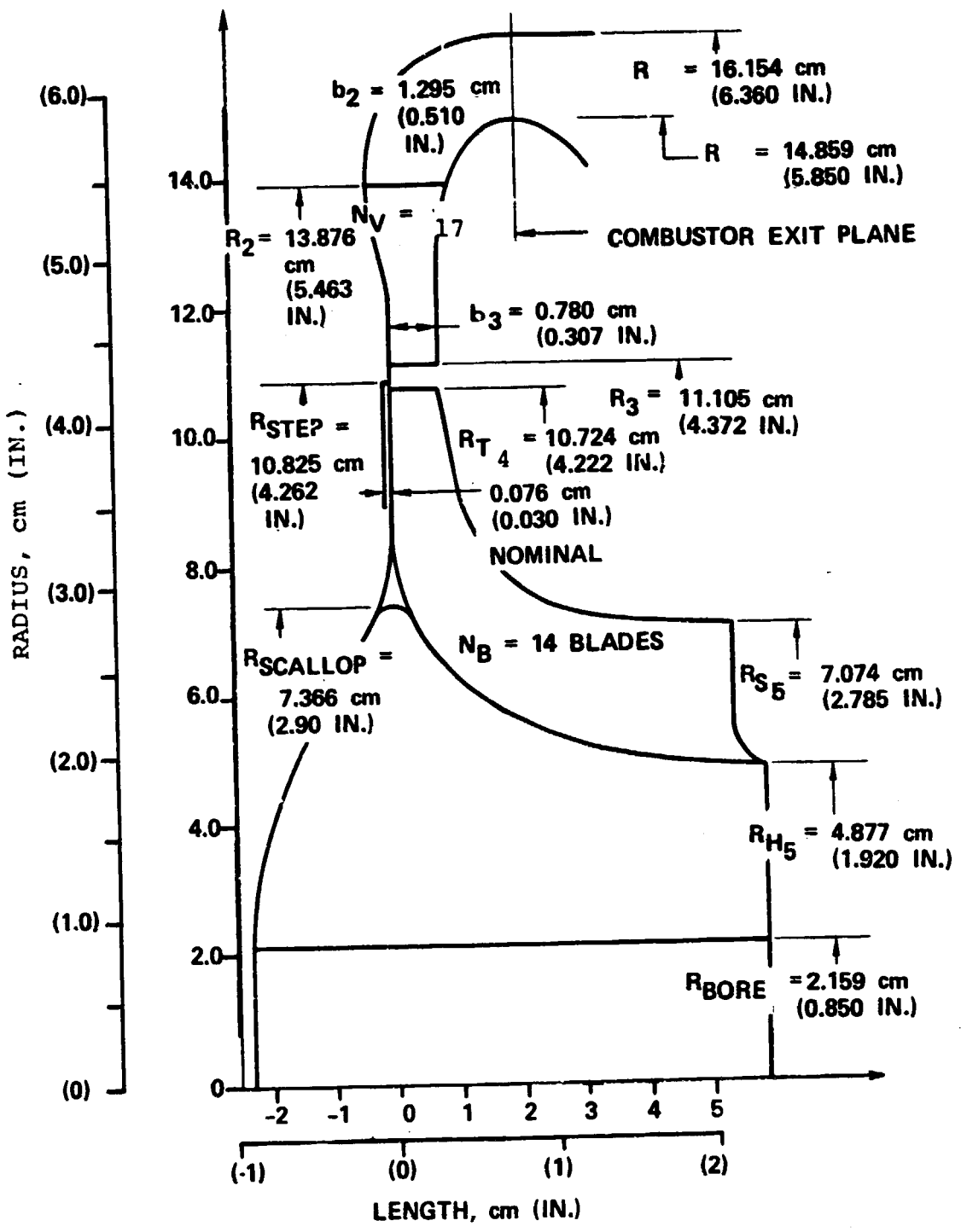


Figure 128. Final Variable-Area Radial Turbine Meridional Flow Path With Articulated Trailing Edge Stator. Shown at 100-Percent Power.

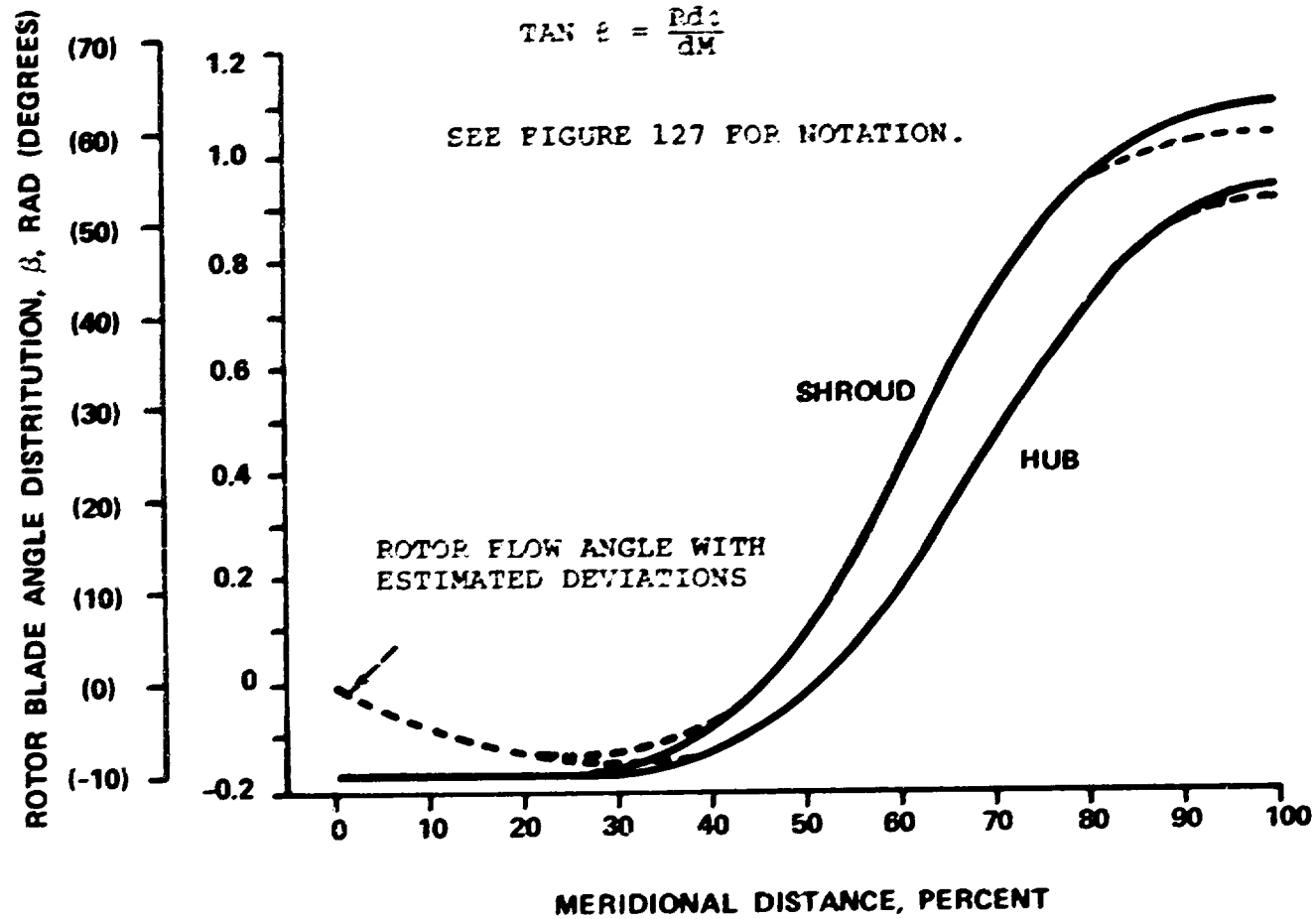


Figure 129. Final Rotor Blade Angle Distribution.

The rotor inlet deviations are apparently due to rotor relative vorticity effects. The location where the flow starts to follow the blade is estimated from criteria developed by Stanitz (3) and applied to radial turbines by Katsanis (35). The deviations at the rotor exit were even more complex, since the rotor relative vorticity effects are compounded by large, secondary flow migrations to the rotor-exit tip region. The approach used at Garrett to solve this problem assumes that the rotor-exit flow is turned to the rotor midthroat angle. The additional uncovered downstream turning was the total deviation at each radial location. The net effect with this procedure was to assume deviation increases from approximately zero at the hub to a relatively high value at the tip. This accounted for deviations in the tip region from the secondary flows. However, the parametric study results were based on precise inducer-to-exducer work splits. Achieving the exact vector diagrams desired required either a significant increase in rotor internal flow knowledge or experimental iterations of rotor-exit blade angles.

The rotor suction- and pressure-side surface velocity distributions for 60- and 100-percent power are presented in Figure 130 as a function of meridional distance. At 100-percent power, the diffusions were relatively low and were followed by rapid accelerations. At 60-percent power, the velocity levels and accelerations were significantly reduced. This was expected and indicates why rotor reaction efficiency penalties are required. The rotor inlet and exit vector diagrams at hub, mean, and tip are presented in Figures 131 and 132.

7.2 Detailed Substantiation of Cooled Rotor Design

7.2.1 Mechanical Configuration

Performance, life, and burst margin are all prime considerations in the design of turbine rotors; gains made in one area are often at the expense of another. This mutual dependency makes design optimization difficult and the cooled, variable-area radial rotor is no exception. Aerodynamic analysis predictions showed that introducing 0.17 radian (10 degrees) of nonradiality in the blade would result in noticeable performance configuration improvement, hence, nonradial backward-curved blading was used for the radial rotor design. As expected, this nonradiality caused high bending stress in the blade resulting in decreased durability. Thus, maintaining performance gains without sacrificing blade life became a major design goal. The following options were considered to achieve this goal.

- o Introduction of a rake angle
- o Increased blade surface-to-surface distance;

$$\beta_B = -0.17 \text{ rad} \\ (-10 \text{ DEG})$$

$$\text{RAKE ANGLE} = -0.26 \text{ rad} \\ (-15 \text{ DEG})$$

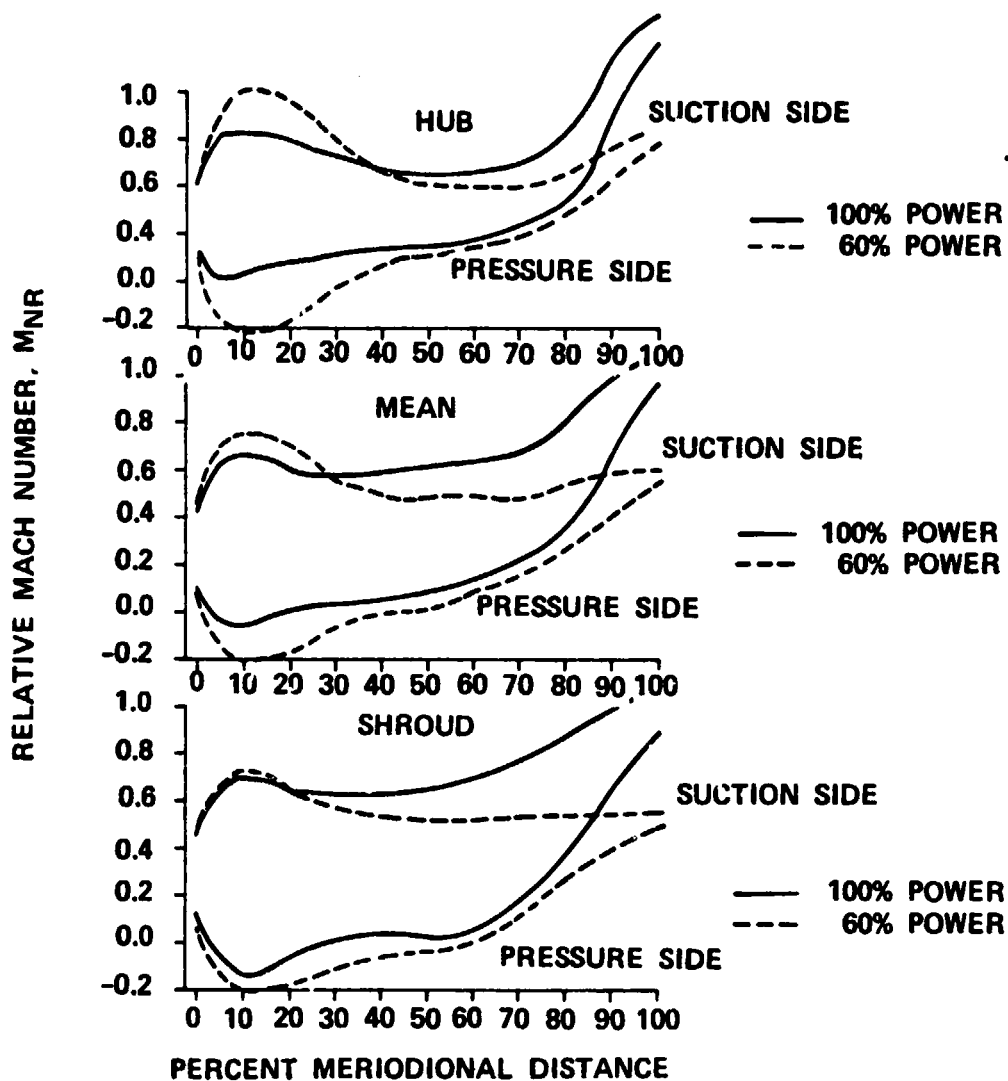
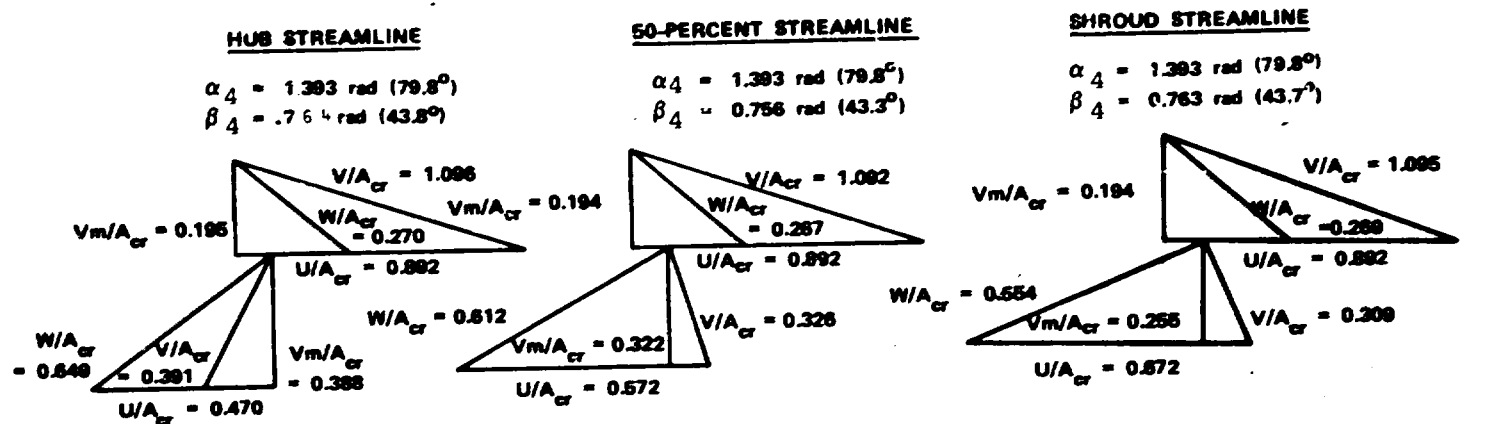


Figure 130. Rotor Blade Velocity Distribution at 60- and 100-Percent Power Condition (14 Blades).



R_4	= 10.72 cm (4.22 IN.)	R_4	= 10.72 cm (4.22 IN.)	R_4	= 10.72 cm (4.22 IN.)
R_{H5}	= 4.90 cm (1.93 IN.)	R_{M5}	= 5.99 cm (2.36 IN.)	R_{T5}	= 7.09 cm (2.79 IN.)
$A_{cr',4}$	= 718 m/s (2356 FT/SEC)	$A_{cr',4}$	= 718 m/s (2356 FT/SEC)	$A_{cr',4}$	= 718 m/s (2356 FT/SEC)
$A_{cr',H5}$	= 621 m/s (2039 FT/SEC)	$A_{cr',M5}$	= 626 m/s (2063 FT/SEC)	$A_{cr',T5}$	= 633 m/s (2077 FT/SEC)

V_m = MERIDIONAL VELOCITY, m/s (FT/SEC)
 $= (V_x^2 + V_R^2)^{1/2}$
 V_x = AXIAL (Z) COMPONENT
 V_R = RADIAL (R) COMPONENT

203 Figure 131. Variable-Area Radial Turbine Rotor Inlet and Exit Vector Diagram, 60-Percent Power Condition.

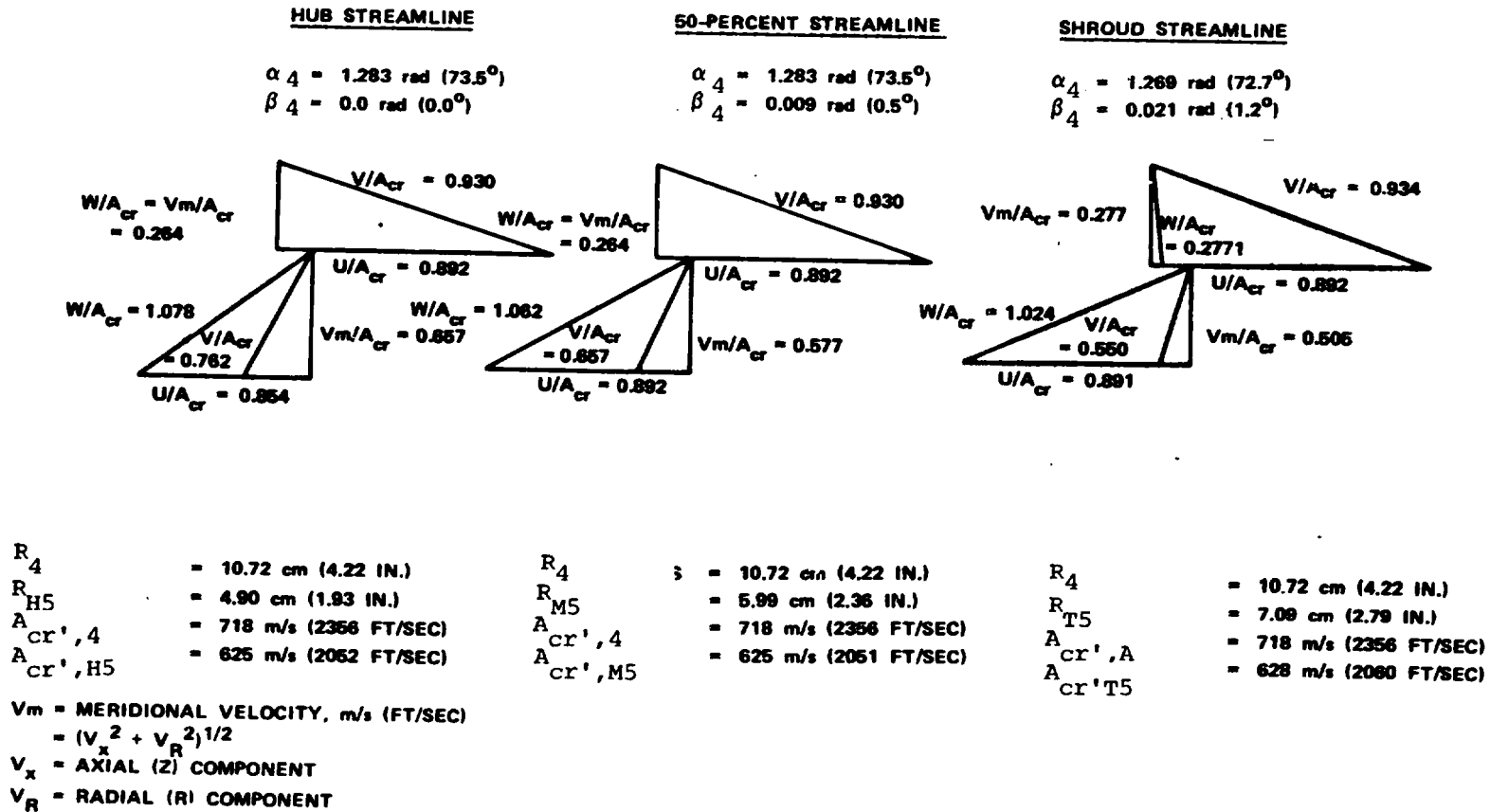


Figure 132. Variable-Area Radial Turbine Rotor Inlet and Exit Vector Diagram, 100-Percent Power Condition.

- o Insertion of nonsymmetrical blade thickness relative to the cooling passage.

No single method sufficiently reduced stresses to acceptable levels. Therefore, several iterations utilizing these options were performed until acceptable results were reached.

The feasibility of using an uncooled turbine rotor was also investigated. Results showed inadequate burst margins, and the uncooled rotor was eliminated from further design consideration.

Both 2- and 3-dimensional finite-element models were used in these analyses to obtain stress and vibration results. Burst margin and life were then calculated based on these results and on material properties.

7.2.2 Rotor Thermal Design Analysis

7.2.2.1 Rotor Blade Aerodynamic Boundary Conditions

The cooled variable area radial turbine final design included a 1589K (2400°F) turbine rotor inlet total temperature design constraint, resulting in a total relative inlet temperature of 1425K (2105°F) and a tip speed of 640 m/s (2100 ft/sec). The rotor speed was 5969 rad/s (57,000 rpm). The resulting compressor discharge temperature that served as the coolant source was 716K (829°F). The 17:1 compressor pressure ratio produced a discharge total pressure of 1722.3 kPa (249.8 psia). The variable nozzle geometry provided a cycle in which the turbine total inlet temperature and the rotating group speed remained constant from these values at 100-percent maximum power to a 60-percent power level. Changes in the rotor inlet vector diagram decreased blade relative total inlet temperature to 1359K (1986°F) at 60-percent power.

It was assumed that 100-percent maximum power represented a worst condition from a rotor heat-transfer and life analysis standpoint. This was verified at the completion of the design phase. Temperature goals for the cooling design were established from the stress analysis to exceed 800 hours of life at maximum power and provided a 4000-hour mission life. A detailed thermal analysis was performed at 60-percent power that verified a reduction in environmental severity.

Aerodynamic solutions based on rotor inlet conditions, blade relative critical velocity ratio along the suction- and pressure-side streamlines, and rotor tip inlet conditions, were used to predict turbulent heat-transfer coefficients and local adiabatic wall temperatures. Standard Garrett computer tools for radial turbine rotors were used for this computation. Blade pressure-side velocity profile solutions indicated large areas of negative velocity (recirculation) in the inducer. The aerodynamic solution

technique was not adequate in this region, and the flow field was not well-understood. Experimental evidence in the literature indicates that true fluid behavior consists of low velocities in a downstream direction. Pragmatically, the assumption that a lower threshold value for pressure-side surface velocities of near Mach 0.10 exists was made for the purpose of predicting inducer heat-transfer rates. This provided values that were consistent with the design requirements for the design of the rotor cooling system. Local heat-transfer coefficient and gas temperature values are discussed later in this report.

7.2.2.2 Geometric Assumptions

The rotor cooling design was based upon certain assumptions concerning the limiting sizes of the geometric features which could be used to augment heat-transfer and to provide adequate structural rigidity and strength. It was predicated on the use of a Garrett-developed laminated construction technique that has been used for several existing rotor designs. A selected laminate thickness of 0.076 cm (0.030 in.) [in comparison with the thicknesses of 0.038 cm (0.015 in.), 0.051 cm (0.020 in.), and 0.081 cm (0.032 in.) currently employed] reflected a restriction to design flexibility. This approach appeared feasible when based on an assumption that laminates of Mar-M 247 could be produced using a slicing procedure, rather than the rolling technique used for production of Waspaloy and Astroloy sheets.

A deviation from the current technique of chemically etching each laminate to produce the required cooling passage features was necessary with the Mar-M 247 alloy constituents. A laser-machining process was selected as a viable technique for producing the necessary features. Tests were conducted to assess the feasibility of this process. A thickness-to-slot width ratio of 5:1 and angle cuts of up to 0.87 radian (50 degrees) were achieved. Small tolerances were possible with existing laser equipment. Therefore, a numerically controlled laser-machining process was believed to be well within the scope of the program for production of laminated parts. The main advantage of the laser technique over the etching process was the angle-cutting ability of the laser that would allow complex cooling geometries in the turbine disk.

7.2.2.3 Blade Cooling Configuration

The blade cooling configuration was established at the conclusion of the preliminary design and flow-path selection process.

A series of studies that examined alternatives for cooling the inducer and exducer regions were conducted. With the incorporation of laser-angle laminate machining, streamwise flow of internal coolant that had not been possible in earlier Garrett designs was made possible. The large exducer Beta angle and the restriction of normal to surface slots in each laminate had previously resulted in a requirement for shroud line-discharge of coolant. Trailing-edge discharge has been identified as a method for accomplishing exducer cooling without exceeding the cooling flow requirements of the serpentine design and also achieving a more uniform metal temperature.

Preliminary 3-dimensional, finite-element stress analyses of the blade (along with stress rupture life calculations that established the maximum allowable blade-wall temperatures) indicated the criticality of the inducer region in developing an adequate cooling configuration. Prior Garrett experience with cooled radial turbines led to the conclusion that the rotor rupture life is limited in the inducer region. Efforts to reduce bending stresses due to nonradiality led to increased wall-to-wall spacing (passage width) in the low- to midinducer. Moreover, the increased cooling passage channel height made the establishment of high internal cooling heat-transfer rates difficult. Low external heat-transfer coefficients on the pressure-side along with high values on the suction-side of the inducer were added complications. These factors indicated that the inducer region cooling circuit design would control the total configuration. Design work proceeded on this basis, with each region of the blade examined separately. The final overall configuration for internal cooling is presented in Figure 133. The primary control of internal cooling is by metering at the exits to establish flow distribution, and by pin-fin arrays density in various regions.

At the onset of the design procedure, variations in cooling flow that might result from changes in blade external aerodynamics from 60-percent to 100-percent power were of primary concern. Since cooling flow discharges at the inducer tip and at the exducer trailing-edge into the mainstream, it was believed that static pressure changes at these locations might influence the amount of cooling flow rate or internal distribution. Also, changes in local flow rates could result in creep-rupture problems at either end of the power range. To alleviate this, all discharge points were metered to a choked pressure ratio, such that physical flows internal to the blades were influenced only by supply pressure. Increases in the percentage of core flow at 60-percent power to large values were unavoidable since the heat-transfer problem does not change significantly from 100-percent power, but physical core flow does. Figure 134 shows the target values of passage internal static pressure adjacent to the location shown. This ensured choking for the worst case at either a

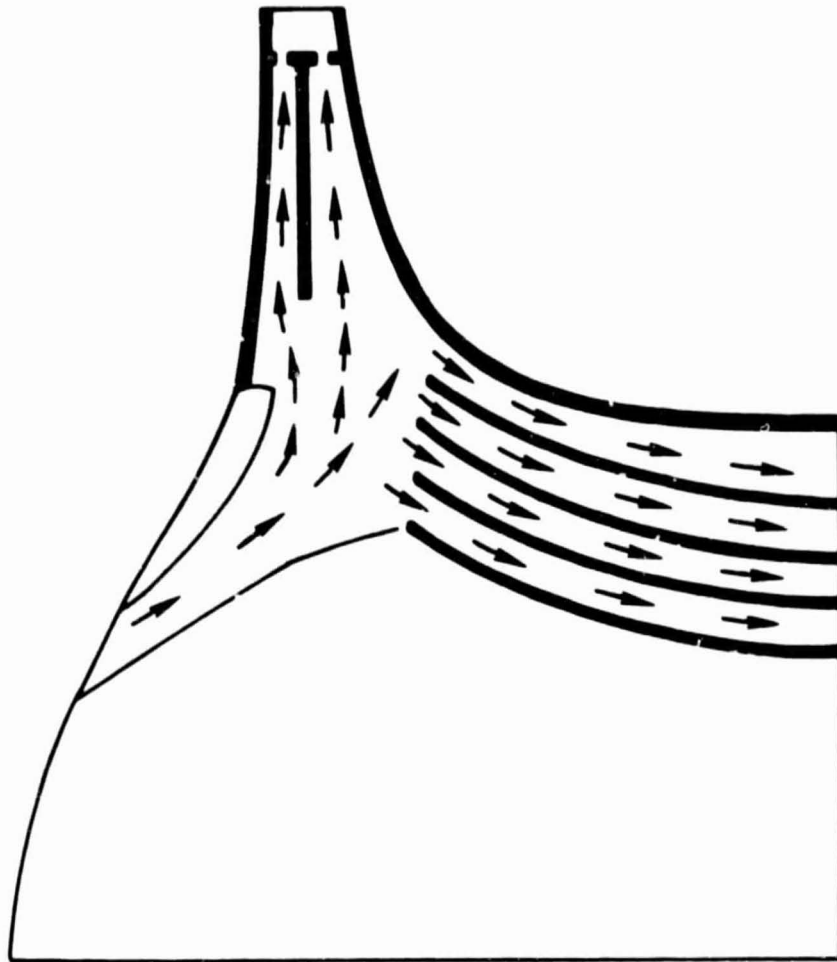


Figure 133. Airfoil Cooling, Final Configuration.

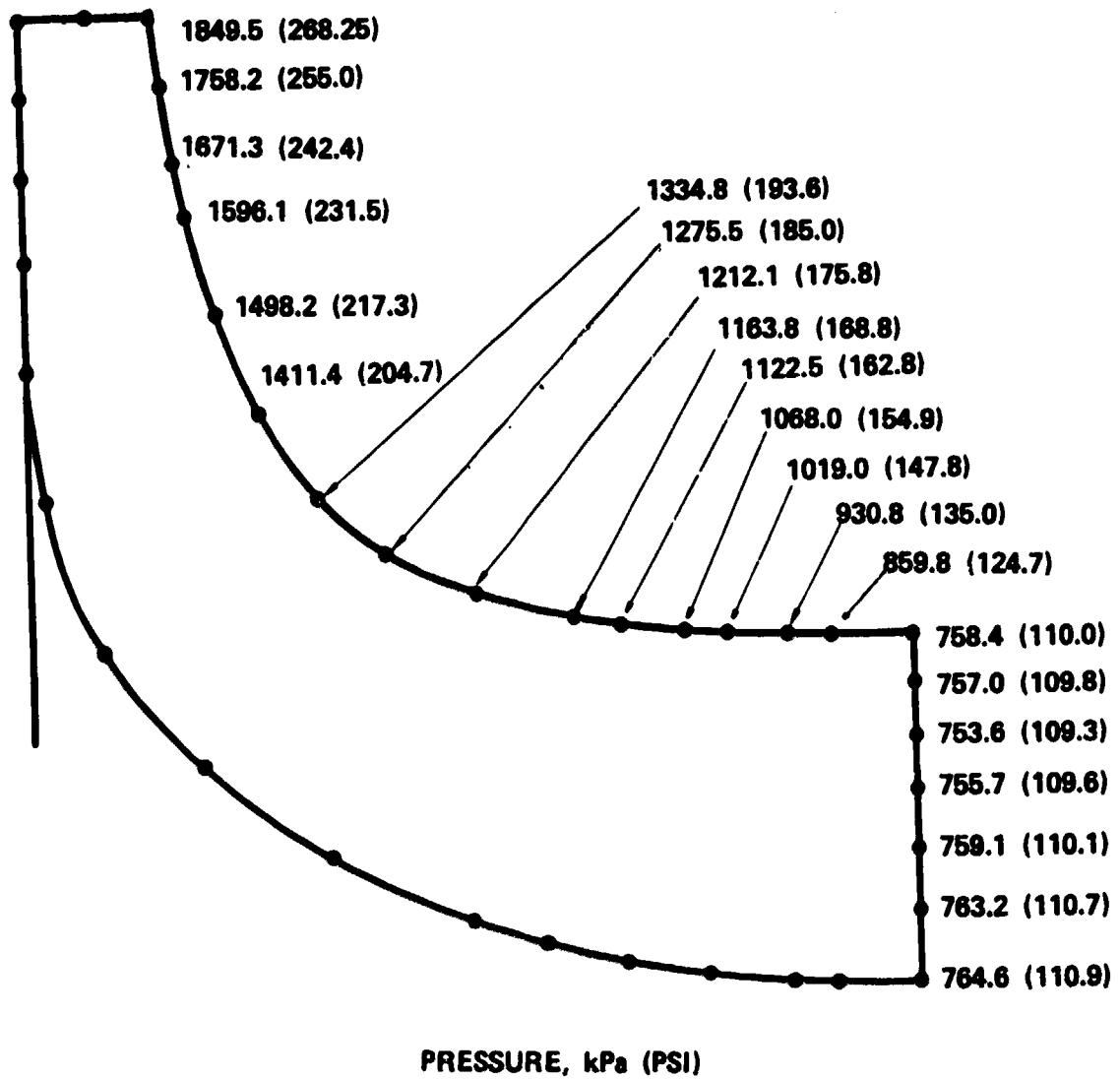


Figure 134. Cooling Passage Internal Pressure at Blade Periphery (Choke Discharge Orifice Requirement).

60- or a 100-percent power situation. The final design satisfied this goal.

7.2.2.4 Thermal Analysis Method

Examination of alternate radial turbine blade cooling circuit design schemes showed the importance of in-depth analysis in obtaining desired flow distributions in a multiplicity of passages connected in series and parallel. At Garrett, the general approach for solving flow distribution problems is a computerized, compressible flow network analysis. This procedure considers the impact of heat-transfer between the coolant and passage surfaces for fixed, external-boundary conditions, fluid friction effects, the effect of passage rotation about a reference axis, passage area changes (including sudden turns, expansions, and contractions), and variations in fluid transport properties. Boundary conditions at the passage exit- and inlet-supply locations were used with the geometry to define the flow distribution. In conjunction with the solutions defining fluid temperatures and pressures within the cooling circuit, a 1-dimensional heat-conduction solution yielded passage inner- and outer-wall surface temperatures at discrete points along each fluid passage centerline. These solutions for blade wall temperatures were then used to make accurate estimates of final steady-state blade temperatures occurring at the 100-percent, maximum power operating condition. The resultant blade metal temperatures were used for stress and life analyses.

7.2.2.5 Blade Cooling Passage Design

7.2.2.5.1 Hub Supply Passage

Cooling air was ducted to the rotor from compressor discharge downstream of the diffuser through a structural path and between labyrinth seals at the rotor front face. These labyrinth seals provided a pressurized cavity that allowed cooling flow to enter the hub supply passage at a radius of approximately 5.1 cm (2.0 in.). The pressure available at the rotor inlet hole was assumed equal to compressor discharge pressure.

The hub cooling-air supply passage has an equivalent diameter of 0.38 cm (0.15 in.). Beyond the laminated blade ring and approaching the airfoil, the diameter of the passage increased significantly. Cooling air entering at the airfoil base experiences a decrease in velocity due to the large passage height at this location. As stated previously, the pressure-side heat flux is not great, but suction-side external velocities are high enough to require promotion of internal cold-side heat transfer. A turbulence-promoting pin-fin array with a 4- by 4-diameter spacing of 0.076 cm (0.030 in.) dimension pins adequately cools the suction-side wall. A slight overcooling of the pressure-side surface was

unavoidable. The geometry selected for this region of the blade (Zone 1) is shown in Figure 135. The temperature requirements for adequate rupture life in this region precluded the use of turbulator ribs that otherwise could be used to control suction-sidewall temperatures without overcooling the pressure-sidewall.

A parametric study was conducted to determine if the supply region design (with minor flow variations in individual passages) would affect the supply region pressure level and hence, other portions of the blade. It was determined that the design was relatively insensitive to this behavior, a fact that was advantageous in the design process--particularly in maintaining flow balance with normal hardware tolerances.

The downstream portion of the supply passage (Zone 2) that entered the inducer had a greater density of pin fins (3- by 3-diameter array). External gas temperatures and bending stress in this region were primary concerns during the design process.

7.2.2.5.2 Inducer Passages

Adequate cooling of the inducer region of the blade was difficult with the 4000-hour mission-life stress-rupture goal. Dense pin-fin arrangements in both the forward and aft inducer passages inducer were required to achieve sufficient internal heat-transfer rates. As the gas temperature external to the airfoil increased with the increased radius, a rise in internal-coolant temperature occurred due to heat pickup and the solid-body pumping effect. The design selected for the inducer passages is shown in Figure 136. Greater than 40-percent total blade coolant was required to cool this region--despite the fact that it constituted less than 15 percent of the blade surface area.

Based on early 3-dimensional blade stress results, target temperatures to obtain 800 hours of 100-percent power stress rupture life were established (Figure 137). This figures shows the temperatures calculated from channel flow and 1-dimensional heat transfer for each passage for the final flow rate selected. It is apparent that considerable margin exists between required maximum temperatures and those achieved, but it should be noted that this margin is at a minimum with a radius of 10.2 cm (4.0 in.). Final life analysis of the entire blade revealed that stress-rupture life was minimum at that radius and exceeded the design goal.

7.2.2.5.3 Inducer Tip

Inducer tip cooling was also a problem in that high-stagnation region external heat-transfer rates existed in combination with poor internal-to-external surface ratios. This problem could be alleviated by using impingement cooling techniques and

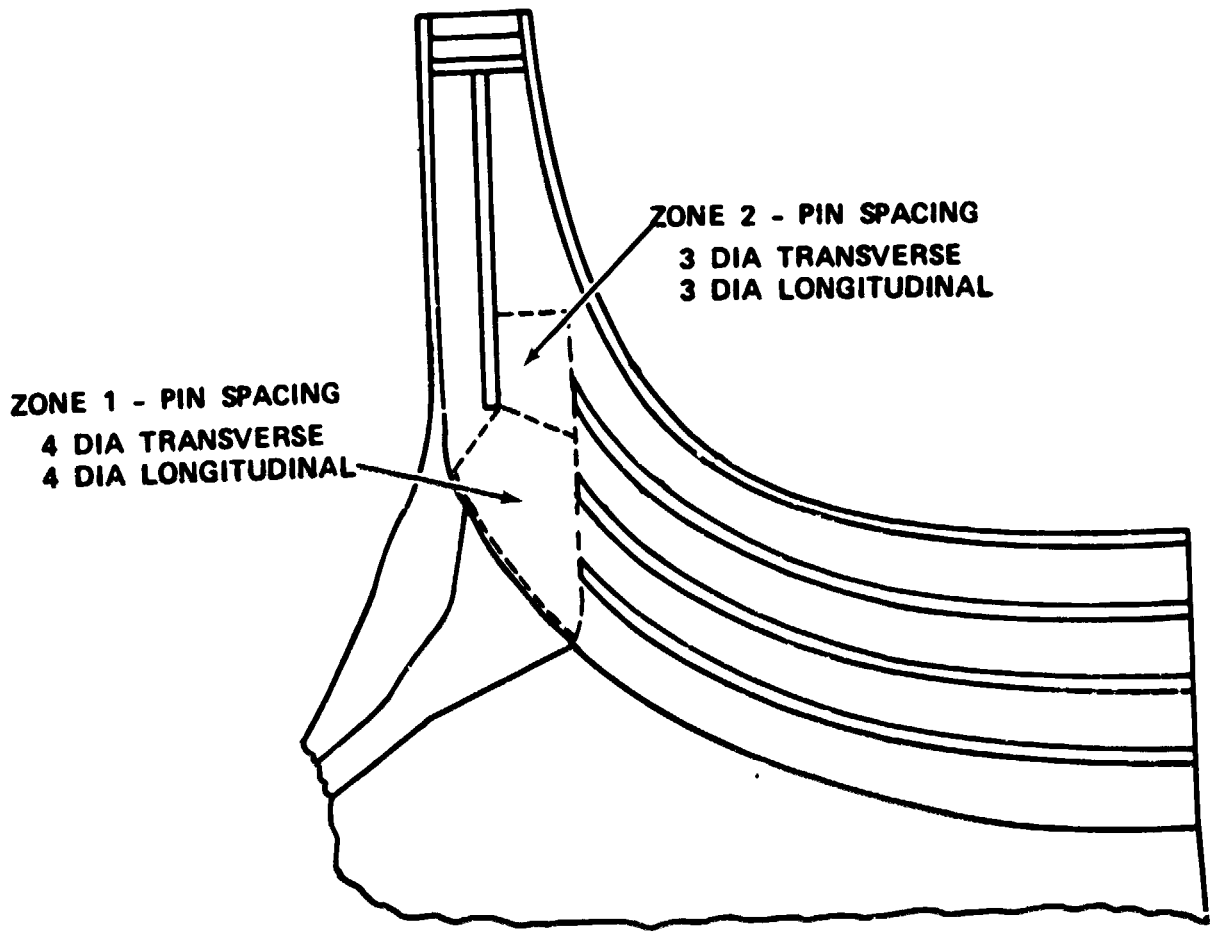


Figure 135. Hub Supply Passage for Blade Cooling Configuration.

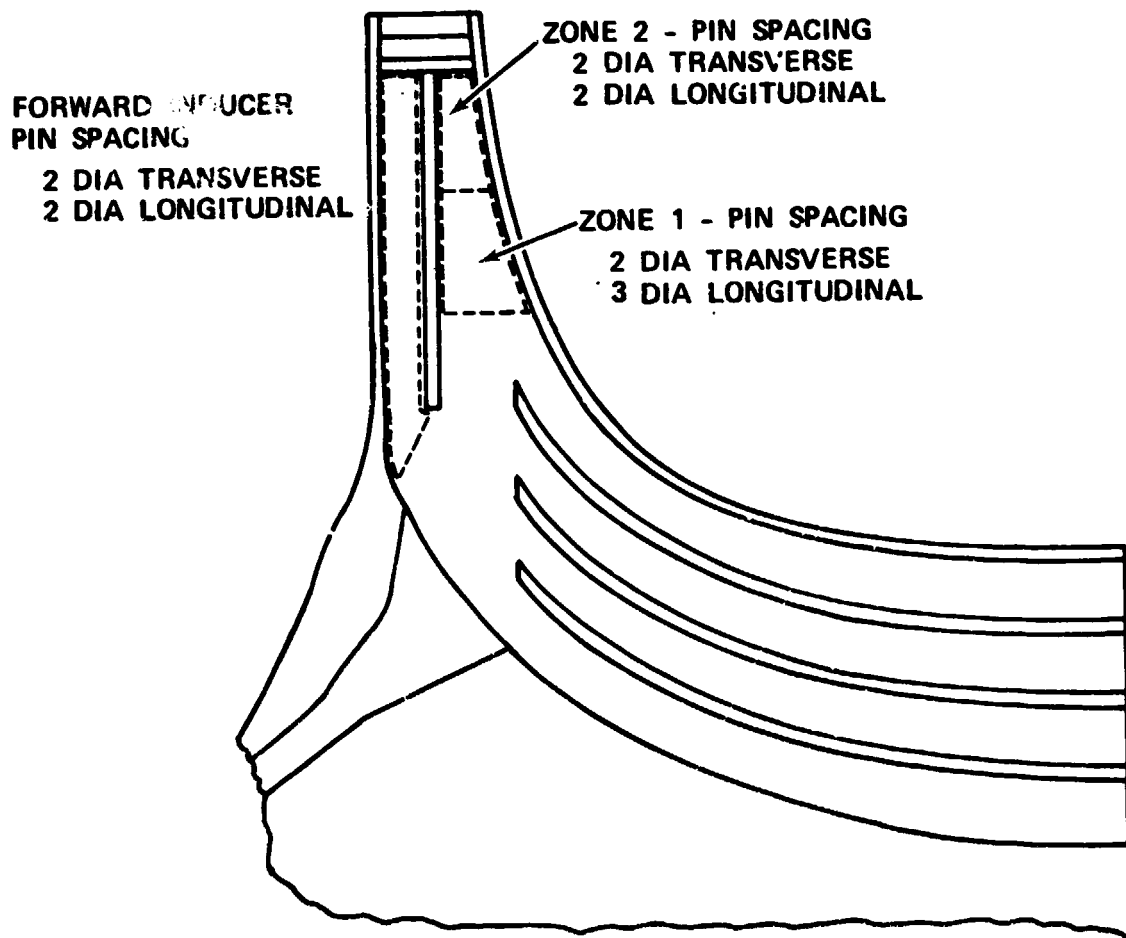


Figure 136. Final Inducer Cooling Configuration Showing Cooling Flow Passages.

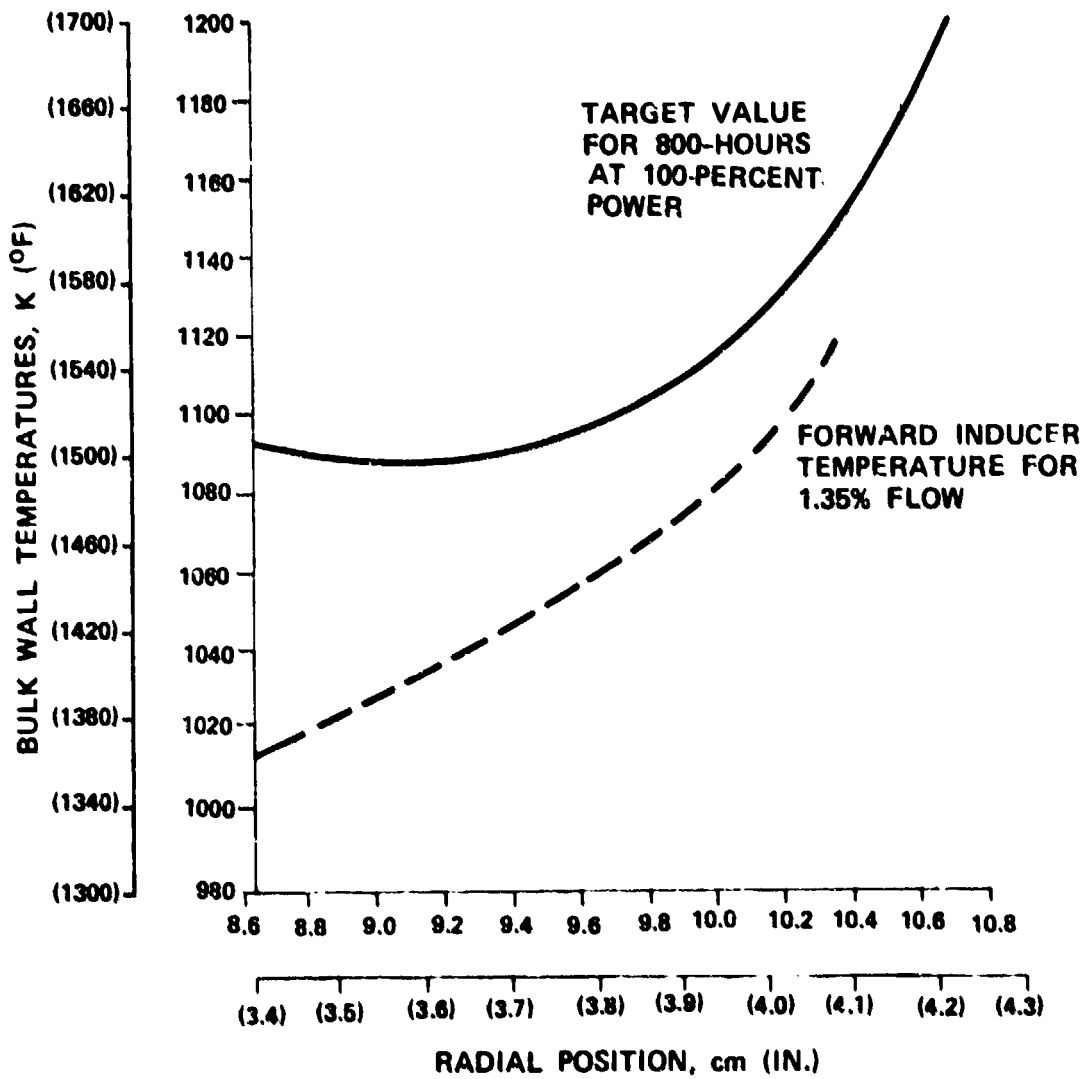


Figure 137. Inducer Wall Target Temperatures Versus Achieved Temperatures.

the geometries shown in Figure 138. Impingement at the leading-edge provided the high level of coolant side heat-transfer coefficients necessary to obtain acceptable metal temperatures. After impingement, the "spent" air was axially discharged through slots along the shroud line and backface. Coolant discharged at the shroud line tended to reduce the effective gap between the blade and the shroud and hence, improved aerodynamic performance. Correspondingly, coolant discharged at the backface tended to fill the gap between the blade hub and the adjacent part, and produced similar aerodynamic performance improvements.

The location of these impingement coolant discharge slots resulted in a straight-through passage that can be visually inspected and easily cleaned. Severe rub can occur on either the shroud or hub line if axial clearances are not properly established. However, it is doubtful that severe rub could occur on both the shroud and hub in any given rotor. If the rub was sufficiently severe, the coolant discharge passage could be partially closed, restricting coolant discharge at that location. This presents another advantage of this design, since the system works reasonably well with either the hub or the shroud discharge location completely closed. This resultant blockage could be removed easily at overhaul. Another advantage of this leading-edge cooling scheme is that the blade remains integral, even with severe leading-edge erosion or damage.

With the very high impingement heat-transfer rates achieved, the leading-edge portion average metal temperature was 1166K (1640°F) at 100-percent power and 1105K (1530°F) at 60-percent power. As shown, the leading-edge was 0.102-cm (0.040-in.) thick and had a high heat flux that produced surface-to-surface temperature differences of 100K (180°F) at 100-percent power and 83K (150°F) at 60-percent power.

An alternate design for future consideration would increase the leading-edge width from the current value of 0.178 cm (0.070 in.) to approximately twice that value, then taper down to normal inducer width. This could be accomplished by increasing the passage size rather than by making significant changes in the wall thickness. This change would have significant thermal advantages and would have no serious effect on aerodynamic performance. A reduction in hot-side heat-transfer due to an increase in "cylinder" size and improved cooling-surface area ratio would also be possible.

7.2.2.5.4 Exducer Region

Internal cooling of the blade exducer region was generally easier than the inducer region because of the reduction in relative gas temperature experienced with reduced radial turbine

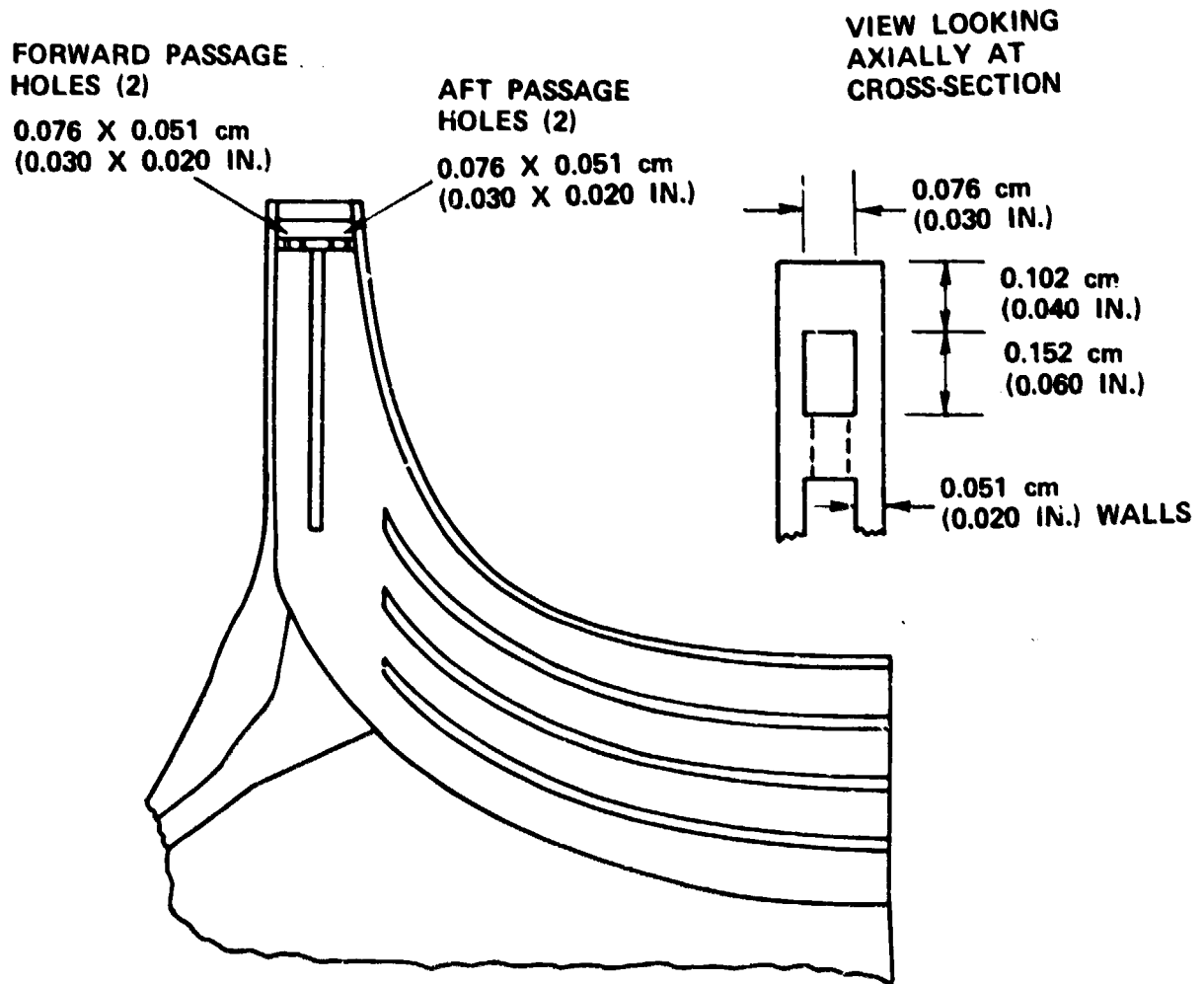


Figure 138. Inducer Tip Cooling Configuration with Impingement Cooling Techniques.

radius. Again, temperature goals were established using the preliminary 3-dimensional stress analysis results. The region was divided into four separate streamwise flow channels (Figure 139). The flow passage height variation was not extreme in this region and presented no particular difficulties. Each passage contained pin-fins distributions in array densities that increased closer to the trailing-edge, with the coolant temperature rising with heat pickup. The pin fins were 0.076 cm (0.030 in.) in dimension and extended the full height of the flow passage. The passage followed the blade contour with equal suction- and pressure-side wall thicknesses to the extent possible, and 0.076-cm (0.030-in.) thick laminates laser-machined at prescribed angles.

The partitions between exducer passages were formed by 0.102-cm (0.040-in.) thick walls. As previously discussed, the exit holes for each passage have choked pressure ratios for both the 60- and 100-percent power conditions. Hole sizes ranged from 0.061 cm (0.024 in.) to 0.053 cm (0.021 in.) at the passage terminations.

The lower passage flow was sized at 0.75 percent for 100-percent power to reflect the required blade wall cooling. This flow could be increased if a 3-dimensional heat-transfer analysis indicated that benefits could be achieved by cooling the hub rim.

7.2.2.6 Thermal-Analysis Results

Final design cooling-flow distributions for the 100- and 60-percent power conditions are presented in Figure 140. Again, it should be noted that the same physical cooling-flow rate exists at both conditions, with changes occurring only in the mainstream flow rate. Temperatures were computed throughout the blade for internal and external surfaces of the pressure- and suction-sidewalls using the cooling circuit analysis computer program. These temperatures were adjusted to reflect the proximity of ribs and other interwall connections that were significant from a thermal-conduction standpoint. Resulting temperature distributions used for the 2-dimensional stress analysis and life prediction for the four blade surfaces and the axisymmetric portion of the rotor are shown in Figures 141 through 145. These temperatures are for 100-percent power, steady-state only.

Pertinent values resulting from the thermal design of this turbine at 100-percent power were as follows:

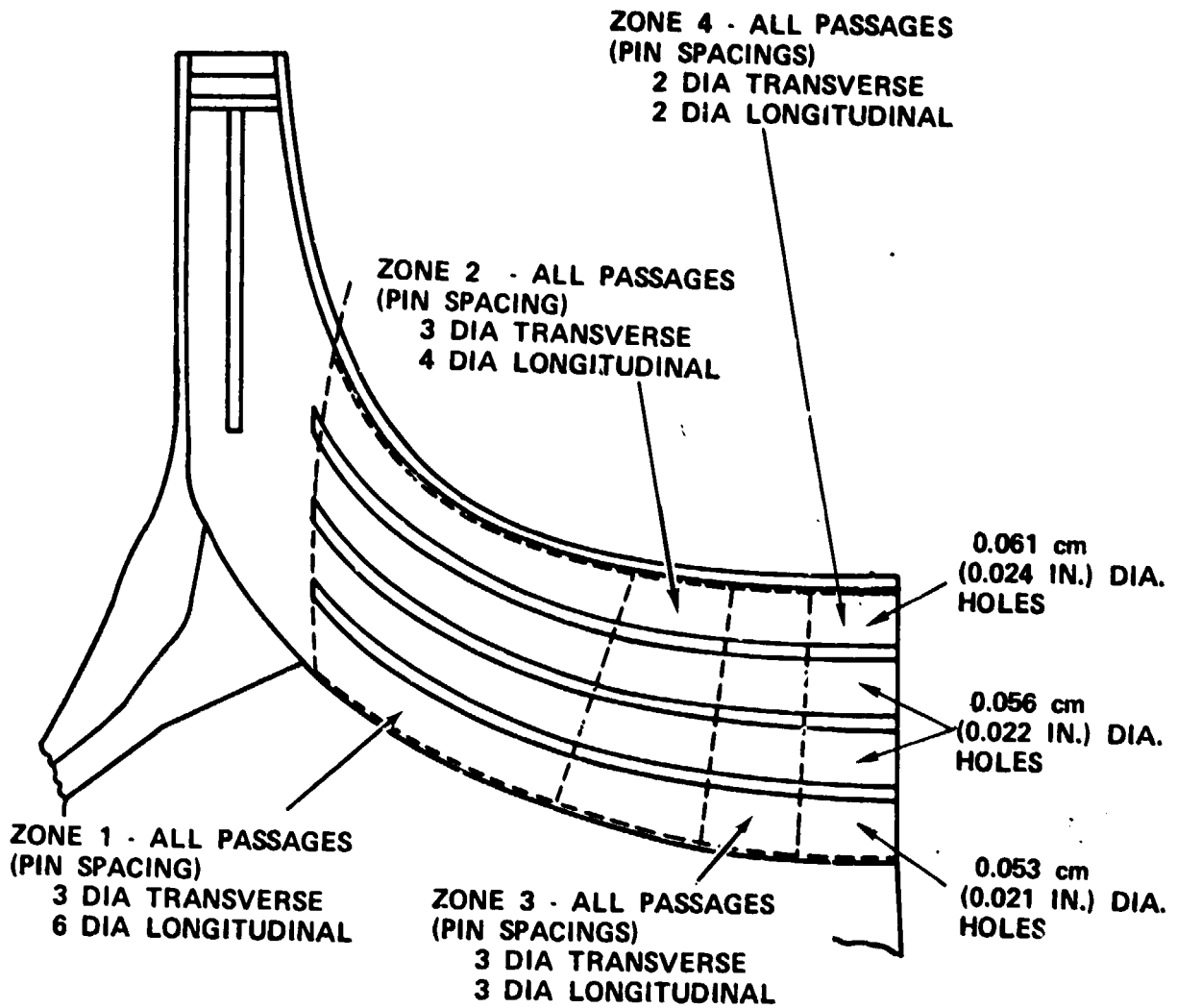
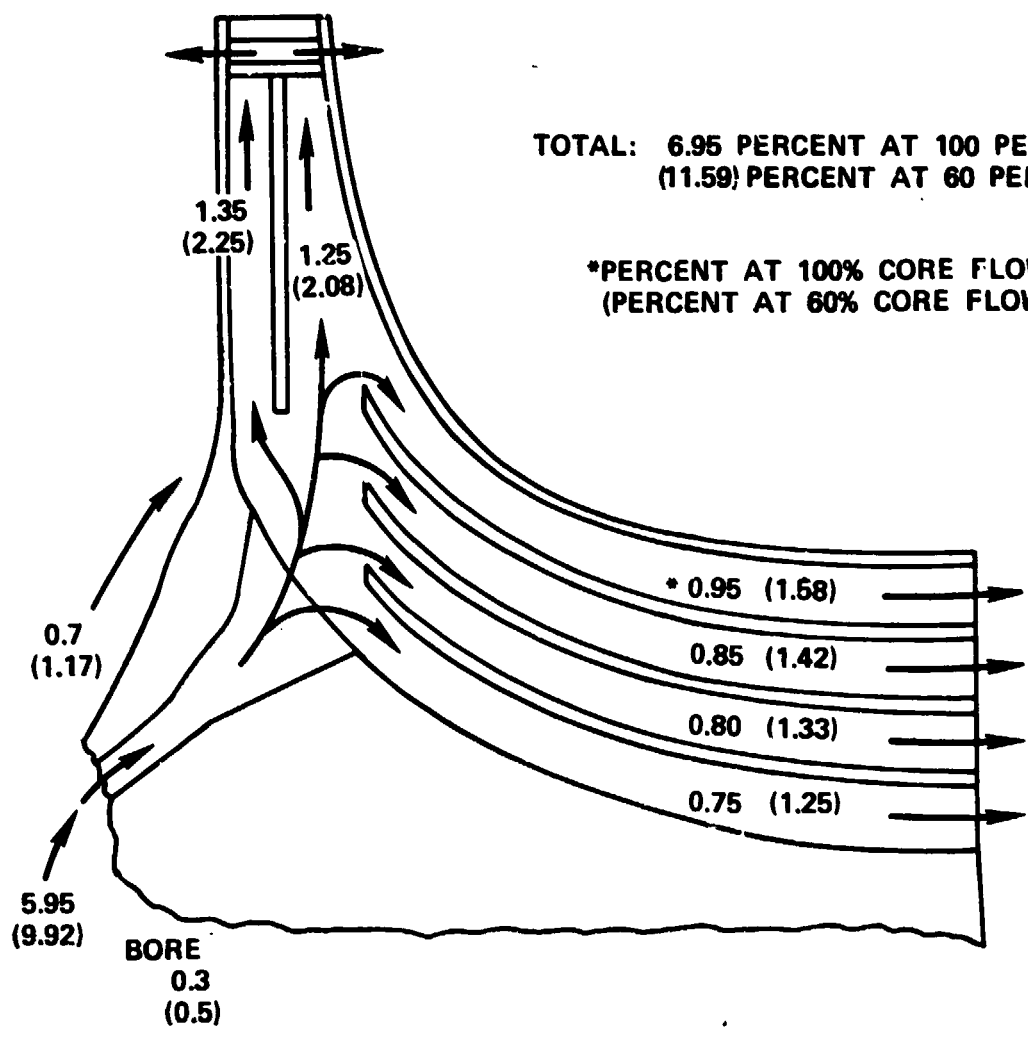


Figure 139. Exducer Cooling Passage Configuration.



TOTAL: 6.95 PERCENT AT 100 PERCENT
(11.59) PERCENT AT 60 PERCENT

*PERCENT AT 100% CORE FLOW
(PERCENT AT 60% CORE FLOW)

Figure 140. Final Rotor Cooling Flow Design (Percent of Core Flow at 60- and 100-Percent Power).

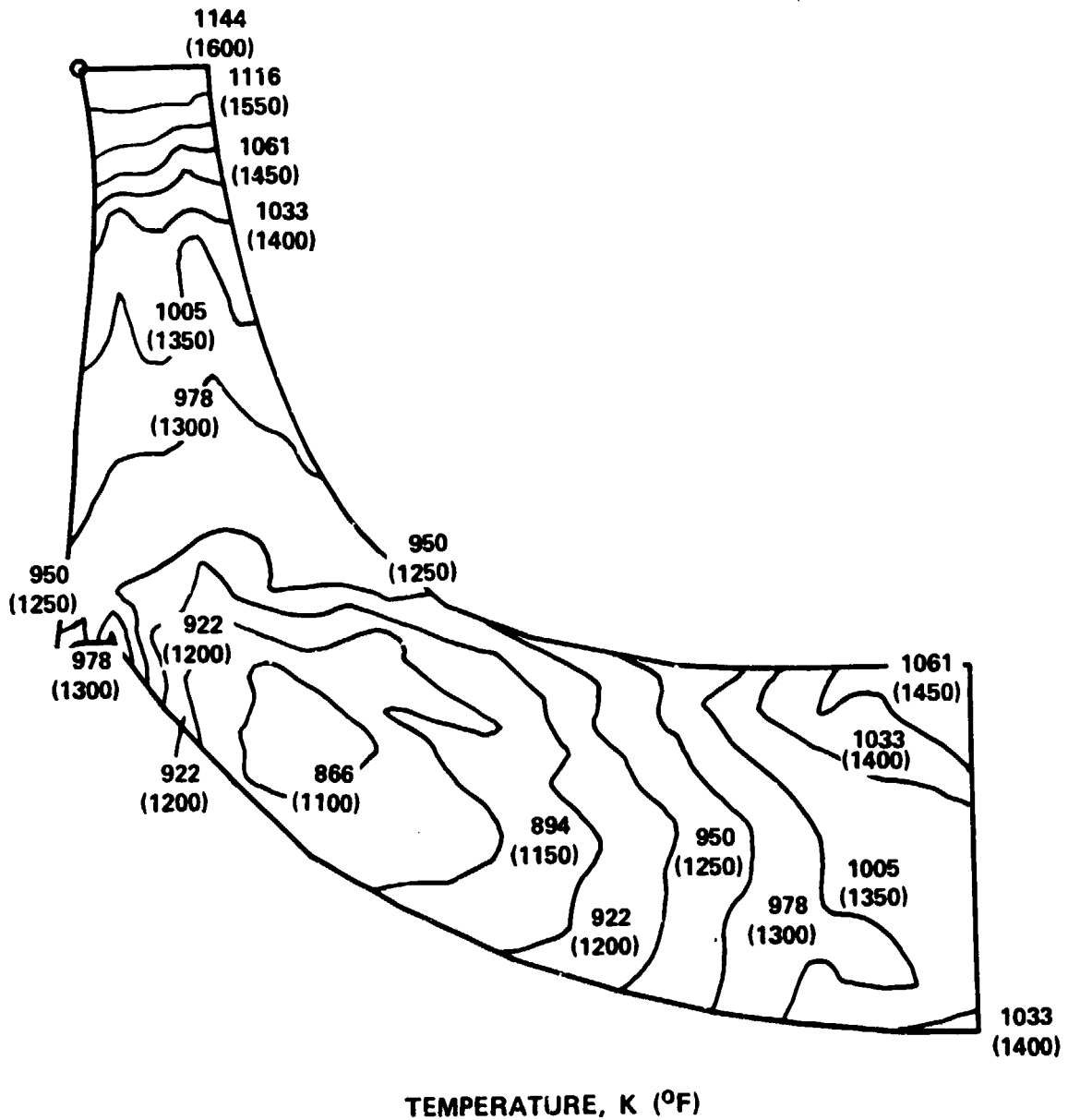


Figure 141. Pressure-Side External Surface Temperature Distribution at 100-Percent Power.

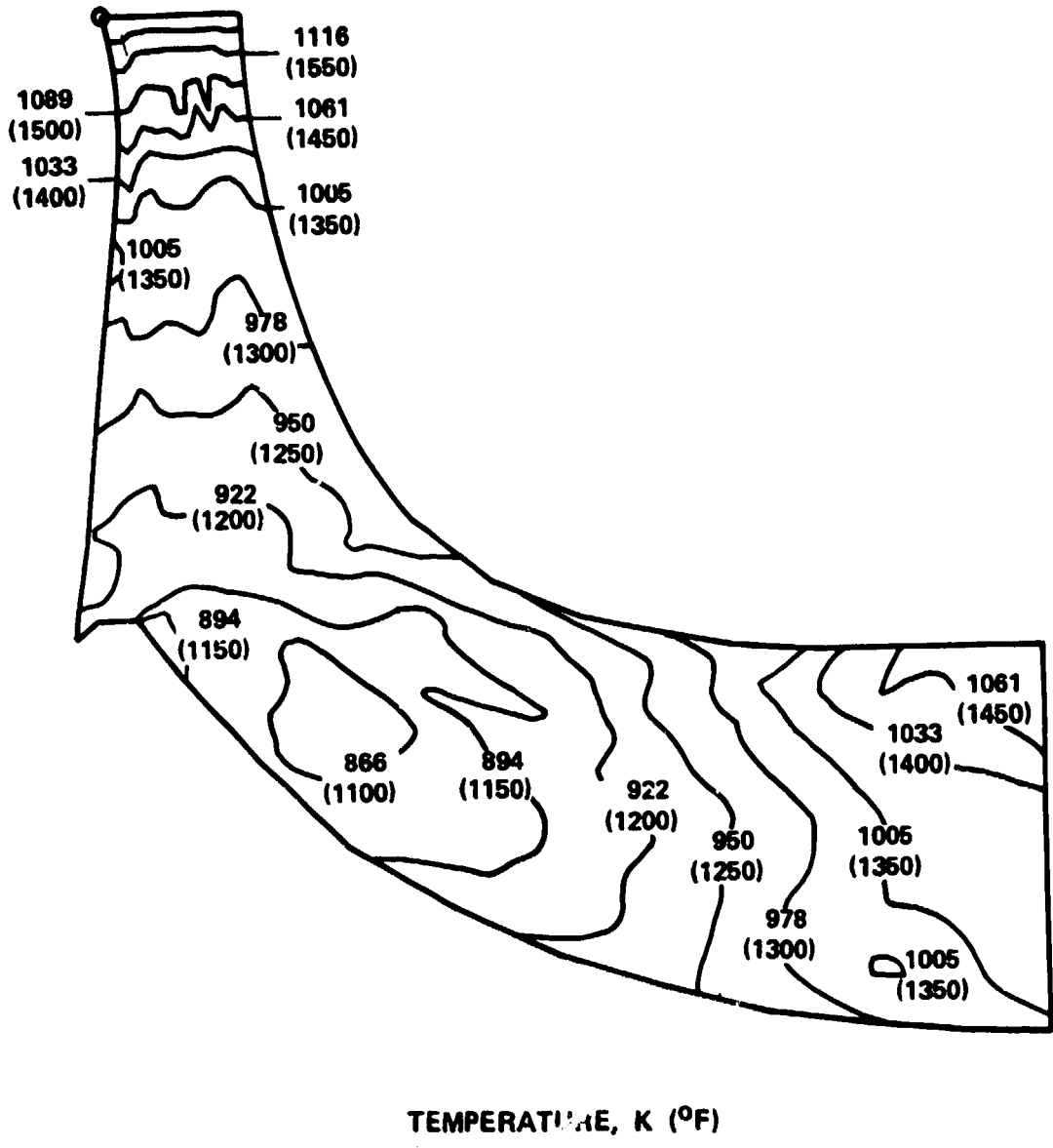


Figure 142. Pressure-Side Internal Surface, Temperature Distribution at 100-Percent Power.

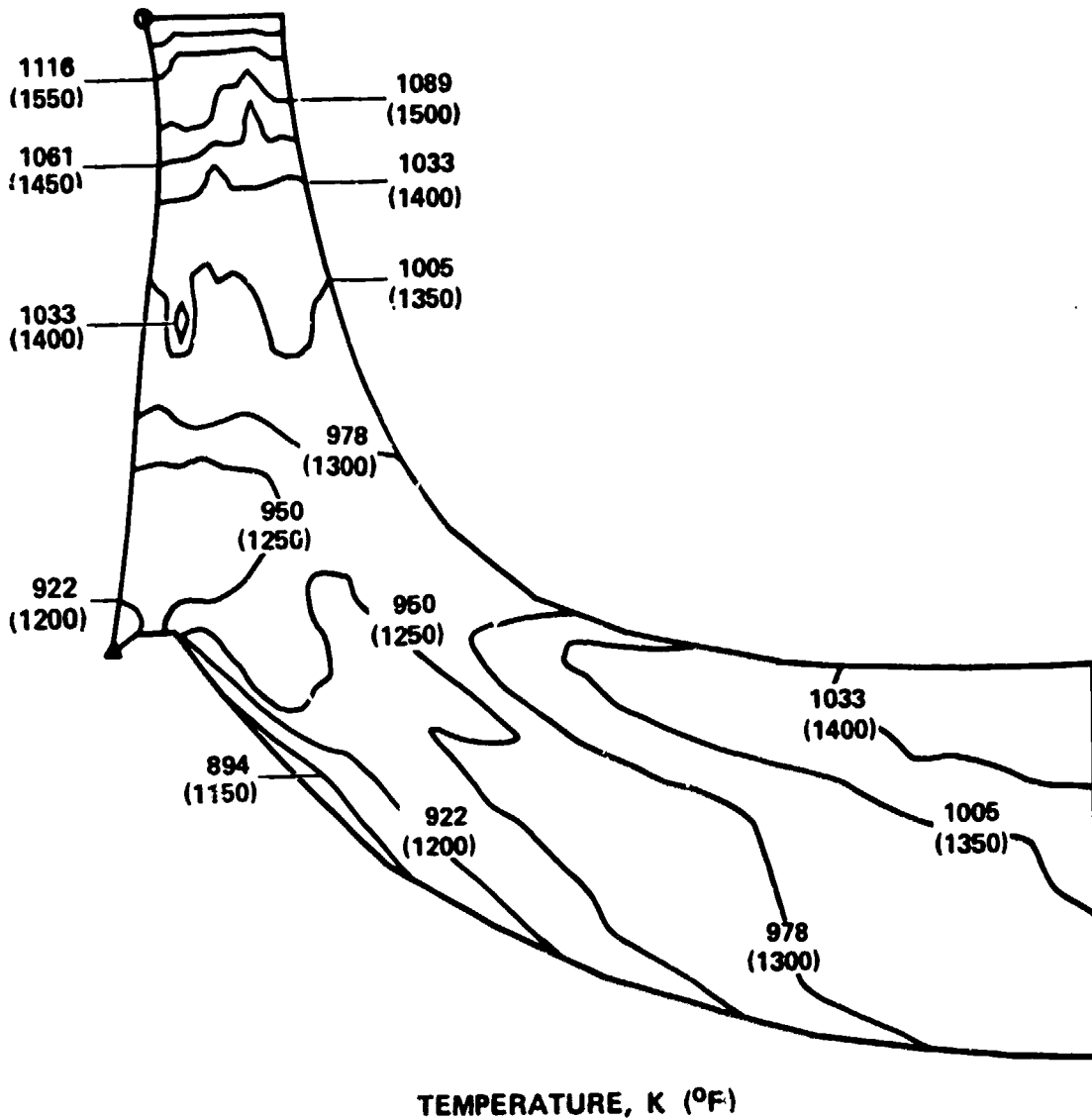


Figure 143. Suction-Side Internal Surface Temperature Distribution at 100-Percent Power.

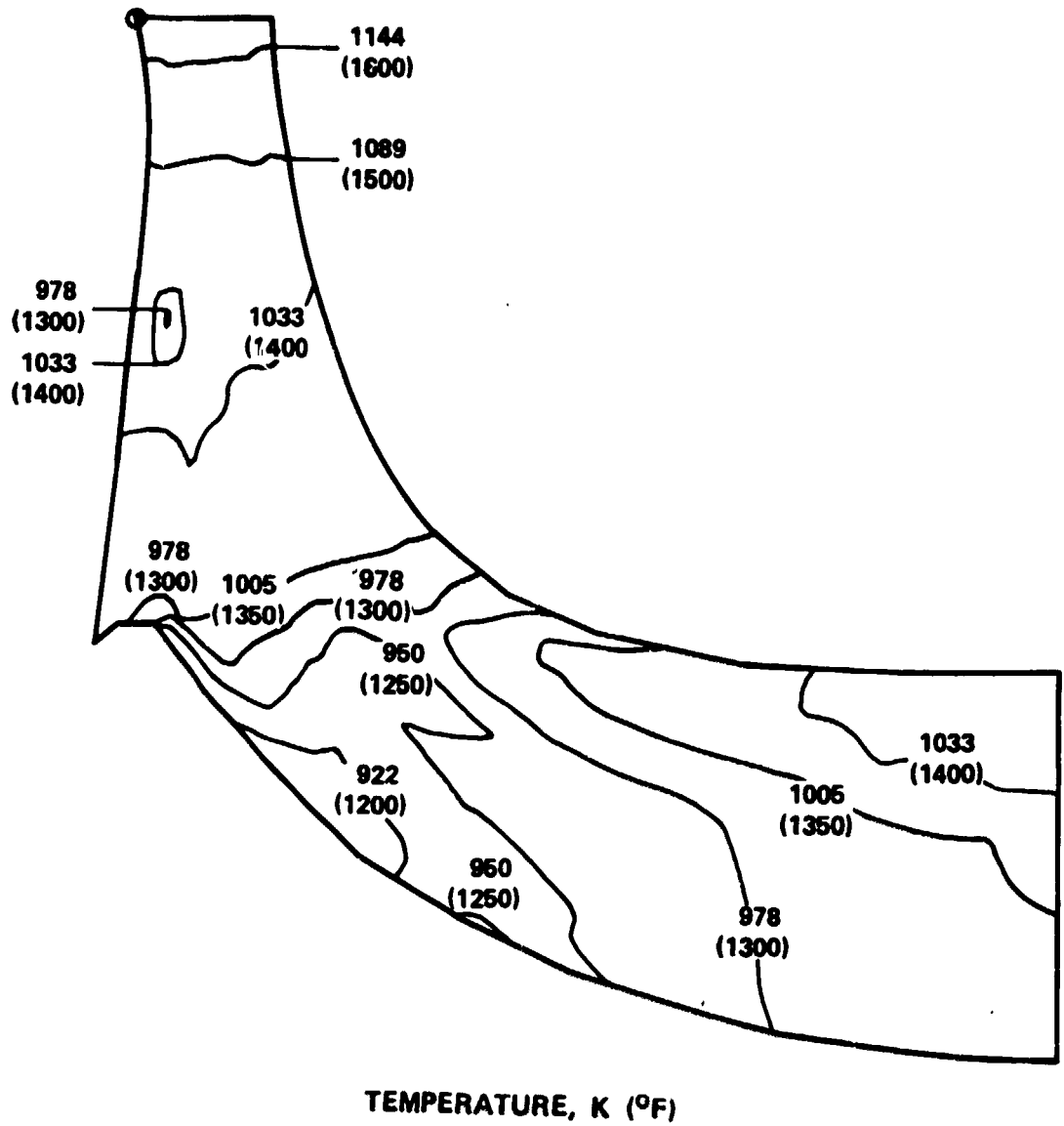


Figure 144. Suction-Side External Surface Temperature Distribution at 100-Percent Power.

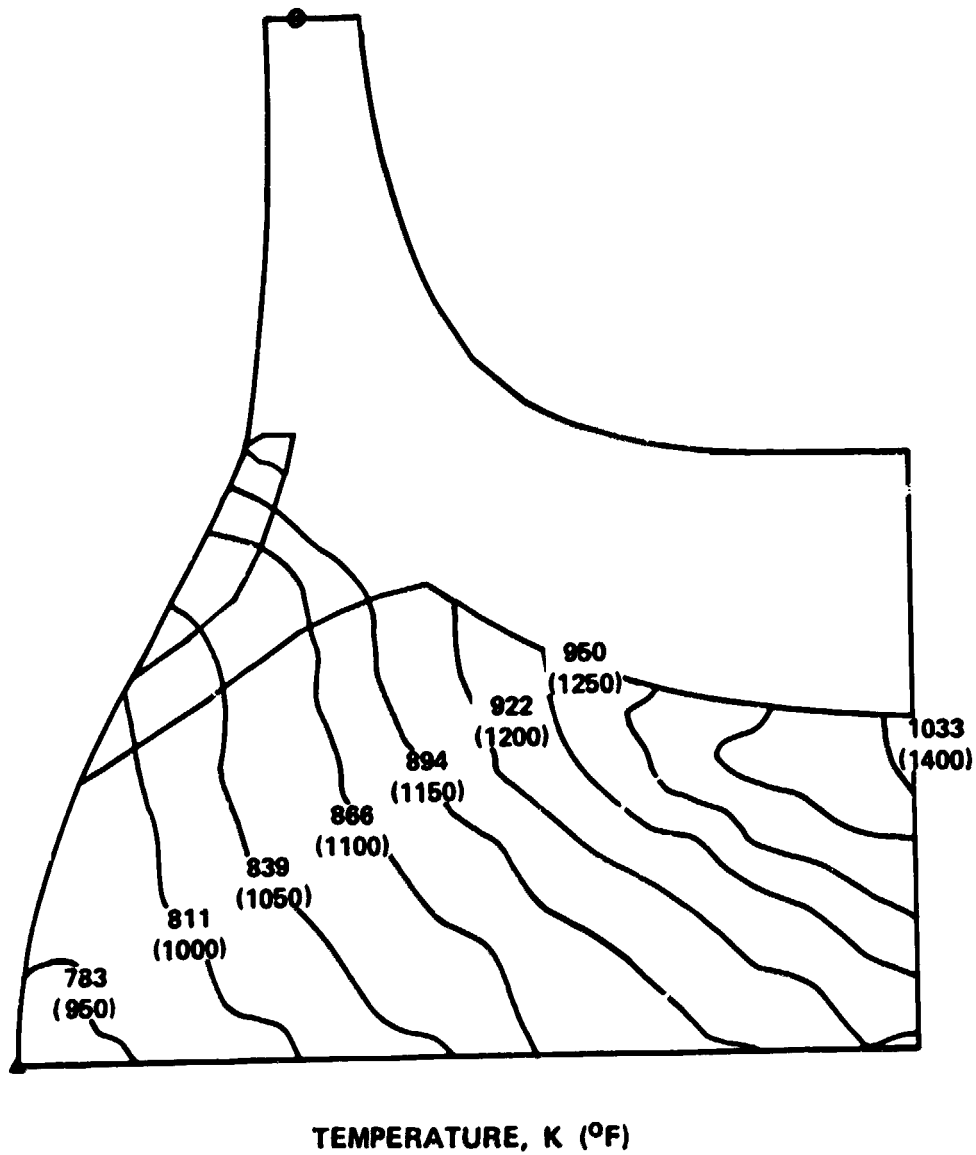


Figure 145. Disk Axisymmetric Temperature Distribution at 100-Percent Power.

$$T_4 = 1589\text{K} (2400^\circ\text{F})$$

$$T_{\text{REL}_4} = 1425\text{K} (2105^\circ\text{F})$$

$$T_3 = T_{\text{Coolant}} = 729\text{K} (852^\circ\text{F})$$

$$\text{Blade Coolant} = 5.95\% W_{\text{Core}} = 0.136 \text{ kg/s} (0.30 \text{ lbm/sec})$$

$$T_{\text{Metal Average}} = 993\text{K} (1328^\circ\text{F})$$

$$\text{Average Cooling Efficiency, } \eta_{\text{avg}} = \frac{T_{\text{REL}_4} - T_{\text{Metal}}}{T_{\text{REL}_4} - T_{\text{Coolant}}} = 0.62$$

$$\text{Life Critical-Section Radius} = 10.2 \text{ cm} (4.0 \text{ in.})$$

$$\text{Metal Temperature at Critical Section, } * T_{\text{Metal Critical}} = 1099\text{K} (1519^\circ\text{F})$$

$$\text{Cooling Effectiveness at Critical Section, } * \eta_{\text{Critical}} = 0.47$$

*Critical Section is Minimum Stress-Rupture Life Location

7.2.3 Rotor Mechanical Design Analysis

7.2.3.1 Blade Configuration

Mechanical design analysis of the cooled turbine rotor was performed in parallel with cooling configuration design and thermal analysis. To proceed in this fashion, initial estimates of achievable blade wall average temperatures (Figure 146) and corresponding blade total wall thickness distribution (Figure 147) were made. Optimization of the geometry progressed from this initial configuration as described in the following discussion.

A unique feature of the selected turbine design is the 0.17-radian (10-degree) nonradiality in the blade inducer. Theoretically, a rotor with 0.17-radian (10-degree) lean would achieve higher performance than a similar design without this feature. However, this nonradiality also causes high-magnitude bending stress in the blade. A direct approach used to reduce this effect is to simply increase the blade surface-to-surface distance. By doing this, the blade cross-section area bending stiffness is increased and consequently reduces the bending stress magnitude according to beam theory. However, the blade thickness had a practical limit arising from consideration of flow-path blockage. An additional approach for solving this problem is the introduction of a rake angle (γ) in the blade. This rake angle would effectively moderate the nonradiality at some regions, but

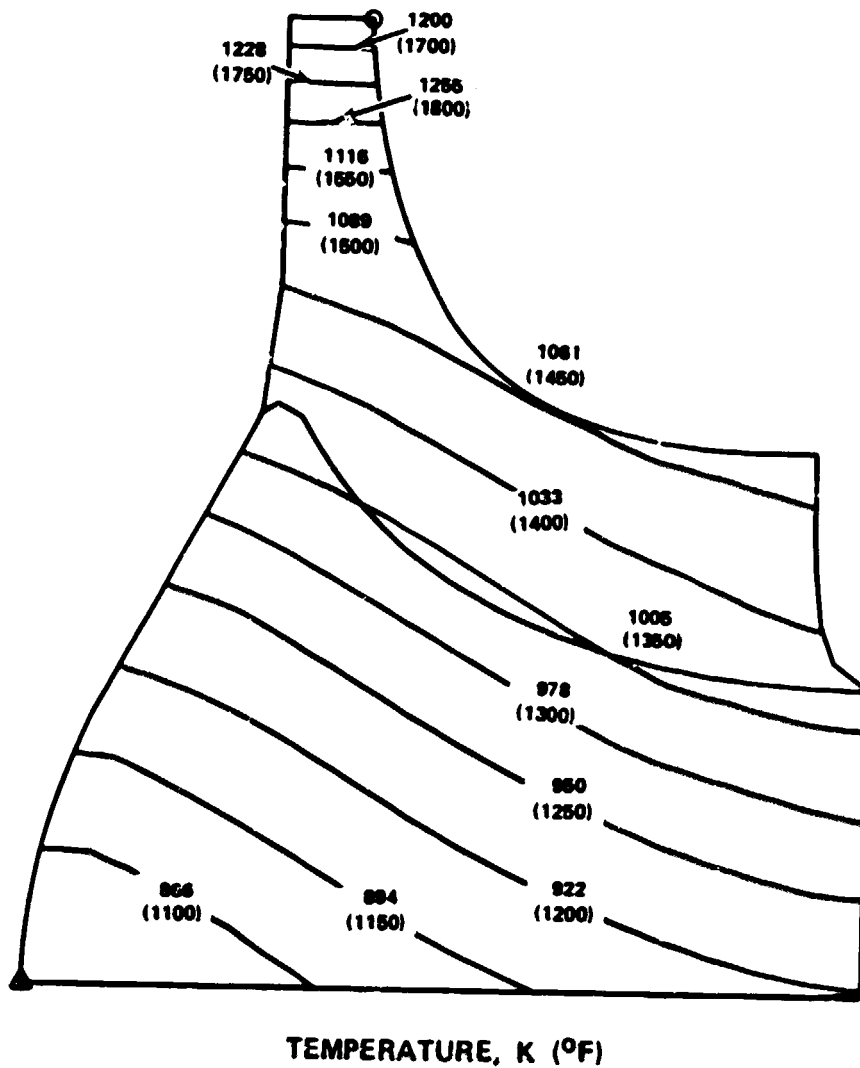
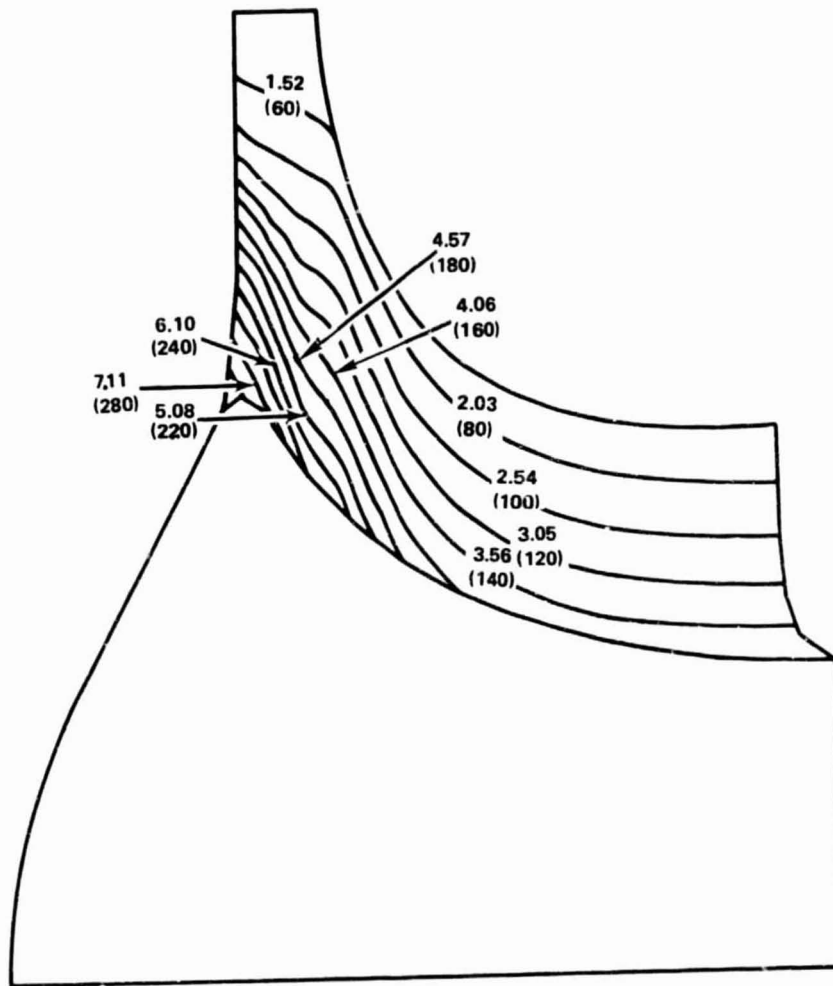


Figure 146. Blade Temperature Distribution for Cooled Rotor Configuration at 100% Power.



THICKNESS, mm (INCHES X 10³)

Figure 147. Blade Thickness Distribution for Cooled Rotor Configuration.

would also reverse this effect at other areas of the blade. Figure 148 illustrates the relationship between the rake angle and the nonradiality. This rake-angle effect can result in stress-pattern changes in the blade, i.e., the blade-bending stress is lowered in one region, but increased in others. Thus, an optimum rake angle could help reduce the magnitude of peak stress, but would not resolve the problem completely. In a reexamination of the beam theory, an attempt was made using a nonsymmetrical thickness distribution with respect to the cooling passage of the blade. This asymmetry ultimately shifted the neutral axis to either the pressure-side or suction-side surface, as desired. However, this design variation has limitations and also increases complications in the cooling scheme. No single method significantly reduces bending-stress magnitude but each contributes. Therefore, a combination of the above options appeared to be a successful approach.

Using this concept, a definition of the blade configuration was reached. This configuration had an 0.26-radian (15-degree) rake angle, an unbalanced wall-thickness distribution (i.e., wider at the pressure-side than at the suction-side), as shown in Figures 149 and 150, and a tapered hub-to-shroud external contour. The overall wall thickness (i.e., pressure-side and suction-side combined) is shown in Figure 151. The actual surface-to-surface distance differs from the total thickness as shown in Figure 152, due to the variance in cooling passage height. Ribs and pin-fins were inserted between two walls to direct cooling flow to ensure structural integrity.

7.2.3.2 Disk Configuration

The final disk geometry was determined from the flow-path definition, neighboring components, and material properties. The major design parameter was the bore diameter, since a complete engine for this design was not available. This was set at 4.32 cm (1.70-in.) to accommodate front drive from the power turbine. The other design parameter considered was the location of the bond line that united the Mar-M 247 and Astroloy alloys. Since Astroloy has higher tensile properties than Mar-M 247, it was selected for the major portion of the disk. It was decided to locate the bond line at as large a radius as possible. Also, a limitation existed with the strength capabilities of the bond joint. The latest material technology indicates that a bond joint will demonstrate the same strength capabilities as its parent material, but should carry as small a load as possible. For the selected configuration, the disk radial stress was less than 345 MPa (50 ksi) at the bond line. Therefore, a failure due to bond separation was not considered a problem.

RAKE ANGLE = γ

$$\gamma = \text{TAN}^{-1} \left[\frac{(R\phi)_b - (R\phi)_{\text{HUB}}}{Z_b - Z_{\text{HUB}}} \right]$$

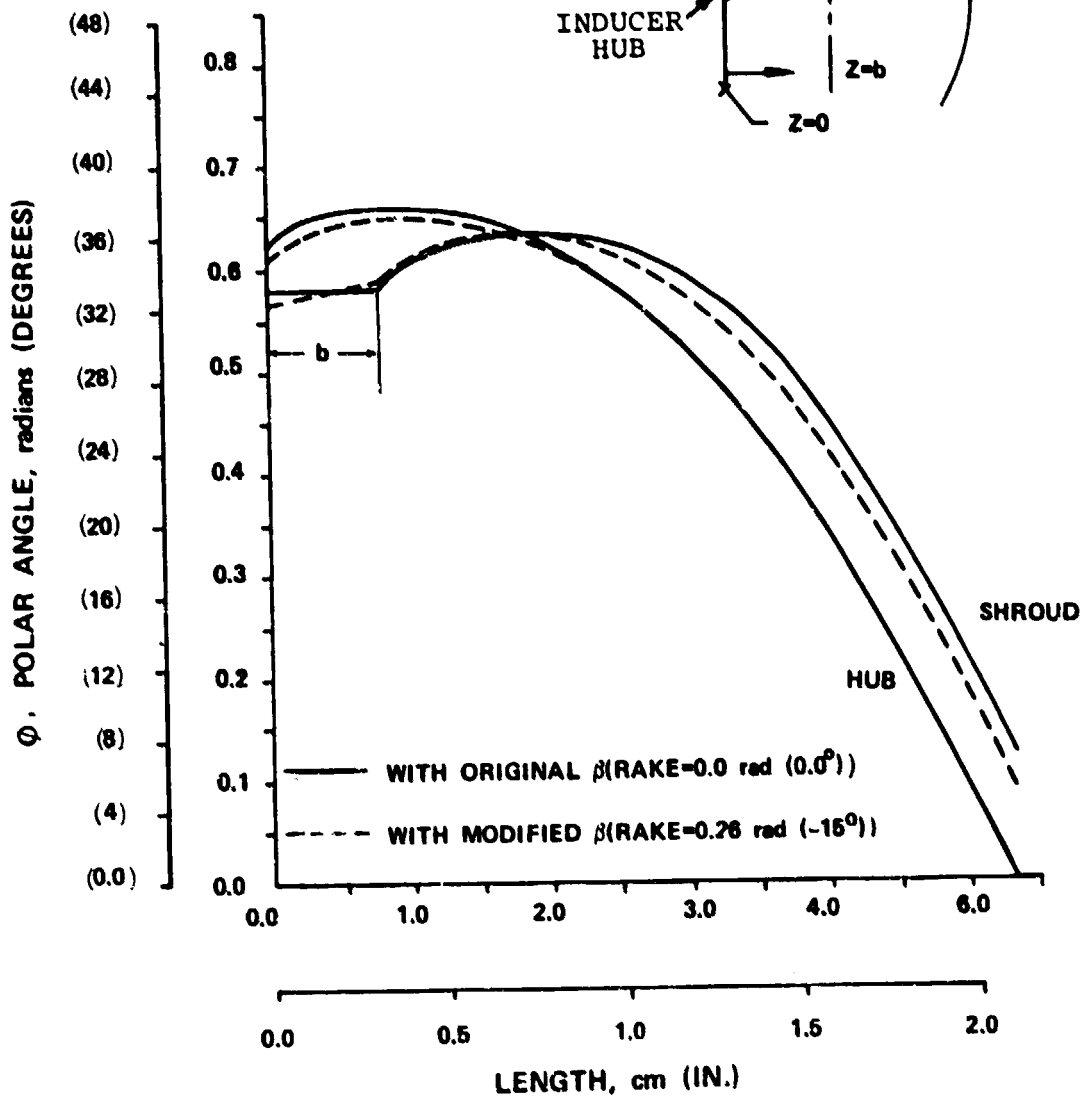
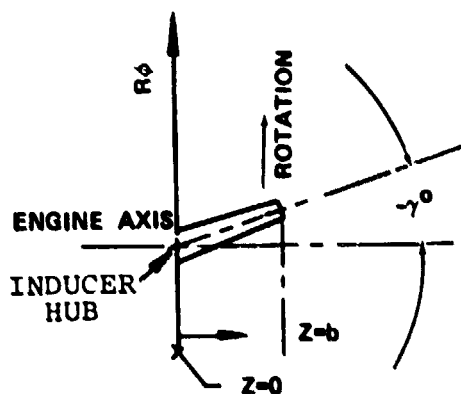


Figure 148. Rake Angle and Polar Angle Relationships.

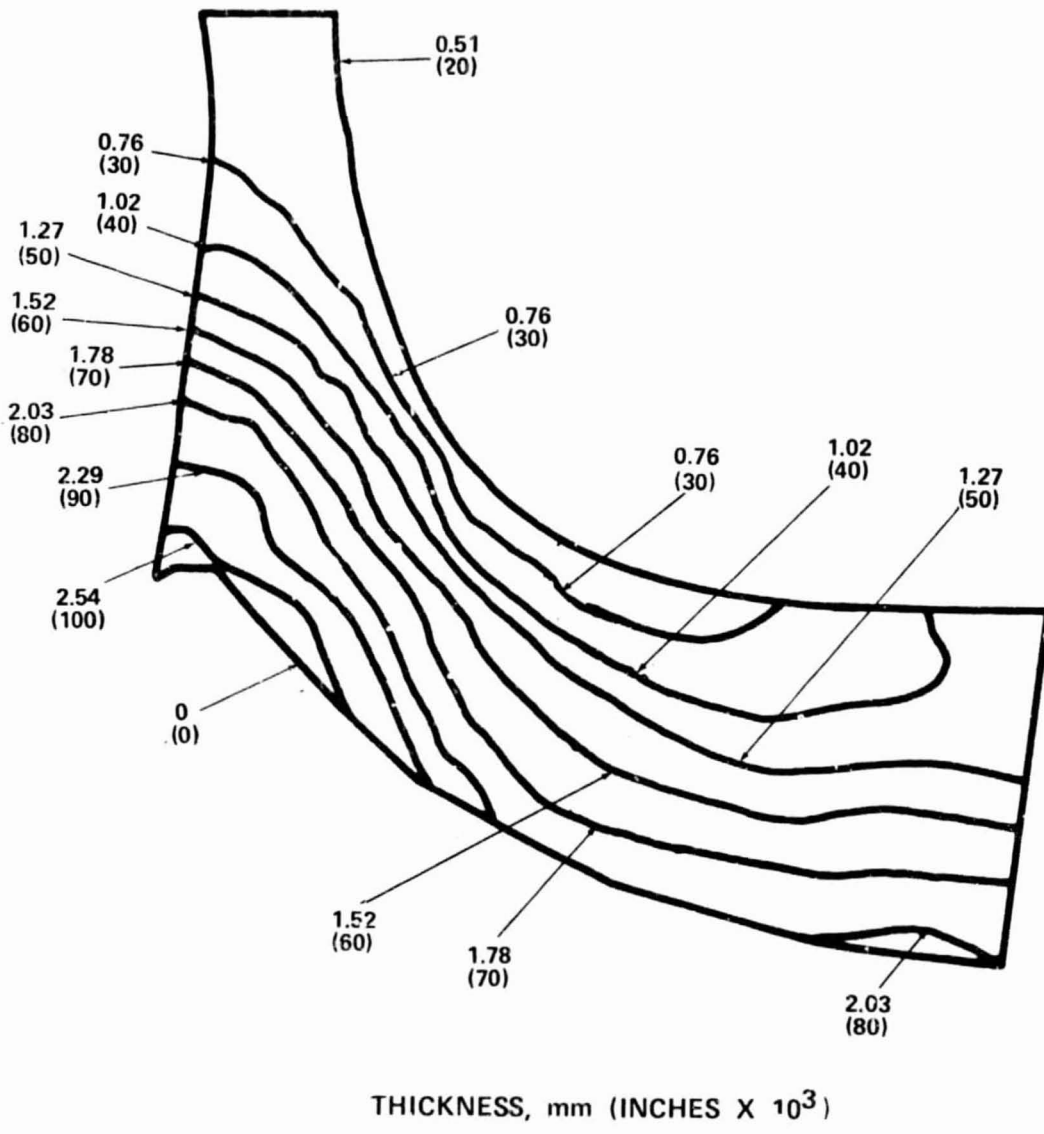
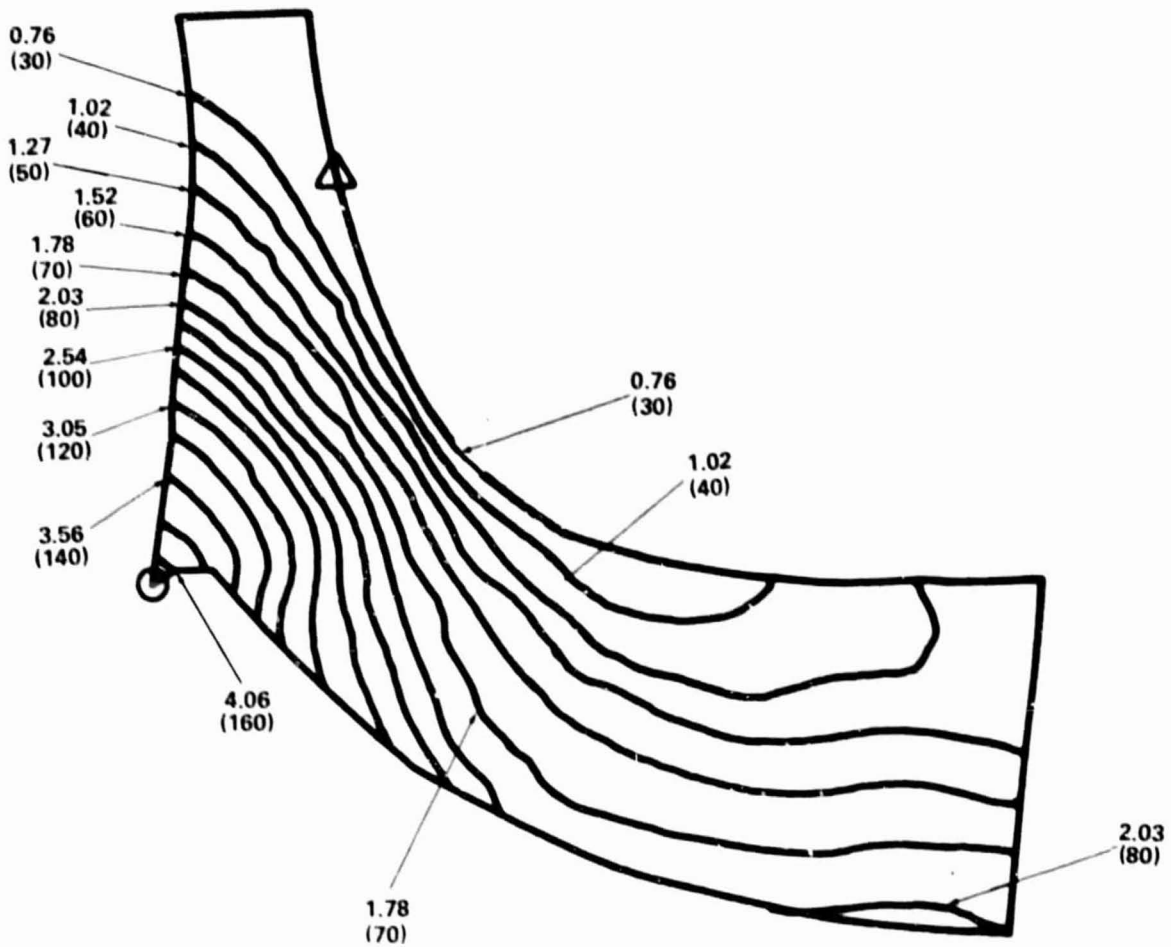


Figure 149. Suction-Side Surface Wall Thickness Distribution, Final Configuration.



THICKNESS, mm (INCHES X 10³)

Figure 150. Pressure-Side Surface Wall Thickness Distribution, Final Configuration.

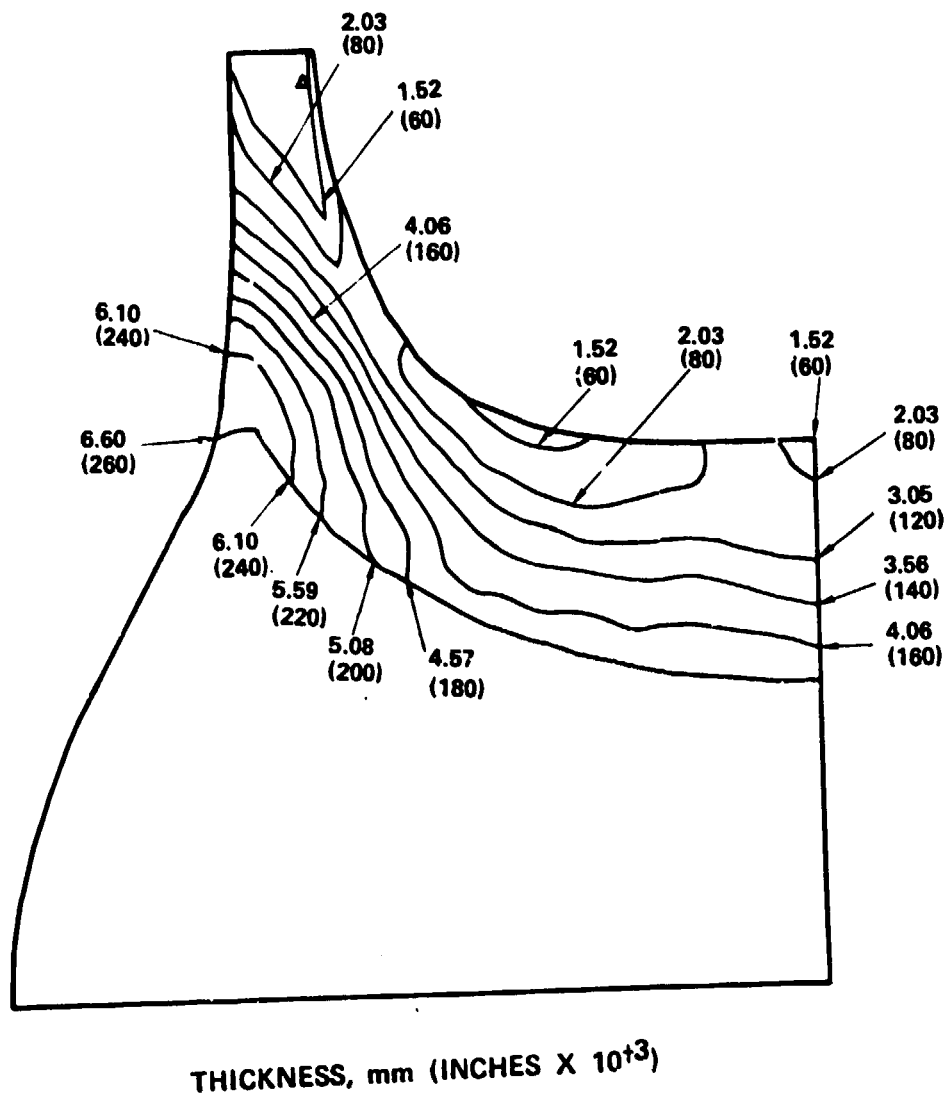
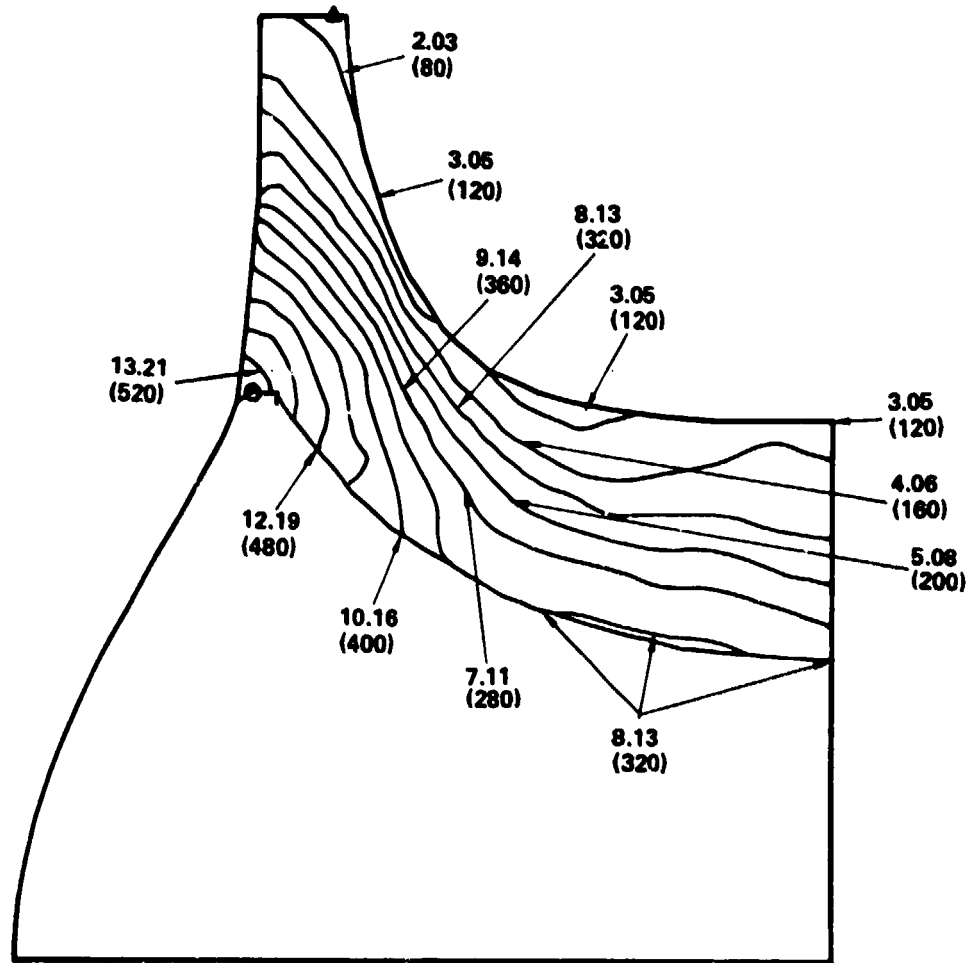


Figure 151. Total Wall Thickness Distribution.
(Pressure Plus Suction Side Thickness)



THICKNESS, mm (INCHES X 10³)

Figure 152. Blade Total Surface-to-Surface Distance Distribution.

7.2.3.3 Stress Analysis

Both 2- and 3-dimensional finite-element models were used to obtain stress results. The 3-dimensional model accurately simulated the blade curvature and the cooling-passage geometry in the blade and also included the disk geometry. The 2-dimensional model was a quicker, more cost-effective method to correctly predict stress for the axisymmetric region in the disk hub. These two models are illustrated in Figures 153, 154 and 155, respectively.

Two different operating conditions were of major interest for the turbine and were simulated in the analyses. The first was for the turbine rotating at a speed of 5969 rad/s (57000 rpm) with a uniform temperature of 294K (70°F). The second was the maximum power, sea-level, static condition. Previous design experience indicated a probable stress-range increase in the turbine during mission-transient, but was not taken into account in the design substantiation.

Figures 156 through 159 represent the equivalent elastic blade stresses for an initial nonoptimized design for the uniform temperature, rotating condition. A large stress magnitude 1813 MPa (263 ksi) and gradient were observed at the pressure-side external surface and clearly indicated the nonradiality bending effect. Figures 160 through 163 represent the equivalent blade stresses at uniform temperature rotating condition of the final design. This magnitude reduction was significant when compared with previous results, and was attributed to an increase in cross-sectional area bending stiffness. The stress gradient was attenuated at either horizontal-thickness or a span-wise direction, and was attributed to both the rake angle and the asymmetric blade thickness. Regional-stress concentrations were due to modeling limitations. Figures 164 through 166 represent the disk-bore stresses at the same running conditions as the initial design. The maximum tangential and equivalent bore stresses were 1082 MPa (157 ksi) and 1151 MPa (167 ksi), respectively. Figures 167 and 168 show the equivalent blade stress for the final design at maximum power state. As expected, the stress gradient was accentuated by the applied temperature gradient. Localized high-magnitude stresses were also observed in this calculation. These high stresses were attributed to the temperature distribution and gradient calculated by the 2-dimensional thermal analysis. It is believed that these high stresses could be minimized by performing a full 3-dimensional thermal analysis to smooth the temperature gradient. Figures 169 through 171 represent the disk stresses at the maximum power state. The maximum tangential and equivalent stresses at the base were 1289 MPa (187 ksi) and 1310 MPa (190 ksi), respectively.

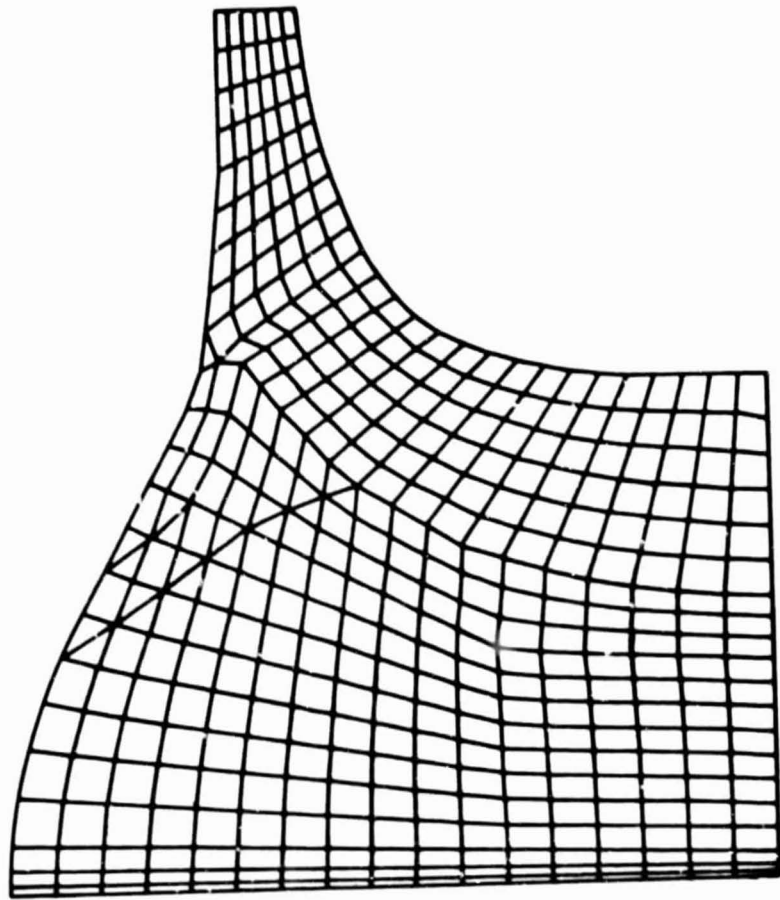


Figure 153. 2-Dimensional Finite-Element Stress Model.

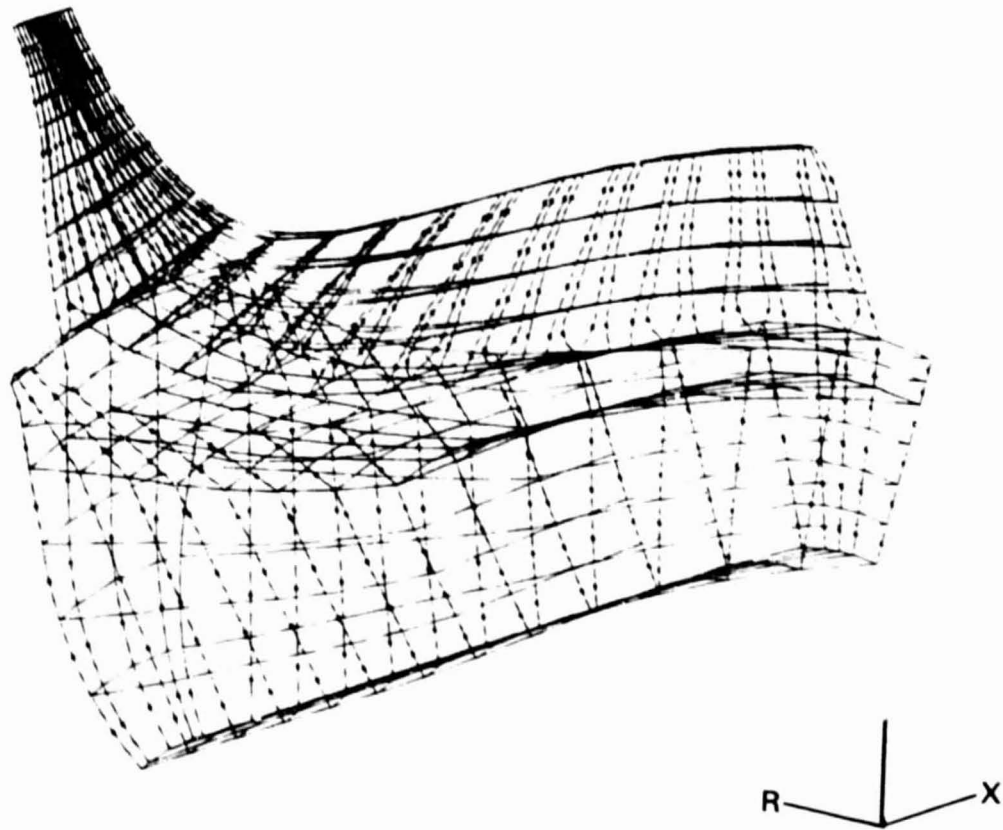


Figure 154. 3-Dimensional Finite-Element Stress Model, Axiometric View.

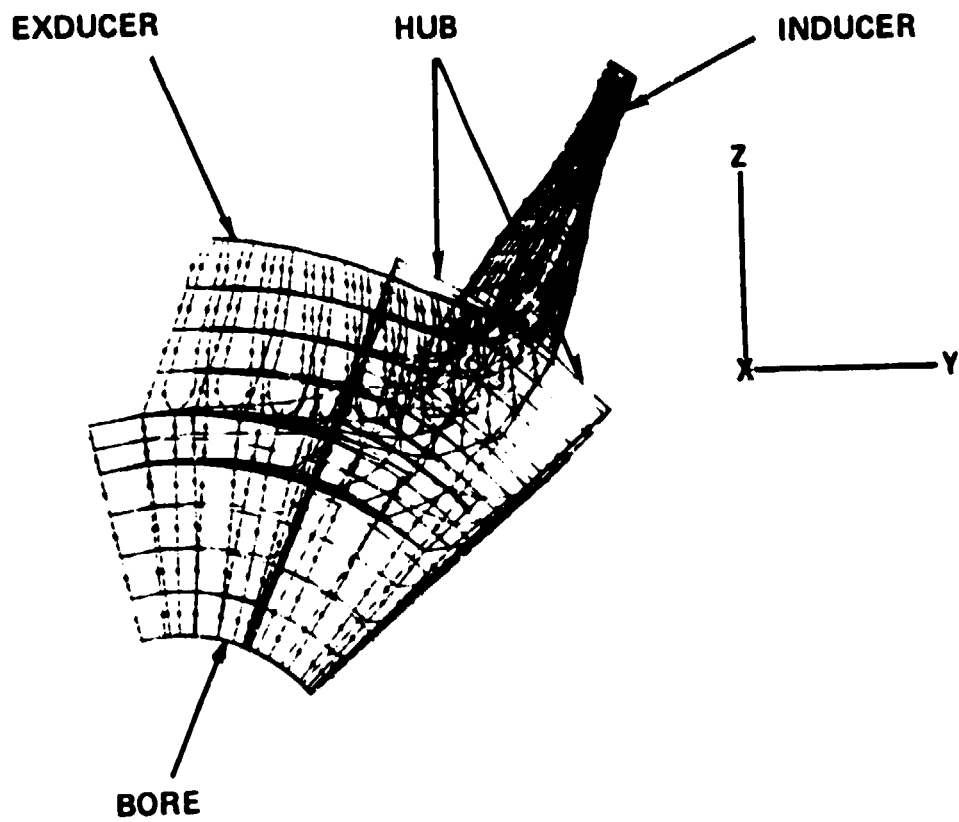


Figure 155. 3-Dimensional Finite-Element Stress Model, End View.

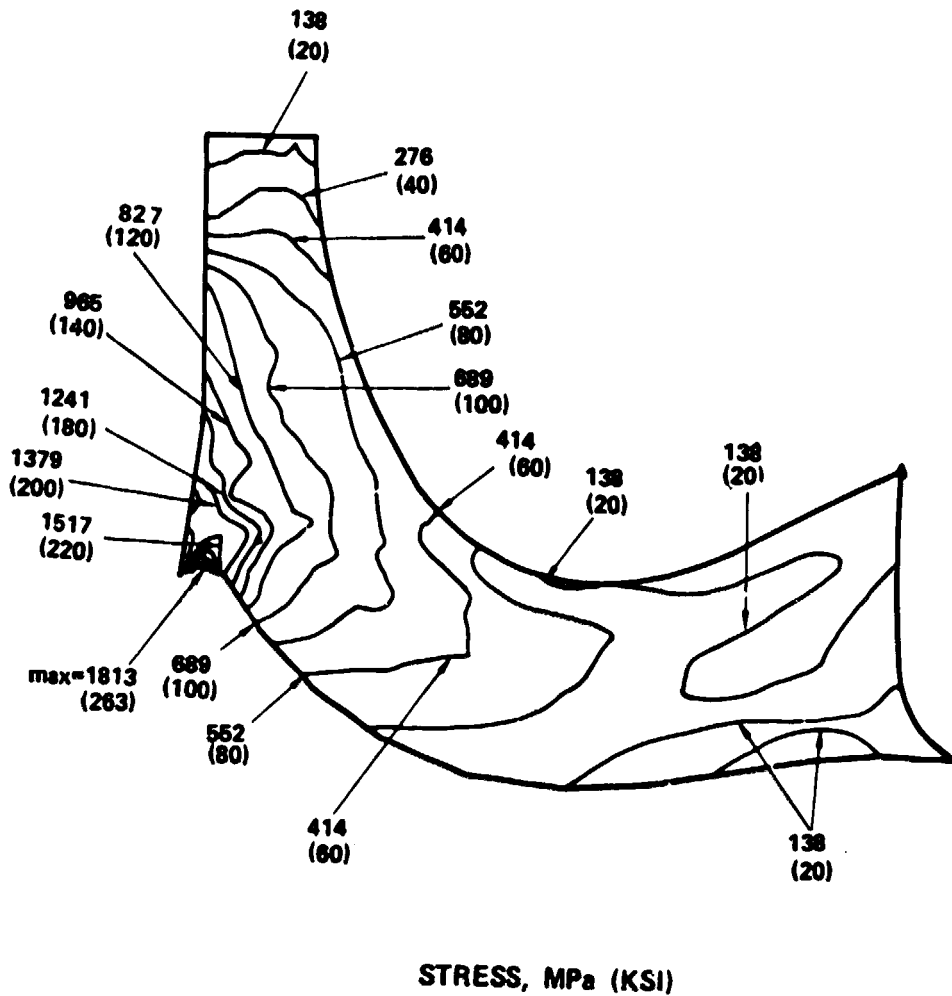


Figure 156. Initial Turbine Design Equivalent Elastic Blade Stress, Pressure-Side External Surface (Fore-shortened View). Uniform Temp - 294K (70°F).

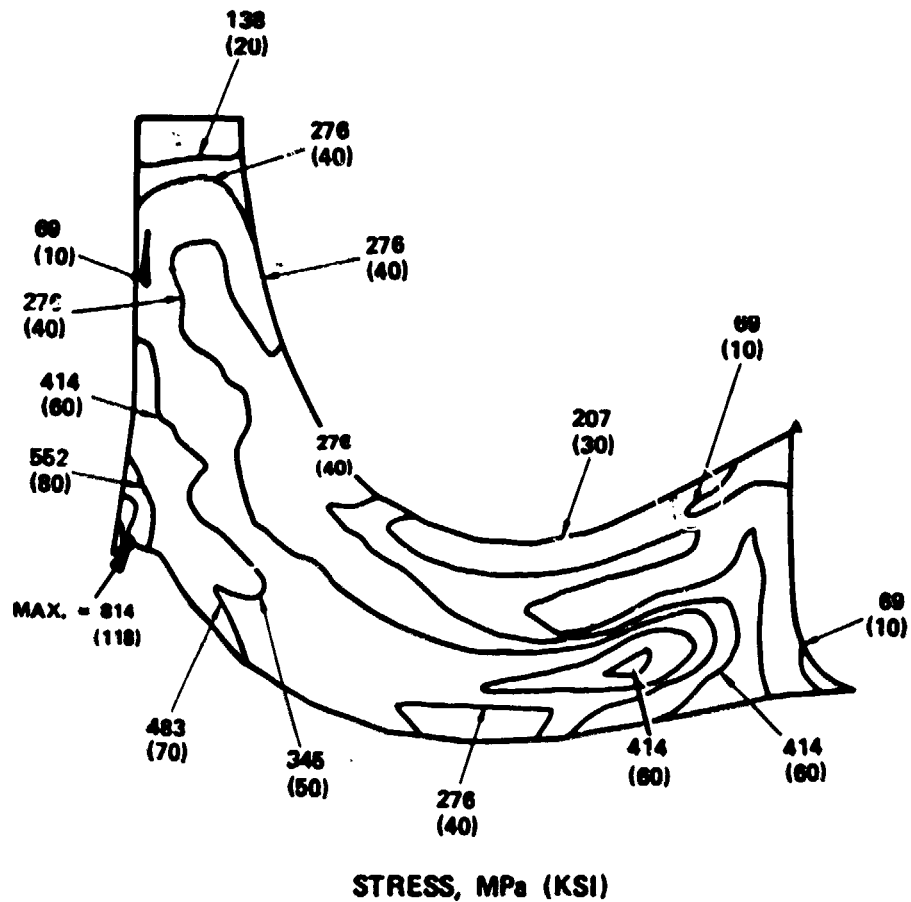


Figure 157. Initial Turbine Design Blade Pressure-Side Internal Surface Equivalent Stress at 5969 rad/s (57,000 RPM). Uniform Temp - 294K (70°F).

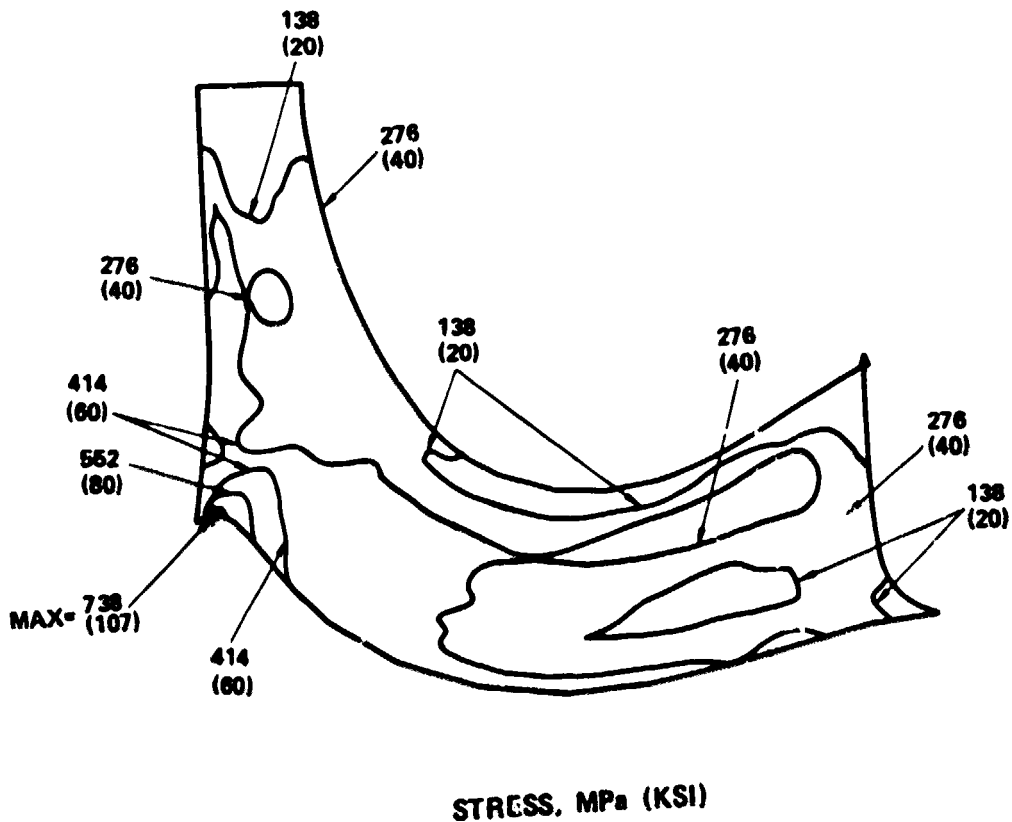


Figure 158. Initial Turbine Design Suction-Side Internal Surface
 Equivalent Stress at 5969 rad/s (57,000 RPM).
 Uniform Temp - 294K (70°F).

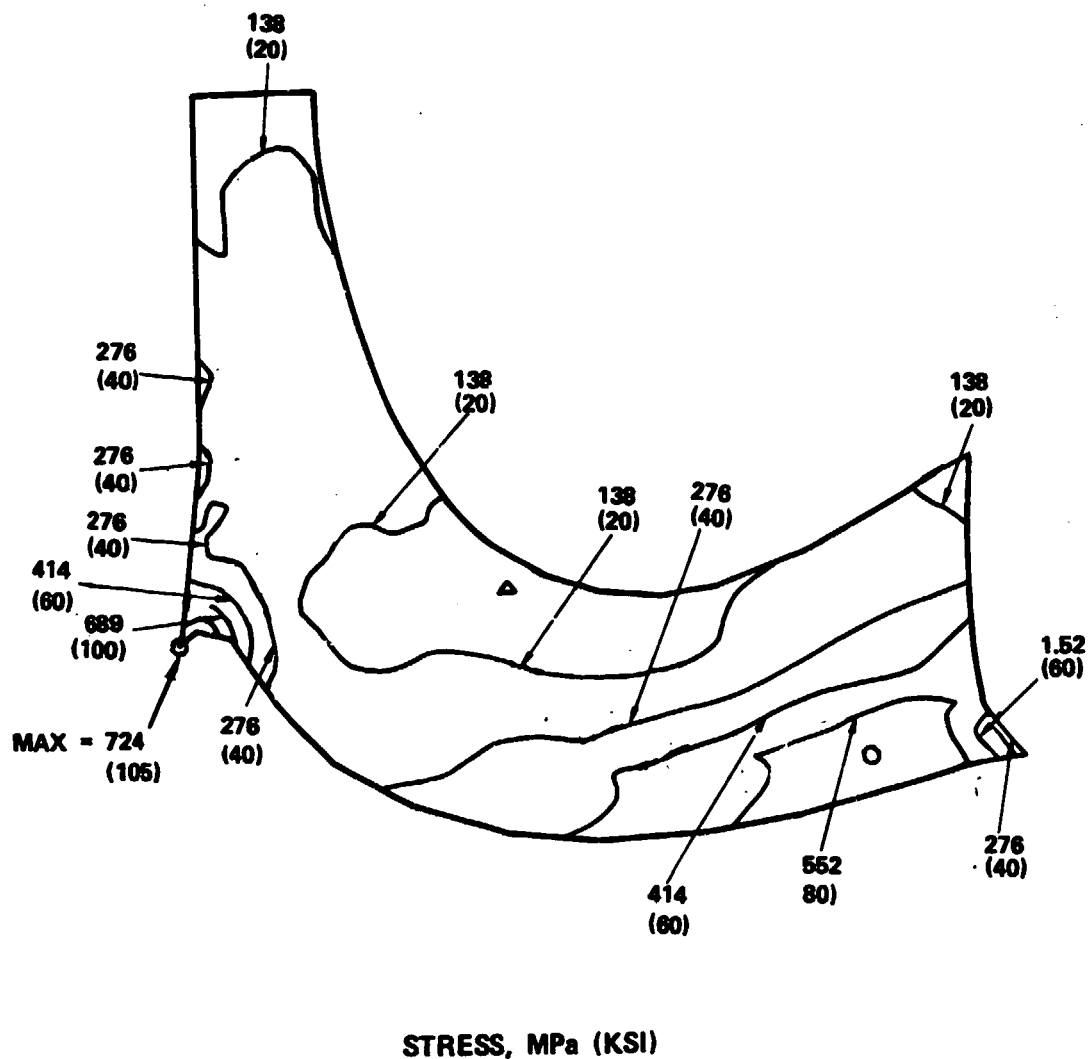


Figure 159. Initial Turbine Design Blade Suction-Side External Surface Equivalent Stress, 100-Percent Power at 5969 rad/s (57,000 RPM). Uniform Temp - 294K (70°F).

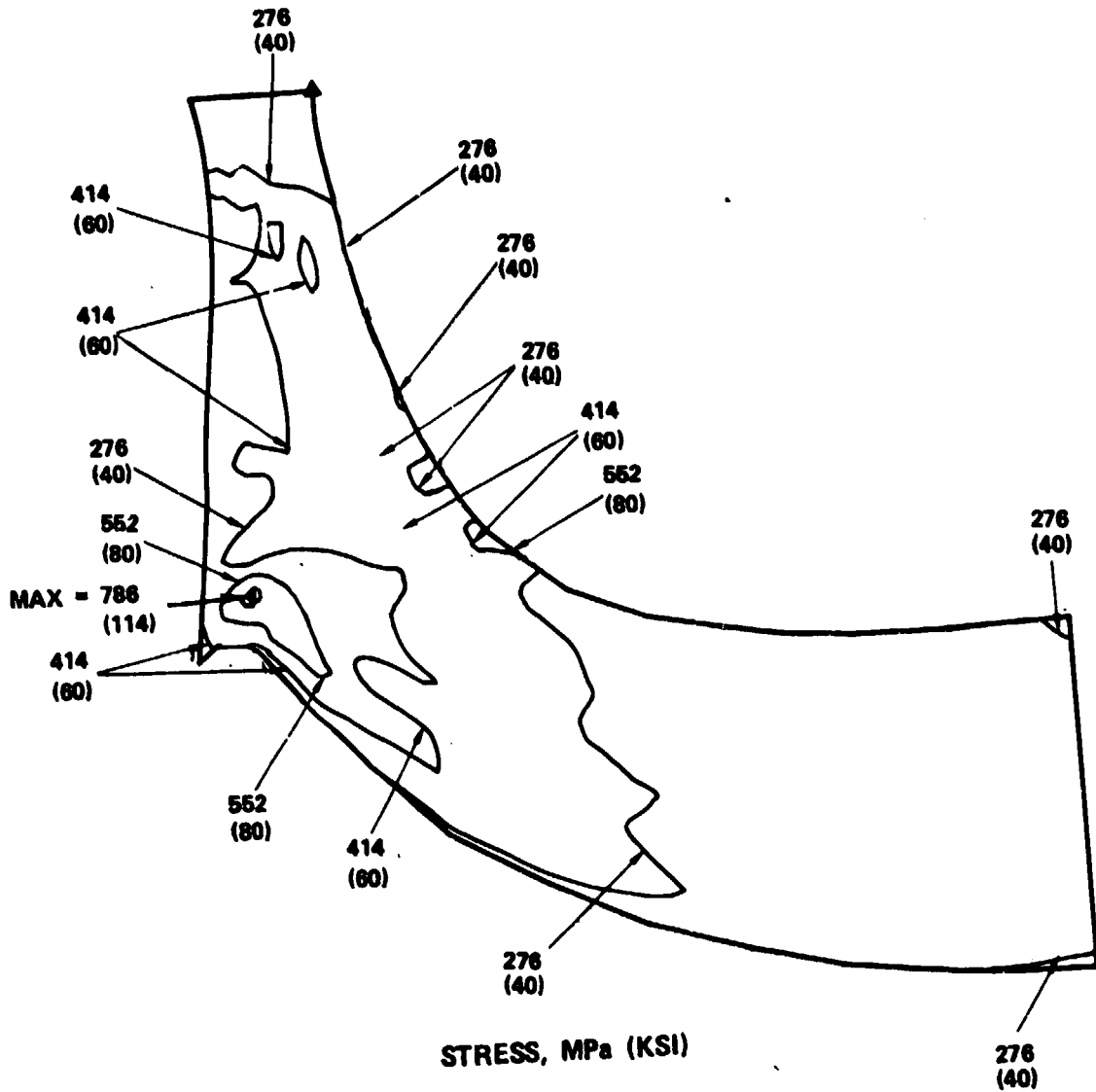


Figure 160. Blade Pressure-Side External Surface Equivalent Stress, Optimized Design at 5969 rad/s (57,000 RPM). Uniform Temp - 294K (70°F).

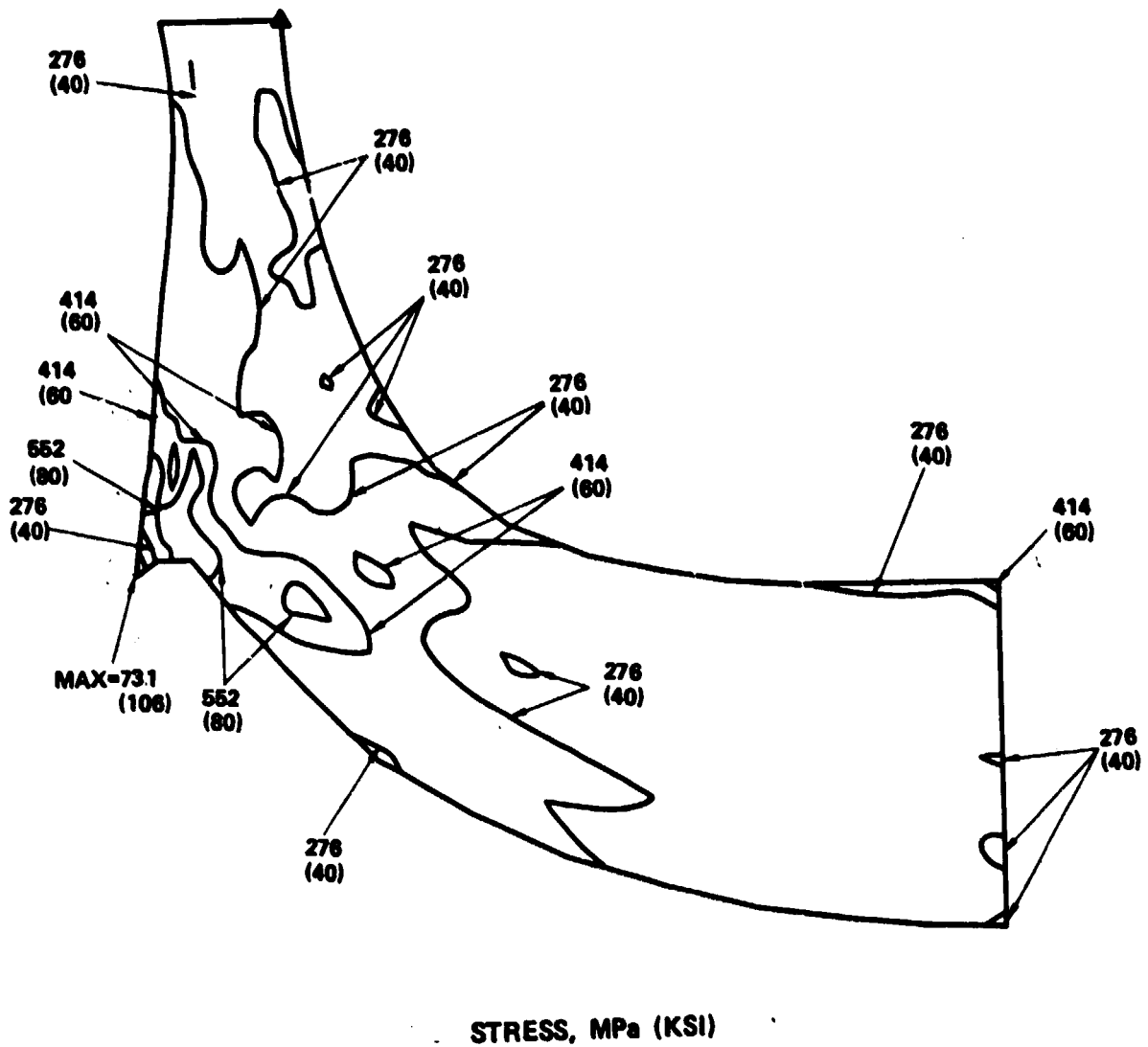


Figure 161. Blade Pressure-Side Internal Surface Equivalent Stress, Optimized Design at 5969 rad/s (57,000 RPM). Uniform Temp - 294K (70°F).

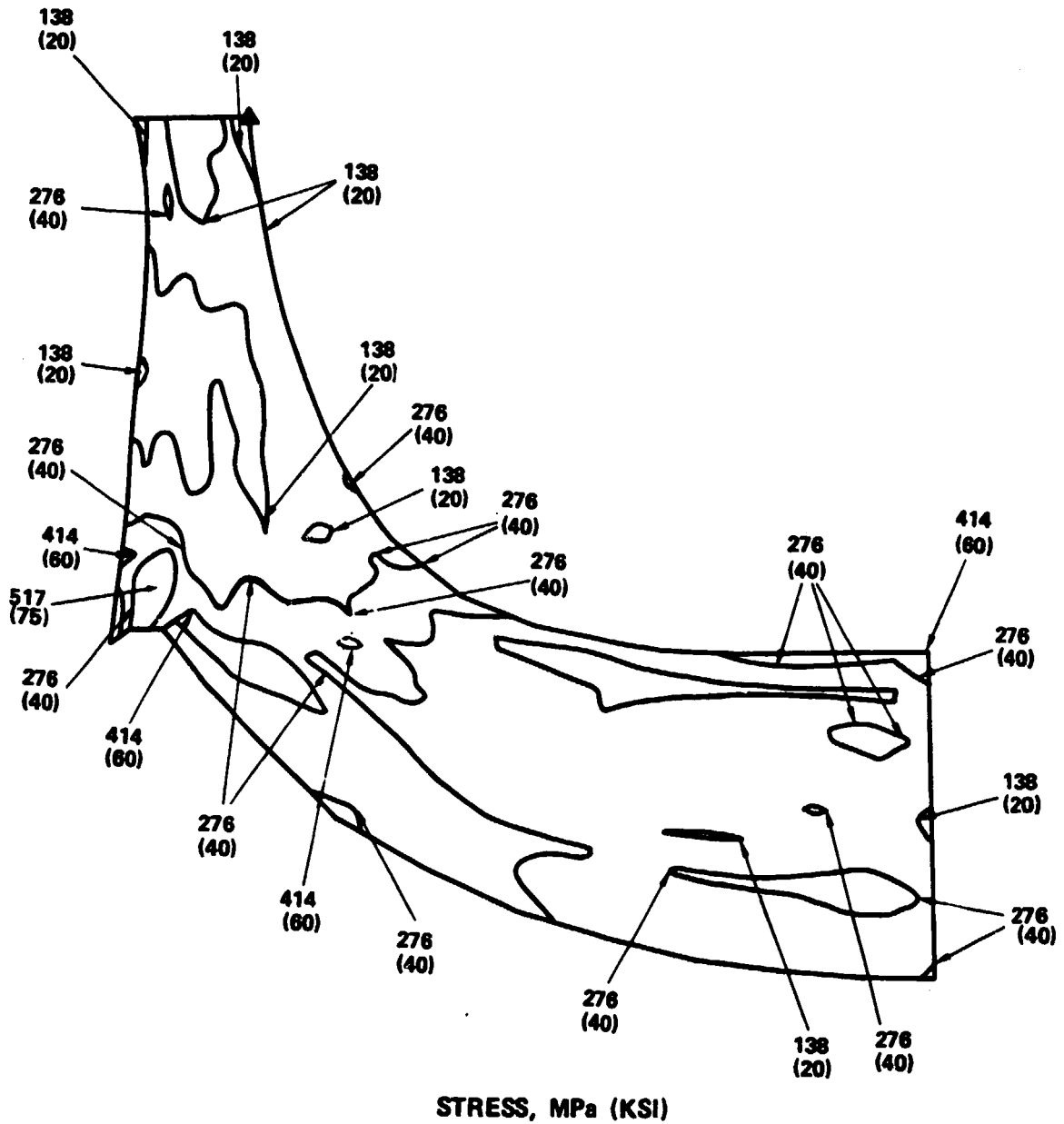


Figure 162. Blade Suction-Side Internal Surface Equivalent Stress, Optimized Design at 5969 rad/s (57,000 RPM). Uniform Temp - 294K (70°F).

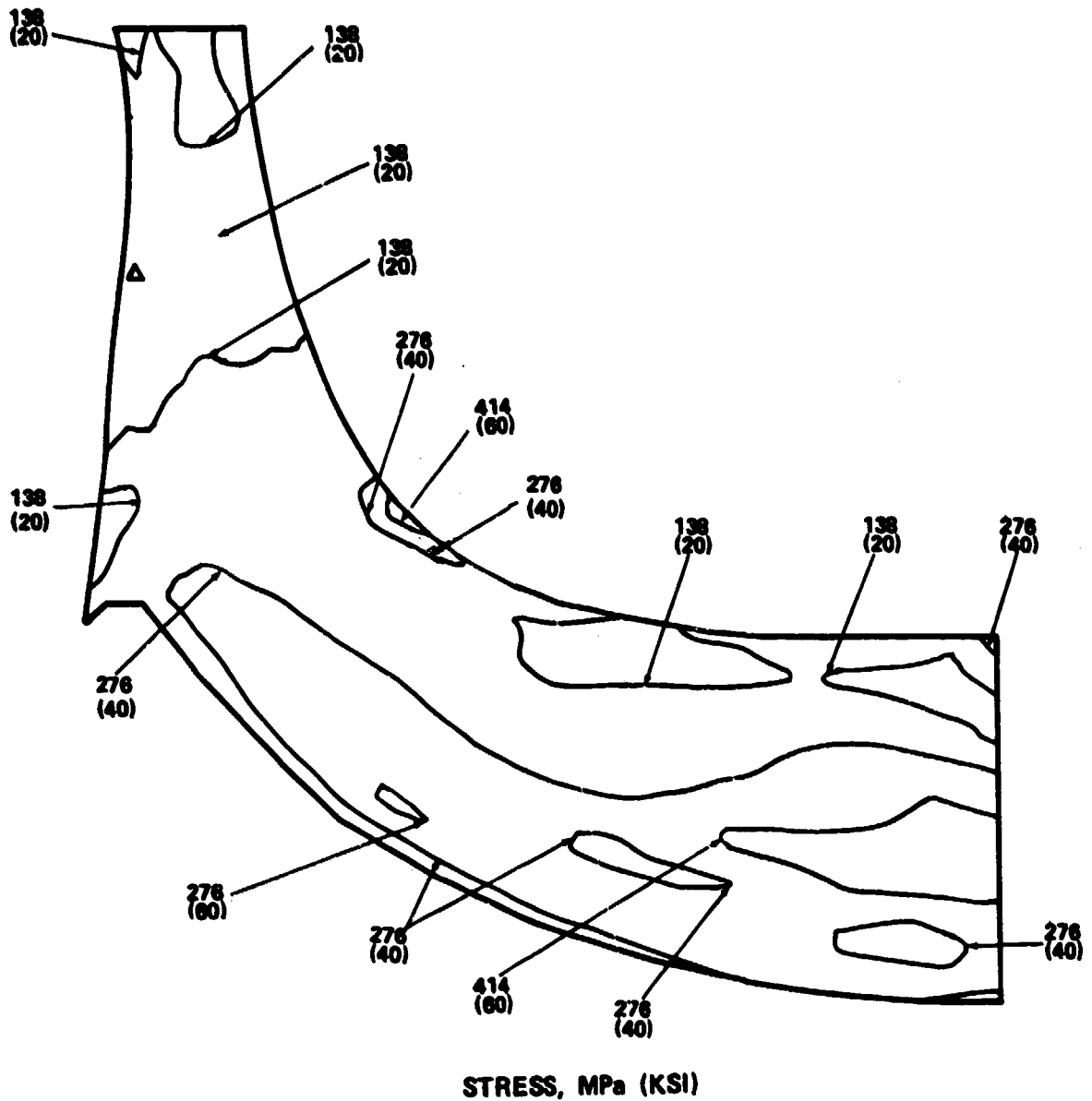


Figure 163. Blade Suction-Side External Surface Equivalent Stress, Optimized Design at 5969 rad/s (57,000 RPM). Uniform Temp - 294K (70°F).

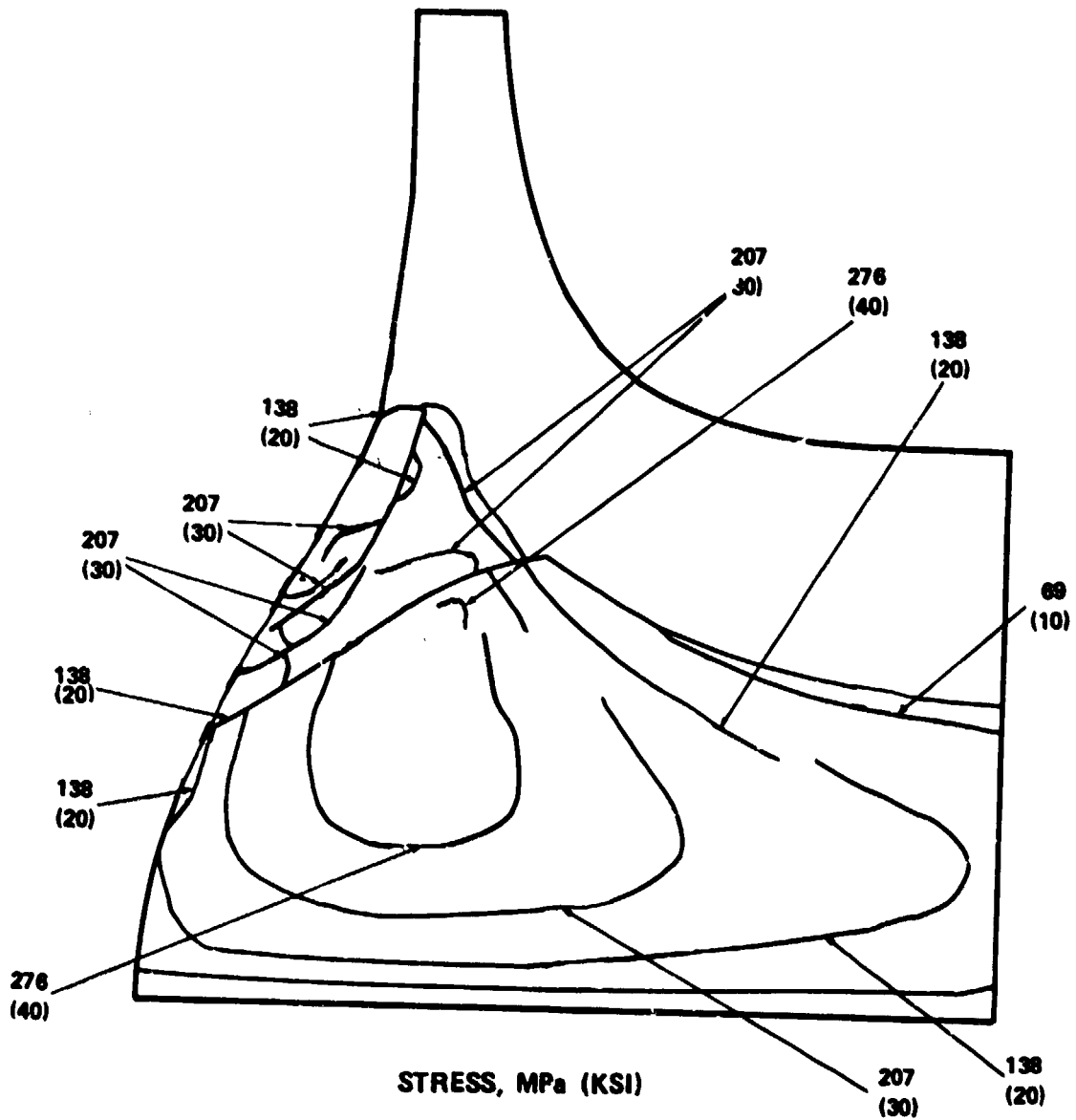


Figure 164. Initial Design Disk Radial Stress at 5969 rad/s (57,000 RPM). Uniform Temp - 294K (70°F).

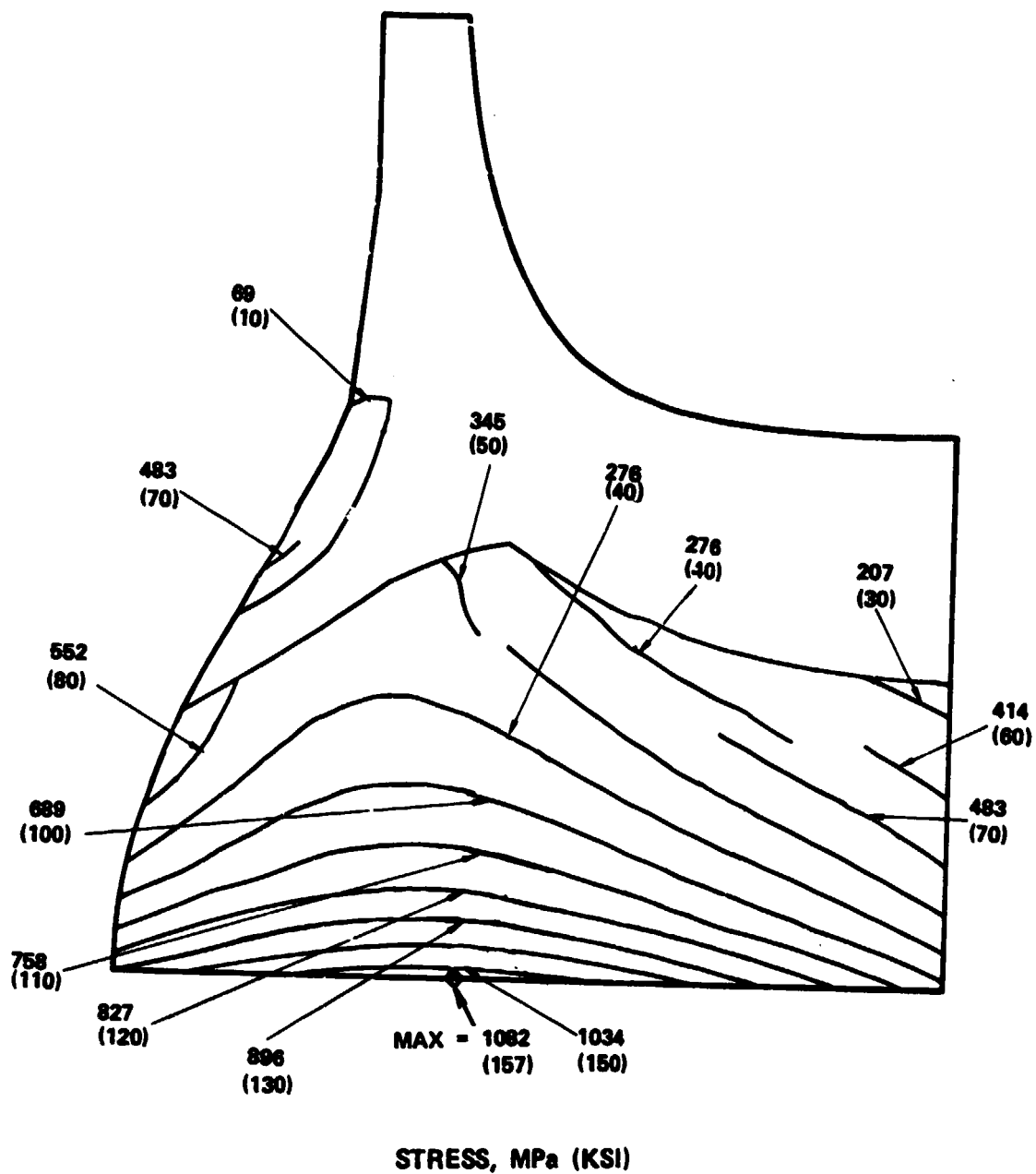


Figure 165. Initial Design Disk Tangential Stress at 5969 rad/s (57,000 RPM). Uniform Temp - 294K (70°F).

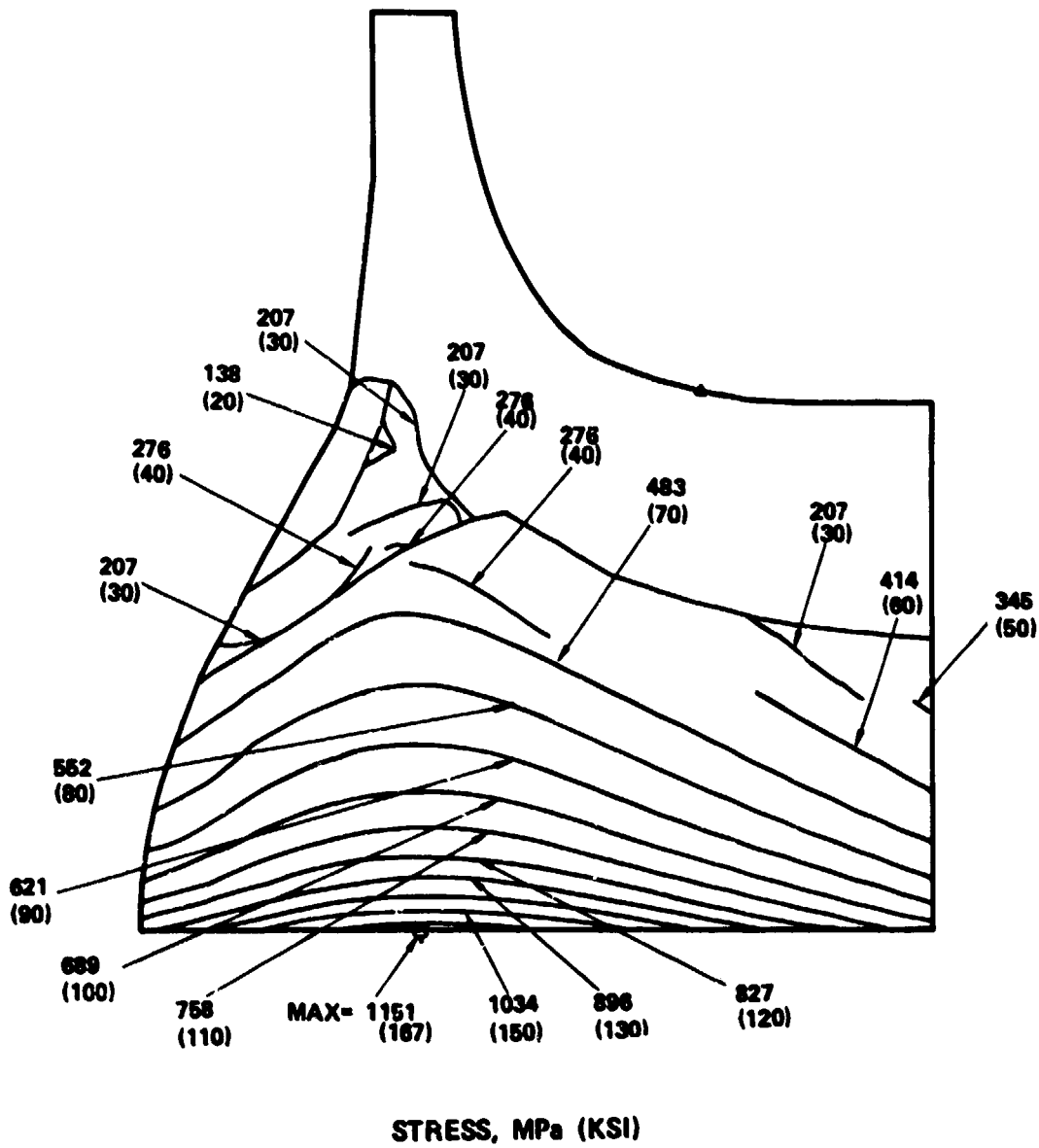


Figure 166. Initial Design Disk Equivalent Stress at 5969 rad/s (57,000 RPM). Uniform Temp - 294K (70°F).

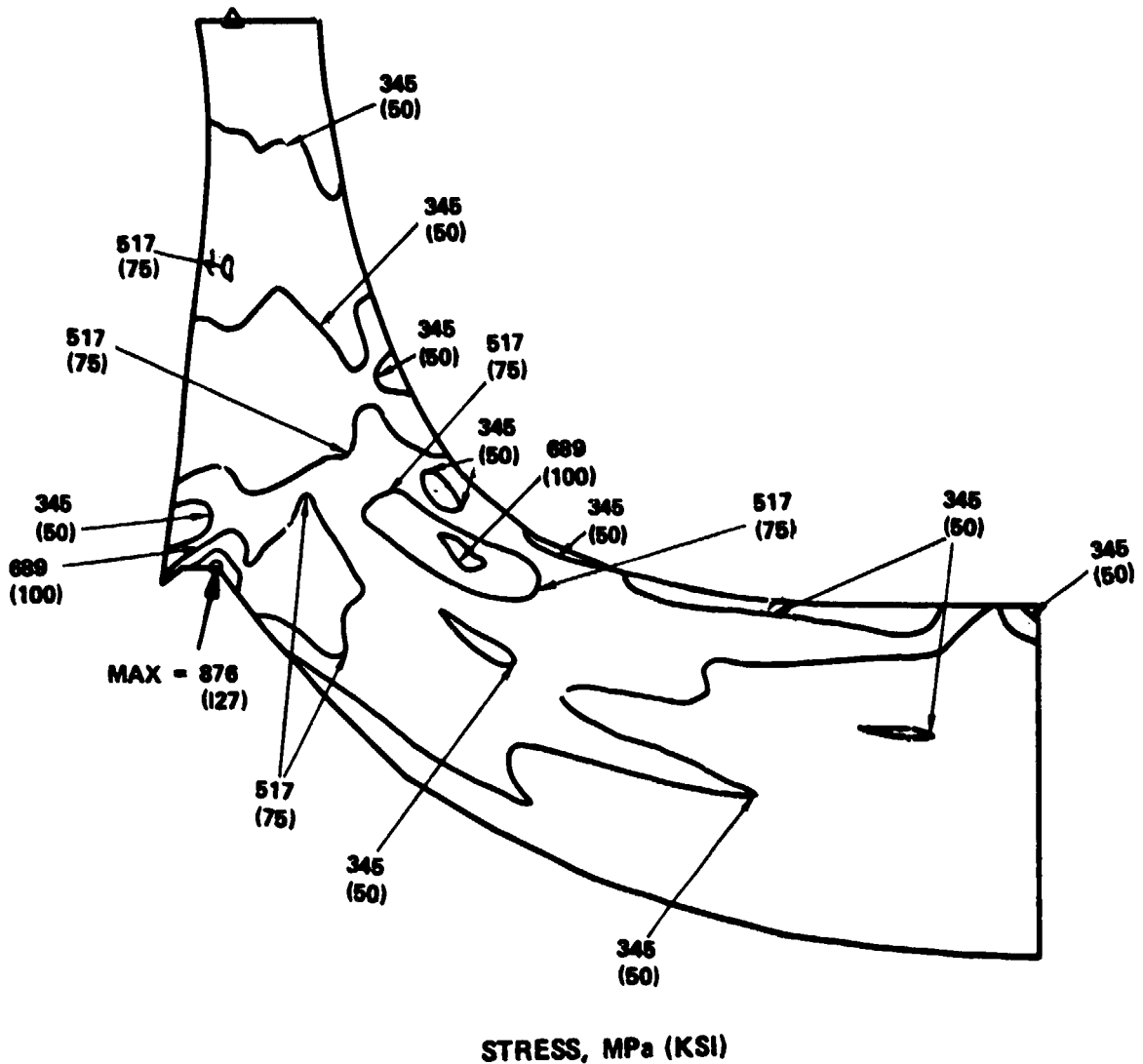


Figure 167. Final Design Blade Pressure-Side External Surface Equivalent Stress at 100-Percent Power.

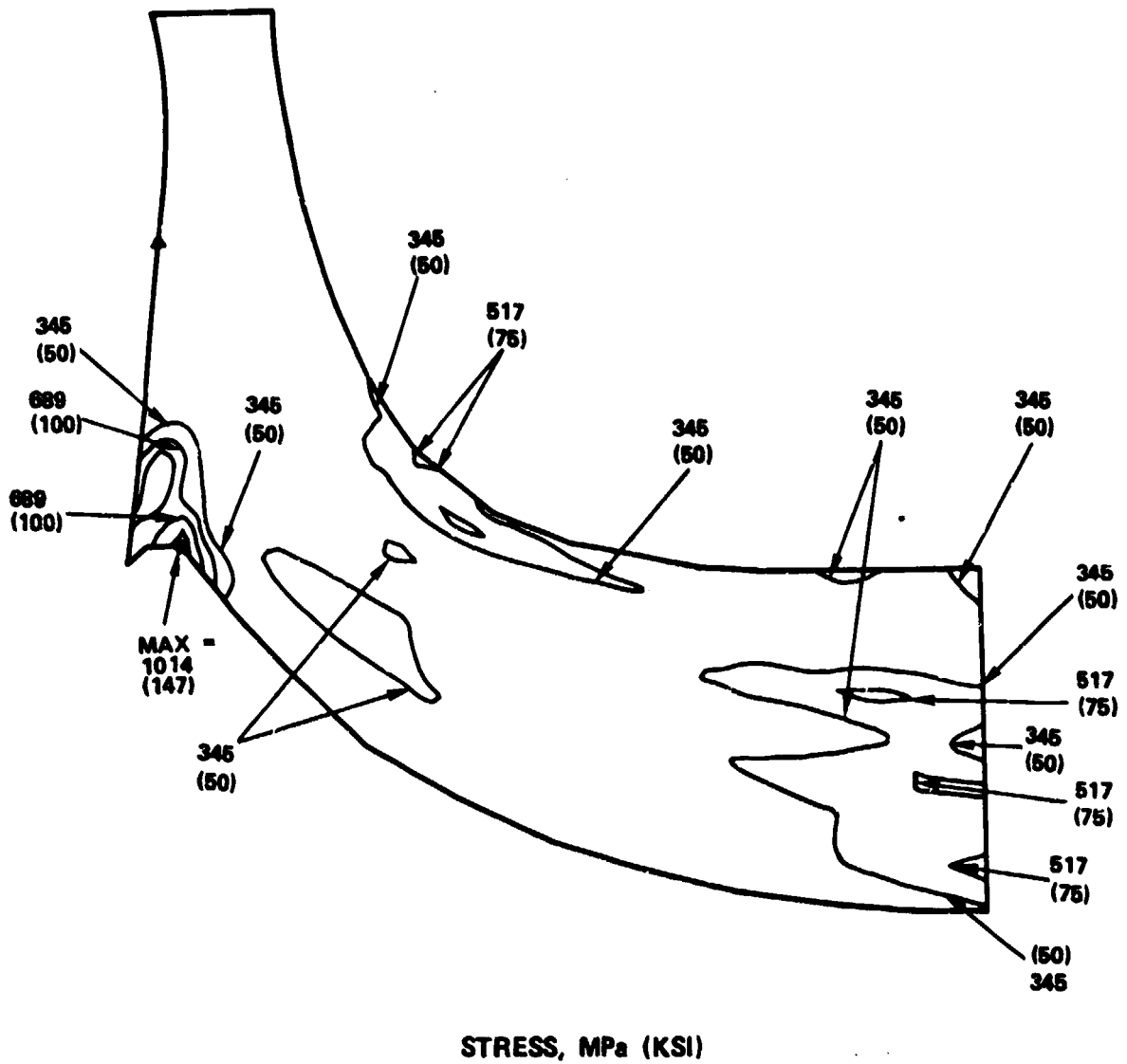
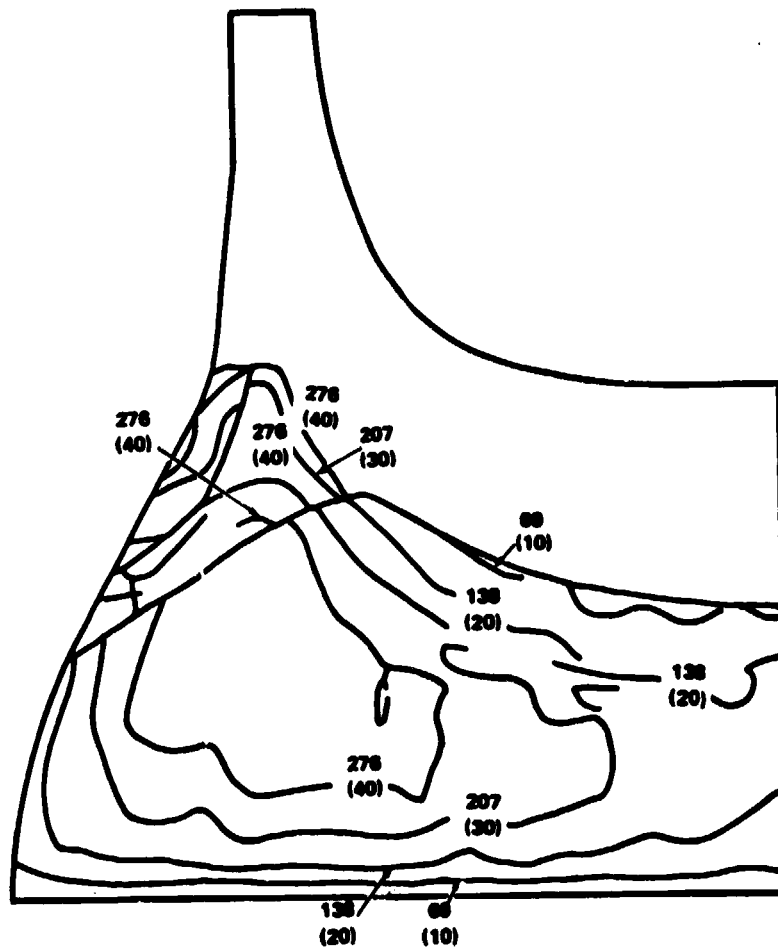


Figure 168. Final Design Blade Suction-Side External Surface Equivalent Stress, Optimized Design at Maximum Power.



STRESS, MPa (KSI)

Figure 169. Final Design Disk Radial Stress at Maximum Power.

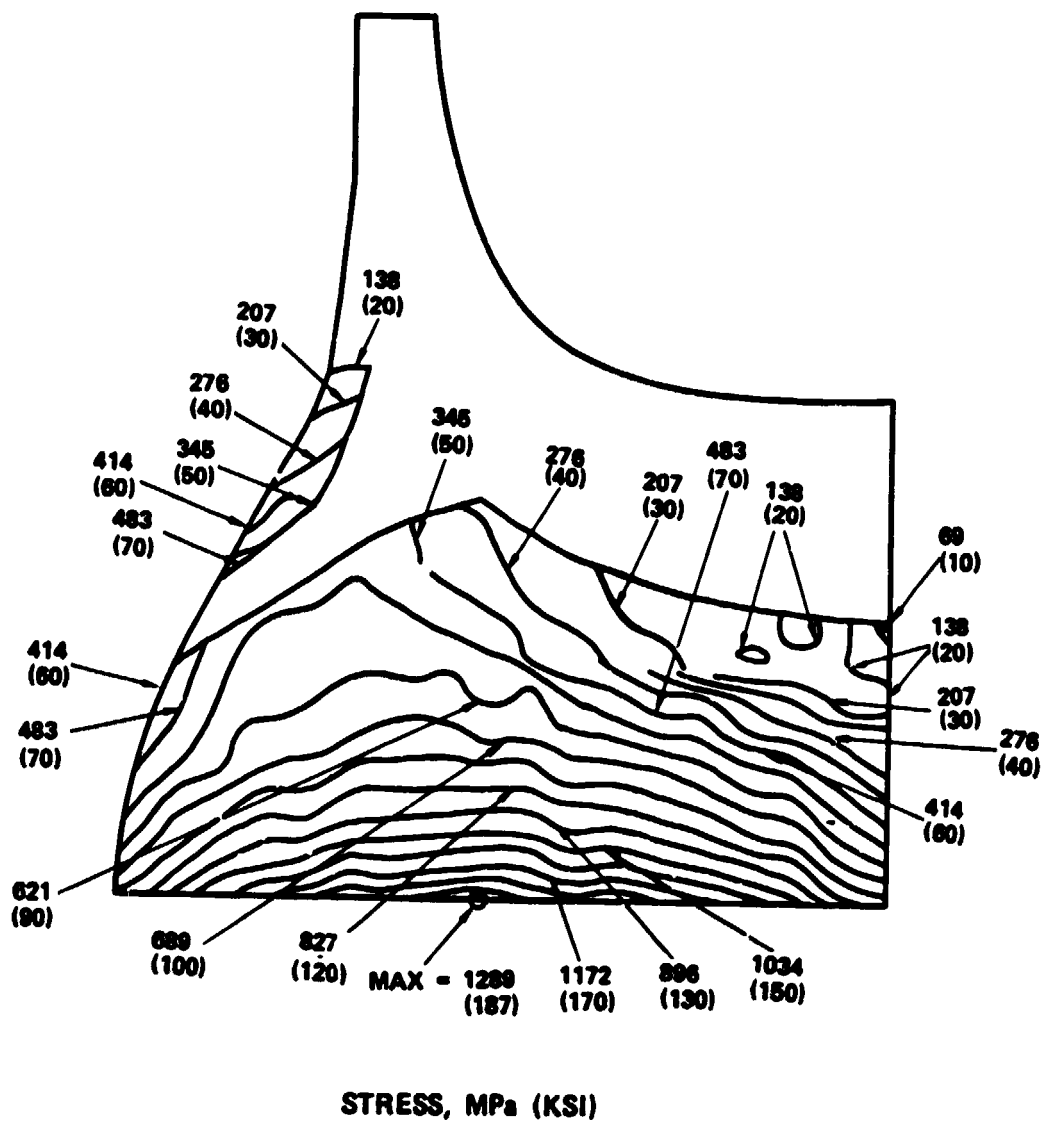


Figure 170. Final Design Disk Tangential Stress at Maximum Power.

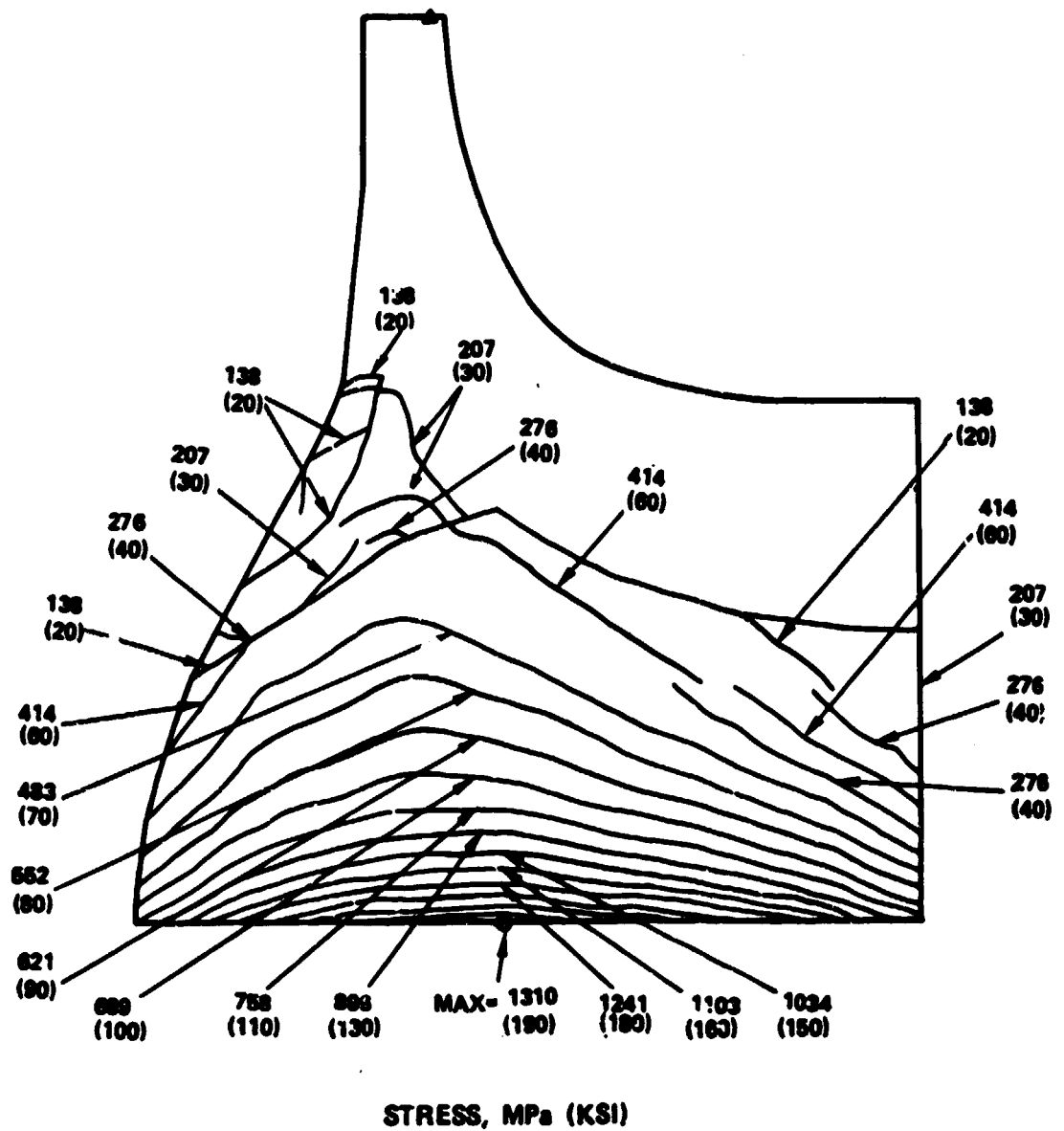


Figure 171. Final Design Disk Equivalent Stress, 100-Percent Power Condition.

Burst margin is calculated as:

$$BM = \sqrt{0.85 \frac{\sigma_{TANG}}{\sigma_{ULT}}}$$

where:

- BM = Burst margin
- 0.85 = Material utilization factor
- σ_{TANG} = Average disk tangential stress
- σ_{ULT} = Average disk material ultimate strength

Using the stress results and Astroloy tensile properties, the burst margins at 100-percent maximum power and whirlpit-test conditions were computed as 1.23 and 1.25, respectively. These burst margins are acceptable to Garrett for a preliminary turbine rotor design.

7.2.3.4 Vibration Analysis

A 3-dimensional finite-element model with airfoil section only was used to obtain blade-vibration characteristics. Two running conditions (as defined by the stress analysis) were analyzed, and natural frequencies and vibration-mode shapes were examined.

Figure 172 presents a Campbell diagram indicating the interference between the blade natural frequencies and the engine excitation orders at room temperature that will be of interest for the build and test of turbine hardware. Figure 173 shows a Campbell diagram at the 100-percent power condition. Figures 174 through 178 illustrate the first mode shapes for the pressure- and suction-side of the blade. The fundamental frequencies fall between the 5th and 6th engine orders. In previous turbine-design experience, a blade with a fundamental frequency higher than the 4th engine order should not have vibration problems--provided the higher natural frequencies do not interfere with integral multiples of stator count.

7.2.3.5 Life Analysis

- o Blade Stress-Rupture Life - For a 4000-hour total mission life, the following duty cycles are required to meet the blade stress-rupture life goals:

<u>Power (%)</u>	<u>Time (%)</u>
100	20
60	50
55	20
35	5
Idle	5

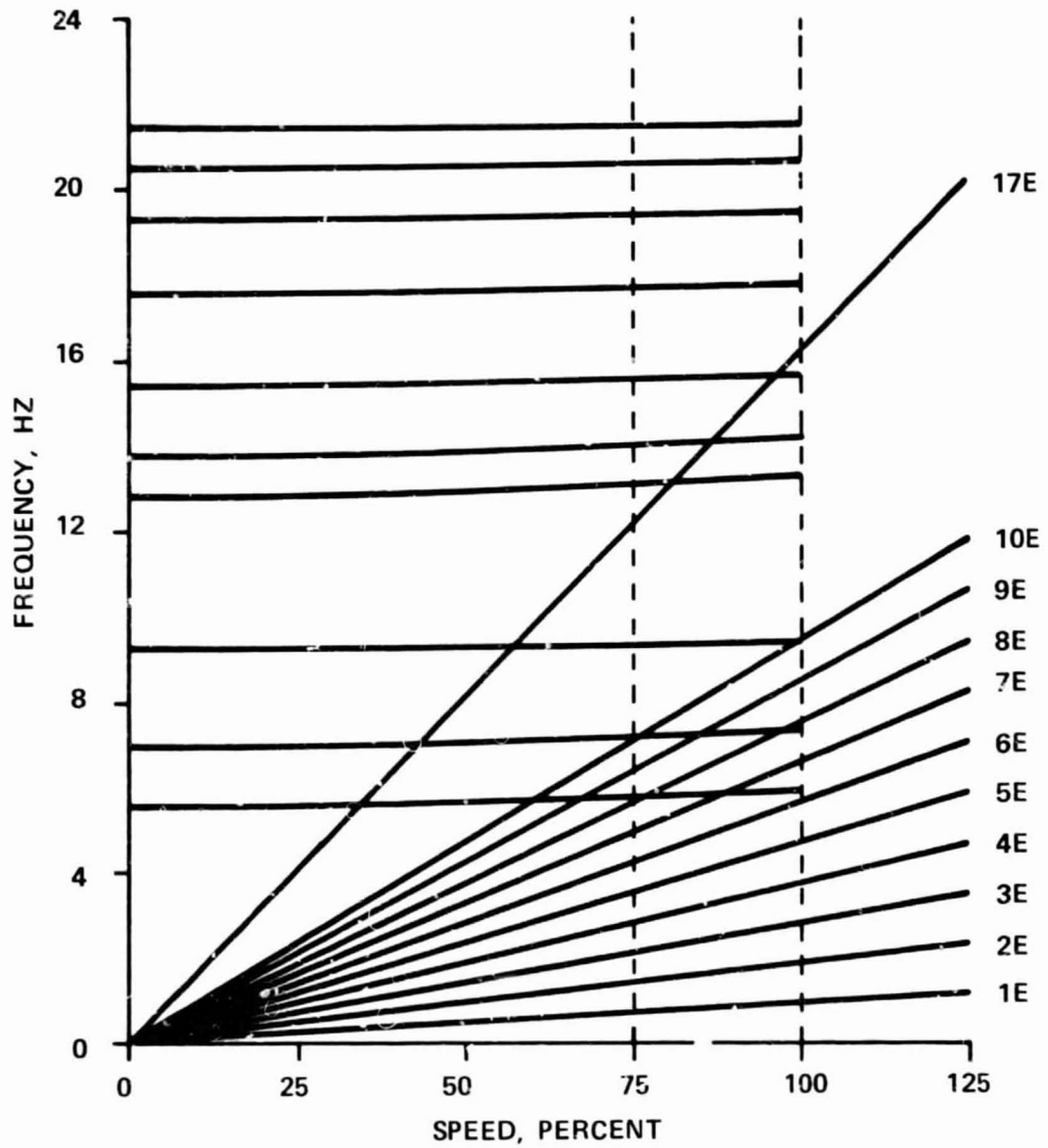


Figure 172. Campbell Diagram Showing Interference between Natural Blade Frequencies and Engine Excitation Orders at Room Temperature.

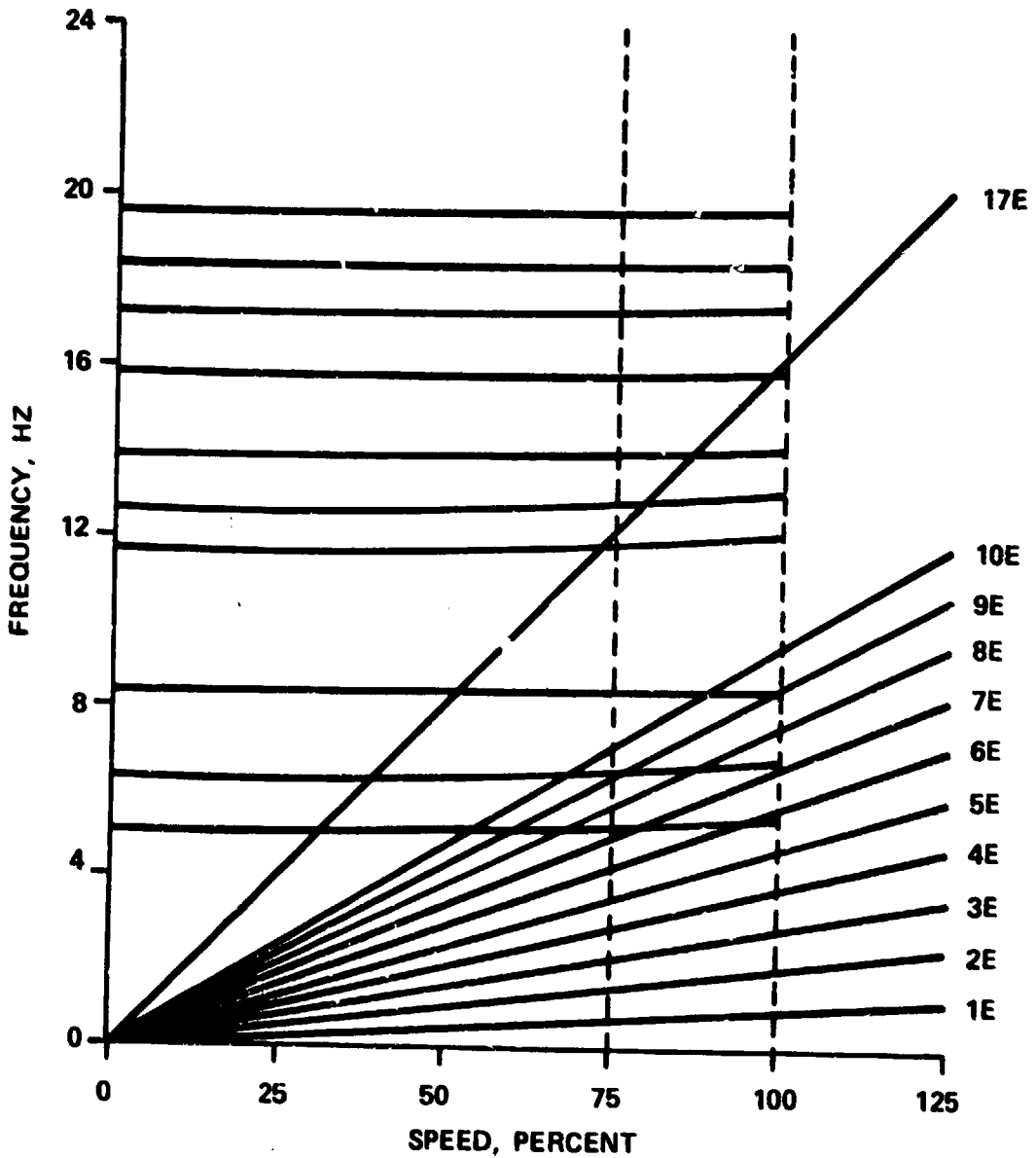


Figure 173. Campbell Diagram Showing Interference Between Natural Blade Frequencies and Engine Excitation Orders at Maximum Power.

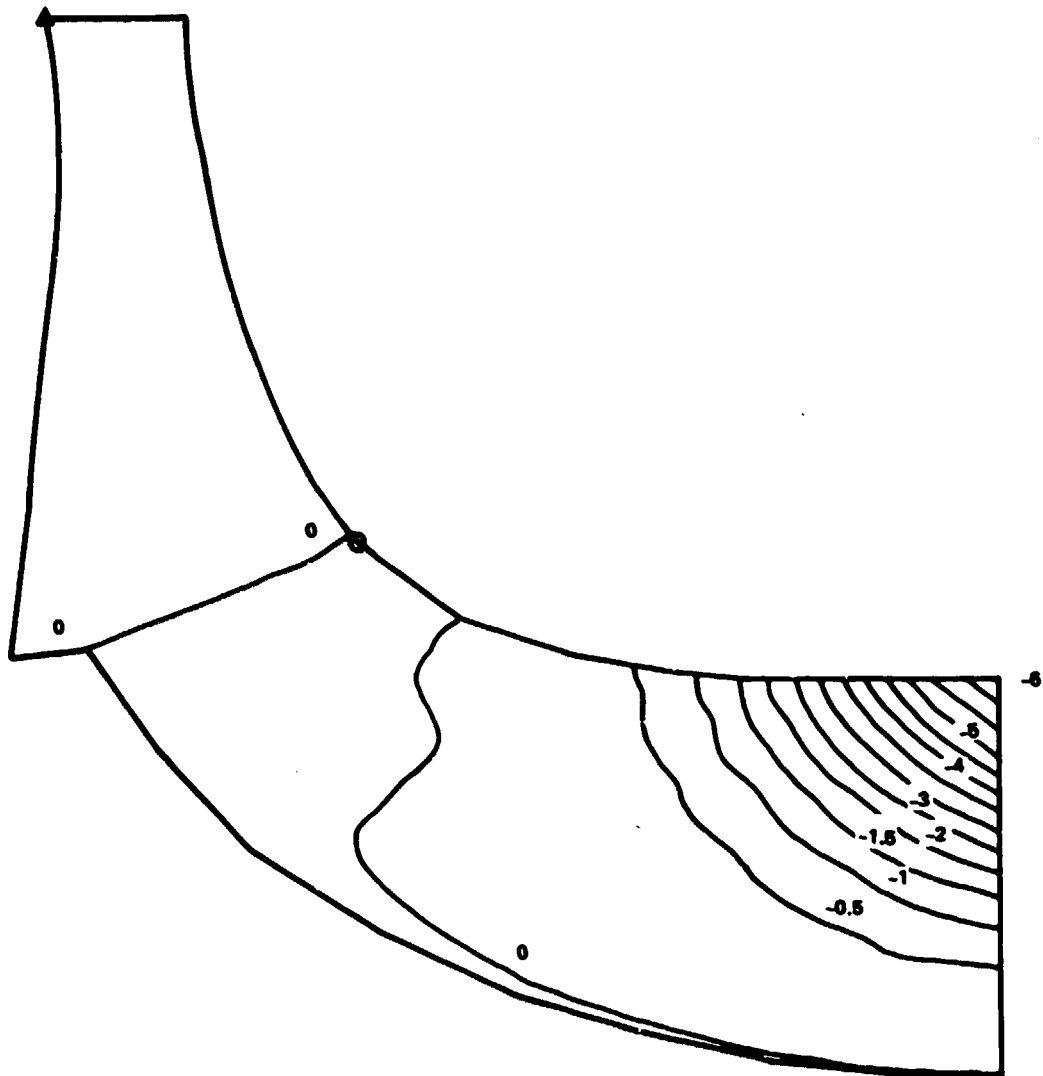


Figure 174. Mode Shape No. 1 with Normalized Displacements at 5969 rad/s (57,000 RPM).

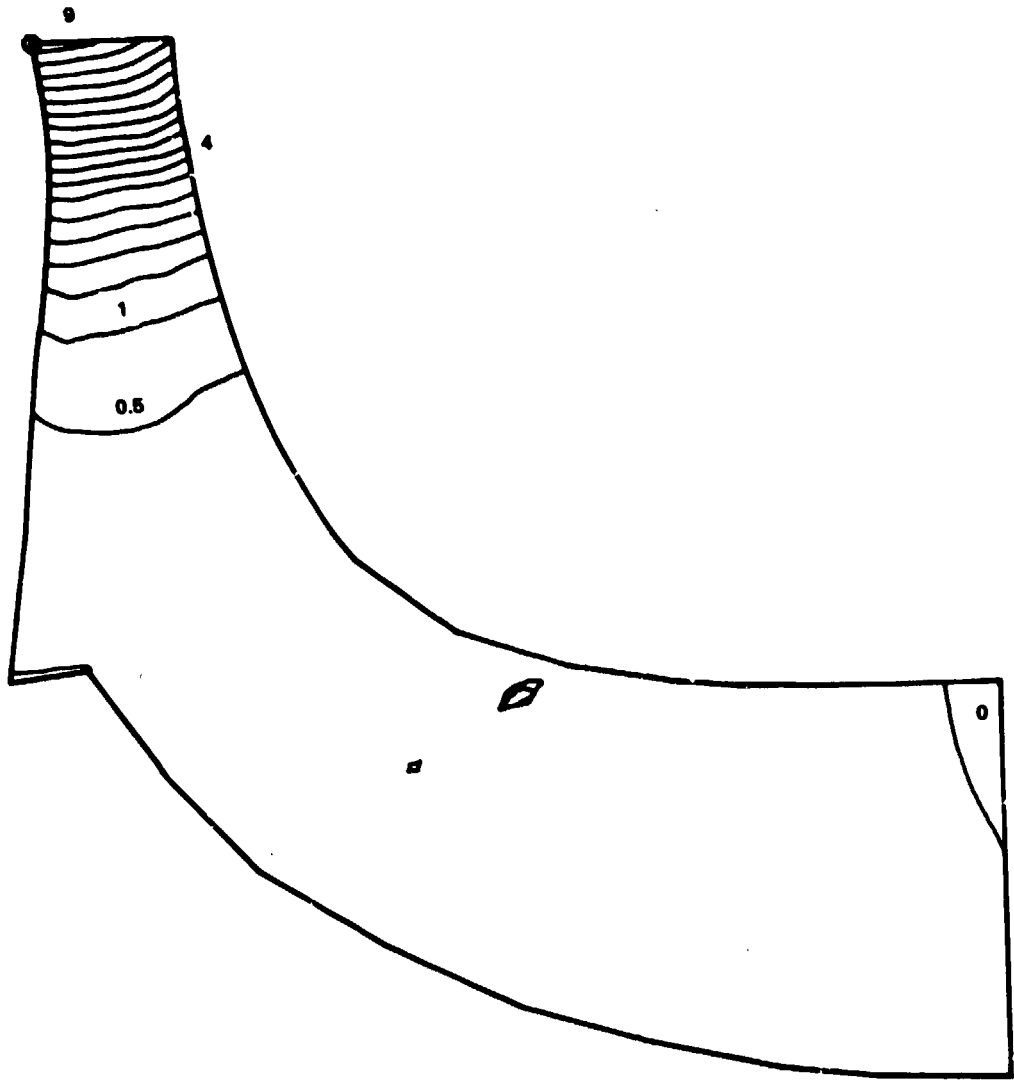


Figure 175. Mode Shape No. 2 with Normalized Displacements at 5969 rad/s (57,000 RPM).

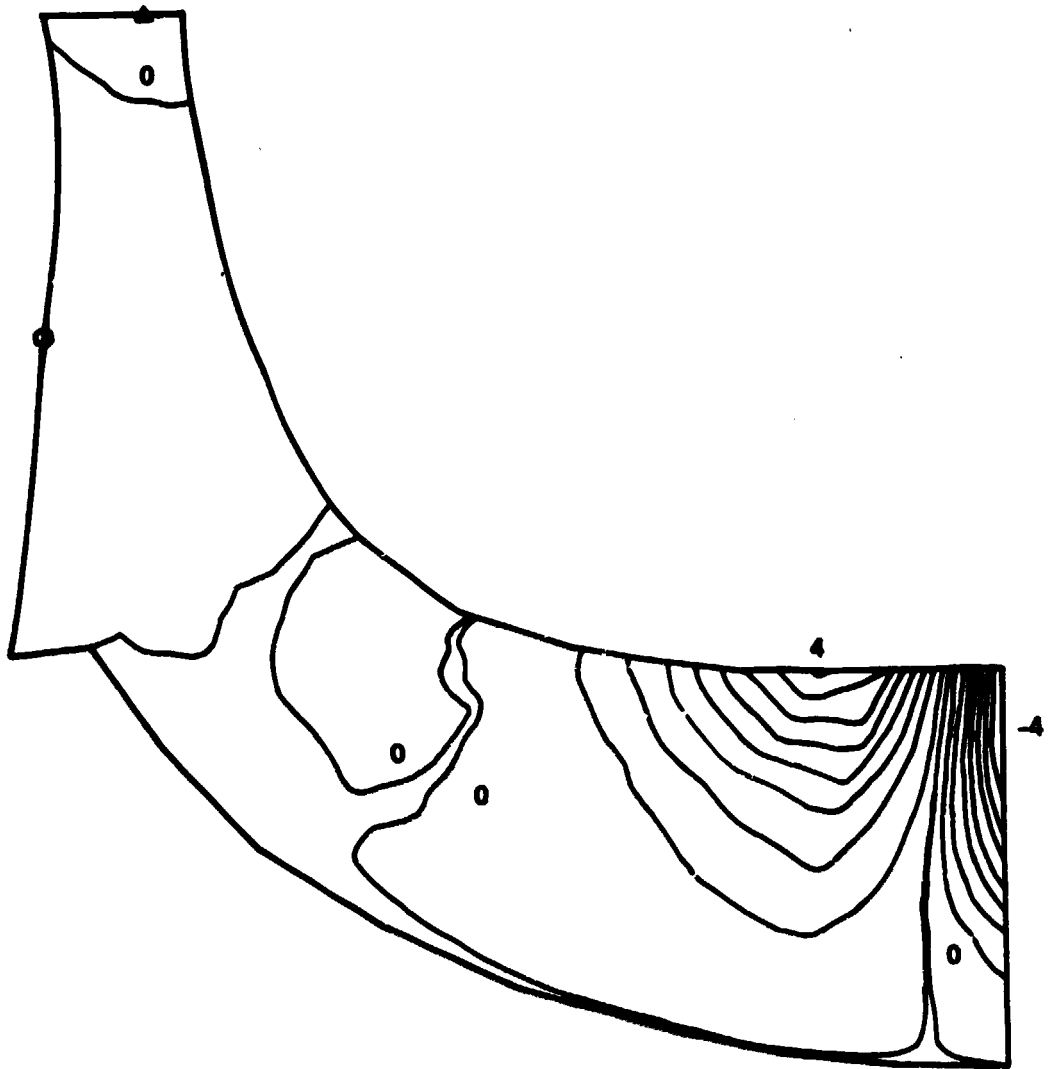


Figure 176. Mode Shape No. 3 with Normalized Displacements at 5969 rad/s (57,000 RPM).

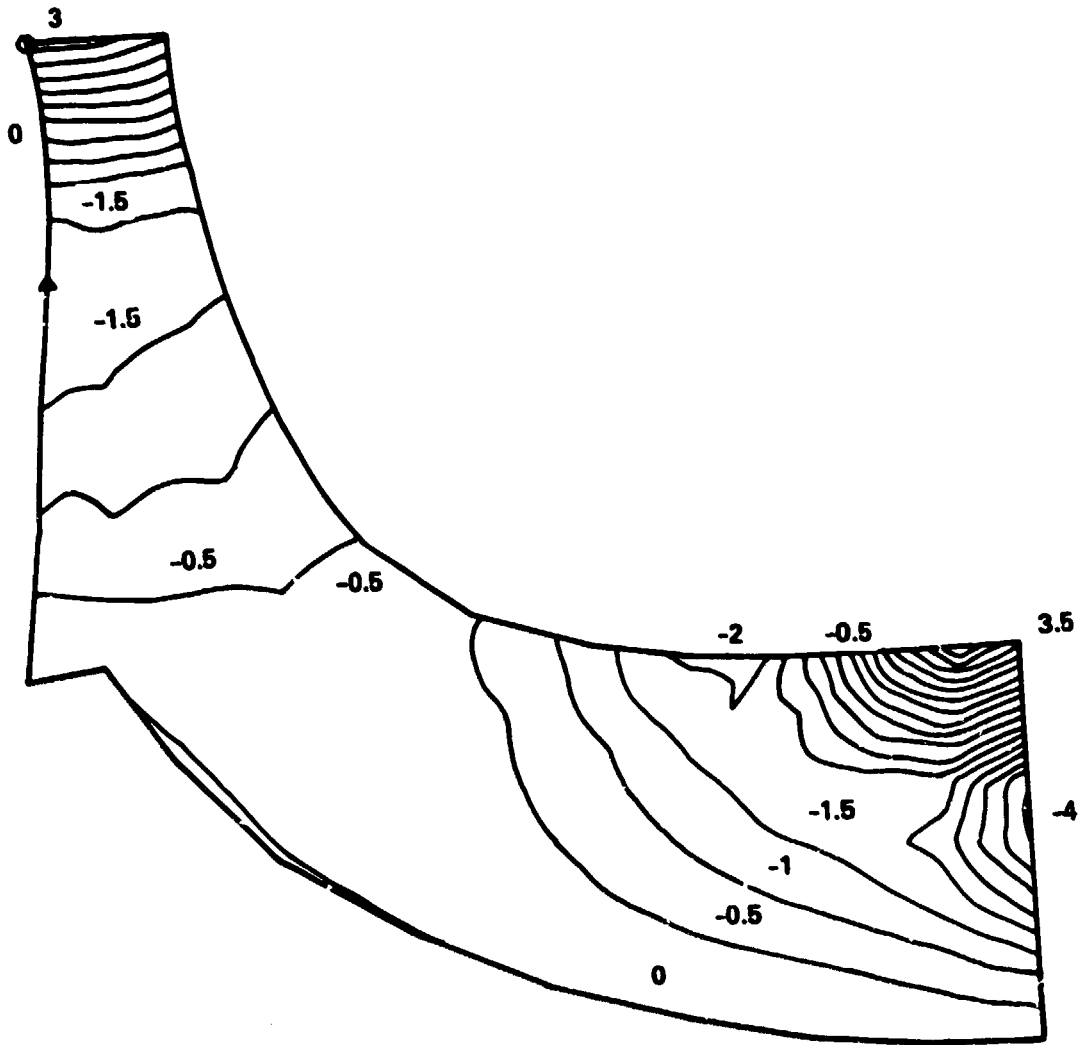


Figure 177. Mode Shape No. 4 with Normalized Displacements at 5969 rad/s (57,000 RPM).

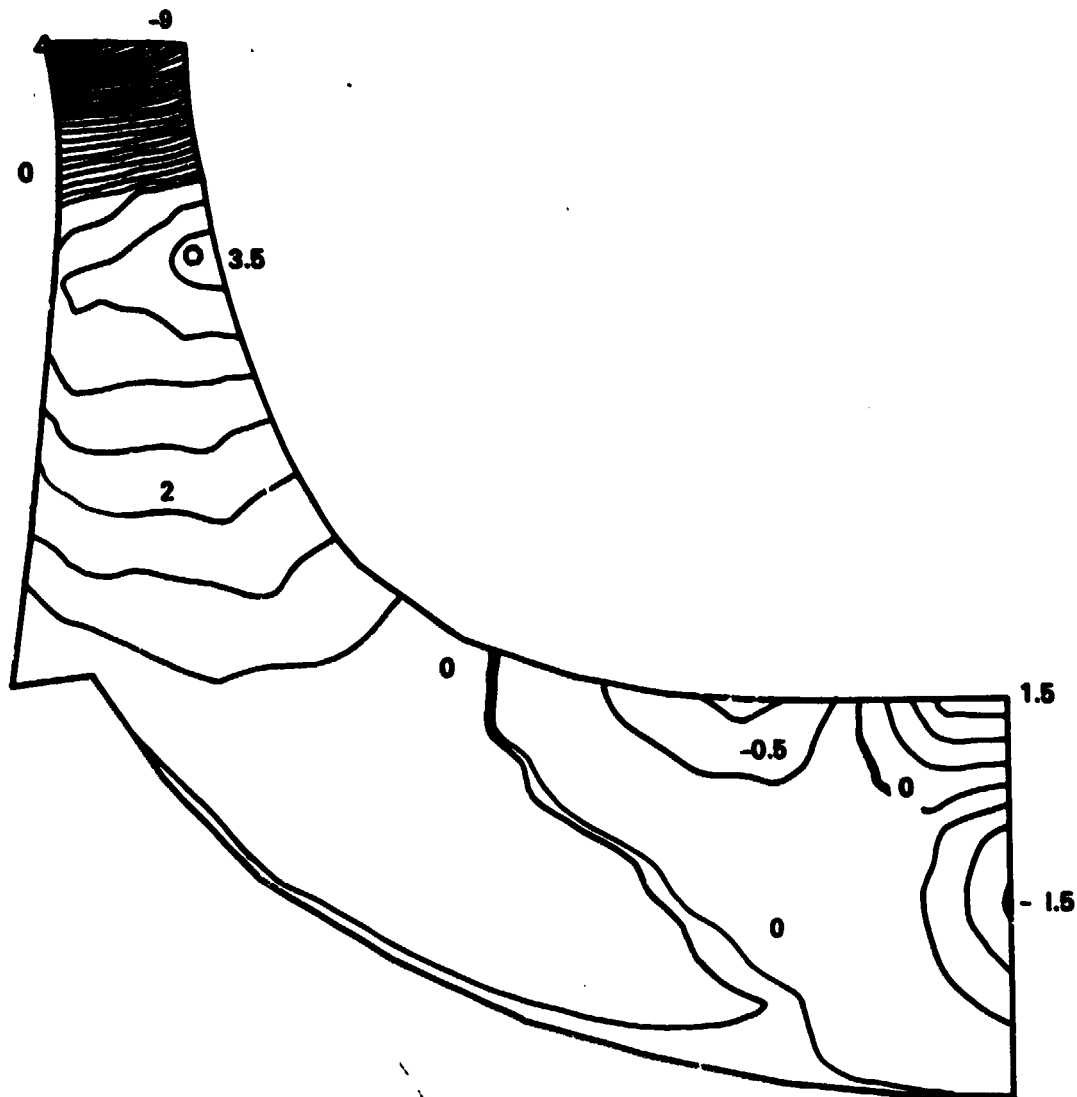


Figure 178. Mode Shape No. 5 with Normalized Displacements at 5969 rad/s (57,000 RPM).

The minimum stress-rupture blade life at the maximum power condition is 2570 hours. This number was calculated by increasing the average-section radial stress from the 3-dimensional analysis by 20 percent, and was based on prior Garrett experience with both radial and axial turbines. This accounted for locally high stress influences and possible geometry variations from blade to blade. A corresponding section average temperature plus 28K (50°F), and the -3σ stress-rupture properties of DS Mar-M 247 were used to calculate a conservative rupture-life estimate. This calculation was performed at various sections until a minimum life was identified. The critical area in this design was located at a radius of 10.2 cm (4.0 in.) near the inducer tip and displayed a stress of 269 MPa (39 ksi), with an associated metal temperature of 1128K (1570°F).

The same procedure was used to calculate rupture damage at other critical power points. At 60-percent power, despite a rotor total inlet temperature remaining at 1589K (2400°F), the blade relative total temperature dropped over 56K (100°F) at the maximum power point. Internal and external heat-transfer rate changes resulted in a decrease in metal temperature of approximately 33K (60°F). Even with greater mission time, rupture damage at 60-percent power was substantially less than that shown at 100-percent power. With a linear damage accumulation, the total mission life of the rotor was 8500 hours.

- o Bore LCF Life - Bore LCF life is determined by the stress range endured during each mission cycle. To determine the stress range, total knowledge of engine-operating environmental-boundary conditions along with a specific engine design is required so that thorough transient-thermal and stress analyses can be made. Transient analysis is not available since this was beyond the scope of this study. However, a 1310 MPa (190 ksi) stress range was assumed, and was the maximum pseudo-elastic bore stress at the full-engine-power condition.

Neuber equations that relate a nonlinear and history-dependent stress/strain behavior of notch roots to the nominal stress and strain of surrounding material were used to refer pseudo-elastic calculated stress to uniaxial tensile specimen data. The calculations indicated that the disk would have a minimum life of 2000 engine-start cycles.

The established design goal in conjunction with the 4000-hour mission life was 4800 cycles. Improvements in the existing design could be made by a reduction in peak bore stress if the bore diameter were decreased. This diameter is not considered a hard, fixed value and could be optimized in further engine studies. However, this was beyond the scope of the present study.

- o Blade HCF Life - Blade HCF is not considered a problem for this turbine because the blade fundamental frequency is above the 5th engine order, and the selected stator count avoids excitation of the blade vibration.

7.2.3.6 Rotor Design Conclusions and Recommendations

The current design incorporating a nonradiality concept successfully solved blade-stress problems. Further improvements can be achieved with a detailed final mechanical design effort. Although the bore life does not meet the 4000-cycle turbine life requirement, improvements can be made by modifying the disk geometry in a full-scale engine-design program and by conducting detailed transient-thermal and stress analyses.

Blade cooling-flow passages are a vital part of the current design. However, without a complete 3-dimensional thermal analysis it is difficult to achieve an accurate blade-temperature distribution and thermal-stress analysis. Finally, material properties used in this design and analysis were based on current available test data. With the material technology advancements that are expected by 1988, the present turbine design durability is likely to increase substantially.

8.0 FINAL PERFORMANCE EVALUATION - SELECTED COOLED, VARIABLE-AREA RADIAL TURBINE DESIGN

Upon completion of the detailed aerodynamic design and mechanical substantiation phase of the Cooled, Variable-Area Radial Turbine Program, turbine performance was reanalyzed for the entire duty cycle (50- to 100-percent power). As previously indicated, the duty-cycle performance optimization was based on iterating the 100-percent power vector diagram until acceptable part-power characteristics were achieved. The predicted duty cycle efficiency characteristics are therefore based on the selected 100-percent power vector diagram, geometry, and efficiency level. The optimized one-dimensional vector diagram is presented in Figure 72, and the final stage meridional geometry is shown in Figure 128. A detailed estimate of the 100-percent power efficiency, starting with the specific speed correlation (Figure 1), is presented in Table X. The part-power efficiency characteristics were predicted using the techniques described in Section 3.2. Additional aerodynamic and cooling flow effects established during the program were applied to arrive at the duty cycle performance characteristics shown in Figure 179. The interturbine duct loss correlation shown in Figure 4 was applied to obtain the overall cooled, variable-area radial turbine system performance.

Table X shows that the major loss associated with the uncooled stage total efficiency is due to the combined effects of rotor shroud and backface clearance (-4.67 points). However, based on previous Garrett radial turbine designs, further reductions in these clearance values are not considered realistic. With fixed backface and shroud clearances, the performance penalties are directly related to rotor inlet and exit passage height. The rotor inlet passage height (b_4) is established from continuity with the inducer tip radius (set by rotational and tip speeds) and a specified absolute flow angle (α_4). The absolute flow has already been increased from 72.0 to 75.0 degrees to minimize the passage width reduction which resulted from the turbine-compressor speed study (Section 5.1). Therefore increasing absolute flow angle further (say to 80.0 degrees) would increase the rotor inlet passage height and reduce clearance penalties. The problem with this approach is the uncertainty associated with the additional stator turning and trailing edge blockage which result from the higher flow angle (assuming the vane trailing edge thickness is fixed). If the vane exit blockage losses are similar to that experimentally determined for the axial stator, this approach would result in an unfavorable tradeoff.

Although extensive test data are not available for radial stators, Calvert(11) reported a 0.3 point reduction in efficiency for an increase in radial stator blockage from 4.0 to 14.0 percent. This result indicates that the radial nozzle is less sensitive than axial nozzles to blockage effects. However, further radial nozzle test data are needed before a meaningful performance

TABLE X. ESTIMATED COOLED, VARIABLE-AREA RADIAL TURBINE EFFICIENCY FOR SELECTED STAGE CONFIGURATION WITH ARTICULATED TRAILING EDGE STATOR CONCEPT (100-PERCENT POWER).

Effect	STAGE EFFICIENCY	
	$\eta_{T-T/2-5}$	$\Delta\eta_{T-T/2-5}$
Base efficiency from specific speed correlation	0.945	
Reynolds number effect at $R_E = 3.73 \times 10^5$	0.947	+0.0018
Rotor inducer incidence effects	0.943	-0.0041
Shroud clearance effects at 0.038 cm (0.015 in.)	0.911	-0.0318
Rotor backface clearance effect at 0.076 cm (0.030 in)	0.896	-0.0149
Rotor blade number effects: $N_B = 14$	0.891	-0.0060
Rotor backface disk friction for $N = 5969$ rad/s (57,000 rpm)	0.885	-0.0063
Rotor reaction effects ($R_{STG} = 0.638$)	0.885	0.000
Rotor exit hub blockage effects at $B_R = 0.347$	0.880	-0.0045
Uncooled total-to-total stage efficiency, $\eta_{T-T/2-5}$	0.880	
Variable-stator leakage effect 0.013 cm (0.005 in.) endwall clearance	0.880	0.0
Stator and rotor cooling flow effects	0.866	-0.014
Cooled stage total-to-total stage efficiency with leakage	0.866	
Interturbine duct, ($\Delta P/P _{5-6} = 0.060$)	0.833	-0.033
Cooled system total-to-total efficiency, $\eta_{T-T/2-6}$	0.833	

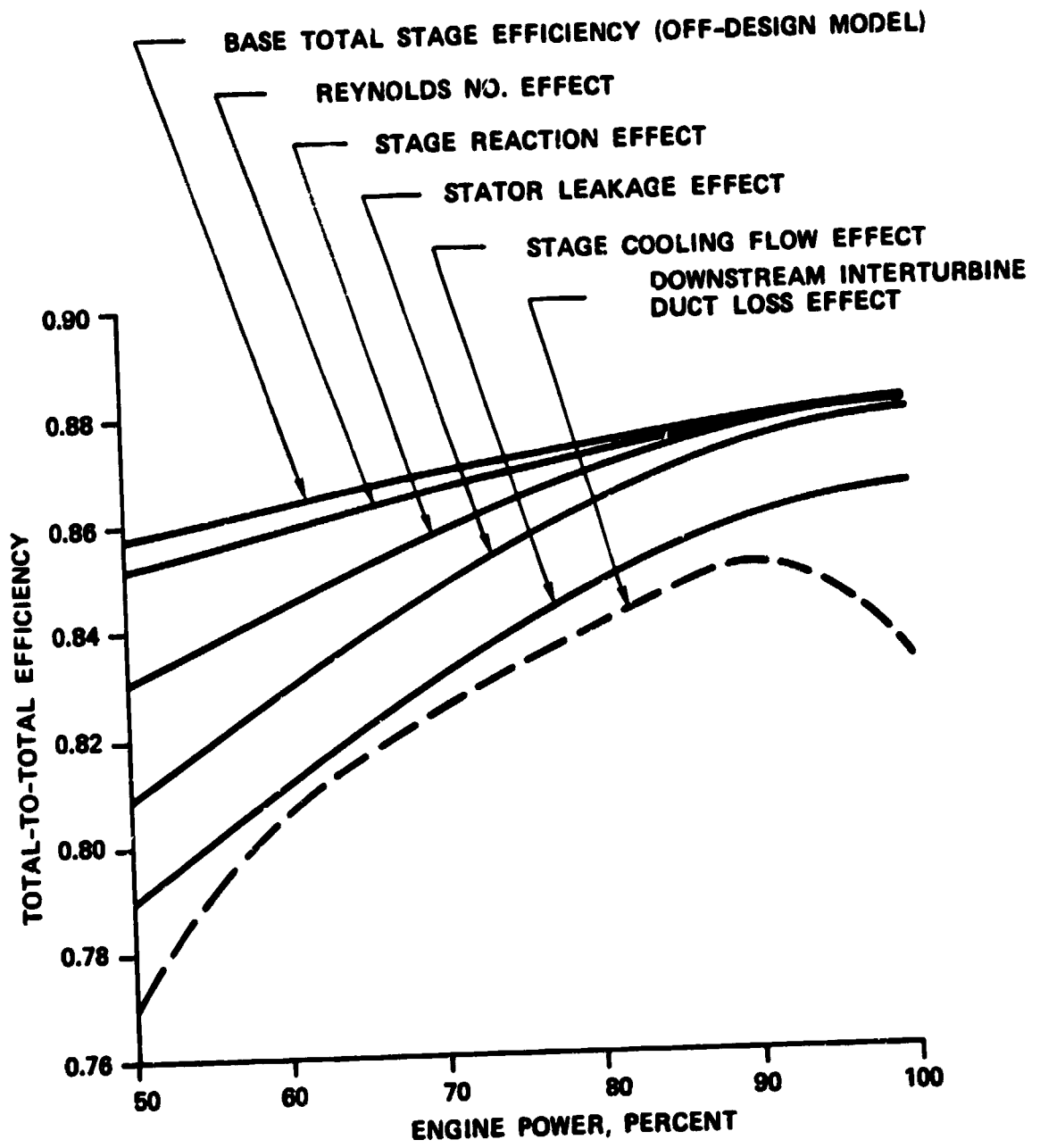


Figure 179. Part-Power Efficiency Characteristics for the Selected Cooled, Variable-Area Radial Turbine with the Articulated Trailing-Edge Stator Concept.

tradeoff between stator blockage and rotor inducer clearance can be established. The situation is similar at the rotor exducer, that is, as the rotor exit passage height is increased to minimize clearance effects, blade turning and trailing edge blockage increases. Although analytical results in conjunction with rotor exit survey traces indicate the radial turbine is less sensitive than axial rotors, experimental data are not available.

Future reductions in clearance penalties may be possible with innovative shroud treatment concepts. Shroud treatment methods to minimize clearance effects for axial turbines have been evaluated with promising results but have not yet been applied to radial turbines. The use of a shroud and backface clearance treatment appears feasible for radial turbines, but was not attempted for this study since extensive experimentation and analysis to verify and optimize the concept would have been required and was beyond the scope of this program.

Performance improvements could also be projected for the low-aspect ratio variable-area stator. Sidewall contouring and forced work distribution (to unload the vane sidewalls) have been successfully applied to axial turbine designs over the past few years. These methods should also apply to radial turbine stators. Although sidewall contouring was used with the variable-area stator concepts, no additional performance credit was assigned, since the stator was an integrated design and identification of sidewall contouring effects alone would be difficult to assess in the follow-on test program.

The performance penalty for the articulated trailing-edge stator endwall leakage is predicted to be zero at 100-percent power since the pivot angle is equal to the average vane exit angle (Equation 6 on page 77). However, Figure 95 shows that, although the trailing edge loading is relatively low at 100-percent power, zero leakage is not expected. This again illustrates the uncertainties associated with predicting the performance of the variable-area radial turbine without meaningful experimental data.

The predicted performance penalty for all cooling flow effects is -1.4 points at maximum power. The majority of the cooling flow penalties are associated with either stator cooling or rotor external cooling which is introduced into the rotor main-stream flow (see Section 5.2). Since the models for these cooling flow effects were based on previous radial and axial turbine experimental data, these predictions are considered reliable.

Therefore, the major uncertainty is associated with the effect of rotor internal cooling flow. The final rotor internal cooling flow distribution and design is shown in Figure 140. This design shows 5.95 percent cooling flow introduced at a rotor back-face radius of 4.953 cm (1.950 in.). The cooling flow is divided

in the inducer hub region: 2.6 percent is directed to the inducer tip, and the remainder is directed to the exducer trailing edge through four separate passages. In order to achieve the efficiency shown in Table X, the pumping work required to deliver the cooling flow to the inducer and exducer regions must be offset by either expansion work (derived from the cooling flow upon entering the rotor mainstream flow in the inducer region) or by a reduction in rotor tip clearance effects (due to the cooling flow discharging into the clearance area in the exducer region). Since the rotor internal cooling flow scheme used for the detailed parametric study (Figure 42) differs considerably from the final scheme derived from the detailed rotor mechanical design (Figure 140), the logic for the prediction of the final rotor internal cooling flow effects must be reevaluated.

Assuming no preswirl of the rotor internal cooling flow, the inducer pumping work is 2.38 percent of the turbine output and the exducer pumping work is 0.985 percent. However, if the cooling flow is preswirled to the rotor cooling flow entry wheel speed (295.6 m/s, 970 ft/sec), the inducer cooling flow pumping work is reduced to 1.87 percent and the exducer pumping work is reduced to 0.33 percent which results in a total reduction in turbine output power of 2.2 percent (again assuming no offsetting effects).

The total effect of preswirl alone, therefore, is an increase in turbine output of 1.165 percent. Since there appears to be no fundamental mechanical or aerodynamic problems associated with incorporating the cooling flow preswirl (equal to rotor wheel speed), the application of preswirl is implicit in the follow-on test program described in Section 9D.

Even with preswirl vanes, however, there is still a 2.2 percent decrement in efficiency between what is predicted by the cooling flow model and the remaining pumping work required. In the inducer region, 1.87 percent pumping work must be offset by either cooling flow expansion work after entering the rotor mainstream in the inducer region, or by a reduction in backface and exducer shroud clearance effects. If the inducer cooling flow expansion work is similar to that measured for the introduction of shroud and backface seal cooling flow in the inducer tip region (which was 55 percent effective), this will offset 1.03 percent of the required inducer pumping work. The remaining 0.83 percent inducer pumping work must be offset by a reduction in backface and inducer shroud clearance effects. This reduction is considered to be realistic in the light of previous axial turbine tip discharge cooling flow test data. In the exducer, the rotor trailing edge discharge cooling flow must offset 0.33 percent cooling flow pumping work. Based on previous inhouse axial turbine experimental data with rotor trailing edge discharge, this is also considered to be realistic.

The 6.0-percent interturbine duct total pressure loss at maximum power is derived from the loss model presented in Figure 4. This model was based on typical interturbine duct configurations with struts and swirl. Alternate interturbine duct configurations are certainly possible and should be investigated in future programs. For instance, the duct struts could be eliminated with an articulated downstream power turbine vane. The leading-edge portion of the vanes would then be used to support the duct hub contour.

The turbine efficiency characteristics from 50- to 100-percent power are presented in Figure 179. The reduction in efficiency at lower power settings is due to an increase in stator and rotor losses at constant speed and pressure ratio. The stage reaction effect is due to a reduction in rotor exit relative velocity as through-flow is reduced. This effect could be minimized by increasing reaction at maximum power (higher rotor exit swirl and velocity). However, duct loss would increase rapidly and would offset the gains achieved at part-power. (For example, reducing reaction effects by 0.25 point at 50-percent power would decrease performance at 100-percent power by 1.0 to 1.5 points.)

C-4

9.0 FOLLOW-ON TEST PROGRAM PLAN

9.1 Program Objective

The Variable-Area Radial Turbine follow-on test program plan will consist of:

- o Completion of detailed design;
- o Preparation of fabrication drawings; and
- o Fabrication and aerodynamic testing.

The overall program objective is to establish the performance potential of the cooled, variable-area radial turbine concept within a 30-month period. The test program will consist of the following tasks:

- o Task I - Completion of detailed design and preparation of rig detail drawings;
- o Task II - Test-rig hardware fabrication;
- o Task III - Overall stage performance evaluation for both the articulated trailing-edge and movable sidewall variable-area radial turbine design concepts;
- o Task IV - Analysis of stage results;
- o Task V - Detailed flow measurements at both stator and rotor exit planes; and
- o Task VI - Detailed flow measurements.

9.2 Test Rig Description

The variable-area radial turbine test rig will be similar to previous Garrett radial turbine test rigs. The rig will consist of an inlet plenum that will house a pressure-drop screen and flow straightening tubes to ensure uniform flow through the turbine test component. The test-rig turbine rotor will be overhung on a double spring-loaded ball-bearing assembly. This design precludes skidding of the ball bearings and makes assembly and disassembly of the rig more straightforward when compared to a straddle-mounted design. For the variable-area laminated rotor, a tie bolt will be used to simplify assembly and disassembly.

The turbine exhaust duct will be connected via an adapter to an adiabatic mixing duct, which in turn will be connected to the plant vacuum system. When the rig is mounted on the test stand,

the rotor shaft will be connected first to a reduction gearbox and then to a power absorption dynamometer. For the variable-area radial turbine test, a high-speed torque meter will be installed between the rig and the reduction gearbox.

Plant air will be blended to the desired inlet temperature upstream of the turbine plenum, then pass through an air filter. The mass flow will then be measured using an orifice plate. Further downstream, a portion of the flow will be directed to smaller air lines for cooling flow simulation, as shown in Figure 180.

9.3 Overall Turbine Performance Measurement Instrumentation

Aerodynamic and mechanical instrumentation will be provided for determining overall turbine performance and for monitoring test-rig integrity. Table XI lists the instrumentation that will be incorporated into the test rig for overall performance definition. Overall stage performance for the cooled rotor will be evaluated over a range of:

- o Corrected speeds;
- o Stage total pressure ratios;
- o Stator area ratios; and
- o Cooling flow rates.

To obtain detailed stator and rotor exit flow measurements, use of a sophisticated probe actuator system will be required. Garrett has developed a microcomputer-controlled survey actuator/data acquisition system for use in fan-rig testing. A more compact and versatile version of this system is scheduled for development in 1981 for use in compressor and turbine testing. This modified version of the survey system will be available for use in the cooled, variable-area radial turbine testing program.

9.4 Program Plan

Figure 181 is the program schedule and shows completion of the first-stage performance testing in 18 months, detailed flow measurements in 26 months, and culmination with the submission of the final report in 30 months.

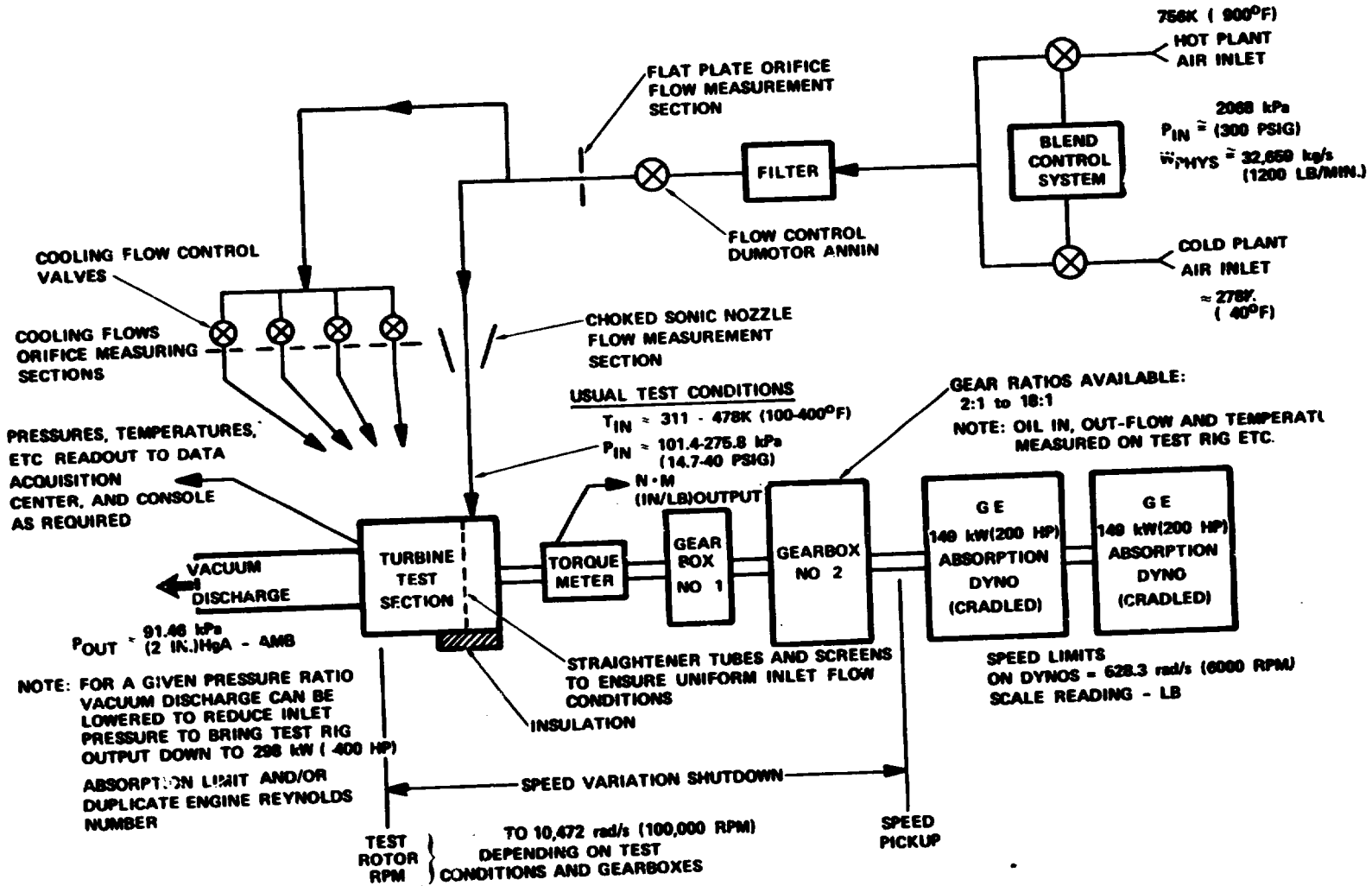


Figure 180. Cooled Variable-Area Radial Turbine Component Cold-Air Test Rig.

TABLE XI. INSTRUMENTATION FOR OVERALL TURBINE PERFORMANCE.

<u>Description/Location</u>	<u>Type</u>
Turbine inlet	Rosemont temperature sensors
Turbine inlet	Thermocouples
Turbine inlet	Total pressure (Kiel probes)
Turbine inlet	Survey probe
Turbine inlet	Static pressure
Rotor backface clearance probes	Capacitance
Rotor shroud axial clearance probes	Capacitance
Rotor shroud radial clearance probes	Capacitance
Rotor exit shroud	Static pressure
Rotor exit hub	Static pressure
Rotor exit	Total pressure (Kiel probes)
Rotor exit	Cobra survey probes
Downstream adiabatic duct	Rosemont temperature sensors
Downstream adiabatic duct	Thermocouples
High-speed torque meter	Phasemeter

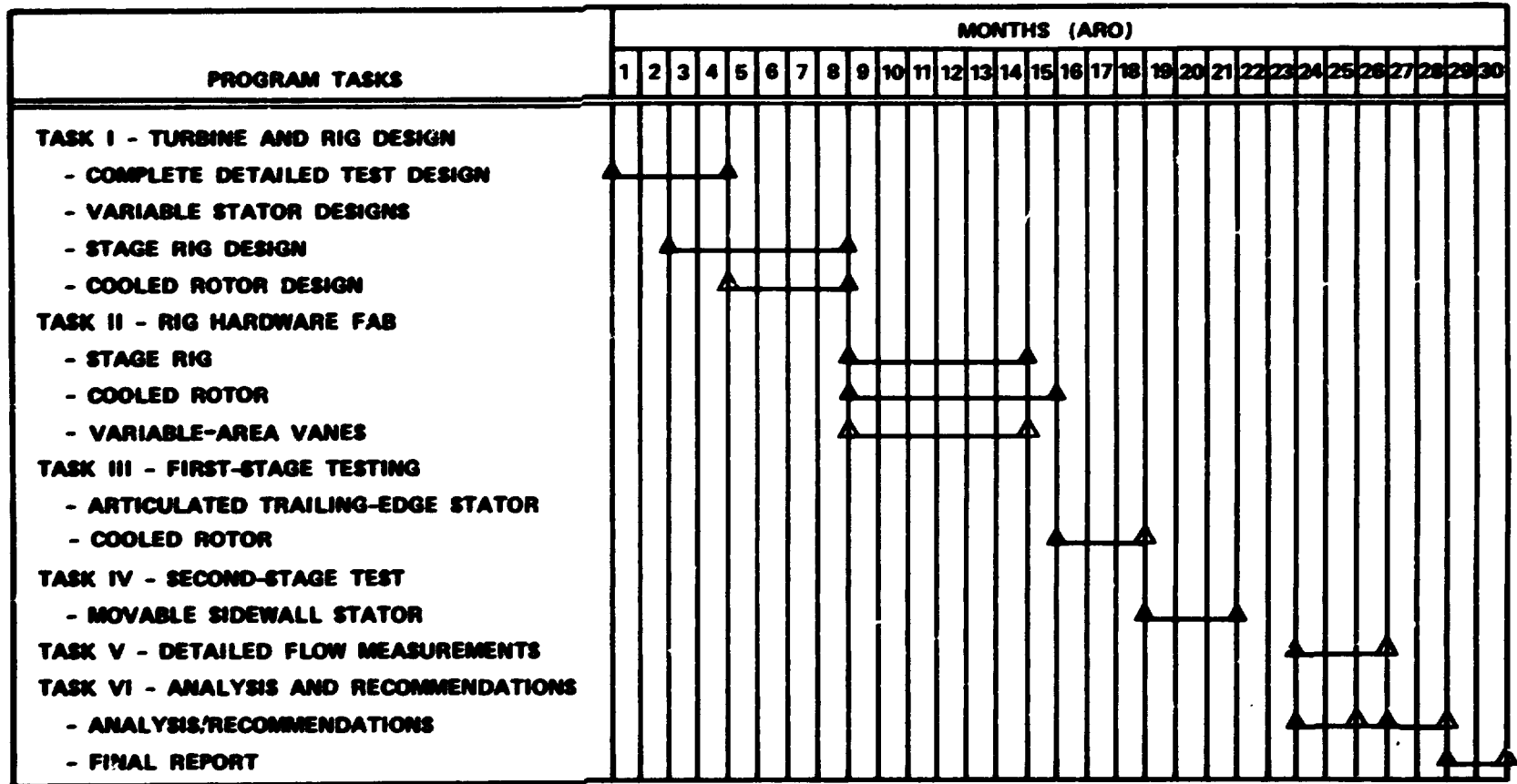


Figure 181. Cooled, Variable-Area Radial Turbine, Program Schedule.

10.0 CONCLUSIONS AND RECOMMENDATIONS

The results of the Cooled, Variable-Area Radial Turbine Program show that a high-temperature 1589K (2400°F) turbine is mechanically feasible with projected 1988 material properties. The design duty cycle life of 4000 hours was achieved with cooled Mar-M 247 DS laminated blades and a powder metal disk. The optimized rotor design allows a relatively high inducer tip speed of 640 m/s (2100 ft/sec) and a 0.17-radian (10-degrees) rotor inlet blade angle. Optimized duty-cycle performance was established from the detailed parametric study that showed high rotor exit swirl and reaction were required at 100-percent power. Establishing the performance potential of the variable-area radial turbine was complicated by the lack of meaningful correlations for stator leakage and stage cooling flow effects. In addition, the performance was limited by a lower-than-desired rotational speed due to the combined compressor-turbine performance characteristics. At an optimized cycle pressure ratio of 17:1 and a rotational speed of 5969 rad/s (57,000 rpm), the maximum attainable stage efficiency at 100-percent power is 0.98. The program established two viable variable stator concepts: the articulated trailing-edge and the rotating-translating movable sidewall.

Additional conclusions and recommendations resulting from the Cooled Variable-Area Radial Turbine Program are:

- o The characteristically large vane sidewall surface area of the radial stator (compared to axial stator sidewalls) results in high sidewall cooling flows.
- o Maintaining a constant pressure ratio over the entire duty cycle results in significant increases in vane and endwall cooling flow percentages (since cooling flow orifice pressure and temperature remain constant) as the turbine mainstream flow is reduced from 100- to 60-percent engine power. However, since the mainstream temperature is constant and the local vane and endwall velocities are relatively constant, with engine power setting, the cooling flow magnitude must remain fixed to achieve the desired metal temperatures. Therefore, metering the stator cooling flow as a function of power setting is not feasible.
- o It may be possible to meter the rotor cooling flows at reduced power since rotor-inlet relative temperature decreases with reduced through-flow. Further detailed analyses and improved predictions for the rotor inducer velocity distribution will be required to define the reduction possible.
- o The limited correlations available for the performance of a variable-geometry radial turbine with vane leakage and cooling result in significant performance uncertainties.

- o Preswirling the rotor internal cooling flow to the rotor wheel speed increases the turbine output power by 1.165 percent. Nevertheless, an additional 2.2 percent cooling flow pumping work must be offset in order to achieve predicted performance levels. The uncertainties associated with vane leakage and stator and rotor cooling flows illustrates the need for a comprehensive follow-on test program.
- o The turbine system (stage plus interturbine duct) optimization technique is an effective method for identifying optimum overall duty-cycle performance.
- o Evaluation of the predicted turbine performance suggests the following: 1) Stator performance can be increased by further optimization of vane endwall contouring in conjunction with a forced work distribution, 2) The effects of rotor backface and shroud clearance can be reduced with shroud treatment concepts. 3) Interturbine duct losses can be reduced by either eliminating the duct struts, reducing the duct endwall curvature by incorporating a conical power turbine flow path or eliminating the duct altogether with a close-coupled power turbine. It is suggested that these areas should be investigated in future research.

11.0 REFERENCES

1. Vershure, R. W., Jr., G. D. Large, L. J. Meyer, and J. M. Lane, "A Cooled Laminated Radial Turbine Technology Demonstration," Paper AIAA-80-0300, presented at AIAA 18th Aerospace Sciences Meeting, Pasadena, California, 1980.
2. Kofskey, M. G. and W. M. Nusbaum, "Effects of Specific Speed on Experimental Performance of a Radial-Inflow Turbine," NASA TN D-6605, February 1972.
3. Stanitz, J. D., "Some Theoretical Aerodynamic Investigations of Impellers in Radial and Mixed Flow Centrifugal Compressors," Trans. ASME Vol. 74, No. 4, May 1952.
4. Large, G. D., "Advanced Radial Turbine Study Program," TARADCOM R&D Technical Report No. 12370, June 1978.
5. Large, G. D., Finger D. G., and Linder C. G., "Analytical Design of an Advanced Radial Turbine," NASA CR-16570, February 1981.
6. Dovzhik, S. A. and V. M. Kartavenko, "Measurement of the Effect of Flow Swirl on the Efficiency of Annular Ducts and Exhaust Nozzles of Axial Turbomachines," Fluid Mechanics Soviet Research, Vol. 4, No. 4, July-August 1975.
7. Kidwell, J. R. and G. D. Large, "Advanced Technology Components for Model GTC305-2 Aircraft Auxiliary Power System," AFAPL-TR-2106, February 1980.
8. Nusbaum, W. J. and C. A. Wassenhauer, "Experimental Performance Evaluation of a 4.59-Inch Radial Inflow Turbine Over a Range of Reynolds Numbers," NASA TN D-3835, February 1967.
9. Penny, N., "Rover Case History of Small Gas Turbines," SAE Paper No. 634A, January 1, 1963.
10. Futral, Jr., W. M. and D. E. Holeski, "Experimental Results of Varying the Blade-Shroud Clearance in a 6.02-Inch Radial-Inflow Turbine," NASA TN D-5513, 1970.
11. Calvert, G. S. and U. Opapuu, "Design and Evaluation of a High-Temperature Radial Turbine," USAAVLABS Technical Report 68-69, Phase I - Final Report, January 1969.
12. Daily, J. W. and R. E. Nece, "Chamber Dimensions Effects on Induced Flow and Frictional Resistance of Enclosed Rotating Disks," Journal of Basic Engineering, Vol. 82, No. 1, March 1960, pp. 217-232.

13. Turbine Design and Application, NASA SP-290, Vol. 2, 1973, pp. 131-138.
14. Meitner, P. L. and A. J. Glassman, "Loss Model for Off-Design Performance Analysis of Radial Turbines with Pivoting Vane; Variable-Area Stators," NASA Technical Memorandum 81532, October 1980.
15. McLallin, K. L. and J. E. Haas, "Experimental Performance and Analysis of 15.04-Centimeter Tip-Diameter, Radial In-Flow Turbine with Work Factor of 1.125 and Thick Blading," NASA Technical Paper 1730, October 1980.
16. Wasserbauer, C. A. and A. J. Glassman, "Fortran Program for Predicting Off-Design Performance of Radial-Inflow Turbines," NASA TN D-8063, September 1975.
17. Hoppin III, G. S., T. E. Strangman, R. E. Dennis, and C. E. Corrigan, "Materials for Advanced Turbine Engines, NASA Contract NAS3-20073, Interim Reports for 1980.
18. Sink, L. W., G. S. Hoppin III, M. Fujii, "Low-Cost Directionally-Solidified Turbine Blades," NASA CR-159464, January 1979.
19. Felten, E. J., T. E. Strangman, and N. E. Ulion, "Coatings for Directional Eutectics," NASA CR-134735, October, 1974.
20. Gemma, A. E., B. S. Langer, and G. R. Leverant, "Thermo-mechanical Fatigue Crack Propagation in an Anisotropic (Directionally Solidified) Nickel-Base Superalloy," in Thermal Fatigue of Materials and Components, ASTM STP 612, pp. 199-213, 1976.
21. Bizon, P. T., R. L. Dreshfield, and F. D. Calfo, "Effect of Grain Orientation and Coating on Thermal Fatigue Resistance of a Directionally-Solidified Superalloy," NASA TM 79129, April, 1979.
22. Bizon, P. T. and Spera, D. A., "Comparative Thermal Fatigue Resistances of Twenty-Six Nickel- and Cobalt-Base Alloys," NASA TN D-8071, October, 1975.
23. Carlson, D. M., "P/M AF115 Dual Property Disk Process Development," (Proceedings of the Fourth International Symposium on Superalloys)," Champion, Pa., pp. 501-511, 1980.
24. Ewing, B. A., "A Solid-to-Solid HIP-Bond Processing Concept for the Manufacture of Dual-Property Turbine Wheels for Small Gas Turbines," (Proceedings of Fourth International Symposium on Superalloys)" Champion, Pa., pp. 169-178, 1980.

25. Katsanis, T. and W. McNally, "FORTRAN Program for Calculating Velocities and Streamlines on the Hub-Shroud, Mid-Channel Flow Surface of an Axial- or Mixed-Flow Turbomachine", NASA TN D-7343, July 1973.
26. Japikse, D., "Progress in Numerical Turbomachinery Analysis", Numerical/Laboratory Computer Methods in Fluid Mechanics, presented at the ASME Winter Annual Meeting, New York, NY, 1976, pp. 253-278.
27. DeVries, G. and D. H. Norrie, "The Application of the Finite-Element Technique to Potential Flow Problems", Trans. AME, Journal of Applied Mechanics, December 1971.
28. Thompson, D. S., "Finite-Element Analysis of the Flow-Through a Cascade of Aerofoils," Turbo, TR 45, Engineering Department, Cambridge University, 1973.
29. Prince, T. C., "Prediction of Transonic Inviscid Steady Flow in Cascades by Finite-Element Methods," General Electric Report No. R76AEG192.
30. Laskaris, T. E., "Finite-Element Analysis of Three Dimensional Potential Flow in Turbomachines," AIAA Journal, Vol. 16, No. 7, July 1978.
31. Hutton, S. and D. Anderson, "Finite Element Method, A Galerkin Approach," Journal of Eng. Mech., ASCE, Vol. 96, 1971.
32. Hamed, A. and E. Baskharone, "Analysis of the Three Dimensional Flow in a Turbine Scroll," Journal of Fluids Engineering, Vol. 102, No. 3, Sept. 1980.
33. Baskharone, E. and A. Hamed, "A New Approach in Cascade Flow Analysis Using the Finite-Element Method," AIAA Journal, Vol. 13, No. 1, January 1981.
34. Smith, Jr., L. H., "The Radial-Equilibrium Equation of Turbomachinery," Journal of Engineering for Power, January 1966, pp. 1-12.
35. Katsanis, T., "Use of Arbitrary Quasi-Orthogonals for Calculating Flow Distribution in the Meridional Plane of a Turbomachine," NASA TN D-2546, December 1964.
36. Stanitz, J. D. and V. D. Prian, "A Rapid Approximation Method for Determining Velocity Distribution of Impeller of Centrifugal Compressors," NACA TN 2421, 1951.

PRECEDING PAGE BLANK NOT FILMED

No. of
Copies

- | | | | |
|----|---|-------------|----|
| 1. | NASA-Lewis Research Center
21000 Brookpark Road
Cleveland, OH 44135 | | |
| | Attn: Report Control Office | M.S.
5-5 | 1 |
| | Technology Utilization Office | 7-3 | 1 |
| | Library | 60-3 | 2 |
| | Science & Technology Directorate | 3-7 | 1 |
| | Aerothermodynamics & Fuels
Division | 86-5 | 1 |
| | G. Virosteck | 501-11 | 1 |
| | H. E. Rohlik | 77-2 | 1 |
| | L. A. Povinelli | 77-2 | 1 |
| | P. L. Meitner | 77-2 | 15 |
| | K. C. Civinskas | 77-2 | 1 |
| | R. J. Roelke | 77-2 | 1 |
| | K. L. McLallin | 77-2 | 1 |
| | J. E. Haas | 77-2 | 1 |
| | R. W. Koenig | 500-208 | 1 |
| | D. G. Evans | 500-210 | 1 |
| | H. W. Davison | 500-210 | 1 |
| | R. E. Kielb | 49-6 | 1 |
| | W. C. Strack | 501-10 | 1 |
| 2. | NASA Scientific and Technical Information Facility
Attn: Accessioning Department
P.O. Box 8757
Balt./Wash. International Airport, MD 21240 | | 25 |
| 3. | E. E. Bailey
AFAPL/DO
Wright Patterson Air Force Base, OH 45433 | | 1 |
| 4. | Director
Propulsion Laboratory MS 302-2
U.S. Army Research & Technology
Laboratories (AVRADCOM)
21000 Brookpark Road
Cleveland, OH 44135 | | 2 |
| 5. | Director
Applied Technology Laboratory
U.S. Army Research & Technology
Laboratories (AVRADCOM)
Attn: DAVDL-ATL-AT
Ft. Eustic, VA 23604 | | 2 |

	<u>No. of Copies</u>
6. Director U.S. Army Research & Technology Laboratories (AVRADCOM) Attn: DAVDL-As (H. Wilsted) MS 207-5 Ames Research Center Moffett Field, CA 94035	1
7. Director U.S. Army Research & Technology Laboratories (AVRADCOM) Attn: DAVDL-POM MS 206-4 Ames Research center Moffett Field, CA 94035	7
8. Commander U.S. Army Aviation R&D Command Attn: DRDAV-N (Borgman, Titus) 4300 Goodfellow Boulevard St. Louis, MO 63120	2
9. Commander U.S. Army Aviation R&D Command Attn: DRDAV-EQP 4300 Goodfellow Boulevard St. Louis, MO 63120	1
10. Commander U.S. Army Mobility Equipment R&D Command Attn: DRDME-ZT (Mr. Dinger) Ft. Belvoir, VA 22060	1
11. Commander U.S. Army Tank-Automotive R&D Command Attn: DRDTA-RGE (Mr. Whitcomb) Warren, MI 48090	1
12. Raymond M. Standahar Staff Specialist for Propulsion OSD/OUSDR&E(ET) Room 1809, The Pentagon Washington, DC 20301	1
13. Commander Army Research Office Attn: Mr. Murray P.O. Box 12211 Research Triangle Park, NC 27709	1

	<u>No. of Copies</u>
14. Commandant U.S. Military Academy Attn: Chief, Department of Mechanics West Point, NY 10995	1
15. Commander Southwest Research Institute U.S. Army Fuels & Lubricants Research Laboratory P.O. Drawer 28510 San Antonio, TX 78284	1
16. Department of the Army Aviation Systems Division ODCSRDA (DAMA-WSA, R. Ballard) Room B454, The Pentagon Washington, DC 20310	1
17. U.S. Army Material Systems Analysis Activity Attn: DRXSY-MP (Mr. Herbert Cohen) Aberdeen Proving Ground, MD 21005	1
18. Commander U.S. Army Troop Support & Aviation Material Readiness Command Attn: DRSTS-DIL 4300 Goodfellow Boulevard St. Louis, MO 63120	1
19. Teledyne CAE Attn: C. Rogo 1330 Laskey Road Toledo, OH 43612	2
20. Detroit Diesel Allison Attn: Don Tipton P.O. Box 894 Indianapolis, IN 46206	1
21. AVCO-Lycoming Attn: Steve White 550 South Main Street Stratford, CT 06497	1
22. Solar Turbines International Attn: Colin Rodgers 2200 Pacific Highway San Diego, CA 92112	1

	<u>No. of Copies</u>
23. Sundstrand Corporation Attn: Paul Hermann 4747 Harrison Avenue Rockford, IL 61101	1
24. Williams Research Corporation Attn: R. F. Honn MS 4-8 2280 West Maple Road Walled Lake, MI 48088	1
25. Creare, Inc. Attn: D. Japikse Hanover, NH 03755	1
26. Cummins Engine Company Attn: Roy Kamo 1900 McKinley Columbus, IN 47201	1
27. Northern Research & Engineering Attn: K. Ginwala 219 Vassar Street Cambridge, MA 02139	1
28. General Electric Company Aircraft Engine Group Attn: Bart J. Ferrari MS 240G1 1000 Western Avenue Lynn, MA 01910	1
29. Pratt & Whitney Aircraft Government Products Division Attn: J. Pete Mitchell MS R16 Palm Beach Gardens Facility P.O. Box 2691 West Palm Beach, FL 33402	1
30. Wallace Murray Corporation Attn: Robert C. Bremer, Jr. 1125 Brookside Avenue P. O. Box 80-B Indianapolis, IN 46206	1
31. Tuskegee Institute Attn: R. Jenkins Department of Mechanical Engineering Tuskegee Institute, AL 36088	1

	<u>No. of Copies</u>
32. General Motors Research Laboratory Attn: David C. Sheridan 12 Mile and Mound Roads Warren, MI 48090	1
33. Ford Motor Company Research and Engineering Center Attn: Robert R. Baker Room E-3172 P.O. Box 2053 Dearborn, MI 48121	1
34. Howmet Turbine Component Corporation Attn: William R. Freeman, Jr. 475 Steamboat Road Greenwich, CT 06830	1